A novel approach for the calibration of the hadronic recoil for the measurement of the mass of the W boson with the ATLAS Experiment

Dissertation zur Erlangung des
Naturwissenschaftlichen Doktorgrades
der Julius-Maximilians-Universität Würzburg

vorgelegt von

Verena Herget

aus Fulda

Würzburg 2018

Eingereicht am: 29.08.2018
bei der Fakultät für Physik und Astronomie

1. Gutachter: Prof. Dr. Raimund Ströhmer
2. Gutachter: Prof. Dr. Ansgar Denner
3. Gutachter: ....
der Dissertation

Vorsitzender: Prof. Dr. Jean Geurts
1. Prüfer: Prof. Dr. Raimund Ströhmer
2. Prüfer: Prof. Dr. Ansgar Denner
3. Prüfer: Prof. Dr. Matthias Kadler
im Promotionskolloquium

Tag des Promotionskolloquiums: 1. Februar 2019

Doktorurkunde ausgehändigt am: ....

Abstract

The measurement of the mass of the W boson is currently one of the most promising precision analyses of the Standard Model, that could ultimately reveal a hint for new physics. The mass of the W boson is determined by comparing the W boson, which cannot be reconstructed directly, to the Z boson, where the full decay signature is available. With the help of Monte Carlo simulations one can extrapolate from the Z boson to the W boson.

Technically speaking, the measurement of the W boson mass is performed by comparing data taken by the ATLAS experiment to a set of calibrated Monte Carlo simulations, which reflect different mass hypotheses. A dedicated calibration of the reconstructed objects in the simulations is crucial for a high precision of the measured value. The comparison of simulated Z boson events to reconstructed Z boson candidates in data allows to derive event weights and scale factors for the calibration.

This thesis presents a new approach to reweight the hadronic recoil in the simulations. The focus of the calibration is on the average hadronic activity visible in the mean of the scalar sum of the hadronic recoil ΣE_T as a function of pileup. In contrast to the standard method, which directly reweights the scalar sum, the dependency to the transverse boson momentum is less strongly affected here. The ΣE_T distribution is modeled first by means of its pileup dependency. Then, the remaining differences in the resolution of the vector sum of the hadronic recoil are scaled. This is done separately for the parallel and the perpendicular component of the hadronic recoil with respect to the reconstructed boson.

This calibration was developed for the dataset taken by the ATLAS experiment at a center of mass energy of 8 TeV in 2012. In addition, the same reweighting procedure is applied to the recent dataset with a low pileup contribution, the *lowMu* runs at 5 TeV and at 13 TeV, taken by ATLAS in November 2017. The dedicated aspects of the reweighting procedure are presented in this thesis. It can be shown that this reweighting approach improves the agreement between data and the simulations effectively for all datasets.

The uncertainties of this reweighting approach as well as the statistical errors are evaluated for a W mass measurement by a template fit to pseudodata for the *lowMu* dataset. A first estimate of these uncertainties is given here. For the pfoEM algorithm a statistical uncertainty of 17 MeV for the 5 TeV dataset and of 18 MeV for the 13 TeV are found for the $W \to \mu\nu$ analysis. The systematic uncertainty introduced by the resolution scaling has the largest effect, a value of 15 MeV is estimated for the 13 TeV dataset in the muon channel.

Zusammenfassung

Die Messung der Masse des W-Bosons ist im Augenblick eine der vielversprechendsten Präzisionsanalysen des Standard Modells, welche letztendlich einen Hinweis auf neue Physik geben kann. Die Masse des W Bosons wird bestimmt, indem das W-Boson, welches nicht direkt rekonstruiert werden kann, mit dem Z-Boson verglichen wird, bei dem die vollständige Zerfallssignatur verfügbar ist. Mit Hilfe von Monte Carlo Simulationen kann vom Z-Boson auf das W-Boson extrapoliert werden.

Genau genommen wird die Messung der Masse des W-Bosons durchgeführt, indem die Daten, die mit dem ATLAS Experiment aufgenommen wurden, mit einem Satz von kalibrierten Monte Carlo Simulationen verglichen wird. Die Simulationen spiegeln dabei verschiedene Massenhypothesen wider. Eine dezidierte Kalibrierung der rekonstruierten Objekte in den Simulationen ist entscheidend für eine hohe Präzision des gemessenen Werts der Masse des W-Bosons. Aus dem Vergleich von simulierten Z-Boson Ereignissen und Z-Bosonen, die aus den Daten rekonstruiert werden, können Ereignisgewichte und Skalierungsfaktoren für die Kalibrierung erzeugt werden.

In dieser Arbeit wird ein neuer Ansatz für die Umgewichtung des hadronischen Rückstoßes in den Simulationen vorgestellt. Der Fokus der Kalibrierung liegt auf der mittleren hadronischen Aktivität, die in der mittleren skalaren Summe des hadronischen Rückstoßes ΣE_T als Funktion des Pileups sichtbar ist. Im Gegensatz zur Standardmethode, welche die Skalarsumme direkt umgewichtet, wird hierbei die Abhängigkeit zum transversalen Impuls des Bosons weniger stark beeinflusst. Die ΣE_T-Verteilung wird zunächst mittels ihrer Abhängigkeit zum Pileup modelliert. Danach werden die verbleibenden Unterschiede in der Auflösung der vektoriellen Summe des hadronischen Rückstoßes skaliert. Dies geschieht separat für die parallele und senkrechte Komponente des hadronischen Rückstoßes, welche in Bezug auf die Richtung des rekonstruierten Bosons gemessen werden.

Die Kalibrierung wurde zunächst für den Datensatz entwickelt, der im Jahr 2012 bei einer Schwerpunktsenergie von 8 TeV mit dem ATLAS Experiment aufgenommen wurde. Zusätzlich wird die Umgewichtungsmethodik auf die neuen Datensätze angewendet, welche von ATLAS im November 2017 bei niedrigem Pileup aufgenommen wurden, den *lowMu* Datensätzen bei Schwerpunktsenergien von 5 TeV und 13 TeV. In dieser Arbeit werden die verschiedenen Aspekte der Kalibrierung präsentiert. Es kann gezeigt werden, dass diese Herangehensweise für die Umgewichtung des hadronischen Rückstoßes zu einer effektiven

Verbesserung der Übereinstimmung zwischen Daten und Simulationen in allen verwendeten Datensätzen führt.

Die zugehörigen Unsicherheiten dieser Kalibrierungsmethode sowie die statistischen Fehler für eine Messung der Masse des W-Bosons werden anhand der Template-Fit-Methode mit Pseudodaten für die *lowMu* Datensätze ausgewertet. Es wird eine erste Abschätzung dieser Unsicherheiten gegeben. Für den pfoEM Algorithmus wird ein statistischer Fehler von 17 MeV für den 5 TeV Datensatz und von 18 MeV für den 13 TeV Datensatz in der $W \to \mu\nu$ Analyse ermittelt. Die systematische Unsicherheit, welche durch die Auflösungsskalierung erzeugt wird, hat den größten Effekt. Für den 13 TeV Datensatz wird ein Fehler von 15 MeV im Myonkanal abgeschätzt.

Contents

CHAPTER 1

Introduction

The Standard Model of elementary particles is one of the most successful theories of modern physics, which comprises theoretical predictions for particle interactions on an energy scale spanning multiple magnitudes. A wide range of phenomena can be precisely explained by the Standard Model, which for example includes the anomalous magnetic dipole moment of the electron a_e[1]. Several particles like the top quark[2], the Higgs Boson[3] or the last missing lepton, the τ neutrino[4], were experimentally detected and their properties measured exactly as predicted by the Standard Model. With all these findings, the Standard Model was wonderfully confirmed over the past decades and has earned its rightful place in the halls of physics.

Nevertheless, several mysteries were discovered over time, like the neutrino mass puzzle, which hint for physics beyond the Standard Model. The interaction of new physics with visible matter must be quite subtle, otherwise something would have already been discovered by now. But it might be at energies just in the reach of today's powerful particle accelerators like the LHC. Direct searches on new physics are one of the main measurements that are performed at high energy experiments like the ATLAS experiment. But also indirect approaches can give new hints on the physics beyond the Standard Model. For example, if the free parameters from the electroweak sector of the Standard Model are experimentally determined, which includes a measurement on the mass of the Higgs boson, the predictions from electroweak theory allow a direct comparison between the current understanding of electroweak physics and the influence of new scenarios. When looking at loop corrections by a top-bottom pair or by a Higgs boson on the W boson propagator, the correlation could be modified by loop corrections of a new high energetic particle (see Fig.1.1). The predictions from the latest electroweak fit [8] including the measurements of the mass of the Higgs boson are found to be just agreeing with the results of the direct measurements of the W boson

---

[1] The experimentally measured value for a_e agrees on more than ten significant figures with the predictions of quantum electrodynamics [1, 2].

[2] The top quark was discovered in 1995 by the two collaborations CDF and D0 at the Tevatron, Fermilab [3, 4].

[3] The Higgs boson was discovered by the ATLAS and CMS experiments in 2012 at the LHC, CERN [5, 6]

[4] The τ neutrino was discovered in the year 2000 by the DONUT collaboration at Fermilab [7].

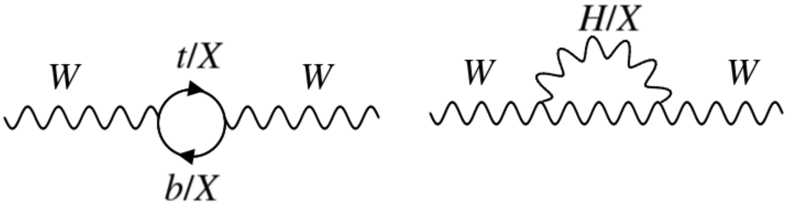

Figure 1.1.: Loop corrections by a top-bottom pair, a Higgs boson and possibly new physics X on the propagator of the W boson in a Feynman diagram representation.

and top quark masses (see Fig.1.2). This bare agreement could turn out to be the effect of a discrepancy, which is currently not measured with high enough precision. Only further measurements can shed light on the question whether the experimental results continue to be in agreement with theory or if a hint for physics beyond the Standard Model is revealed. Therefore, an improvement of the measured values is crucial. As can be seen from the figure, the largest handle is on the uncertainty of the W boson mass. The latest measurement performed by the ATLAS experiment achieved the already precise value of $M_W = (80\,370 \pm 19)\,\text{MeV}$ [9].

The precision measurement of the W boson mass is a challenging endeavor. The cleanest signature of the decay of a W boson can be obtained in the leptonic decay channel into a muon and its neutrino or into an electron and its neutrino, since any hadronic decay into a pair of quarks is nearly impossible to distinguish from the overwhelming background from quark and gluon interactions of a hadron collider. However, the weakly interacting character of the neutrino makes it impossible to directly measure it in a typical experimental setup like the ATLAS detector and thus forbids a direct measurement of the full decay kinematics via its decay products. With indirect methods, which make use of energy and momentum conservation by determining the transverse energy of the balancing recoil against the W boson, a handle is given to nevertheless reconstruct the W boson in the transverse plane. The dedicated hadronic recoil algorithm was developed by the ATLAS W mass working group. It was validated and applied in the first measurement of M_W at a center of mass energy of $\sqrt{s} = 7\,\text{TeV}$ with the ATLAS detector.

The resolution and bias of the hadronic recoil are strongly influenced by the number of simultaneous interactions inside the detector volume. Collisions of the same proton-proton bunch crossing can give these pileup events, but also other fragmentation processes of the same interaction might result in additional particles (underlying event). The numbers of background particles coming from pileup depends on the luminosity of the collision, whereas the recoil, the underlying event and the kinematics of the W boson decay depend on the center of mass energy of the run campaign.

Over the past years several different datasets with different pileup conditions and center of mass energies were recorded by the ATLAS detector. In November 2017, a dedicated one week run was commissioned where the beam optics were adjusted so that the pileup was kept at a minimum value of around 2. Two datasets at a center of mass energy of $\sqrt{s} = 13\,\text{TeV}$ with an integrated luminosity of $\mathscr{L}_{int} = 146.6\,\text{pb}^{-1}$ and at $\sqrt{s} = 5\,\text{TeV}$ with $\mathscr{L}_{int} = 258.4\,\text{pb}^{-1}$ were recorded. These excellent conditions allow for an as clean as possible measurement of the W boson mass.

The value of the W boson mass is determined by comparing the measured distributions

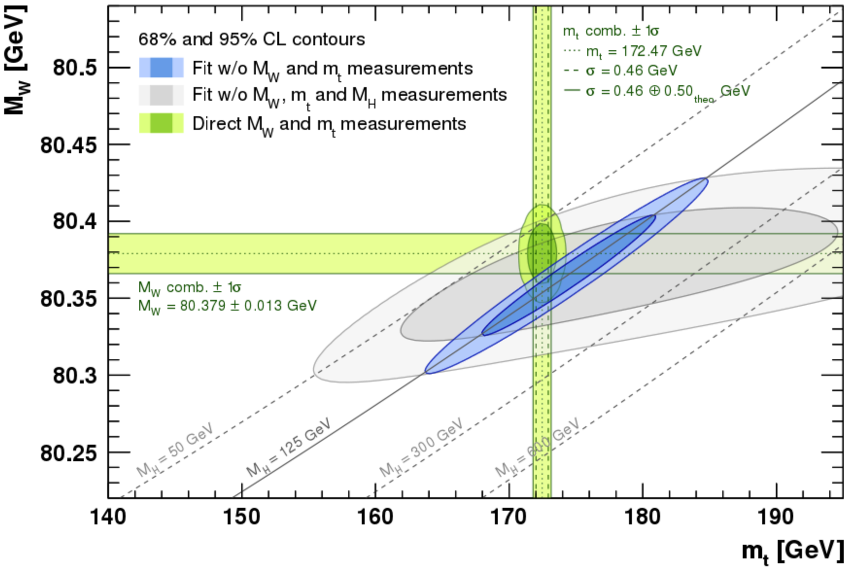

Figure 1.2.: Comparison between the predictions of the electroweak fit on the Standard Model parameters with the direct results of the latest measurements by the LHC experiments on the W boson mass and top quark mass. The electroweak fit in blue includes the measured mass of the Higgs boson of $M_H = (125.1 \pm 0.2)\,\text{GeV}$, while the gray ellipse represents the fit without the Higgs boson mass constraint. The direct measurements are derived from a combination of the world average with the 2017 ATLAS measurements to values of $M_W = (80\,379 \pm 13)\,\text{MeV}$ for the W boson mass and of $M_t = (172.47 \pm 0.46)\,\text{GeV}$ for the top quark mass. [8]

of the transverse mass and the charged lepton momentum to a set of simulations of different mass hypotheses. Those simulated templates mimic the production and subsequent decay of a W boson inside the detector and the identical reprocessing of the data. The value of the W boson mass is determined by a χ^2 test, which identifies the best agreement between data and the different modelings of the mass in simulation.

The modeling of the Monte Carlo simulations needs to be done beforehand and is performed as accurately as possible within the given framework. The simulations nevertheless show inevitable difference to real data in reference samples. The limitations come on the one hand from the precision of the theoretical calculations and from the available computing power and the conformity of the simulated detector on the other hand. The simulation of the particle interactions with the detector is also not perfectly identical to real physics, since only finite models can be implemented. The reconstructed physics objects therefore need calibrations to show an identical behavior as real data, for example the scale and resolution of the measured momentum is equalized to data.

For most analysis, a robust set of calibrations is sufficient, whereas for precision measurements, that aim on an overall uncertainty of the order of $10-30\,\text{MeV}$, corrections with an identically high precision need to be applied. The general tools available usually do not provide this accuracy. Therefore, own methods need to be developed that are tailored to the analysis signature.

The calibration of the hadronic recoil can be performed with events containing a Z boson.

For this standard candle the kinematics are similar to the W boson kinematics. It has the advantage, that the decay into two oppositely charged leptons allows a full reconstruction of the boson and thus gives the possibility to calibrate the recoil algorithm. By using Z boson events, the calibrations are also derived for a subset of the dataset which will not be used in the measurement of the W boson mass, since events containing a Z boson and two charged leptons are naturally filtered by a W boson signal selection, which requires exactly one charged lepton.

This thesis presents a novel approach for the calibration of the hadronic recoil algorithm with respect to the background modeling of the pileup and the underlying event. A first estimate on the influence of the calibration method on the systematic uncertainty will be given.

The outline of this thesis is the following: The second chapter presents all relevant theoretical basics of the Standard Model as well as a few of its shortcomings. The third chapter introduces the experimental machinery of the Large Hadron Collider and the ATLAS experiment. The process of simulation is also described here. All important concepts for the analysis, including a detailed discussion on the event variables, a description of the hadronic recoil algorithm and the measurement strategy with the template method, will be given in chapter 4. In chapter 5 the datasets, selection criteria and the general performance of the hadronic recoil algorithms are introduced. The main analysis of the recoil calibrations will be discussed in chapter 6, where a reweighting procedure is presented in detail. The final chapter 7 gives a first look at the systematic uncertainty of the recoil calibration for a W mass measurement with pseudodata.

CHAPTER 2

Theoretical framework of W and Z boson production at the LHC

2.1. The Standard Model of Particle Physics

Almost all phenomena in our complex world are based on four fundamental interactions along with two small sets of particles, the fundamental fermions and bosons. The group of fermions consists of all particles that form matter whereas the group of bosons are the mediators of the fundamental interactions (see Tab. 2.1 and 2.2 for a description with some properties). In our modern understanding the electromagnetic, weak, strong and gravitational forces explain all interactions of visible matter. The Standard Model of Particle Physics is the mathematical description of particles and forces on this fundamental level. In form of a quantum field theory it brings together the necessary concepts of the theory of special relativity and quantum theory by making use of gauge symmetries, that allow space and time constrains, as well as spontaneous symmetry breaking. With the Standard Model Lagrangian the individual field equations describing the fundamental interactions can be derived. Three fundamental interactions are described in the Standard Model: the strong, weak and electromagnetic interaction and with that it gives a set of rules for the elementary particles, which are the leptons, quarks and bosons, which can carry a weak, an electric or a color charge.

One set of fundamental particles is the group of quarks. Six types of quarks are known today. The strong force allows for interactions of quarks and hadrons, which are particles consisting of quarks such as the proton or the neutron. The other set of fundamental fermions are the group of leptons. Also here, six different types - three charged leptons and three neutrinos - are included in the lepton family. All electrically charged particles can participate in the electromagnetic interaction, while all lefthanded[1] fermions interact weakly. The elementary particles are all complemented by corresponding antiparticles, which have the same masses as their partners but carry opposite quantum numbers, like an opposite electric charge.

Many experimental verifications of predictions based on the Standard Model could be made over the last decades, which are proof of its success. Nevertheless, one important as-

---

[1] A definition will be given in Sec. 2.1.2

	family			*color*	*el. charge*	*weak charge*	*spin*
Leptons	electron neutrino ν_e	muon neutrino ν_μ	tauon neutrino ν_τ	-	0	1	$\frac{1}{2}$
	electron e	muon μ	tauon τ		-1		
Quarks	up u	charm c	top t	r, g, b	$+\frac{2}{3}$	1	$\frac{1}{2}$
	down d	strange s	bottom b		$-\frac{1}{3}$		

Table 2.1.: The 12 fundamental fermions of the Standard Model: The leptons and quarks along with several properties.

Interaction	*couples to*	*Gauge bosons*	*mass* (GeV/c^2)
strong	color charge	8 gluons (g)	0
electromagnetic	electric charge	photon (γ)	0
weak	weak charge	$W^{\pm}, Z$	≈ 100

Table 2.2.: The three fundamental interactions of the Standard Model: The strong, electromagnetic and weak interaction along with the according charges to which they couple, and the gauge bosons.

pect was just validated recently. The first basic description of the fundamental forces did not explain why the particles have masses. One approach, which allowed the concluding description in form of the Standard Model in the first place, was already made by P. Higgs, F. Englert and Brout in two separate proposals in 1964, which is today known as the Brout-Englert-Higgs mechanism [10, 11]. Despite the theory's phenomenal achievement to solve the mass puzzle, its only experimental verification is the detection of the resonance of the Higgs field, the discovery of a Higgs boson. It was only in July 2012 when two LHC experiments ATLAS and CMS announced the discovery of a new particle [5, 6] (with a mass of $M = (125.09 \pm 0.24)\,\text{GeV}$ [12]), which finally validated the Higgs mechanism.

The following chapter gives a brief introduction into the two main concepts of the Standard Model, which is the theory of Quantum Chromo Dynamics and the Electroweak unification. The principles described here mainly follow [13, 14]. The original sources are indicated where applicable. After a quick look at the tools of perturbation theory, which allow a prediction of possible processes of the Standard Model, some phenomena where the Standard Model reaches its limitations will be discussed. Finally, the behavior of W and Z bosons at a proton-proton collider like the LHC will be introduced.

2.1.1. Quarks, gluons and the strong interaction

The field theory describing the strong interactions of color charge carrying quarks and gluons is the theory of Quantum Chromo Dynamics (QCD). It is a non abelian gauge theory with the structure of a $SU(3)$ group[2]. With it, the formation of hadrons out of the set of quarks as well as the involved strong interactions can be described. The elementary processes of QCD are the exchange of gluons and the generation and annihilation of quark-antiquark pairs. The gauge bosons, which couple to the color charges *red (r)*, *green (g)* and *blue (b)* are the massless gluons, they are the mediators of the strong interaction. Following group theory, the gluons are grouped into two multiplets, one color octet and one singlet. One possible representation would be [14]

$$\{r\bar{g},\ r\bar{b},\ g\bar{b},\ g\bar{r},\ b\bar{r},\ b\bar{g},\ \sqrt{1/2}(r\bar{r}-g\bar{g}),\ \sqrt{1/6}(r\bar{r}+g\bar{g}-2b\bar{b})\}$$

for the octet and for the singlet:

$$\{\sqrt{1/3}(r\bar{r}+g\bar{g}+b\bar{b})\}.$$

The latter color singlet mode is an equal composition of all colors and thus is not color specific. An exchange of this singlet cannot result in an exchange of color. Therefore gluons carrying only a color combination of the octet participate in the mediation of the strong force by performing a color exchange between the coupling particles. The fact that gluons carry color charge themselves allows for self coupling, an interaction that involves three or four gluons but no quarks. This process is highly relevant because of its large interaction strength.

All experiments performed over the past decades confirm the theory that quarks are confined to composite particles and that only the fundamental quarks and gluons carry color charge while the composite particles are color neutral. Hadrons consisting of three quarks or three antiquarks are baryons like the proton. Each quark within a baryon carries a different color, which add up to the net color *white*. Another possibility is the combination of a quark and an antiquark carrying color and the corresponding anticolor. The resulting meson is then also color neutral. Therefore the color charge gives a set of rules for the formation of hadrons and allows a simple determination if fundamental particles can interact strongly.

The main properties of hadrons are defined by the valence quarks. However, deep inelastic scattering experiments showed, that the valence quarks do not carry the full momentum of accelerated particles but rather a comparably small fraction. As a consequence, hadrons consist of many more particles than those valence quark. The remaining momentum is distributed among a sea of gluons and quark-antiquark pairs generated from gluons. Those sea quarks again annihilate quickly to gluons. When hadrons are brought to collision, these extra quarks and gluons are essential for the production of particles that cannot be created from valence quarks only, for example in Drell-Yan processes, where a quark interacts with an antiquark by forming a photon or a Z boson.

The strength of strong interactions is related to the strong coupling constant α_s, although technically speaking, it is not a constant but rather dependent on the energy transfer Q of the process and the QCD scale Λ, a free parameter, $\alpha_s \propto ln^{-1}(Q^2/\Lambda^2)$ (see Fig. 2.1). The gluon self coupling is responsible for the fact that this energy dependence is quite strong. Large distances between two quarks correspond to small energy transfers and thus a high value of the coupling constant. Quarks cannot be separated without strong interactions happening, which will form new pairs of quarks and antiquarks in between, eventually forming

---

[2] The $SU(3)$ group is the **S**pecial **U**nitary group of degree 3, where the transformations are based on unitary matrices (determinant 1).

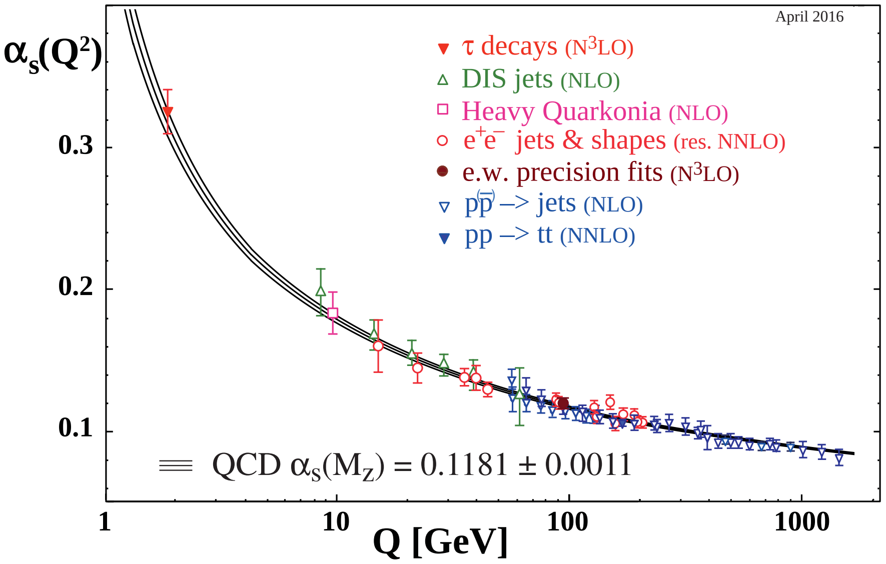

Figure 2.1.: Measured values and QCD fit for the strong coupling constant α_s as a function of the energy transfer Q. In brackets are the respective degrees of QCD pertubation theory used in the different measurements. [12]

color-neutral hadrons. This process is called hadronization. Opposed to this, quarks can be regarded as free if the energy transfer is getting large $Q^2 \to \infty$. This is the case when the distance between the quarks decreases and the coupling strengths disappears asymptotically. The effect goes by the name asymptotic freedom. The quasi free quarks inside hadrons can be regarded as more or less independent partons if at the right energy. It is this freedom that allows strong interactions on the quark level in parton collisions with high energy transfers.

2.1.2. Lepton and quark interactions with the electroweak unification

The field theory of the electroweak unification was first derived by S.L. Glashow, S. Weinberg and A. Salam and initiated the completion of the Standard Model as a full quantum field theory for the elementary particles and their interactions [15]. It is a representation in the $SU(2)_L \times U(1)$ group space, combining the $SU(2)_L$ characteristics of the weak interaction by the weak isospin T, which distinguishes between left- and right-handed particles, thus the index L and the $U(1)$ representation of the weak hypercharge Y. The main concept on the unification evolves around the two new quantum number, which has been introduced, the weak isospin and the hypercharge Y, and which allows a neat description of the characteristics of both the electromagnetic and the weak force.

Following the general spin concept, the third component of the weak isospin vector T_3 represents the relevant quantum number of interest, which is conserved under weak interactions. The left-handed fermions of the standard model are rearranged into weak isospin doublets with $T_3 = \pm\frac{1}{2}$, while the right-handed fermions are isospin singlets. Right-handed neutrinos have not been observed in any experiment until today and are therefore not part of the representation. Antiparticles form doublets if right-handed and singlets if left-handed. Here, the quantum numbers for T_3 and the electric charge z_f have opposite sign compared to their counter-particles.

The weak hypercharge and the third component of the isospin together with the charge z_f satisfy the relation: $z_f = T_3 + \frac{1}{2}Y$.

Table 2.3 gives an overview over the classification.

	Multiplets			T	T_3	z_f	Y
Leptons	$\begin{pmatrix} \nu_e \\ e \end{pmatrix}_L$	$\begin{pmatrix} \nu_\mu \\ \mu \end{pmatrix}_L$	$\begin{pmatrix} \nu_\tau \\ \tau \end{pmatrix}_L$	$\frac{1}{2}$	$+\frac{1}{2}$ $-\frac{1}{2}$	0 -1	-1
	e_R	μ_R	τ_R	0	0	-1	-2
Quarks	$\begin{pmatrix} u \\ d' \end{pmatrix}_L$	$\begin{pmatrix} c \\ s' \end{pmatrix}_L$	$\begin{pmatrix} t \\ b' \end{pmatrix}_L$	$\frac{1}{2}$	$+\frac{1}{2}$ $-\frac{1}{2}$	$+\frac{2}{3}$ $-\frac{1}{3}$	$\frac{1}{3}$
	u_R	c_R	t_R	0	0	$+\frac{2}{3}$	$\frac{4}{3}$
	d_R	s_R	b_R	0	0	$-\frac{1}{3}$	$-\frac{1}{3}$

Table 2.3.: Fermion representation in the electroweak unification. The magnitude of the weak isospin T and its third component $T_3 = \pm T$ for leptons and quarks are stated together with the particle's charge z_f in units of the elementary charge e. The weak hypercharge Y is indicated in the last column.

A transition within each doublet is allowed by emission and absorption of a $W^\pm$ boson while conserving the weak isospin. For the quark doublets, the final state of the transition is a linear combination of the flavor states q', because of the non-zero probability of cross-generation transitions under absorption and emission of a W boson described in the CKM matrix. The matrix can be defined by four free parameters, that are the three real angles and a phase [16]. Isospin singlets do not couple to W bosons.

The W bosons themselves are assigned a weak isospin of $T_3(W^-) = -1$ and $T_3(W^+) = +1$. This integer character suggests, that the two charged W bosons form a triplet state together with a third boson W^0 with $T_3(W^0) = 0$. In addition, a singlet state exists, which represents a fourth boson B^0 with $T(B^0) = T_3(B^0) = 0$. It is the associated boson to the hypercharge group $U(1)$. The coupling strength of the triplet state is denoted as g, while the singlet state should couple with g'. Both W^0 and B^0 couple to fermions without changing the particle's type or weak isospin. The connection of the two neutral bosons to the experimentally observed Z and γ bosons is done by introducing the parameter of the Weinberg angle θ_W. W^0 and B^0 mix to the two orthogonal states by [13]:

$$|\gamma\rangle = +\cos\theta_W\,|B^0\rangle + \sin\theta_W\,|W^0\rangle$$

$$|Z\rangle = -\sin\theta_W\,|B^0\rangle + \cos\theta_W\,|W^0\rangle$$

The fact that the photon only interacts with charged particles allows to derive the following relations of the coupling strengths, the Weinberg angle and the electric charge:

$$\tan\theta_W = \frac{g'}{g}, \quad \sin\theta_W = \frac{g'}{\sqrt{g^2+g'^2}}, \quad \cos\theta_W = \frac{g}{\sqrt{g^2+g'^2}}, \quad e = g\sin\theta_W$$

The Weinberg angle can be determined experimentally from several signatures like neutrino-electron scattering in its $\sin^2\theta_W$ representation with a high precision of $\sim 0.52\,\%$¸ to:

$$\sin^2\theta_W = (0.23116 \pm 0.00012)\ [12].$$

The coupling of a Z boson can be expressed in terms of the charged current strength by

$$g_Z(f) = \frac{g}{\cos\theta_W}\cdot\hat{g}(f) \qquad \text{with} \quad \hat{g}(f) = T_3 - z_f\sin^2\theta_W.$$

The Z boson's coupling strength differs for charged and neutral fermions. It can easily be calculated that the coupling of Z bosons to neutrinos is a about a factor 2 larger than the coupling to the charged leptons.

Another important connection relates the Weinberg angle to the masses of the W and Z boson:

$$\frac{M_W}{M_Z} = \cos\theta_W.$$

Nevertheless the values for all three parameters θ_W, M_W and M_Z are not predicted by theory so far. Without the concept of spontaneous symmetry breaking masses are not even allowed and the orthogonal mixing of the two bosons W^0 and B^0 to the real Z boson and the photon cannot be described like this. The difference between the massless photon and the heavy Z and W bosons is quite large. With the Higgs mechanism, the concept of spontaneous symmetry breaking comes to the rescue.

For this purpose, a complex two dimensional Higgs doublet Φ and the Higgs potential $V(\Phi)$ are postulated:

$$\Phi = \begin{pmatrix}\phi^+\\ \phi^0\end{pmatrix}, \quad V(\Phi) = \mu^2\Phi^\dagger\Phi + \lambda(\Phi^\dagger\Phi)^2$$

The factors μ^2 and λ define the ground state of the potential. If $\mu^2 > 0$ and $\lambda > 0$ the state of lowest energy is found for $\Phi = 0$. This is also illustrated in a two dimensional representation of the Higgs potential in Fig. 2.2 on the left side. The form of the potential changes as a function of μ^2. For $\mu^2 < 0$ the lowest energy state results in a fixed amplitude of the vacuum expectation value, e.g.

$$\Phi_{min} = \begin{pmatrix}0\\ v\end{pmatrix} = \begin{pmatrix}0\\ \sqrt{\frac{-\mu^2}{2\lambda}}\end{pmatrix},$$

but also in infinite possible positions in the complex plane. For a given random position the ground state is no longer symmetric.

This potential introduces four new degrees of freedom in form of four quanta of the Higgs fields. In this spontaneously broken symmetry state the Z and $W^\pm$ bosons now obtain a mass by each absorbing a quantum of one of the four Higgs fields. By this, they gain a bit of weight. The photon stays massless in this concept and the remaining quantum of the fourth field is observable as a free massive Higgs boson.

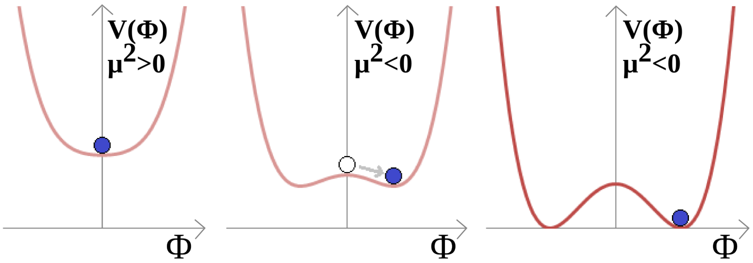

Figure 2.2.: Illustration of the Higgs potential $V(\Phi)$ in a two dimensional representation for different values of μ^2. Right after the big bang before the universe cooled down to lower temperatures, the Higgs potential could have been in a state with $\mu^2 > 0$. Adapted from [17].

When fermion fields interact with the Higgs field via a Yukawa coupling, they acquire a mass. This gain mass is proportional to the coupling between the fermion and the Higgs field. As a consequence, the Higgs boson itself predominantly interacts with heavy particles, if kinematically allowed.

2.1.3. Perturbation theory: A framework for predictions on particle interactions

In quantum mechanics, the wave function that solves the Schroedinger equation contains all information necessary to describe a particle's behavior in this context. For a relativistic quantum field theory the situation is much more complex. A single interaction between two particles can result in a many-body final state because of easily produced particle-antiparticle pairs. A scattering matrix is therefore a more adequate description mechanism of the transition from a given initial state to certain final states. The amplitude of one matrix element determines the probability for one final state. Unfortunately the calculation of this matrix is non-trivial. A solution for this dilemma was introduced with perturbation theory, which allows to calculate a quite detailed approximation of the true process. An intuitive description of this procedure is possible with the help of Feynman diagrams. Next to a visualization of the process itself, they allow the calculation of the scattering amplitude for each subprocess by following the set of rules of the Feynman calculus [18]. By careful summation of the amplitudes of all diagrams involved it gives the probability for the process of interest. The caveat of this technique is that every possible way from the initial state to the final state needs to be included. The obvious diagrams of the ground state are accompanied by complex varieties of the same by including so-called loops. There are no restrictions, which would for example forbid a gluon to quickly decay into a pair of quarks and shortly afterwards being recreated from the pair again. These loop corrections can be included at any possible position in the process (see Fig. 2.3 for an example for a simple toy model). Although the individual contribution of those complex diagrams are less relevant than the obvious, simple diagrams, the sum of those Feynman diagrams play a significant role. The modern computing technique allows for a comparably easy calculation of a few lower order corrections, but the precision of the resulting amplitude is nevertheless limited by the computing power.

When calculating the amplitudes without further measures, inevitable divergences arise. The field theories are supposed to be universally valid on all energy scales. But the con-

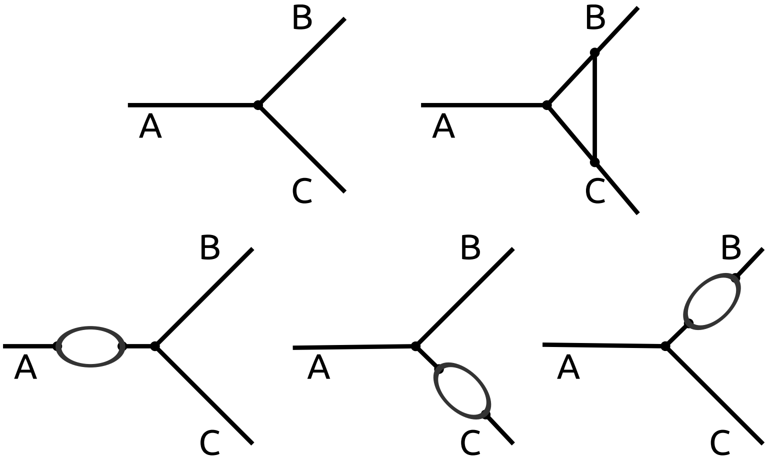

Figure 2.3.: Feynman vertices for a toy model with the lowest tree level and all possibilities to include one loop. Concept adopted from [19]

cept of perturbation theory as an approximation method is only an effective theory, meaning that the concepts can only be applied in a given energy range. Although this range can be comparably large, energies allowed by the field theories can exceed this range nevertheless. For example, the momentum of the virtual particles in the loop of a Feynman diagram are not restricted. The integral over all possible values for the momentum from $-\infty$ to ∞ leads to a diverging amplitude. This strongly contradicts any experimental observation. To solve this puzzle, the concepts of regularization and renormalization are applied. The method of regularization restricts the infinite energy range to the range at which the renormalization takes place for this part of the calculations. The renormalization redefines the fixed character of constants like a particle's mass or its charge. They can only be considered as being constant for a given energy scale. Nevertheless, when measured at this scale, the value is still well defined. With the concept of renormalization, the constants entering the theory are redefined to be independent of the current scale. After regularization however, the resulting values cannot be calculated at the current scale, but need to be determined with experimental observations of those constants at this energy scale. With this input, the amplitudes can be calculated by avoiding divergences. The concept of perturbation theory was validated successfully with several phenomena. The agreement between calculated and measured values are astonishingly good. [20]

2.1.4. Selected phenomena beyond the Standard Model

The Standard Model in today's representation does a wonderful job in describing almost all phenomena observable on the fundamental level of quarks, leptons and gauge bosons. Nevertheless there are a few shortcomings, which cannot be explained by the theories of the Standard Model yet.

The masses of the three neutrinos were initially determined to be much smaller than the electron mass and thought to be zero. Thus, the Standard model was built in a way that sets the masses of all neutrinos to zero. However, several experimental observations contradict this fact. Neutrino mixing, the phenomenon that a neutrino, which was originally generated as one specific lepton family type, arrives at the detector as a superposition of all possible types, can only be explained if the neutrinos have different masses each. Unfortunately, absolute values of the masses cannot be derived from oscillation experiments. Together with studies on structure formation in the early universe, which set an upper boundary on the sum of all masses to $\Sigma m_{\nu_i} < 0.23\,\mathrm{eV}/c^2$, they allow an experimental prediction on the mass ranges of the lightest and the heaviest neutrino after all. The lightest neutrino could stay massless or have small mass up to $m_{\nu_{light}} \leq 0.071\,\mathrm{eV}/c^2$ while the heaviest of the three, it is also unknown to which families they correspond, must have a mass in the range of $0.05 \leq m_{\nu_{heavy}} \leq 0.087\,\mathrm{eV}/c^2$ [12]. Several theoretical suggestions on extensions of the Standard Model could explain the mass phenomenon and the corresponding mixing angle of the neutrinos. However, the experimental facts are far too vague for any conclusive proposal.

Next to the neutrino mass phenomenon, no theoretical predictions arise out of the Standard Model for its other free parameters like the fermionic masses and the coupling constants. In total, 18 free parameters are undetermined (not including neutrino masses). Another strange fact is the observed mass range of the fermions, starting from the few eV of neutrinos to the top mass of $172\,\mathrm{GeV}/c^2$, spanning 10^{12} orders of magnitude.

One can also wonder where the corresponding antimatter of all matter in the universe has gone. Charge and parity violating processes (CP) are the only mechanisms in the Standard Model that distinguishes between matter and antimatter and CP violating processes result in an unequal number of particles and antiparticles. However, the effect is far too small to explain the imbalance of the universe.

One of the biggest puzzles however is the question of what the universe is actually made of. Astrophysical observations from studies on the cosmic microwave background, the effect of gravitational lenses, discrepancies between classical models and observations on the expansion of the universe and many other results suggest that 95% of the universe are not made from visible matter but consists of dark matter (26%) and dark energy (69%). Thus, the part of the universe that can be described by the Standard Model is smaller than 5%.

Many theories exist that are capable of explaining at least some or maybe even all of the shortcomings of the Standard Model. Particularly nice concepts include an attempt for a unification of all forces, something that was already achieved for the weak and the electromagnetic interaction. The energy dependence of the coupling constants allows for a scenario in which they could be in agreement if at really high energies at the order of 10^{14} to $10^{16}\,\mathrm{GeV}$. The agreement is only feasible with a bit of new physics included in the energy range in between. For example, supersymmetric models predict a supersymmetric partner to every particle of the Standard Model. This new zoo of particles and parameters can easily result in the new physics at scales in between what we can measure now and where the unification can take place.

New particles could only be observable at energies higher than what has been tested up to now or their interaction with visible matter must be quite subtle, otherwise they would have already been discovered. However, they might be at energies just in our reach. Many direct and indirect searches for signatures of new particles are ongoing and the data accessible with the LHC might shed some light on the many mysteries out there.

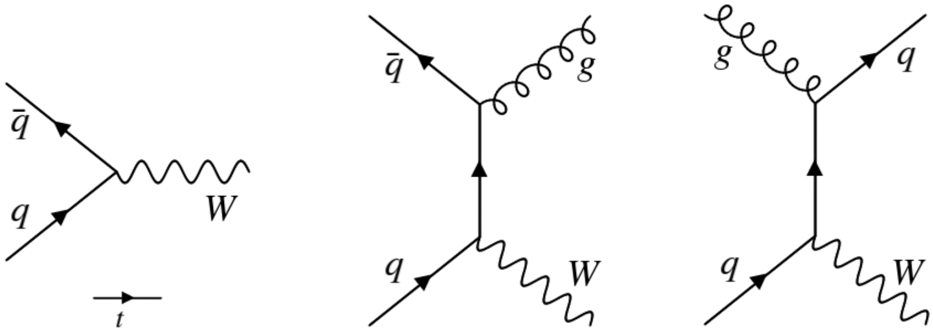

Figure 2.4.: Feynman diagrams for the Drell-Yan process for the W and Z boson production at the LHC. Left plot: direct production from a quark-antiquark pair, central plot: production with an additional gluon in the final state, right plot: production from a quark and a gluon with an additional quark in the final state. [21]

2.2. Production and decay of the W and Z boson at the LHC

The production of a W boson and a Z boson in proton-proton collision can be described by the Feynman diagrams for the Drell-Yan process [22] shown in Fig. 2.4 on the left side. This single production should be supplemented by the associated productions, described by the second and the third diagram in Fig. 2.4 (central and right plots), where the boson emerges in association with a quark and a gluon respectively. When considering a possible transverse momentum p_T carried by the boson, the single production only allows for a small value of the transverse momentum coming from an intrinsic transverse momentum k_T carried by one of the quarks. In the associated production however, the boson can recoil against the other emerging parton, allowing also higher transverse momenta [21]. In total, the transverse momentum distribution is peaking at $\simeq 5-10\,\text{GeV}$.

The total production cross section for a W boson was measured by the ATLAS detector and found to be $\sigma_{7TeV} = (98.71 \pm 0.028 \pm 2.191)\,\text{nb}$ at $\sqrt{s} = 7\,\text{TeV}$ [23, 24] and $\sigma_{13\text{TeV}} = (190.1 \pm 0.2 \pm 6.4)\,\text{nb}$ at $\sqrt{s} = 13\,\text{TeV}$ [23, 25]. In Fig. 2.5 a summary of several standard model total cross section measurements as well as their agreement with theoretical expectation is shown for the three center-of-mass energy campaigns of $\sqrt{s} = 7\,\text{TeV}, 8\,\text{TeV}$ and $13\,\text{TeV}$. Roughly three times more events containing a W boson than events with a Z boson are expected to be seen in the same dataset.

The possible decay modes of a W boson can be either hadronically into a pair of a quark and an antiquark or leptonically into a pair of a charged lepton and its neutrino. Tab. 2.4 shows the branching ratios for the individual decay modes. Although favored by numbers, the hadronic decay mode is an unfeasible signature for studies on W bosons due to the overwhelmingly large background of two jets at a hadron collider. The leptonic decay modes present a cleaner signal to background ratio. However, the neutrino escapes the detector without leaving a trace, making it impossible to directly measure the full decay kinematic and methods for indirect measurements have to be taken into account.

For the Z boson, table 2.5 gives the measured values for the branching fractions for the

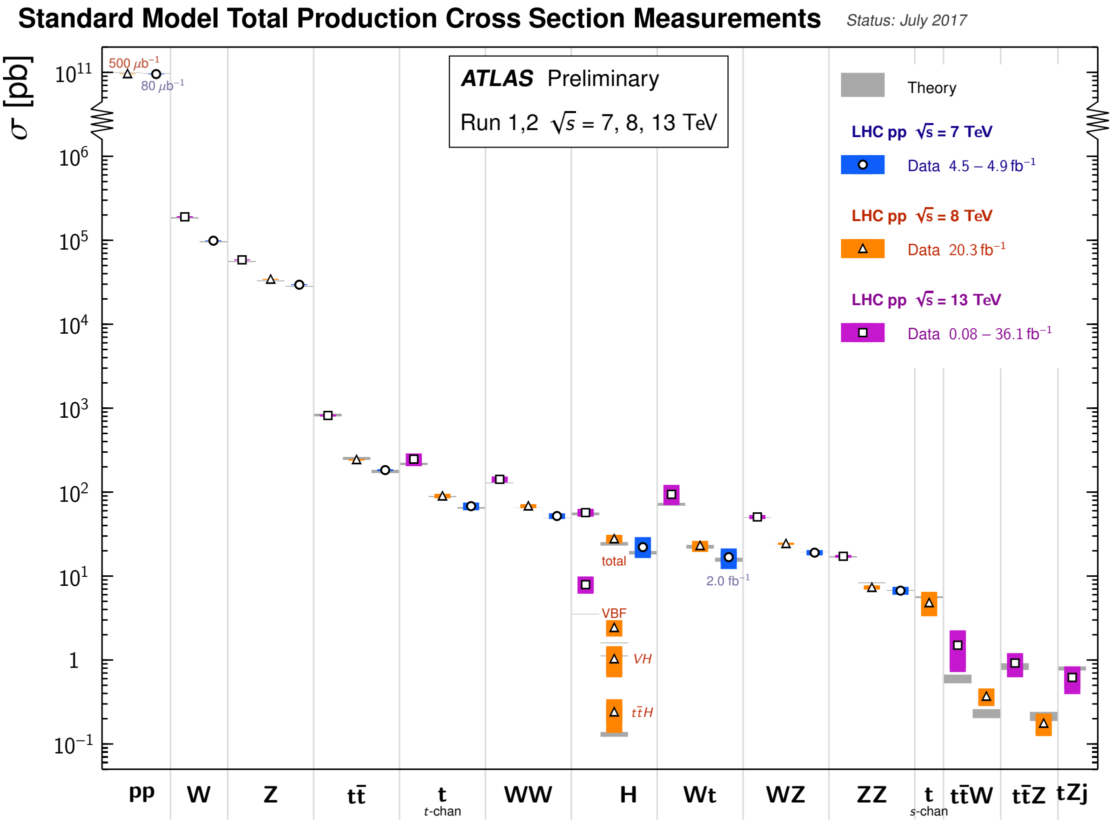

Figure 2.5.: Comparison between measured results for several standard model total production cross sections with the ATLAS detector and corresponding theoretical expectations [23]. The total cross section for the W boson was measured by the ATLAS collaboration to $\sigma_{7TeV} = (98.71 \pm 0.028 \pm 2.191)\,\mathrm{nb}(\sqrt{s} = 7\mathrm{TeV})$ [23, 24] and $\sigma_{13TeV} = (190.1 \pm 0.2 \pm 6.4)\,\mathrm{nb}(\sqrt{s} = 13\mathrm{TeV})$ [23, 25]. For the Z boson, the measured values for the total cross section are: $\sigma_{7TeV} = (29.53 \pm 0.03 \pm 0.77)\,\mathrm{nb}(\sqrt{s} = 7\mathrm{TeV})$ [23, 26], $\sigma_{8TeV} = (34.24 \pm 0.03 \pm 0.92)\,\mathrm{nb}(\sqrt{s} = 8\mathrm{TeV})$ [23, 26] and $\sigma_{13TeV} = (58.43 \pm 0.03 \pm 1.66)\,\mathrm{nb}(\sqrt{s} = 13\mathrm{TeV})$ [23, 26]. The reference theoretical prediction is in all cases based on DYNNLO next-next-to-leading-order calculations with the CT14NNLO PDF set.

W^+ decay modes	Fraction (Γ_i/Γ)
$e^+\nu_e$	$(10.71 \pm 0.16)\%$
$\mu^+\nu_\mu$	$(10.63 \pm 0.15)\%$
$\tau^+\nu_\tau$	$(11.38 \pm 0.21)\%$
hadrons	$(67.41 \pm 0.27)\%$
invisible	$(1.4 \pm 2.9)\%$

Table 2.4.: Relative decay fractions of the different experimentally measured decay modes for the W^+ boson. The branching fraction into *hadrons* represents the sum over the decay modes containing an up or charm quark as well as combinations of mesons or hadrons like the decay into $\pi^+\gamma$ ($< 8 \times 10^{-5}$) or into $D_s^+\gamma$ ($< 1.3 \times 10^{-3}$). The invisible decay mode includes the fraction of decays into undetectable charged particles (momenta threshold used here: $p < 200\,\mathrm{MeV}$). [12]

different decay modes. The leptonic decays, especially into an electron or a muon pair, leave the cleanest detector signature and are widely used as standard candles for detector and simulation calibrations. Because of the lower cross section and the possible decay of Z bosons into neutrino pairs, the cross section × branching ratio is by a factor $3 \times 3 = 9$ smaller for the process $Z \to \mu\mu$ compared to $W \to \mu\nu$. In the same dataset obtained at the LHC, a significantly lower number of leptonically decaying Z bosons can be identified compared to the number of leptonic W candidates.

Z decay modes	Fraction (Γ_i/Γ)
e^+e^-	$(3.363 \pm 0.004)\%$
$\mu^+\mu^-$	$(3.366 \pm 0.007)\%$
$\tau^+\tau^-$	$(3.370 \pm 0.008)\%$
hadrons	$(69.91 \pm 0.06)\%$
invisible	$(20.00 \pm 0.06)\%$

Table 2.5.: The different experimentally measured decay modes for the Z boson are listed with their relative decay fraction. The branching fraction into hadrons represents the sum of the various quark pair decays and decays into a combination of mesons and photons. The invisible decay mode is dominated by the decay into invisible neutrino pairs. [12]

2.3. History of W and Z boson mass measurements

In 1967 already, Steven Weinberg proposed a calculation for the prediction of the masses of the W and the Z boson [27], but the by that time unknown value of the Weinberg angle was to be measured first. C.H. Albright was able to estimate a range for the Weinberg angle of $0.3 \leq \sin^2\theta_W \leq 0.5$ in 1973 from neutrino and antineutrino inclusive cross section measurements [28]. The first measured value was derived in 1982 from data of the Gargamelle experiment by calculating the ratio of the neutrino-antineutrino cross section measurements to $\sin^2\theta_W = 0.215 \pm 0.015$ [29]. With this a prediction for the two masses was found to be $M_W = (83.1 -$

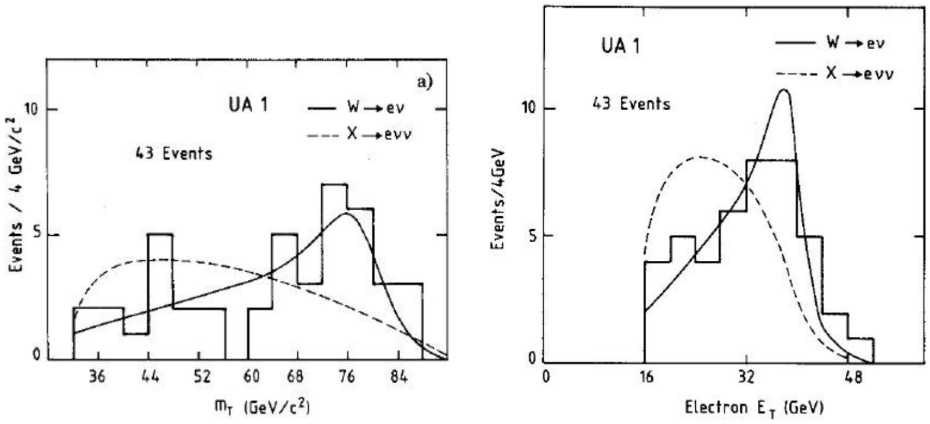

Figure 2.6.: First measurement of the mass of the W boson with the UA1 experiment with the transverse mass as well as with the lepton distributions. The analysis consisted of only 43 events. [32]

$2.8+3.1)\,\mathrm{GeV}/c^2$ and $M_Z = (93.8-2.2+2.5)\,\mathrm{GeV}/c^2$ in 1982. Shortly after, the group of Carlo Rubbia from the UA1 Experiment as well as the collaboration of the UA2 Experiment announced the discovery of the W boson in January 1983 and a few month later in May that same year the discovery of the Z boson. The UA1 Experiment obtained the following masses $M_W = (81 \pm 5)\,\mathrm{GeV}/c^2$ [30] and $M_Z = (93.1 \pm 1.0 \pm 3.0)\,\mathrm{GeV}/c^2$ [31], which are in astonishing agreement with the predictions. Fig. 2.6 shows the corresponding distribution for the determination of the W mass with the UA1 Experiment.

With newer experiments at higher energies and with detectors with an improved resolution, the values for the mass of the two bosons were measured much more precisely over the next decades. The electron-positron collider LEP, the predecessor of the LHC, was designed as an optimal machine for the production of Z bosons by setting the beam energy to around 45 GeV, what results in a collision energy close to the Z resonance. The beam energy was later increased to enable the production of W bosons pairs. This lepton collider allowed for very clean signals without large QCD background contamination. Especially the resonance of the Z boson could be measured quite precisely by the four experiments ALEPH, DELPHI, L3 and OPAL [33]. The datasets available allowed for a precise measurement of the many Z and W boson properties, summarized in various publications of the LEP Electroweak Working Group [34, 35].

The data from the proton-antiproton collider of the Tevatron could of course also be analyzed to measure the two mass parameters. For the mass of the Z boson, the incredible precision of the LEP experiments could not be reached. For the W boson however, the obtained values for M_W by the two experiments D0 and CDF were quite crucial for an improvement on the world average (see Fig. 2.7) [36].

The latest measurement on the mass of the W boson was performed by the ATLAS experiment with the analysis of the run 1 dataset at a center of mass energy of $\sqrt{s} = 7\,\mathrm{TeV}$ and was published in 2018 [9].

In summary, the current world averages for the mass M_Z and the width Γ_Z of the Z boson

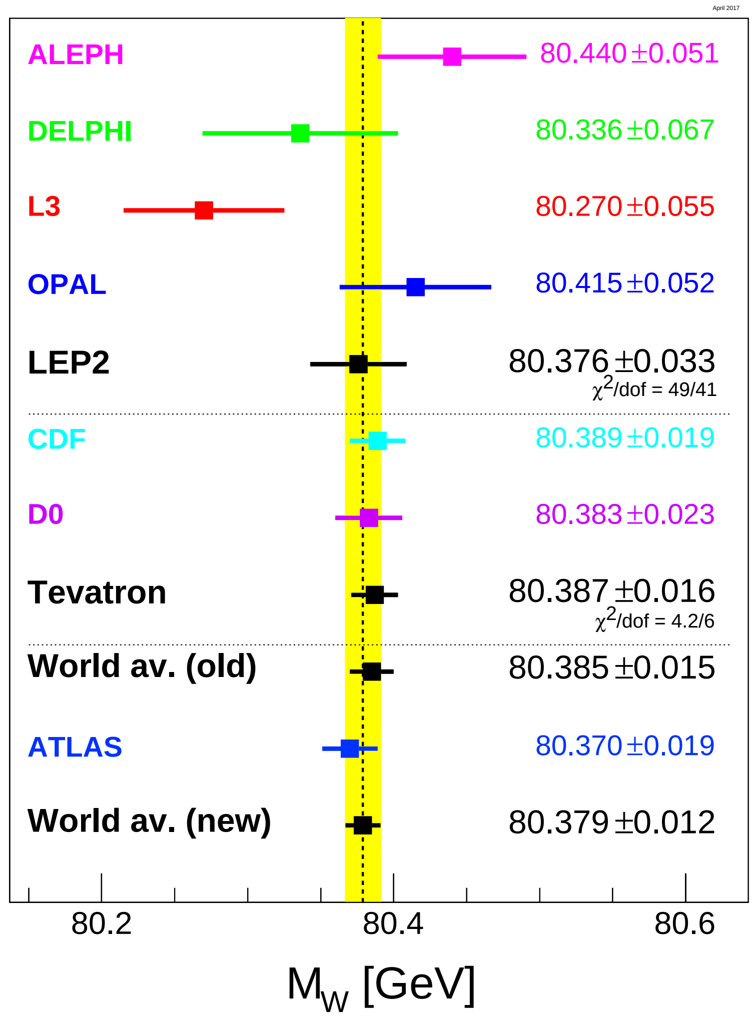

Figure 2.7.: Individual M_W measurements from the experiments at the LEP collider, at the Tevatron collider and from the ATLAS experiment at the LHC together with a new world average combination. [12]

are found to be

$$M_Z = (91.1876 \pm 0.0021)\,\mathrm{GeV}/c^2$$

$$\Gamma_Z = (2.4952 \pm 0.0023)\,\mathrm{GeV}/c^2$$

where the values are based on LEP measurements only [34]. The world average for the mass M_W and width Γ_W of the W boson currently combines the measurements from LEP, Tevatron and LHC [12]:

$$M_W = (80.379 \pm 0.012)\,\mathrm{GeV}/c^2$$

$$\Gamma_W = (2.085 \pm 0.042)\,\mathrm{GeV}/c^2$$

CHAPTER 3

Experimental setup of the ATLAS detector

The biggest and most powerful accelerator, which has been built until today is located at CERN[1], the European Organization for Nuclear Research. But this is by far not the only achievement of this laboratory. It has come a long way with many successes along its path since its foundation in 1954 [37]. Many major discoveries took place at CERN, like the first observations of antinuclei in 1965 [38] or the first detection of neutral currents in 1973 by the Gargamelle bubble chamber [39]. The Z and W bosons were detected at the Super Proton Synchrotron in 1983 respectively by the two experiments UA1 [31, 30] and UA2 [40, 41]. One of the largest successes was the discovery of the Higgs boson, which was published in 2012 by ATLAS [5] and CMS [6], giving the long awaited confirmation to the explanation of the mystery of the origin of mass in the Standard Model.

Today, CERN brings together Nations world wide by enabling fundamental research at a spectacular experimental setup. The various fields of research do not only contribute to the understanding of the universe, but they also push the frontiers of technology, from research on accelerators and detectors over developments in the computing sector to medical radiation therapy breakthroughs. [42]

3.1. The accelerator complex with the Large Hadron Collider

The center piece of CERN's current physics program is the accelerator complex around the Large Hadron Collider (LHC), which is able to accelerate particles up to record energies of 6.5 TeV. The standard beam configuration is set up for protons, but heavy ions like Lead ions can be accelerated as well. The way of a proton beam begins at a simple hydrogen bottle, where H_2 molecules are extracted and ionized. The resulting proton bunch is injected into the accelerator chain, where each machine in the complex increases the proton energy further by applying larger accelerating fields (see Fig. 3.1). The process starts with comparably low energies at the end of a linear accelerator (Linac 2) of 50 MeV via a first circular accelerator

---

[1] **C**onseil **e**uropéen pour la **r**echerche **n**ucléaire

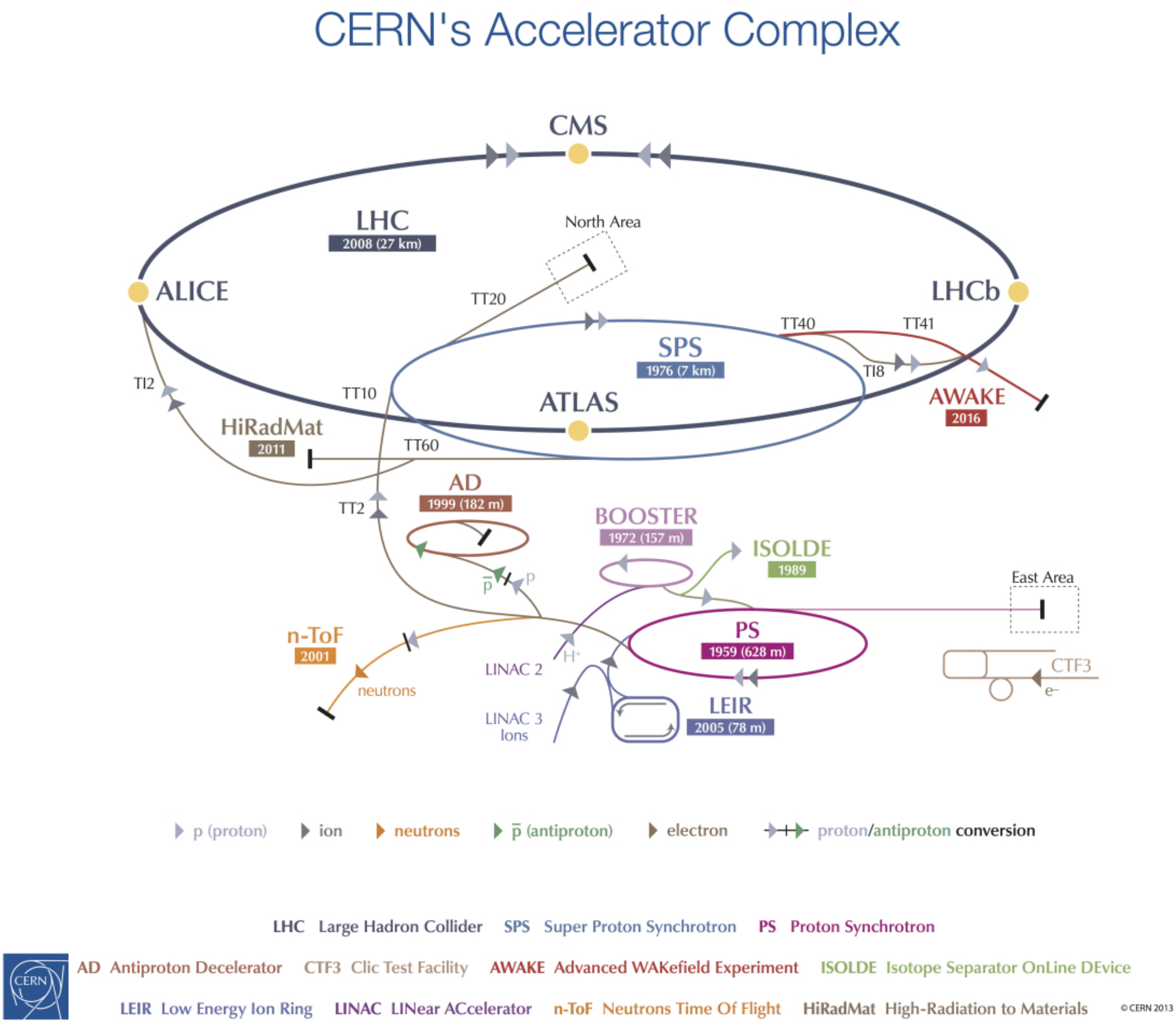

Figure 3.1.: The CERN accelerator complex. The way of the protons starts at the linear accelerator LINAC2 (purple, light gray arrows) and continues to the BOOSTER, where an energy increase to 1.4 GeV is reached before entering the Proton Synchrotron (pink). The next step, where energies of up to 450 GeV are reached, is the Super Proton Synchrotron (blue). Subsequently, the proton bunches are injected into the LHC (dark gray) where they are accelerated to the final energy of currently 6.5 TeV and are brought to collision at one of the four interactions points (yellow). Alternatively, LINAC3 and the LEIR accelerator (blue, dark gray arrows) are the starting points for LHC operations with heavy ion beams. Also shown are various other accelerators and experiments, which make use of the generation and acceleration of other particles like neutrons (yellow arrows), antiprotons (green arrows) or electrons (brown arrows) [43].

of the Proton Synchrotron Booster (BOOSTER) with energies up to 1.4 GeV and successively the Proton Synchrotron, which increases the beam energy to 25 GeV. Before entering the LHC, the particles circulate in the Super Proton Synchrotron, which pushes the beam energy to 450 GeV. Two separate proton beams containing several bunches of protons will then enter the 27 km tunnel of the LHC, circulating in opposite directions while more bunches are added to both beams. It takes only 4 minutes and 20 seconds to fill each beam with the design number of 2808 bunches. After the last round of acceleration, which takes about 20 minutes, the beams reach a final energy of 6.5 TeV. Superconducting electromagnetic cavities provide the radio frequency field necessary for the high energy gain. Additionally, the beams are bent to follow the circular shape of the accelerator by powerful superconducting dipole magnets and the beam profile is adjusted by superconducting quadrupole magnets and collimators to squeeze the beams into perfect collision shape before they can be brought to collision at one of the four interaction points, where the large detectors ALICE, ATLAS, CMS and LHCb are located. [44]

The LHC can deliver high luminosities[2] for many hours under standard operating conditions, leading to an integrated luminosity of up to $\mathscr{L}_{int} = 0.9\,\text{fb}^{-1}/\text{day}$ in 2017. A high number of collision that follows from a high luminosity data taking period, is crucial for the discovery of rare processes. A record peak luminosity of $\mathscr{L} = 20.9 \cdot 10^{33}\,\text{cm}^{-2}\text{s}^{-1}$ delivered to the ATLAS detector was achieved in November 2017. The total integrated luminosity recorded by the ATLAS detector from January 2015 to November 2017 at a center of mass energy of $\sqrt{s} = 13\,\text{TeV}$ reached the spectacular value of $\mathscr{L}_{int} = 86\,\text{fb}^{-1}$. Fig. 3.2 gives an overview over the recorded luminosities for the different data taking periods as well as the peak interactions per bunch crossing achieved. [46]

Since the start of the LHC in 2009 several datasets with different run parameters could be recorded by the experiments of the LHC. The first data taking period of run 1 from 2009 to 2013 included three major datasets of proton-proton collisions at the center of mass energies of $\sqrt{s} = 2.36\,\text{TeV}$ (2009), $\sqrt{s} = 7\,\text{TeV}$ (2010-2011) and $\sqrt{s} = 8\,\text{TeV}$ (2012-2013) at bunchcrossing separations of up to 50 ns as well as several setups with heavy ions [48]. After a first long shutdown, the machine started operating again in 2015 at $\sqrt{s} = 13\,\text{TeV}$ with 25 ns bunchcrossings [49]. This setup is used for proton-proton collisions in run 2, which will be ending with the next long shutdown starting at the end of 2018. In November 2017, a special run configuration was implemented for the two big experiments ATLAS and CMS. The number of colliding protons per bunch was reduced to $1-3$ interactions per bunch crossing. This setup gives optimal conditions for precision analyses like the measurement of the mass of the W boson. [50]

An upgrade to the current accelerator complex is planned with the high-luminosity (HL) LHC project. The technologically advanced HL-LHC will start operating in the year 2025, with an expected increase of the Higgs boson production rate to 15 million events per year, which corresponds to a 12 times larger statistics per year than achievable now [51]. This allows to precisely study the recently discovered particle, but might also enable the detection

---

[2] The instantaneous luminosity characterizes the performance of an accelerator, since it is a measure for the number of collisions per time. It can be calculated by $\mathscr{L} = \frac{\Sigma_i N_1^i N_2^i}{4\pi\sigma_x^*\sigma_y^*} \cdot F \cdot f$, where N_1^i and N_2^i describe the number of particles in each colliding bunch i and σ_x^* and σ_y^* being the transverse widths of the bunches, assuming Gaussian bunch shapes. The factor F accounts for the non-zero crossing angle and f is the frequency of interactions. The events per second for a certain process with a cross section σ_{event} generated in the collisions can then be calculated by $N_{event} = \mathscr{L}\sigma_{event}$. [45]

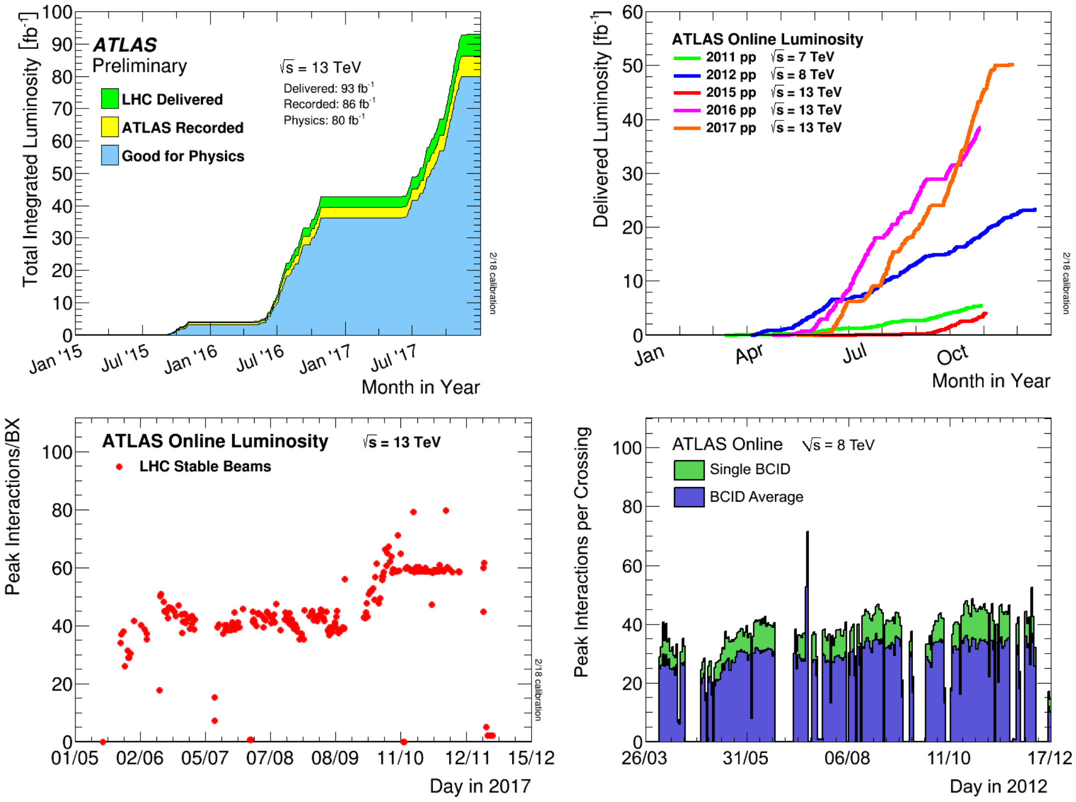

Figure 3.2.: Total integrated luminosity vs. time recorded by the ATLAS experiment for Run2 at $\sqrt{s} = 13\,\text{TeV}$ (top left) and for all data taking periods since 2011 (top right). The plateaus in the curves correspond to maintenance periods in the winter when the LHC was not operating. Also shown are the peak interactions per bunch crossing for the 2017 (bottom left) and 2012 (bottom right) data taking periods. [46, 47]

of other rare processes not accessible with the current setup. Among other improvements, this will be achieved by generating as much as 140 collisions per bunch crossing. This needs several new technological developments, for example a high intensity, more concentrated beam optics. With more powerful quadrupole and dipole magnets, achieved by switching from a niobium-titanium alloy to a compound of niobium and tin, a field strength of 12 T (currently 8 T) for the focusing magnets and 11 T (currently 8.3 T) for the bending magnets can be achieved. [52]

The myriad of particles produced in the collisions at the four interaction points of the LHC are analyzed by currently seven distinct experiments, which cover the various physics aspects of the proton-proton as well as heavy-ion collisions. The two general-purpose detectors ATLAS and CMS provide the largest variety of physics analyses available at the LHC, from precision measurements of Standard Model parameters to the searches for physics beyond the Standard model, including supersymmetry, leptoquarks, dark matter and many other scenarios. Both detectors are built to precisely measure the broad spectrum of final state particles with a centrally installed tracker, followed by calorimeters and a dedicated muon system. However, the technical details and the concept for the magnet system differ. The redundancy by having two experiments with the same physics scope allows for an immediate cross-confirmation. The ATLAS experiment will be further described in the following section. [53, 54]

A more specialized strategy is followed by the LHCb experiment, which analyses heavy flavor physics by studying the rare decays of bottom as well as charm hadrons. The analysis of CP violation might lead to hints for new physics but can also shed light on the answer to the question why there are slight differences between matter and antimatter. The detector is mainly built in the forward direction of one side of the interaction point. Focusing on b quarks, a dedicated identification scheme was developed with a movable tracking system. [55]

The ALICE detector focuses on the study of the quark-gluon plasma by specializing on the analysis of heavy-ion collisions in dedicated LHC runs. These collisions create a quark-gluon plasma with very high temperatures and densities inside, what is currently thought to be the conditions right after the Big Bang. In this scenario, quarks and gluons are not confined in hadrons and their behavior can be studied, allowing a deeper understanding of how matter forms and possibly of the Big Bang itself. A specialized detector layout is necessary to cope with the high particle multiplicity expected for heavy-ion collisions, which focuses on an extraordinary particle identification over a broad range in momentum as well as a good high-momentum resolution. [56]

Next to the big four, a few smaller experiments are located in the vicinity of the big experiments: TOTEM, installed at the CMS interaction point, performs total elastic and diffractive cross section measurements to precisely analyze the scattering pattern of protons by measuring in the very forward directions around CMS with two tracking telescopes [57]. The LHCf experiment, closely sitting next to ATLAS detector, complements the studies in the forward direction by measuring the scattering of neutral particles with two imaging calorimeters. These measurements are crucial for the understanding and calibration of cosmic rays, which show a similar scattering pattern when entering earth's atmosphere [58]. The MoEDAL experiment, added to the LHC family in 2015 and located close by the LHCb detector, is a small detector, which focuses on the direct search for magnetic monopoles and exotic physics by making use of unconventional methodologies such as plastic nuclear trackers. [59]

3.2. The ATLAS detector

The high interaction rates and the particle multiplicity of the collisions of the LHC and the physics scope, which spans from precision measurements to discoveries of new physics phenomena, require a sophisticated design of the particle detector. The performance goals of a detector are usually not easily set, if searching for the unknown. A wide variety of measurement techniques is needed to ensure an excellent potential over a large range of final states. For example until the Higgs boson was detected, its unknown mass allowed many scenarios for its best detection mode, which required to have a broad analysis strategy with many different final states[3]. This, and the wide variety of other experimental goals put demanding requirements on the detector performance.

3.2.1. Physics program

One of the largest benchmark processes over the past decades, which influenced the accelerator and detector designed immensely, was the discovery and further characterization of the Higgs boson. Accordingly, its discovery in 2012 was the largest success of the ATLAS experiment and the CMS experiment so far. With the measurement of its mass an enormous step was taken towards the confirmation of the standard-model like Higgs mechanism. Many Higgs parameters as the various couplings to other particles, its spin and its true character as a Standard Model Higgs Boson or as a product of a theory that goes beyond the aforementioned, is still ongoing (see [60] for a list of recent ATLAS publications available). The measurement of the Higgs self coupling, a process where one Higgs boson is radiating a second Higgs boson, is one of the most challenging objectives because of its tiny cross section and will probably only be available with the HL-LHC.

During the current setup of the LHC, the average production rate per second yields one Higgs boson together with ~ 1200 Z bosons, ~ 4000 W bosons, 17 events with a pair of top quarks and about 12.5 million pairs of b quarks, when an average luminosity of $\mathscr{L} = 20.9 \cdot 10^{33}\mathrm{cm}^{-2}s^{-1}$ as for the 2017 data taking period at a center of mass energy of 13 TeV is assumed [46]. These never seen production rates enable a large potential for precision measurements of standard model parameters. Analyses of QCD and electroweak interactions as well as flavor physics are feasible, with a special remark on top quark physics. But also new heavy gauge bosons Z' and W' bosons can be accessible at the center of mass energies of the LHC, if their masses are below 6 TeV. The leptonic decay products need a good resolution of high momenta of a few TeV. Jet cross section measurements from the QCD parameter sector could be an open window to new physics. Also, a large cross section for flavor changing neutral currents or the observation of lepton flavor violating processes like $\tau \to 3\mu$ are looked into.

Direct searches in the exotics sector outside the Standard Model include supersymmetry, leptoquarks, extra dimension models or dark matter candidates. As an example, the final

---

[3] A low mass Higgs boson ($m_H < 2m_Z$) can be discovered with the non-dominant decays, like into two photons or a pair of Z bosons, where one of them is off the mass shell. The dominant decay into two hadrons is overwhelmed by QCD background at a hadron collider. At the time when the ATLAS detector was designed, a few other scenarios were possible as well. A Higgs boson mass of more than 600 GeV would set the focus on searches primarily to WW or ZZ pairs with a decay into jets or modes including neutrinos. In addition, Higgs boson models that go beyond the Standard Model could not be excluded (and some of them are still possible today), which made the search even more complicated.

states of supersymmetric particles like squarks and gluinos will contain a cascade producing leptons and jets. If R-parity is not violated, a light stable supersymmetric particle (LSP) will escape the detector, leaving behind a signature with a significant amount of missing transverse energy E_T^{miss}.

The high production rate of interesting events is accompanied by an overwhelming number of uninteresting processes, which are a side effect of the high luminosity. A big challenge next to the analyses themselves, is the filtering of these interesting processes from the abundant inelastic scattering interactions as well as QCD jet productions. These events will not only happen frequently, but also additionally in the same bunch crossing as an interesting event.

A large dataset including several data taking campaigns at different center of mass energies is available by now and a large number of interesting results from analyses thereof have already been published, generally confirming the predictions of the Standard Model [61]. But more potential is still to come for the next years with a special regard on the high-luminosity runs.

3.2.2. Technical design

The ability to measure the wide physics potential described above can be summarized by these general performance requirements:

- Particle identification with full track measurement including a reconstruction of the particle's energy, momentum and charge sign as well as the track's direction
- Charged particle momentum resolution from a few GeV up to TeV momenta for muons and high reconstruction efficiencies in the tracking systems
- Very good calorimetry, which enables accurate electron and photon as well as jet energy measurements
- A large detector coverage with a large acceptance in pseudorapidity with as full as possible azimuthal angle coverage
- Good E_T^{miss} and secondary vertex measurements to filter rare processes from abundant background
- Highly efficient triggering with good background rejection capability

The design of the ATLAS detector was taking these requirements into account by using four main instruments: The inner detector tracking system, which aims at the precision tracking of the charged particles emerging at a high rate and with a large multiplicity from the collision point, the calorimeter system, which allows the energy measurement of neutral and charged particles, the muon spectrometer with the purpose of a precise momentum measurement and identification of muons and finally, the magnet system, which enables the momentum measurements for both the tracking and the Muon Spectrometer in the first place. To filter the interesting events from the large background of soft collisions, a sophisticated leveled trigger system is in place, which makes use of hardware as well as software triggers. The components will be described in more detail in the following part. [54]

The magnet system The momentum measurement for charged particles with the ATLAS detector is based on the determination of the curvature of the particle tracks bent by Lorentz force. For high-energetic particles with momenta in the order of a few hundred GeV or more, a very strong magnetic field strength is necessary to guarantee a high resolution. The ATLAS detector includes two separate magnet systems, a solenoid for the magnetic field of the Inner Detector and a toroidal shaped magnet system for the Muon Spectrometer. The first is winded in a thin layer around the Inner Detector cavity and generates a magnetic field of 2 T, while the latter is made up of three toroids, one in each end-cap region and one in the barrel region[4], which generate a field of 0.5 T in the barrel and 1 T in the end-caps of the Muon Spectrometer. This corresponds to a stored energy of 38 MJ for the solenoid and 1.6 GJ for the toroid system. For both magnet systems, these high field strengths are only possible by using superconducting wires. As a result of the solenoidal and toroidal magnetic field the inner detector performs a momentum measurement in the transverse plane and the muon tracks are measured by the full momentum p.

The tracking system The innermost part of the detector consists of finely segmented pixel and strip detectors, which allow a track reconstruction with a precise momentum and vertex measurement. The resolution of the tracking system is designed to be below $\sigma_{p_T}/p_T = 0.05\%\, p_T \frac{1}{\mathrm{GeV}} \oplus 1\%$. The pixel detector is located as close to the beam pipe as possible, with the latest installment, the insertable B-Layer (IBL) being just 3.3 cm away from the beam axis (see also Fig. 3.3) [62]. The high resolution is only possible by making use of fast and small tracking detectors. Here, highly granulated semiconductor silicon pixels with a size of $50(R-\phi)\times 250(z)\,\mu\mathrm{m}^2$ (IBL pixels) and $50(R-\phi)\times 400(z)\,\mu\mathrm{m}^2$ (outer pixels) are used. They are installed in four cylindrical layers in the barrel region and in three discs in the end-cap region. With this a resolution of the pixel system of $14\times 115\,\mu\mathrm{m}^2$ can be achieved.

Following the pixels, semiconductor trackers (SCTs) with silicon strips are installed in 4 layers (barrel) and 18 discs (both end-caps). In the barrel region, stereo strips are installed at a small angle (40 mrad) to measure both coordinates, where one strip is aligned to the beam axis to measure the $R-\phi$ coordinate. For the end-cap region, one set of strips is positioned radially and another set of stereo strips at the small angle of (40 mrad). With this, an intrinsic resolution of $17\times 580\,\mu\mathrm{m}^2$ can be achieved.

A system of 4 mm straw tubes is installed in the Transition Radiation Tracker (TRT). In the barrel region, the tubes are arranged parallel to the beam axis with a length of 144 cm and in the end-caps radially in wheels with a length of 37 cm. In the $R-\phi$ plane, the tracks can be followed through this detector up to $|\eta| = 2.5$ with an accuracy of $130\,\mu$m per straw. The tubes are filled with a xenon-based gas mixture. In addition to the general tracking of the gaseous detector, an electron and pion identification is possible, since the reconstruction is sensitive to electron and pion transition radiation generated when electrons or pions traverse the tubes.

---

[4] The onion-like shape of the ATLAS detector consists of cylindrical layers around the beam pipe in the central region (barrel) and discs or cylinders, which cover the outer caps of the barrel layers (end-caps). The right-handed coordinate system is centered in the middle of the detector and the z-axis follows the beam pipe. Cylindrical coordinates are defined by the polar angle θ, which runs from the beam pipe to the transverse plane perpendicular to it, and the azimuthal angle ϕ, which describes directions in the transverse plane. Usually the pseudorapidity $\eta = -\log(\tan(\theta/2))$ is used instead of θ. Angular distances can be measured by $\Delta R = \sqrt{\Delta\eta^2 + \Delta\phi^2}$.

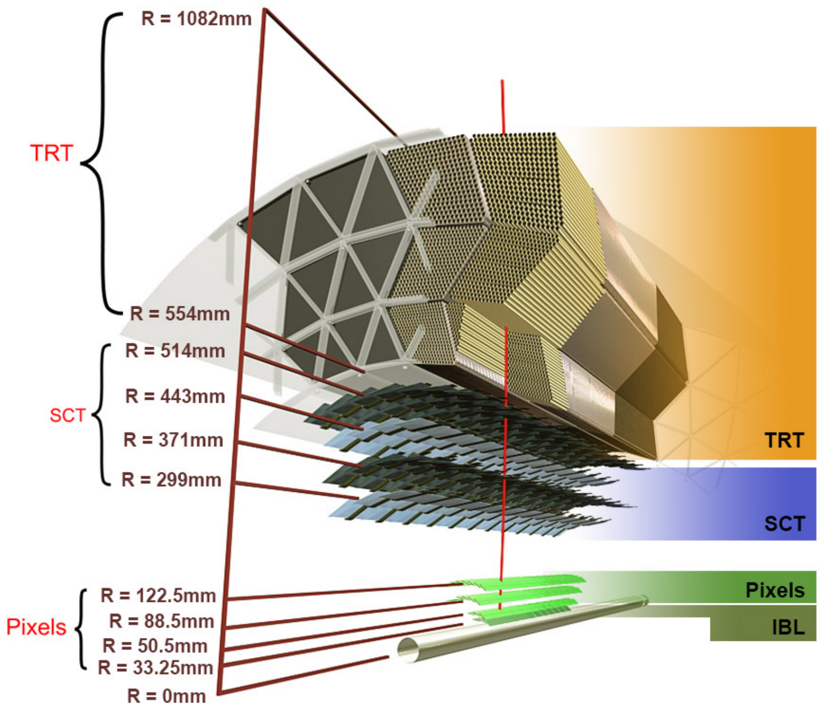

Figure 3.3.: Barrel section of the ATLAS inner detector tracking system. The three subsystems as well as the respective assembly of the different layers with their distance to the beam pipe are indicated. [63]

The overall inner detector track reconstruction acceptance is defined as $|\eta| \lesssim 2.5$, although the physical volume is slightly larger (reaching to $|\eta| \approx 2.7$), but tracks above the reconstruction threshold are not guaranteed to generate enough hits for a reliable track reconstruction.

The calorimeter system The calorimeter system is designed to determine the energy of the electromagnetically and hadronically interacting particles by fully stopping them in the layered system of high-density absorbers and detectors. When showering, the particle leaves a part of its energy in the material of the calorimeter and a summation over the deposited energy allows a measurement of the incident energy of the particle. The system is designed to contain electromagnetic and hadronic showers fully in the electromagnetic (EM) and hadronic calorimeter system respectively. Punch throughs into the muon system are avoided as effectively as possible. This is achieved by choosing a thickness in the EM calorimeter of more than 22 radiation lengths in the barrel ($>$ 24 in the end-cap) and 9.7 interaction lengths in the barrel hadronic calorimeter (10 in the end-caps) for hadronic showers respectively. A schematic overview over the components is given in Fig. 3.4

The electromagnetic calorimeter consists of one barrel and two end-cap components, all enclosed in cryostats operated at 90 K. The working principle of the calorimeters is based on lead absorbers with a high stopping power and liquid Argon (LAr) ionization detectors with kapton electrodes for particle detection. The layers are arranged in an accordion shaped geometry for a full ϕ symmetry. The thickness of the absorber layers is adjusted as a function of η to enable a design energy resolution of $\sigma_E/E = 10\%/\sqrt{E/\mathrm{GeV}} \oplus 0.7\%$ over the whole range. In general, a fine granularity is chosen for the η range matching the tracking system's

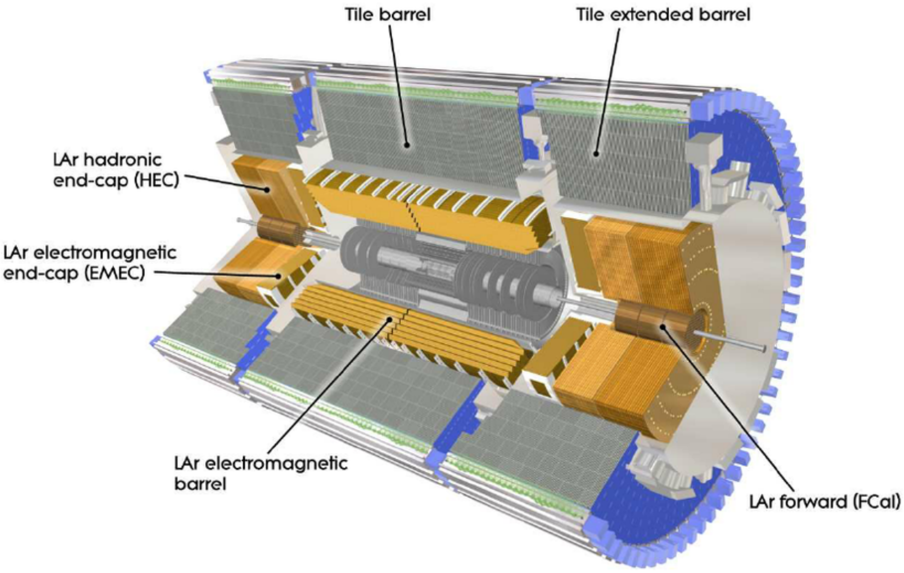

Figure 3.4.: The calorimeter system of the ATLAS detector with its various subsystems for electromagnetic and hadronic calorimetry. The liquid Argon system (orange and brown) is positioned in a cylinder around the inner detector, while the barrel and the extended barrel systems (gray) define the outermost cylinder of the calorimeter. [54]

coverage, while a coarse resolution in the extended range up to $|\eta| = 4.9$ is used for jet reconstruction and missing energy measurements in the outer regions.

The hadronic calorimeter system in the range $|\eta| < 1.7$ is made up from one larger barrel calorimeter ($|\eta| < 1.0$) and two extended barrel cylinders. The barrel calorimeters are complemented by a hadronic LAr end-cap calorimeter (HEC, $1.5 < |\eta| < 3.2$), which is installed following the EM calorimeter end-caps. The barrel tile system encloses the LAr system. For the tile system, steel absorbers and plastic scintillating tiles as the active material are installed in alternating layers. The readout for the scintillators is positioned on both sides of the tile by using wavelength shifting fibers, each side leading to a photomultiplier tube. The liquid argon hadronic end-caps use copper plates for absorption, with a thickness of 25 mm for the inner plates and 50 mm for the outer layers. The liquid argon gaps are 8.5 mm wide.

For the pseudorapidity coverage up to $|\eta| = 4.9$ a smaller forward end-cap (FCal, $3.1 < |\eta| < 4.9$) close to the beam pipe is added for both electromagnetic and hadronic shower measurements. The inner layer uses copper plates inserted between the liquid argon absorbers. The two outer layers, optimized for hadronic showers, use a tungsten absorber. The FCal is positioned 1.2 m further away from the interaction point than the EM end-caps to reduce the neutron albedo in the inner detector, which is created by the showers in the calorimeter and especially relevant in the forward direction.

The design energy resolution for jets of both the barrel and the end-cap hadronic calorimeter is set to $\sigma_E/E = 50\%/\sqrt{E/\mathrm{GeV}} \oplus 3\%$, while the forward LAr hadronic calorimeter follows a design resolution of $\sigma_E/E = 100\%/\sqrt{E/\mathrm{GeV}} \oplus 10\%$.

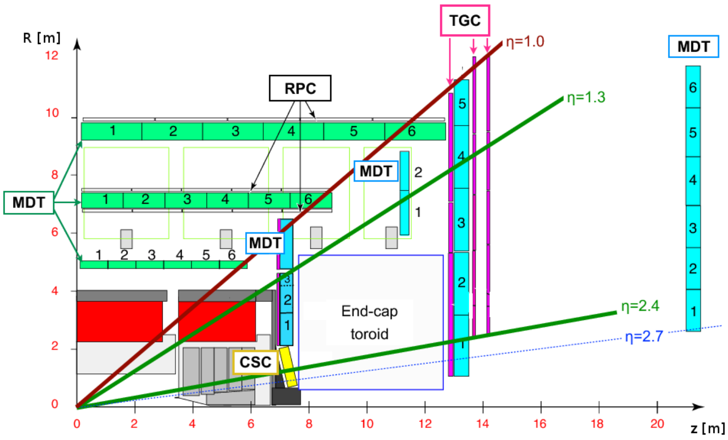

Figure 3.5.: Side view of the ATLAS muon spectrometer with its four chamber technologies: MDTs and CSCs for precision measurements and the two trigger chamber types, TGCs (on the end-cap wheels) and RPCs (in the barrel region). The geometrical acceptance of the barrel and end-cap systems is indicated with various η ranges. [64]

The muon spectrometer Measuring the muon's path with the high resolution muon spectrometer allows for a precise determination of the momenta of high energetic muons in the precision tracking chambers as well as triggering on interesting events with dedicated trigger chambers. The main precision chambers are Monitored Drift Tubes (MDTs), which cover a volume of up to $|\eta| < 2.7$ (see Fig. 3.5). The simple, but robust working principle of gas-filled drift tubes of a diameter of 3 cm gives a good resolution of 80 μm per tube. The chambers are operated with $ArCO_2$ at 3 bar. Each chamber station is equipped with usually two multilayers of 3 to 4 rows of tubes. Three stations of chambers are installed concentrically around the calorimeter in the barrel region at radii of 5 m, 7.5 m and 10 m. Together they make up a ϕ-segmented tower. There are 16 towers in the transverse plane, alternating as 8 larger and 8 smaller towers, slightly overlapping in ϕ to minimize gaps. In the z direction, there are 12 rows of ϕ segmented towers in total. In the end-cap region, the chambers are installed on four discs, the first and the second being on a small wheel before and on top of the end-cap toroid and two large wheels being behind the end-cap toroid, the furthest at a distance of 21.5 m from the interaction point (in z-direction). The MDTs are complemented by Cathode Strip Chambers (CSCs) in the area of large pseudorapidities ($2 < |\eta| < 2.7$), where high particle rates with much background is expected. The multiwire proportional chambers enable a higher granularity by having the cathodes segmented into strips. Each chamber consists of four planes, which allow four independent measurements of η and ϕ of the particle track. The CSCs are installed at the same distance from the interaction point in z direction as the small wheel at ≈ 7.4 m, but with at a smaller radius and thus, being closer to the beam pipe. The resolution for the precision measurement was designed to be as small as $\sigma_{pT}/p_T = 10\%$ at $p_T = 1$ TeV, while also being able to measure momenta as small as 3 GeV. This is only possible, if the relative alignment of the different chambers is known precisely and suffices a precision of 30 μm (within each tower). This is achieved by a special mechanical assembly technique as well as optical alignment systems, which monitor the relative chamber positions.

The muon triggering in ATLAS is largely based on the trigger chambers of the muon spectrometer for the volume of $|\eta| < 2.4$. They provide p_T thresholds for triggering, perform bunch crossing identification and measure the muon coordinate orthogonally to the tracking chamber measurement of the MDTs. Two chamber types are used for this purpose, Resistive Plate Chambers (RPCs) in the barrel region and Thin Gap Chambers (TGCs) in the end-cap regions. The parallel plate RPC detectors are mounted in three layers on the two outer stations together with the MDT chambers (two layers sandwiching the second station and one on the outer station) and the multiwire proportional TGC chambers are added in one layer in front of the first MDT end-cap wheel and in three layers to the second MDT wheel.

3.2.3. Triggering, data acquisition and post processing

The three level trigger system The first step of each analysis starts right after the individual collisions take place, when a decision is made to either write the event information to storage or discard it. The collision rate of 40 MHz does not allow to store all events with the available computing technologies. This sorting of interesting signal events from the abundant background is done with a three level trigger system, where each level refines the selection further. Therefore, interesting events already need to pass the first level and the according selection criteria need to be defined with care, not to miss relevant signatures. Within less than 2.5 μs, the first level (L1) of the trigger performs a decision on a limited amount of the detector information to reduce the event rate to 75 kHz. This hardware trigger searches for high transverse momentum jets, hadronically decaying tauons, muons, electrons and photons as well as large missing and total transverse energy and defines the regions-of-interest(ROI) in η and ϕ, where interesting features were identified. The underlying information is provided by the muon spectrometer and the calorimeters in coarse granularity. In the mean time, the full event information is buffered in the readout buffers (ROB). The second decision is performed by the level 2 trigger (L2). It can access the full precision and granularity within the ROIs to reduce the rate further to 3.5 kHz. On average 40 ms (with an overall 5 s timeout) are available for this process, which is performed in parallel for several events. While the easily distinguishable background has already been filtered, the final stage of the trigger, the event filter (EF), has around 4 s (with a 180 s timeout) per event to refine the decision with a first reconstruction of the full event. The final design readout rate is 200 Hz and around 1.3 Mbyte of data is stored per event at CERN's computer center on easily accessible disc storage as well as redundantly on permanent tape storage.

During the first long shutdown, the two software triggers were optimized and the two separate farms on which the calculations were performed were combined to one farm. The more flexible and less redundant combination of L2 and EF is referred to as the High-Level-Trigger (HLT) [65].

Object reconstruction As a next step, the physical objects need to be reconstructed. Dedicated algorithms for each subsystem were developed and validated to give the best reconstruction of the event.

The track finding for the inner detector measurement starts with the raw data from pixel and SCT detectors by clustering local information. Several approaches exist, but in general, a track extrapolation starts from a seed close to the interaction point and adds hit clusters along the track path through the different subsystems up to the TRT signals. The optimal track trajectory is determined by a refit of all clusters associated to the track candidate by including ambiguity resolving, outlier removal and fake track rejection strategies. The track reconstruction is possible for all tracks that are within $|\eta| < 2.5$ and have a momentum of at least $p_T > 0.5\,\mathrm{GeV}$. However, low momentum tracks only have a limited reconstruction efficiency due to the stopping power of the relatively large amount of material of the inner detector. In addition to the track finder, a vertex reconstruction algorithm identifies primary vertices in a post processing step by analyzing the extrapolated origins of the reconstructed tracks. To reconstruct physics objects like electrons and muons from the set of identified tracks with a high reconstruction efficiency, the information of a second subsystem is needed.

The reconstruction algorithms for the objects identified in the calorimeters depends on the physics quantity of interest. In general, a first cluster reconstruction is done, which groups the energy deposits to local clusters while rejecting as much noise as possible. One approach is the topological cluster algorithm. Local energy deposits are combined in a three dimensional topocluster. The reconstruction starts by searching for a seed cell in the center of the calorimeter, where the energy of the cell exceeds the noise in that cell (mostly electronic noise plus pileup noise), which can be characterized by the energy spread σ_{cell}: $|E_{cell}| > 4\sigma_{cell}$. All neighboring cells are added to the cluster. If a secondary seed can be found among the neighboring cells that fulfills $|E_{cell}| > 2\sigma_{cell}$, also its neighbors are added to the cluster. The search for secondary seeds continues for all neighbors, until no further seeds can be found. Afterwards, a search for multiple maximums allows to split clusters in three dimensions so that each cluster only contains one central energy deposit. Most likely cells with no signal are not added to the cluster, reducing the noise contamination. A calibration is performed on the topoclusters to make up for detector effects such as the smaller response to hadronic energy deposits compared to electromagnetic energy deposits or in general energy deposits in dead material. One example is the local cluster scale α_{cell}, that calibrates each cell signal E_{cell} with a weighted scale: $E_{cell}^{calibrated} = \alpha_{cell} \cdot E_{cell} = (w_{clus}^{EM} \cdot \alpha_{cell}^{em} + (1 - w_{clus}^{EM}) \cdot \alpha_{cell}^{had}) \cdot E_{cell}$ depending on the relative affiliation of the cluster to the electromagnetic (w_{clus}^{EM}) and the hadronic calorimeter ($1 - w_{clus}^{EM}$). The magnitudes of the electromagnetic scales α_{cell}^{em} are significantly smaller compared to hadronic scales α_{cell}^{had}. Another possibility for the calibration is to use the electromagnetic weights for the entire cluster. [66]

The muon spectrometer reconstruction follows a similar approach to the inner detector algorithm. First, a segment finding is performed in each station. Then, the trajectory of the segment is propagated through the magnetic field while adding other reconstructed segments. A combined fit gives the optimal trajectory for all hits associated to the track. The energy loss of the muon in the calorimeter, which is typically around $3\,\mathrm{GeV}$, needs to be determined by using an analytic energy loss parametrization, which is optimized by the measured energy loss of the calorimeter clusters along the extrapolated track. The extrapolation of the track to the interaction point gives the muon spectrometer candidate. A combination with the inner detector measurement can improve the precision as well as the identification efficiency and is done in form of a statistical combination of both tracks or a global refit of both tracks. Several other strategies to form muon candidates from other combinations of subsystem information exist as well, like combing an inner detector track with muon segments only (segment tagged algorithms), if the muon has a too low momentum or interfered with a detector blind spot. This allows a recovery of muons inaccessible to the combined algorithm. For run 1, the two combined algorithms STACO and MuID as well as several specialized algorithms are available. For run 2, a merged reconstruction chain, MUONS, combines the efforts of the separate combined algorithms to one reconstruction strategy [67].

For other particles, the type identification is also performed by combining the reconstructed objects of the subsystems. For example, an electron is identified by successfully matching electromagnetic clusters to an inner detector track candidate. Photons are formed from the EM calorimeter clusters if the matching was unsuccessful. These particle candidates are usually further categorized as tight, medium or loose following a set of selection criteria. The thresholds are independently defined for each data taking period to optimize the identification efficiency and fake object rejection rate, since those parameters vastly depend on the pileup and background conditions. The criteria include momentum thresholds and track quality cuts.

3.3. Monte Carlo event generation

For any analysis signature in high energy physics, a deep theoretical understanding of the underlying processes is essential. For this purpose, Monte Carlo simulations are used. The main key to the generation of simulations, that mimic the behavior of the real interactions, is the detailed understanding of the processes happening a split second after the collision. Since these processes can become very complex, the mathematical description is usually not trivial. As it has been described in the previous chapter, our understanding of the signatures does not only consist of simple tree level processes, but include also higher order corrections. When looking at W and Z bosons, the formation of the transverse momentum only comes in from higher order corrections and initial state radiation. The challenge in simulating these processes is the large amount of calculations necessary to include these corrections and the handling of diverging terms with renormalization regularization techniques, where today's computing power poses an upper limit. Where possible, approximations are included. The way from each processes' differential cross section calculation to the final states, that can be observed in the detector, will be described in this section. The schematic drawing in Fig. 3.3 shows an overview of the development of a typical hard interaction generating a many-body final state.

3.3.1. The anatomy of a collision

The heart of each event is the hard interaction, the process of interest. At a hadron collider such as the LHC, where two bunches of protons are brought to collision, the high center of mass energies in the TeV range make these interesting hard interactions possible. Here, the partons inside the proton are the main ingredients to the process and their characterization must be known in much detail. The parton distribution functions (PDFs) describe the gluon and flavor composition and the energy sharing of the partonic substructure and predict the rates of all possible outcomes of the interaction. Perturbative parameterizations are determined by combining the theoretical assumptions with data from deep inelastic scattering experiments. Based on this approach, a widely used set of PDFs including systematic variations is provided by several collaborations like the latest CT10 set of PDFs from the CTEQ

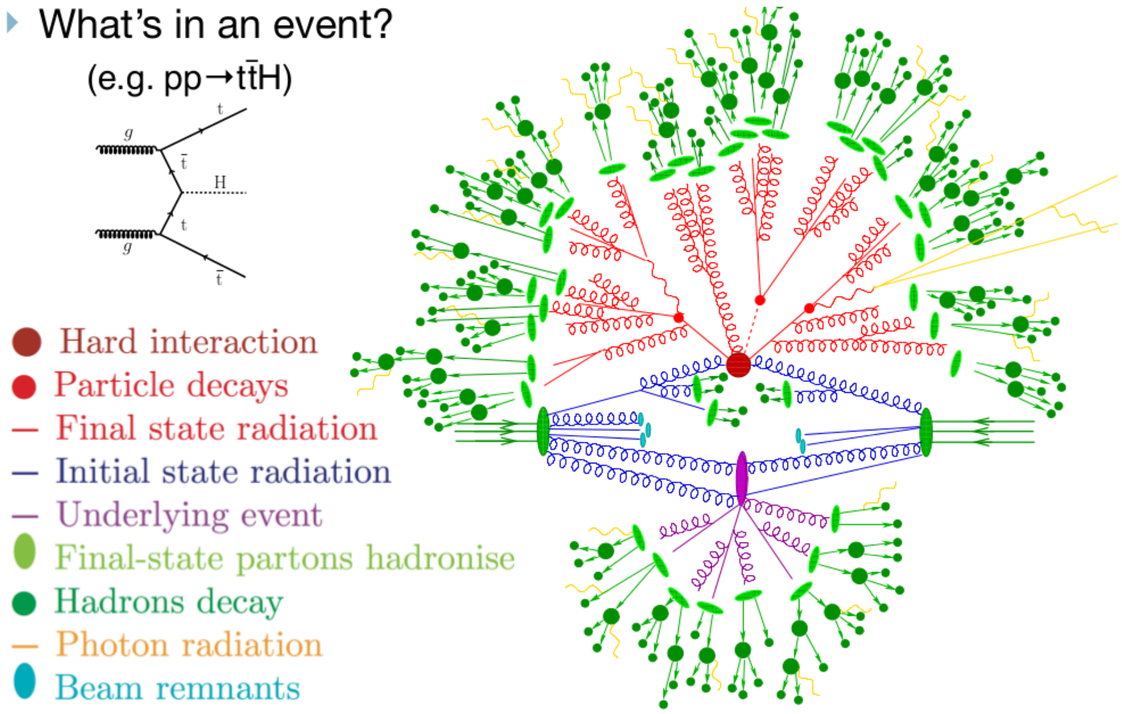

Figure 3.6.: Schematic drawing of the event generation process. Adopted from [68].

collaboration [69] or the MSTW 2008 NLO set of PDFs by A.D. Martin, W.J. Stirling, R.S. Thorne and G. Watt [70].

To first approximation, the partons interact and produce the particles of the final state, in this example (Fig. 3.3) this is a top quark pair and a Higgs boson. Subsequently, the particles can decay themselves. For example the top quarks will almost always decay into a b quark and a W boson. The leading matrix element that describes this process can easily be calculated. Including higher order corrections can already make the calculation quite complicated. Several programs like MADGRAPH, MC@NLO, ALPGEN or SHERPA (cf. [71, 72, 73, 74]) can generate those matrix elements up to a few orders.

As a next step, the calculations need to include initial state radiation (ISR) and final state radiation (FSR), which is gluon and quark radiation. This QCD emission is linked to the strong coupling constant α_s. For small energy transfers α_s becomes large (see again Fig. 2.1) and therefore high rate of gluon self coupling result in a high probability for one QCD emission and even the probability for multiple emissions cannot be neglected, resulting in a large amount of initial and final state radiation. [75].

For a more accurate description of the hard process, corrections in form of loop diagrams need to be taken into account. Since the necessary perturbative calculations are quite extensive, usually only one order of loop corrections can be considered. Combining the calculations with the entangled ISR/FSR effects, some divergences can be avoided. Dedicated algorithms are being developed to gain a higher precision. At the moment the event generator POWHEG [76] gives one of the best predictions for next to leading order corrections for LHC like pp interactions and is used to generate the Monte Carlo samples for a wide variety of ATLAS analyses.

All partons in the final state will hadronize and create color-neutral hadrons, following the rules of quark confinement. This process is non-perturbative, which makes predictions especially challenging. The development of good models that describe the processes in sufficient detail along with an as accurate as possible determination of α_s in this range are quite important. Subsequently those hadrons will decay as well, creating jets. Models for parton showering are implemented in programs such as HERWIG++ [77] or PYTHIA8 [78]. This step takes the input from the hard interaction processes, which is already convoluted with NLO corrections and radiation effects.

The remaining partons from the two colliding protons that did not participate in the hard interaction are color-connected to the hard interaction. Following quark confinement, those beam remnants have to hadronize. Additionally, they can also do semi-hard interactions and create a shower of particles. Since only a fraction of the beam energy is used in the hard interaction, the beam remnants carry most of the initial center of mass energy and leave the interaction point with a forward boost. As a result, they hardly reach the detector but stay in the vicinity of the beam line.

Additionally, other protons in the same bunch crossing can do soft scattering, soft interactions and, in rare cases, even hard interactions, creating additional particles and additional radiation and decays. The sum of the particles that emerge from these interactions will be called in-time pileup.

The high instantaneous luminosity of the LHC can only be achieved by a high rate of colliding bunches of protons. The small bunch spacing of 50 ns (in run 1 collisions) or 25 ns (in run 2 collisions) can result in the overlap of the signals from prior and successive collisions with the main event constituents in the calorimeter due to the large integration time of up to 200 ns. This effect is called out-of-time pileup.

The various generators described above make use of the Monte Carlo method, which allows for calculation of probability values with pseudo-random number generation. With this, large and nearly uncorrelated datasets can be generated.

3.3.2. Detector propagation

The huge amount of particles generated in the Monte Carlo simulations need to be propagated through the detector, while interacting with it in the same way real particles would do. For this purpose, the ATLAS computing model includes a full digital copy of the detector [79]. Where possible, all irregularities of the real detector are implemented as well, e.g. chamber misalignments. The detector description as well as the particle propagation, which simulates the interaction with the detector material, is done in the software suite GEANT 4 [80], which is one of the best toolkits for the modeling of a particles' passage through matter, geometry and hit generation currently available. The hits, which are generated by the simulated particles, are then analyzed in the same way as real data by applying the same reconstruction and identification algorithms. In addition, truth information in form of initial particle coordinates, momenta and much more is also available in the file format available for analysis.

CHAPTER 4

Analysis objects and methodology

4.1. Event variables

For the measurement of the mass of the W boson with the ATLAS experiment, the hadronic recoil is the only method available to model the transverse momentum of the W-Boson in case of a leptonic decay. The neutrino will not be detected by the ATLAS detector and can only be indirectly measured. One of the fundamental concepts of physics, momentum conservation, allows for an indirect approach to measure the sum of all invisible components of an event. When a W or Z boson with transverse momentum is created, it recoils against other particles created in the processes of the same proton interaction to conserve momentum. Mostly this is gluon and quark initial state radiation. A measurement of the detector signatures of these particles is the key to reconstruct the kinematics of the boson decay. This section will describe the relevant variables used for the analysis. The schematic drawing in Fig. 4.1 shows a transverse view of a Z boson decay and the involved objects.

4.1.1. Pileup and underlying event

In general, the final state particles of collisions at a hadron collider include much more than just the hard interactions (see Sec. 3.3). If no restrictions are imposed, the hadronic recoil algorithms will not only pick up true recoil but also all other particles within the detector acceptance, passing the selection. This is the luminosity dependent in-time and out-of-time pileup from other soft collisions happening simultaneously and from successive and previous bunch crossings respectively. These particles will decrease the resolution of the hadronic recoil. If these particles can be removed, the resulting recoil signal would be much cleaner. The 2017 special runs with low pileup (μ) had this goal in mind. But also particles coming from the same proton proton interaction that are not necessarily balancing the recoil, will be included in the hadronic recoil measurement and will decrease the resolution. These particles will be called underlying event and they usually cannot be removed from the measurement.

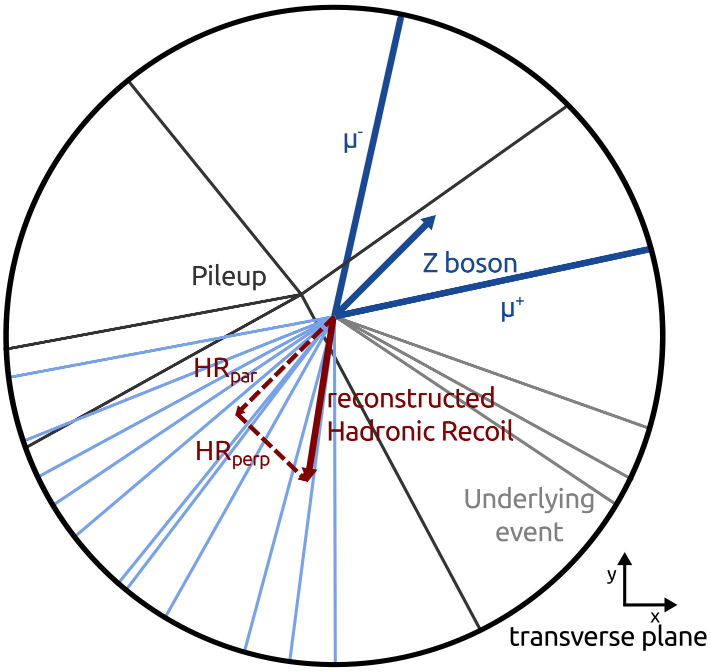

Figure 4.1.: Schematic drawing (transverse view) of a typical event containing a Z boson and its two decay muons (blue), particles from the same hard interaction that carry a fraction of the hadronic recoil (light blue) and the underlying event particles, which do not carry recoil (light gray) as well as pileup particles from other interactions reaching the detectors simultaneously (dark gray). The offset of the pileup vertex visible here is exaggerated. The distance between pileup vertices and the primary vertex with the Z boson is usually much small in the transverse plane compared to the distance on the z-axis. The reconstructed hadronic recoil (red) can be divided into a component parallel to the reconstructed Z boson momentum and a perpendicular component.

4.1.2. Hadronic recoil

The **scalar sum** of the transverse momentum or energy of the particles included in the recoil calculation will be denoted as ΣE_T. It is a measure of the overall hadronic activity of the particles considered in the calculation and eventually of the event. It is very sensitive to pileup and underlying event particles.

The **vector sum** of the momenta/energies is usually referred to as hadronic recoil and is represented by the short formula $\vec{HR}$. Ideally, the hadronic recoil is the exact response to the recoiling boson

$$\vec{HR} = -\vec{p_T}^{boson} = -(\vec{p_T}^{l1} + \vec{p_T}^{l2}),$$

where $\vec{p_T}^{l1/2}$ are the transverse momenta of the two leptons. However, because of the finite detector resolution and pileup as well as underlying event particles, the hadronic recoil vector on a one-event level is randomly distributed around the original recoil direction. On a global level, the spread of the deviation from the true direction is a measure for the noise.

For events, where a Z boson can be reconstructed out of the two decay leptons in addition to the recoil measurement, a finer segmentation of the hadronic recoil is possible. It can be divided into a component that is parallel to the reconstructed Z boson,

$$HR_{par} = \vec{HR} \cdot \frac{\vec{p}_T^Z}{|\vec{p}_T^Z|},$$

and a component perpendicular to it,

$$HR_{perp} = \vec{HR} \times \frac{\vec{p}_T^Z}{|\vec{p}_T^Z|}.$$

The first should be as large as the transverse momentum of the Z boson and the latter should in theory be zero. Because of detector resolution and acceptance, this is however only true for the mean of the distributions. The noise described above can be described by a Gaussian distribution around the expected values, where the width of the Gaussian distribution $\sigma(HR_{perp})$ is a good measure for noise and is referred to as **perpendicular resolution**. The parallel component will on average be smaller than the transverse momentum of the Z boson, since not all particles of the hadronic recoil can be measured. The **bias**, which is the mean of a corrected distribution $\langle HR_{par} + |\vec{p}_T^Z|\rangle$, will therefore peak around values in the order of a few GeV. The Gaussian width of the corrected distribution $\sigma(HR_{par} + |\vec{p}_T^Z|)$ is a measure for the **parallel resolution**.

4.1.3. Missing transverse momentum

For events with a W boson, the **missing transverse momentum** of the neutrino can be calculated from the hadronic recoil and the charged lepton transverse momentum $\vec{p_T}^l$:

$$p_T^{miss} = -(\vec{HR} + \vec{p_T}^l).$$

4.2. Hadronic Recoil algorithms

Several algorithms for the calculation of the hadronic recoil were developed. The general strategy is using either clusters measured by the calorimeters or tracks measured by the Inner Detector. Additionally, several combinations of the two principle strategies are possible. The different approaches are described in more detail in the following section. [81]

4.2.1. Cluster-based algorithms

The hadronic recoil is calculated by summing the transverse energies from the reconstructed clusters measured in the calorimeter system. The vector sum is defined as

$$\vec{HR}^{cluster} = \Sigma_{i=1}^{N_{clusters}} \vec{E}_T^{cluster}$$

with $\vec{E}_T^{cluster}$ being the transverse energy of each cluster pointing in the cluster's transverse direction, while the scalar sum is calculated as

$$\Sigma E_T^{cluster} = \Sigma_{i=1}^{N_{clusters}} E_T^{cluster}.$$

In this way, energies from charged as well as neutral particles are included in the calculation. However, energies deposited by pileup and underlying event particles cannot be distinguished from the recoil and thus, resulting in a worsened resolution. With the high coverage of the calorimeters of $-4.9 < \eta < 4.9$ these algorithms include a large fraction of particles emerging from the hard interaction.

The energy deposits of the boson decay products have to be corrected for. Especially if the boson decayed into electrons, the shower generated by the electron has to be removed from the calculation. This is done by placing a cone around the track and removing the energy clusters inside. Since the cone size affects the energy resolution, this value has to be carefully considered. In the implementation of the cluster algorithm for the run 1 analysis of the 2011 and 2012 dataset at $\sqrt{s} = 7\,\text{TeV}$ and at $\sqrt{s} = 8\,\text{TeV}$ respectively a threshold value of $\Delta R = \sqrt{(\phi_{cone} - \phi_{cluster})^2 + (\eta_{cone} - \eta_{cluster})^2} < 0.2$ with respect to the central cone directions ϕ_{cone} and η_{cone} was chosen. With this removal procedure, also other energy deposits overlapping with the lepton are subtracted. This consists of underlying event and pileup as well as, though hardly significant, also recoil energy. With the removal of pileup and underlying event a directional bias would be introduced, since those quantities are uniformly distributed in the event. To correct for this effect, a suitable replacement cone is chosen in a second step. The cone should have the same pseudorapidity value but different phi, while not overlapping with the removed cone or being in the vicinity of the reconstructed hadronic recoil direction. In case of non-isolated leptons, the isolation value determined by the calorimetric isolation is used as a rough estimate. [81]

Various implementations of the cluster algorithm with different purposes exist. Some are primarily used for performance studies of the cluster algorithm, others will be used for the recoil measurement in the W analyses. Two examples will be given here:

cluster This implementation is the standard cluster algorithm without any constrains. Studies in events with a reconstructed Z bosons with the dataset of the 2011 data taking campaign showed, that the resolution of the corrected parallel and perpendicular hadronic recoil component and the bias showed a good sensitivity on various parameters such as the boson transverse momentum dependence. [81]

clusEta25 This variant mimics the acceptance of the Inner Detector by applying a cut on the pseudorapidity $|\eta| < 2.5$ of each cluster. This allows to study the impact of the loss of tracks that are closer to the beam line.

4.2.2. Track-based algorithms

For this approach, tracks from the Inner Detector with better intrinsic resolution than calorimeter clusters are used for the recoil calculation. The tracks have to fulfill a set of selection criteria. Tab. 4.1 lists the requirements applied in the implementation of the track algorithm for the run 1 analysis. Here, a minimum threshold for the transverse momentum is applied and the tracks need be within the acceptance of the Inner Detector. A minimum number of hits in the pixel and SCT system need to be given to ensure a reliable track fit. For a rejection of pileup tracks, the tracks are matched to the primary vertex, which is defined as the vertex with the largest Σp_T^2 of associated tracks. A cut on the longitudinal (z_0) and transverse (d_0)

impact parameter with respect to the primary vertex are applied[1]. In addition to this set of cuts, signal lepton tracks are excluded from the track selection.

Cut name	*threshold*
Track p_T	$> 500\,\text{MeV}$
Track $\lvert\eta\rvert$	< 2.5
Track Pixel Hits	≥ 1
Track SCT Hits	≥ 6
Track d_0	< 1.5
Track $z_0 \cdot \sin\theta$	< 1.5

Table 4.1.: Criteria for the Inner Detector track selection for the hadronic recoil algorithm at $\sqrt{s} = 8\,\text{TeV}$.

The hadronic recoil for track algorithms is defined as

$$\vec{HR}^{track} = \Sigma_{i=1}^{N_{tracks}} \vec{p_T}^{track}$$

with $\vec{p_T}^{track}$ being the reconstructed transverse momentum of the track measured in the Inner Detector. The scalar sum calculates as

$$\Sigma E_T^{track} = \Sigma_{i=1}^{N_{tracks}} |\vec{p_T}^{track}|.$$

Because of the undetectable neutral tracks and the lower acceptance of the Inner Detector of $-2.5 < \eta < 2.5$, track algorithms miss about half of the actual recoil energy and therefore should be scaled to represent the full hadronic recoil. In this analysis, the following implementations are used:

track500PV This implementation of the track algorithm follows the selection criteria from Tab. 4.1. It is the second main algorithm for the hadronic recoil measurement. Studies on the $\sqrt{s} = 7\,\text{TeV}$ dataset showed, that the energy-corrected algorithm gives good results, but lacks sensitivity on the vector boson transverse momentum compared to the cluster algorithm. [81]

track500 Here, the primary vertex requirements (d_0 and z_0 cuts) are not applied. Therefore, it includes pileup tracks and their influence on the performance of the hadronic recoil can be studied when comparing to the track500PV algorithm.

track1000PV A tighter track selection only considers tracks with $p_T > 1\,\text{GeV}$.

track1000 In addition to the $p_T > 1\,\text{GeV}$ cut, the tracks do not need to come from the primary vertex. When comparing this implementation to the track500 implementation the impact of low momentum tracks can be studied.

---

[1] The impact parameters are defined as the distance of the closest approach to the primary vertex in the transverse plane (d_0) and the corresponding z axis coordinate (z_0).

4.2.3. Combined algorithms

With combined algorithms, an attempt is made to increase the resolution with respect to cluster algorithms and possibly also to introduce an effective pileup rejection without the loss of information. In order to give competitive results, a sophisticated algorithm is needed to not introduce a bias. For the two run campaigns different strategies were implemented:

Tracking-improved cluster algorithm This algorithm was developed for the W boson mass measurement of run 1 to combine the advantages of the track and cluster based algorithms by enabling pileup rejection for the cluster algorithm. If a reconstructed cluster can be associated to a track from a vertex other than the primary vertex, it will be rejected. Tracks that pass the standard track requirements (see Tab. 4.1) are tagged as primary vertex or secondary vertex tracks, depending on the impact parameter cuts. Then they are propagated to the second layer of the calorimeter, where the cluster reconstruction is usually seeded. If a matching in $\Delta R(\phi,\eta) < 0.15$ is positive, the track is associated to the cluster. Consequently, only clusters with no associated tracks from secondary vertices enter the cluster selection. By also including clusters with no primary vertex track associated, the loss of information of neutral particles could be less disadvantageous compared to the track algorithm. Studies on the performance of this algorithm with the pileup conditions of the 2011 dataset showed a good rejection capability in comparison to the standard cluster and track algorithm, but it was concluded that the sensitivity on the boson momentum dependence is worse than for the cluster algorithm. [81]

PFO algorithm The concept of particle flow objects is widely used in many high energy analyses for example to determine the energy of a jet or to indirectly measure missing energy escaping detection while efficiently rejecting background such as pileup. Especially when considering low energy tracks with a better energy resolution in the tracking system than from calorimetric measurements, this leads to an improvement in the total energy resolution of the physics object. An implementation for the hadronic recoil for ATLAS analyses is available since run 2. Input into this algorithm are the charged and neutral particle flow objects. In order to classify tracks and clusters, the tracks are extrapolated to the second layer of the EM calorimeter and a ΔR matching to the nearest cluster is performed. The subsequent procedure is quite sophisticated, but the general concepts of the different possibilities are as follows [82], [83]:

- If a track has no matching cluster, it simply enters the calculation as a charged object. Tracks with energies in the order of a few GeV have a high chance to not seed a shower in the calorimeter.
- If one cluster is associated to one track, the cluster energy is compared to the expected energy by the track. If comparable, the cluster is removed while the track is kept as a charged object. This allows to remove the noise included in the cluster reconstruction. If the cluster energy is too small, it is assumed that the shower is split across several clusters. A cluster matching in ΔR is performed and close by clusters are added until the expected energy is matched. Alternatively, if the energy of the cluster is larger than the track, the cluster is split at cell level. The part matching the track energy is removed, while the remaining part of the cluster is classified as a neutral object.

- If a cluster has more associated tracks, the cluster is split accordingly. The analysis continues similarly to the one-cluster-one-track case.
- Clusters with no associated track are classified as neutral objects. Since the topological cluster algorithm does not apply a calibration of the energies to the clusters themselves, the Local Hadron calibration, the ATLAS calibration algorithm for cluster objects, can be applied before those objects are used in the hadronic recoil algorithm.

The newly defined particle objects enter the hadronic recoil calculation. Also here, several variations exist, but in general, the charged objects undergo a pileup suppression by cutting on the impact parameters. Vertex cuts can be applied as well. The neutral objects need to be calibrated. Here, two calibration scales exist. With the local cluster scale (LC) the standard topocluster calibration method (see Sec. 3.2.3) is applied. Opposed to this, with the EM scale the smaller EM weights are applied for all neutral objects.

The different implementations for the run 2 particle flow algorithm are:

pfo This implementation describes the baseline PFO algorithm with the standard configuration. Neutral objects are calibrated with the standard local cluster scale.

pfoEM In this variant of the pfo algorithm the EM scale is used to calibrate neutral particle flow objects.

pfoCharged Here only charged particle flow objects are used for the algorithm calculation. This allows to study the response of charged particles.

pfoNeutral Opposite to pfoCharged, only neutral particle flow objects with the standard calibration enter the algorithm.

pfoNeutralEM In addition to the pfoNeutral tune, the EM scale is used for calibrating the neutral objects.

4.3. How to measure the mass of the W boson

4.3.1. Observables sensitive to M_W

The mass of the W boson can be extracted from three different variables. The obvious method is to calculate the invariant transverse mass of the reconstructed system of the charged lepton and the missing momentum of the neutrino, which could be indirectly measured via the hadronic recoil. In addition, the transverse momentum of the charged lepton and the missing momentum of the neutrino can be used to determine the mass of the W boson, since these spectra peak at $M_W c/2$. Fig. 4.2 shows a sketch of the three distributions. [84]

Invariant transverse mass Combining the two reconstructed leptons allows to determine the invariant mass by

$$M_T^W = \sqrt{(E_T^l + E_T^\nu)^2 - (\vec{p_T}^l + \vec{p_T}^\nu)^2} \approx \sqrt{2 p_T^l p_T^\nu (1 - \cos\phi_{l\nu})}.$$

The approximation is valid when assuming that the masses of both leptons can be neglected. The value for M_T^W only depends on the transverse momenta of the decay

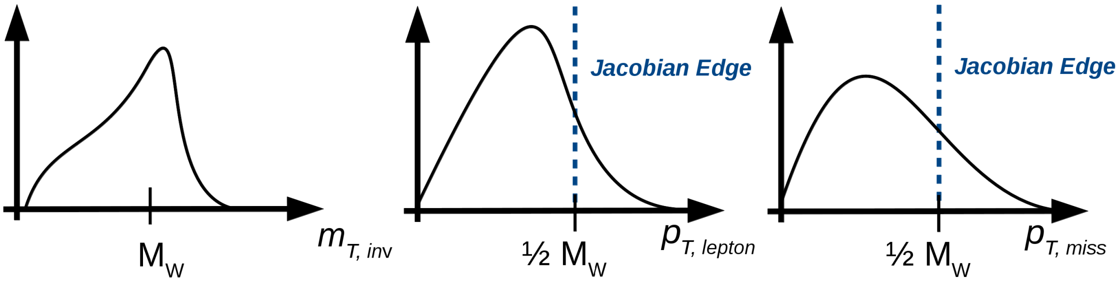

Figure 4.2.: Variables sensitive to the mass of the W boson: invariant transverse mass spectrum of the reconstructed leptons (left plot), transverse momentum spectrum of the charged decay lepton (central plot) and the transverse momentum spectrum of indirectly measured neutrino (right plot). The Jacobian Edge indicates the relation of the two lepton momentum distributions to half the mass of the W boson.

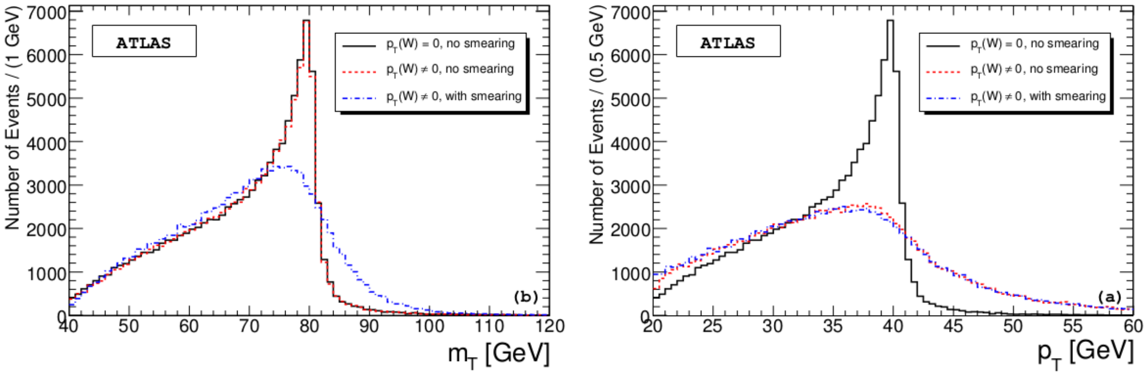

Figure 4.3.: Fitted distribution of the transverse mass M_T^W and the transverse lepton momentum p_T^l from an ATLAS Monte Carlo study. The effect of a boson's transverse momentum $p_T(W) \neq 0$ (red dashed line) and smearing due to finite detector resolution mainly of the recoil measurement (blue dotted dashed line) are shown. [85]

leptons p_T^l and p_T^ν and the opening angle $\phi_{l\nu}$ of the two. The left-hand plot of Fig. 4.3 shows an estimation of the effect on the invariant mass distribution of smearing and of a non-zero transverse momentum of the W boson. Clearly, the influence by smearing dominates the spectrum and the finite momentum only has a small effect. The smearing can mainly be explained by the resolution of the recoil measurement, while the charged lepton resolution only has a minor effect. A precise measurement of M_W by this approach heavily relies on an optimal measurement of the hadronic recoil. [85]

Charged lepton momentum When a heavy particle, such as the W boson, with low transverse momentum decays into two light weighted particles, they are emitted with a momentum of about half the original particle's mass. The transverse momentum of the charged lepton follows as $p_T^l \approx \frac{1}{2} M_W c \cdot \sin\theta$, where θ is the angle between the lepton and the beam line in the rest frame of the boson. The cross section dependence on the momentum follows as

$$\frac{\mathrm{d}\sigma}{\mathrm{d}p_T} = \frac{\mathrm{d}\sigma}{\mathrm{d}\cos\theta}\frac{\mathrm{d}\cos\theta}{\mathrm{d}p_T}$$

The transverse lepton momentum can be rearranged to

$$\cos\theta \approx \sqrt{1 - \left(\frac{2p_T^l}{M_W c}\right)^2}$$

With this, the cross section dependency on the lepton momentum can be written as [13]:

$$\frac{\mathrm{d}\sigma}{\mathrm{d}p_T} \approx \frac{\mathrm{d}\sigma}{\mathrm{d}\cos\theta}\frac{1}{\sqrt{\left(\frac{M_W c}{2}\right)^2 - p_T^{l2}}}$$

The asymptotic maximum of this function is reached at the Jacobian Edge at $p_T^l = \pm\frac{M_W c}{2}$. Because of the finite decay width and the non-negligible transverse momentum of the W boson the transverse momentum of the decay particle is smeared out. The effect of the boson momentum is shown in the right-hand plot of Fig. 4.3. In addition the effect of a finite detector resolution is also estimated. It can be seen, that the value for M_T^W obtained from the lepton distribution is strongly dependent on the modeling of the boson's transverse mass spectrum. [85]

Missing momentum The transverse momentum spectrum calculated by the hadronic recoil shows the same Jacobian Edge as the charged lepton's distribution. However, the detector resolution from the recoil measurement compared to the charged lepton measurement is much worse. The corresponding systematic uncertainty will be quite high and only a small improvement to the overall measurement is expected by including this observable in the measurement.

In addition to the different observables available, the measurement can also be performed separately in the W^+ and W^- boson channel as well as independently for the electron and the muon measurement. Discrepancies would point to inconsistencies from various experimental systematics as well as physics modeling effects. A categorization in the lepton pseudorapidity $|\eta_{lep}|$ allows for a possible reduction of systematic effects by the incomplete coverage of the relevant detector systems. The final value for M_W will be a combination of all measurements. [86, 87]

4.3.2. Template fit approach

The value for the mass of the W boson is extracted from the sensitive distributions M_T, p_T^l and E_T^{miss} as well as two-dimensional combinations thereof by comparing the measured data to the theoretical expectations. The simulations include signal as well as relevant background samples. The necessary signal Monte Carlo simulations that model the theoretical expectations, use the value for the mass of the W boson already as an input parameter. Therefore, a set of simulations - the templates - where different values for M_W are implemented, are compared to data. The templates are not created from scratch but by making use of the natural line width of the W resonance. For one mass point, a high statistics Monte Carlo sample is generated, propagated through the digital version of the detector and analyzed in the same way as the measured data. In order to obtain the templates, the invariant mass distribution from this mass point can be reweighted analytically following a relativistic Breit Wigner [88] parameterization [89]:

$$f_{BW}^{rel}(M,E) = \frac{E^2}{M^2} \cdot \frac{1}{(E^2 - M^2)^2 + M^2\Gamma^2},$$

which is taken from the cross section calculation for a resonance:

$$\sigma_{res} = g(2J+1)13\pi\Gamma_f\Gamma_i \cdot f_{BW}^{rel}$$

with g being the spin weighting, J and M the spin and mass of the resonance particle, Γ_i, Γ_f and Γ being the width of the initial state, final state and the total width and E is the energy of the resonance available in the collision. The reweighting is applied in form of an event weight for each template

$$w_{template} = \frac{f_{BW}^{rel}(M_{template}, E_{ref})}{f_{BW}^{rel}(M_{ref}, E_{ref})},$$

where E_{ref} is the energy of the Monte Carlo truth particle.

This fixed-width parametrization does not allow for next-to leading order electroweak corrections necessary for the Monte Carlo generators or the effects of a running decay width. The corresponding changes to the formula are derived in [90] and the implementation for a W mass measurement can be found in [91].

A χ^2 compatibility test analyzes the residual difference between simulation and data measurement for each template. The mass value describing the data best is determined by minimizing the parabolic χ^2 curve, obtained by interpolating between the distinct mass points of the templates.

This method presents an easy way to determine the impact of experimental and theoretical systematic uncertainties by including them in the compared distributions one by one. The deviation from the ideal fit value gives the impact of the uncertainty investigated. [9]

4.3.3. Statistical and systematic uncertainties

The measurement of the mass of the W boson at a hadron collider comes along with several sources of uncertainty. This section summarizes the main effects of statistics, physics modeling and experimental corrections.

Statistics Statistical uncertainties are common to all measurements in physics, since only a finite dataset is available and each measured value can differ from the true value by random chance. By increasing the size of the dataset, this uncertainty can be reduced. For example, if a sample is divided into various categories, as done for a histogram, the number of entries per category (bin) N is associated with an error of $\sqrt{N}$, if Gaussian statistics are assumed.

The contribution of the statistical uncertainty on a W mass measurement that is performed on the entire run 2 dataset, where abundant events with leptonically decaying W bosons are created, is comparably small, but for the one-week special data taking periods with low pileup, this source of uncertainty will probably exceed the systematic variations. An estimation will be given in the analysis section.

The statistics of the Monte Carlo templates should exceed the statistics of the dataset, so that the statistical uncertainty is only limited by the data taking rather than the simulation effort.

Physics modeling The physics modeling systematic uncertainty summarizes the effects of differences between the finite theoretical predictions and real data. The systematics are minimized by using the best description available in the Monte Carlo generation and by applying corrections afterwards, where applicable. These procedures and remaining effects nevertheless introduce a systematic uncertainty. The dominant source of uncertainty comes from the incomplete knowledge on the parton density functions. The PDF modeling influences the boson momentum and rapidity distribution as well as the angular coefficients. Especially for the extraction of M_W from the lepton distribution, which is highly influenced by the boson momentum, the PDF modeling uncertainty will be relevant. A theoretical estimate on the impact of PDF uncertainties on W mass measurements are found to be of the order of $10\,\mathrm{MeV}$ [92]. In addition, electroweak and QCD higher order loop corrections especially for initial and final state radiation as well as parton showering in the Monte Carlo generators together lead to considerable uncertainties. These effects depend highly on the generators used for the simulation.

The modeling of the transverse boson momentum distribution by making use of a calibration derived in events containing a Z boson introduces another relevant uncertainty.

A detailed discussion of the physics modeling and its uncertainties for the ATLAS measurement at $\sqrt{s} = 7\,\mathrm{TeV}$ can be found in [91]. For this measurement the overall uncertainties on M_W were dominated by the physics modeling uncertainties [9].

Lepton calibration The position of the Jacobian Edge within the lepton distribution is highly influenced by the resolution and scale of the charged lepton. In order to have the same effect of resolution and energy scale in the simulations as in data, the simulated objects need to be carefully calibrated to match the precision in data as identically as possible. In addition, reconstruction, identification and trigger efficiencies have to be adjusted in the simulations. The according systematic uncertainties need to be taken into account. Because of different detector signatures the procedures applied differ slightly for electrons and muons.

In case of muons, the calibration is performed by using the two standard candles J/Ψ and Z bosons and by comparing the performance of the simulated datasets to real data. The correction factors and the according uncertainties are derived for each run campaign separately. A careful consideration should be done if the track measurement from the inner detector only should be preferred to the combined muon object. For the latter the uncertainties for the energy loss in the calorimeter along with the muon spectrometer momentum measurement are added to the inner detector track reconstruction uncertainty. In the $\sqrt{s} = 7\,\mathrm{TeV}$, the momentum measurement of the inner detector only was used.

If possible, the corrections and uncertainties for electron objects are derived by comparison of Z bosons events in simulation and data. Here, calorimeter calibration plays an important role on the energy calibration.

Hadronic recoil calibration The measurement of the hadronic recoil plays a significant role for the precision of the M_T distribution. Here, the resolution as well as the calibration methods, which need to be applied to correct for a different modeling in the simulations, introduce a systematic effect, which influence the measurement. Especially the finite statistics available for the calibration are relevant. Chapter 7.3 presents a first estimate of this uncertainty for the *lowMu* analyses.

CHAPTER 5

Event selection and algorithm performance

Analyses in high energy physics often make use of simulations. They allow a comparison between the experimental observations and the expectations provided by theory. But they also allow to study and calibrate the tools used for analysis. This includes a calibration of the various aspects of the computing model, like the digital copy of the detector, and the various analysis objects.

A precise calibration of the hadronic recoil in the simulations is highly relevant for the extraction of the value of the W boson mass from the transverse invariant mass distribution. One of the main differences between data and simulations is the modeling of the hadronic activity of the event, which is reflected in the scalar sum of the hadronic recoil ΣE_T and which largely depends on the modeling of the pileup. In addition, it shows a strong correlation to the transverse momentum of the boson and a correction thereof could indirectly distort the boson momentum distribution. Since differences between the transverse momentum distributions in data and in the simulations exist, the dependence of the reweighting on the boson momentum needs to be handled carefully.

The calibrations of the simulations are done by using events with the well understood Z boson. Here, the full decay kinematic is accessible by the two charged leptons and the hadronic recoil can be compared to the reconstructed Z boson. The lepton pair can also be used for lepton calibrations. By this, events containing a Z boson are fully exploited for calibrating the simulations. With the best possible calibrations applied to the simulations, a measurement in events with W bosons can be performed subsequently. In this thesis, a novel approach for the calibration of the hadronic recoil was developed and is presented here.

This chapter focuses on different aspects of the basic analysis features for the reweighting of the hadronic recoil. First, the available data basis with the different datasets and the necessary selection cuts to filter the signature of interest from all the available events containing at least one muon or electron is described. The different cuts for a Z boson selection used for the calibrations and for a W boson selection used for a measurement of the W mass are introduced here. Afterwards, the algorithms and their performance in the different quantities of the recoil are discussed. The various aspects of the calibration of the hadronic recoil are presented in the next chapter.

5.1. Datasets and corresponding Monte Carlo simulations

The methods derived in this thesis were developed for the measurement of the W boson mass at a center of mass energy of $\sqrt{s} = 8\,\text{TeV}$. When the latest datasets with special run conditions became available, the same methods were ported to these two dataset at a center of mass energy of $\sqrt{s} = 5\,\text{TeV}$ and $\sqrt{s} = 13\,\text{TeV}$. Thereby, the performance of the reweighting procedure with respect to other collision parameters can be studied in more detail.

The basic parameters of the datasets recorded by the ATLAS experiment along with the according simulations will be discussed in this section. The details of the samples are listed in Appendix A in Tab. A.1 and Tab. A.2.

For the 8 TeV analysis, only a subset of the data was analyzed to reduce the computing time. The statistics within the two run periods B and G are sufficient for this performance study, together the integrated luminosity is $6\,832\,\text{pb}^{-1}$, which corresponds to more than 590 000 Z boson candidates, decaying into a muon pair. In the *lowMu* analyses all available data is used, since these special data takings only lasted a couple of days. The 5 TeV dataset includes a total integrated luminosity of $258\,\text{pb}^{-1}$ and of $147\,\text{pb}^{-1}$ for the 13 TeV dataset. Around half a million events with W boson candidate and 69 000 Z boson candidate events were identified in the 5 TeV dataset and 610 000 W bosons and more than 91 000 Z bosons in the 13 TeV analyses, when the decay channel into muons is analyzed[1].

The according simulations for the W and Z boson samples were done by official ATLAS Monte Carlo productions. The hard scattering process is simulated in POWHEG [93] with the CT14NNLO PDF set [94] for the 8 TeV analysis (CT10 [69] for the *lowMu* analyses). Pythia 8 [78] with the AZNLO tune [95] and the CTEQ6L1 PDF set [96] was used for the underlying event generation, parton showering and hadronization in all samples. Final state radiation in form of electroweak corrections are included by the program Photos [97]. For the *lowMu* analyses, heavy flavor decays are done by EvtGen [98].

The signal simulation is overlayed with two sets of according minimum bias simulations, that mimic the pileup for each event. A high-pt and a low-pt minimum bias sample is used, generated by Pythia8 plus EvtGen with the A2 MSTW2008LO tune [99] for the 8 TeV analysis and with the A3 NNPDF23LO tune [100] for the *lowMu* analyses.

5.2. Selection criteria

The extraction of physics parameters from a set of selected objects, like the measurement of the W mass, is highly dependent on the purity of the signal selection. Several background processes can mimic the same final state properties and will decrease the resolution of the measured parameter. Especially relevant are similar processes. For example when searching

---

[1] The smaller number of Z boson candidates in comparison to the number of events with a W boson is due to two main differences: The $Z \to \mu\mu$ cross section is lower (about a factor 0.3) and the branching ratio into a pair of muons is smaller (also by a factor 0.3) than the decay of the W boson into a muon and a neutrino, since the Z boson can also decay into neutrino pairs. In addition, requiring a second muon within the geometrical acceptance of the detector that passes the lepton selection cuts slightly reduces the number further.

for W bosons, events that include a Z boson where one lepton is outside the detector acceptance can enter the selection. Events with a combination of W and Z bosons play another important role. Another background source are QCD events including a jet, that is misidentified as a lepton or that contains heavy particles decaying leptonically. Although those leptons show a different momentum distribution, a fraction can nevertheless appear in the signal region, since the cross section for QCD events is much larger. With a carefully chosen set of selection criteria, the influence of background processes can be minimized. This set of cuts depends on the performance parameters of each data taking period. Between run 1 and run 2, several hardware and software upgrades were performed, which resulted in some general differences. For example, the analysis framework as well as the data format was updated and thus the applied cuts cannot be directly compared and are discusses separately here.

Since the studies of this thesis were performed before the main aspects of the analysis of the two datasets were finished, a preliminary set of cuts is applied. The selection cuts consist of lepton selection criteria as well as event cuts dedicated to the search for Z or W bosons.

5.2.1. Event based selection

A set of general event cuts is applied to the datasets. Tab. 5.1 gives an overview over the implemented thresholds for the different analyses. For the *lowMu* analyses, several quality cuts are applied in an earlier reprocessing step.

Cut name	*8 TeV thresholds*	*lowMu thresholds*
GRL	pass	pass
LiquidArgon trips	excluded	-[2]
Tile trips	excluded	-[2]
Primary vertex tracks	> 3 tracks	-
Pileup	$10 <$ ActIntPerXing < 35	does not apply

Table 5.1.: Event selection cuts and the respective thresholds for the 8 TeV and the *lowMu* analyses.

During the many hours of the data taking, several minor technical problems can arise, which result in non-ideal detector conditions. For example, problems in the high voltage supply of a single detector chamber, busy readout systems or even a reboot of a full subsystem affect the quality of the recorded data during these outages. For standard analyses these events have to be sorted out on the basis of a good runs list (GRL), that lists events and runs where the nominal conditions needed for precision analyses were met.

For the 8 TeV analysis, the performance of the calorimeter was slightly decreased in some areas by several tripping modules. To ensure a high data quality, the affected events have to be sorted out in this analysis step.

A primary vertex must be apparent in the event and it must have at least 3 tracks associated to it. This increases the rejection of cosmic muon background.

The pileup is restricted to events with sufficient statistics, since the reweighting method is based on this distribution. For the 8 TeV analysis, the actual interactions per bunch crossing (ActIntPerXing) needs to be between 10 and 35 interactions per event.

---

[2] This selection is performed in an earlier reprocessing step

5.2.2. Lepton selection

The selection of leptons focuses on the rejection of objects that are considered as fake leptons without simultaneously decreasing the rate of true leptons as little as possible. For example, fake muons can arise, if other particles create hits that together with noise are misidentified by the track reconstruction algorithms as a muon track. In addition, leptons with a poor track quality are rejected by including cuts on detector related quantities. The selection criteria for leptons are based on the recommendations of the combined performance groups [67, 101, 102]. An overview over the lepton cuts are given in Tab. 5.2 and Tab. 5.3.

Cut name	*muon thresholds*
trigger	EF_mu24i_tight ǁ EF_mu36_tight
quality working point	loose STACO
ID track quality	$n_{Pixel}^{Hits} + n_{Pixel}^{DeadSensors} \geq 1$ $n_{SCT}^{Hits} + n_{SCT}^{DeadSensors} \geq 5$ $n_{Pixel}^{Holes} + {}_{SCT}^{Holes} \leq 2$
	for $0.9 < \lvert\eta\rvert < 1.9$: $\frac{n_{TRT}^{outliers}}{n_{TRT}^{Hits} + n_{TRT}^{outliers}} < 0.9$ and $n_{TRT}^{Hits} + n_{TRT}^{outliers} > 5$
η volume	$\lvert\eta\rvert < 2.5$
momentum	$p_T > 20\,\text{GeV}$
momentum (ID)	$p_T > 25\,\text{GeV}$
impact parameter	$\lvert z_0\rvert < 100\,\text{mm}$ $\lvert d_0/s(d_0)\rvert < 5$
isolation	$(\sum p_{T,i}^{\Delta R<0.2})/p_T^{\mu} < 0.1$

Table 5.2.: Lepton selection cuts and the respective thresholds for the 8 TeV analysis.

Cut name	*muon thresholds*	*electron thresholds*
trigger	HLT_mu14	HLT_e15_lhloose_nod0_L1EM12
quality working point	medium	medium
η volume	$\lvert\eta\rvert < 2.4$	$\lvert\eta\rvert < 1.37$ or $1.52 < \lvert\eta\rvert < 2.47$
momentum	$p_T > 20\,\text{GeV}$	$p_T > 25\,\text{GeV}$
momentum(ID)	$p_T > 25\,\text{GeV}$	$p_T > 25\,\text{GeV}$
impact parameter	$\lvert z_0 \cdot \sin\theta\rvert < 0.5\,\text{mm}$ $\lvert \text{d}_0/s(\text{d}_0)\rvert < 3$	$\lvert z_0 \cdot \sin\theta\rvert < 0.5\,\text{mm}$ $\lvert \text{d}_0/s(\text{d}_0)\rvert < 5$
isolation	$(\sum p_{T,i}^{\Delta R_{max}<0.3})/p_T^{\mu} < 0.1$	$(\sum p_{T,i}^{\Delta R_{max}<0.3})/p_T^{el} < 0.1$

Table 5.3.: Lepton selection cuts and the respective thresholds for the *lowMu* analyses.

The trigger decisions, which sorts interesting events at runtime to be written out, has different sensibility thresholds. The lowest unprescaled[3] single muon trigger for 8 TeV measurement requires a transverse momentum threshold of 24 GeV for isolated muons and of

---

[3] An unprescaled trigger does not limit the number of events written to storage to a fixed output rate of a fraction of randomly selected events like prescaled triggers do.

36 GeV if the muon is not isolated. Both options include a tight trigger identification requirement for muon objects. [103]

For the analysis of the *lowMu* dataset the preliminary recommendation is to use the High Level Trigger (HLT) with a muon momentum threshold of $p_T > 14\,\text{GeV}$ and of $p_T > 15\,\text{GeV}$ for electrons. These low momentum thresholds are only possible because of the low background rate in the *lowMu* datasets. The electron trigger includes a loose likelihood setting (lhloose), where no information from the impact parameter d0 is used (nod0), as well as a requirement for the first level of the trigger, L1, that needs to include a reconstructed transverse momentum measured by the electromagnetic calorimeter of more than 12 GeV (L1EM12). [104, 105]

The reconstructed leptons are categorized by the level of fake lepton contamination in three quality working points *loose*, *medium* and *tight*. These three definitions are optimized for the different needs of physics analyses. The tight working point refers to the purest selection but at the cost of a slightly lowered reconstruction efficiency, whereas the loose categorization has the highest efficiency. The corresponding recommendation for the combined muon reconstruction algorithm STACO, which is used for the 8 TeV analysis, is *loose*. This includes combined muons as well as segment tagged muons that recover efficiency losses in the transition region between the barrel and the end-cap, where combined muons are unavailable. The analysis of the second run campaign (run 2), which includes the *lowMu* runs, uses medium muons and electrons.

For the 8 TeV analysis, a set of quality criteria on the associated inner detector track of combined muons have to be applied to recover some efficiency losses due to not-nominal detector conditions during data taking for the sensors in the silicon system (SCT and Pixel detectors). To guarantee a successful track extension to the TRT in the applicable η range, a limit on the contribution of TRT hits reconstructed as outliers is given. For run 2 analysis, the corresponding quality criteria do not need to be applied at the analysis level any longer but are included in an earlier reconstruction step.

A cut on the pseudorapidity of muons is applied to ensure an ideal track reconstruction within the acceptance of the inner detector. Electrons found to be in the calorimeter transition region, which corresponds to the η range of $1.37 < |\eta| < 1.52$, are excluded to avoid a differing resolution in the simulations compared to data due to poor track matching [106].

In the decay of a heavy boson a distinctive and significant amount of kinetic energy is distributed to the leptons. This allows to reject background coming from other processes with at least one lepton by applying a cut on the transverse momentum of $p_T > 25\,\text{GeV}$. For the muons, the momentum measurement of the inner detector is used for the tight cut and a looser cut of $p_T > 20\,\text{GeV}$ is applied to the combined momentum measurement.

Additionally, impact parameter cuts are applied to ensure that the lepton is associated to the primary vertex. Especially background from cosmic muons traversing the detector can be rejected successfully by these cuts. This cut is performed on the transverse and perpendicular impact parameter (see page 54 for a definition), where $s(\text{d}_0)$ is the uncertainty of the transverse impact parameter from the track reconstruction. The thresholds are optimized for each dataset and lepton type independently.

Finally, the leptons are required to be isolated. This cut allows to reject leptons, that are coming from heavy-flavor decays and in-flight decaying kaons and pions. In this case, the lepton track is accompanied by other energetic tracks in close proximity. Events are rejected, if the sum of momenta of tracks in a cone around the lepton track is larger than

10% of the lepton transverse momentum. Tracks are associated to the cone by a matching of ΔR between the track and the lepton. For the *lowMu* analyses the maximum cone size is set to 0.3, but becomes smaller if the lepton momentum increases above $\gtrsim 33\,\mathrm{GeV}$: $\Delta R = min\left(\frac{10\,\mathrm{GeV}}{p_T}, 0.3\right)$. The cone size for the 8 TeV analysis is fixed to 0.2.

5.2.3. Signal signature selection

For both the 8 TeV and the *lowMu* analyses, the selection of Z boson events is performed by cutting on the transverse invariant mass of the two lepton system. A window of 20 GeV around the Z mass pole of $M_Z = 91.19\,\mathrm{GeV}$ is chosen. If more than two leptons pass the lepton selection, the pair with the invariant transverse mass closest to the Z mass is picked.

Cut name	*thresholds Z boson selection*
invariant transverse mass	$71.19\,\mathrm{GeV} < M_T < 101.19\,\mathrm{GeV}$
number of good leptons	≥ 2

Table 5.4.: Z boson event selection cuts

For a selection of W boson events a looser cut on the transverse mass is applied, since the resolution of the hadronic recoil does not give a good enough lever arm for a tight cut window. Tab. 5.4 and 5.5 lists all selection criteria for the two signal selections.

Cut name	*thresholds W boson selection*
invariant transverse mass	$M_T > 60\,\mathrm{GeV}$
hadronic recoil	$\lvert\vec{HR}\rvert < 30\,\mathrm{GeV}$
missing transverse momentum	$MET > 30\,\mathrm{GeV}$
number of good leptons	1

Table 5.5.: W boson event selection cuts

The cut on the length of the hadronic recoil vector to be less than 30 GeV is not applied to suppress background but rather to reject signal events with a large hadronic recoil. The influence of the poorer resolution as well as the theoretical uncertainties associated to these events is minimized by this.

5.3. General reweightings and calibrations

As explained before, all reconstructed objects within the simulation need a dedicated calibration. Since the analysis is still ongoing, no final set with high enough precision is available yet. To not introduce a bias from inadequate calibrations, the various objects enter the analysis uncalibrated. For the full analysis lepton calibrations in the form of scale factors, which correct the lepton scale and resolution as well as the trigger selection efficiency, should be applied.

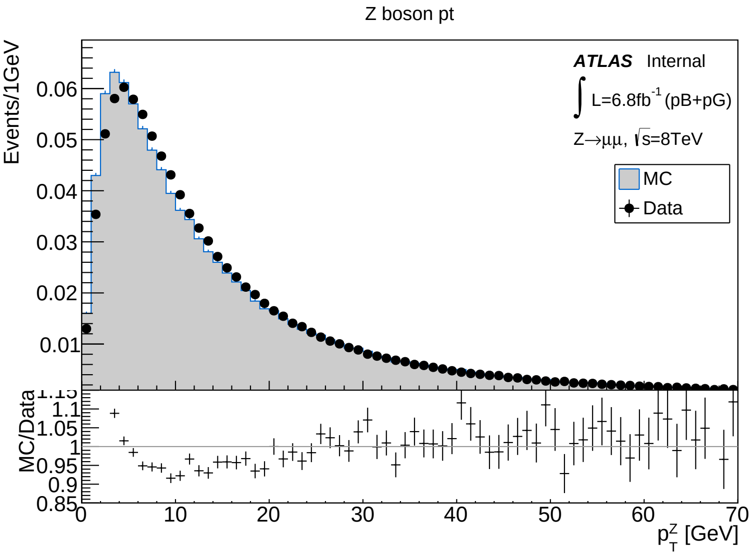

Figure 5.1.: The unweighted transverse momentum distribution in data and Monte Carlo simulation are shown in the top plot. The lower plot shows the agreement between data and simulation, which is used as event weights to reweight the simulations to give the same composition of events with different transverse boson momenta as data.

5.3.1. Transverse boson momentum reweighting

The modeling of the transverse momentum of the boson available in the datasets with a full simulations differs from the true momentum distribution in data. This is especially relevant to the reweighting of the hadronic activity since the transverse boson momentum is correlated to the hadronic activity. If the latter is modeled in the reweighting procedure described in the next chapter and the transverse momentum distributions in data and simulation are not identical, a bias on the transverse momentum will be introduced, when the hadronic activity is reweighted. To avoid this, the transverse boson momentum distribution is adjusted beforehand by simple event weights, which are obtained in bins of the transverse boson momentum (see Fig. 5.1). The weights are calculated from the ratio of data to simulation in bins of boson transverse momentum of 1 GeV. With this, the simulated events are reweighted in order to give the same composition of events per transverse boson momentum bin in simulation as in data.

This simple approach is only possible in events with a Z boson selection, where the momentum can be reconstructed in data as well. The differences between the transverse momentum distribution of W and Z bosons do not allow to plainly port the same weights to the W sample. A dedicated correction procedure has to be performed, which is beyond the scope of this analysis. A description of this procedure for the 7 TeV measurement can be found in [91].

5.3.2. Scaling the energy of the recoil response

As will be seen in the next section, the different implementations of the hadronic recoil algorithms are not comparable, if the set of particles included in the recoil calculation differs

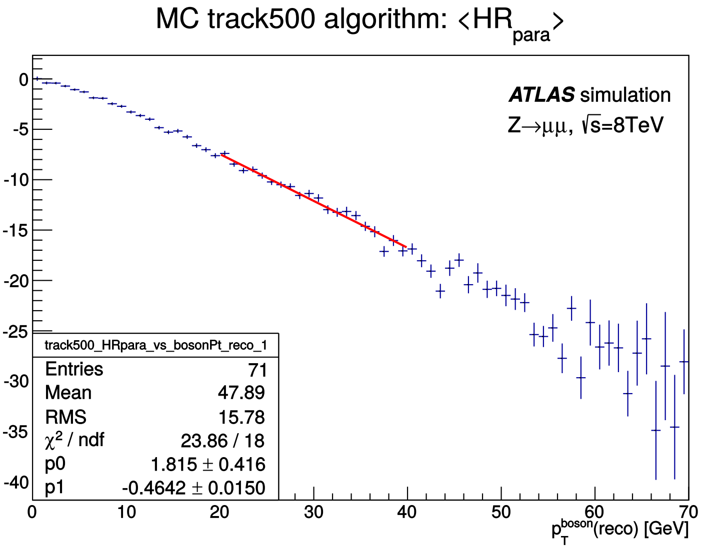

Figure 5.2.: The mean parallel hadronic recoil $\langle HR_{par} \rangle$ as function of the transverse momentum of the Z boson $p_T^{boson}(reco)$ for the track500 algorithm in the simulations for the 8 TeV dataset. The mean values $\langle HR_{par} \rangle$ were derived by a Gaussian fit binned in steps of the boson transverse momentum. The dependency of $\langle HR_{par} \rangle$ on $p_T^{boson}(reco)$ is determined by a linear fit $p0 + p1 \cdot x$ in the range $20\,\text{GeV} < p_T^{boson}(reco) < 40\,\text{GeV}$. The fit results are listed in the box.

substantially. Neutral particles are not accessible to track algorithms, since their track cannot be measured by the ATLAS detector. Thus, track algorithms do not account for energy deposits of neutral particles and the recoil energy carried by them is not included in the hadronic recoil measurement of track algorithms. As a consequence, the track algorithms cannot describe the transverse momentum of the Z boson well without a scaling of the energy. In addition, particles that are not detectable result in a too low recoil estimate. This includes particles with a high forward momentum that fly in the very forward direction outside the detector coverage but still carry a small transverse momentum or particles below the acceptance thresholds. Therefore, the average recoil energy and especially the incorrect response to an increasing transverse boson momentum need to be modified appropriately.

The scaling can be performed by applying scale factors on the magnitude of the hadronic recoil vector. The scale factors are derived from the mean of the parallel hadronic recoil component that is calculated as a function of the reconstructed transverse momentum of the boson $p_T^{boson}(reco)$, see Fig. 5.2. The mean values in these distributions are determined by fitting the parallel hadronic recoil, which is binned in steps of the transverse momentum of the boson, with a Gaussian distribution.

The dependency of $\langle HR_{par} \rangle$ on $p_T^{boson}(reco)$ is subsequently modeled by a linear fit. The fit range is optimized on the subset with the highest precision, while excluding the turn-on curve for low transverse momenta. In this low range, the parallel recoil component does not follow the transverse boson momentum linearly. As a result, the recoil energies cannot be scaled absolutely by this approach, but only the response to an increasing transverse boson momentum can be adjusted, which is sufficient for comparing the different algorithms.

If the mean of the parallel hadronic recoil were exactly representing the full recoil, the slope of the fit would be -1. With the use of the fit value, a scale factor

$$\alpha^{algo}_{scaling} = \frac{-1}{\mathrm{p1}^{algo}_{fit}}$$

is applied to the hadronic recoil vector by $\alpha \cdot \vec{HR}$, thus, scaling both the parallel and the perpendicular component. With this, the resolution of the various algorithms becomes comparable as well.

Algorithm	$\alpha^{8\,\mathrm{TeV}}_{scaling}$
cluster	1.06
track500	2.15
track500PV	2.12
track1000	2.21
track1000PV	2.15

Table 5.6.: Energy scale factors for the 8 TeV analysis obtained from the simulations.

A dedicated scale factor is derived for all algorithms, which is applied to both data and the simulation. Because of the higher statistics available in the simulations, the fit is performed in the simulations. Tab. 5.6 shows the scale factors for the 8 TeV analysis, while Tab. 5.7 gives the values for the *lowMu* analyses. The corresponding plots, from which the scale factors were derived, can be found in Appendix B. The scale factors are not applied to the scalar sum of the hadronic recoil ΣE_T.

If a separate scale factor for data would be generated, the hadronic recoil vector would be scaled differently in the simulations as in data and the resolution of the scaled hadronic recoil components would differ afterwards. The difference in the resolution would need to be accounted for in a resolution calibration step later. It was found that the scale factors for data deviate by a few percent. However, these fluctuations are of the same order as the statistical uncertainty on the data scale factors. Thus, the difference is at least partially artificial. It was therefore decided to apply the scale factor obtained from the simulations to data as well.

	$Z \to \mu\mu$		$Z \to ee$	
Algorithm	$\alpha^{5\,\mathrm{TeV}}_{scaling}$	$\alpha^{13\,\mathrm{TeV}}_{scaling}$	$\alpha^{5\,\mathrm{TeV}}_{scaling}$	$\alpha^{13\,\mathrm{TeV}}_{scaling}$
pfo	0.96	0.97	0.96	0.97
pfoEM	1.12	1.13	1.12	1.14
pfoNeutral	2.45	2.34	2.51	2.39
pfoCharged	2.06	2.18	2.03	2.18

Table 5.7.: Energy scale factors for the $Z \to \mu\mu$ and $Z \to ee$ *lowMu* analyses obtained from the simulations.

5.4. Control plots

The kinematic distributions of the selected objects are a check for the validity of the selection cuts and calibrations. Since only few calibrations are applied in this analysis, discrepancies can be expected. In addition, the simulations only consist of the signal $Z \to \mu\mu$ and no background processes, which are included in data. Z boson and muon kinematics are shown in Fig. 5.3.

The muon transverse momentum shows the typical Jacobian Edge at around 45 GeV of half of the Z boson's mass. The agreement between data and simulation is not ideal, since no muon momentum scale and resolution corrections are applied to the simulations.

The angular distributions are generally in good agreement but show discrepancies between data and simulations in several regions. The η distribution indicates that the muons are dominantly emitted in the transverse plane with low $|\eta|$. The gap in the muon spectrometer at $\eta = 0$, where no muon chambers are installed because of the infrastructure of the inner detector, is clearly visible. The ϕ distribution, which is mostly flat, shows some inefficiencies in those regions, where the magnetic coils of the toroid system are located. Here the disagreement between data and simulation is particularly large.

The reconstructed Z boson transverse momentum distribution is dominated by events with a low transverse momentum and peaks at around 5 GeV. Any disagreement between data and the modeled transverse momentum spectrum in the simulation has been eliminated by the transverse boson momentum reweighting applied here, thus giving this ideal ratio of data and MC.

The invariant mass of the selected lepton system, which is equivalent to the reconstructed mass of the Z boson, can be described by a Breit-Wigner resonance parametrization (see Sec. 4.3.2) with the Z mass pole at 91 GeV. The peak visible in the simulations is narrower than the distribution in data and the rising edge is more populated while the falling edge has less entries. These differences can again arise from the uncalibrated leptons.

The direction of the reconstructed Z boson is described by the angular distributions η and ϕ and the rapidity y. It can be computed by

$$y = \frac{1}{2} \ln \left(\frac{E + p_z}{E - p_z} \right),$$

where p_Z is the boson momentum in z-direction along the beam axis and E the total energy of the boson. The data-MC ratio is found to be deviating up to five percent from unity in the central region and up to ten percent in the more forward region, where the statistics are smallest.

The detector quantity of the pseudorapidity η can only be interpreted as a parameter of the track in case of heavy particles like the Z boson. The ratio of data and MC also shows fluctuations of several percent, caused by the uncalibrated muons. It can be seen that Z bosons are dominantly emitted in the forward direction as expected for a Z boson with low transverse momentum. No preferred direction in the transverse plane is found as indicated by the flat ϕ distribution.

The full list of control plots for the *lowMu* analyses is found in Appendix C. The agreement between data and simulation is comparable, although the individual fluctuations can differ of course. The two analyses containing electrons indicate that the selection and performance of electrons without calibration is slightly less ideal than for muons. However, a dedicated calibration should account for the deficits.

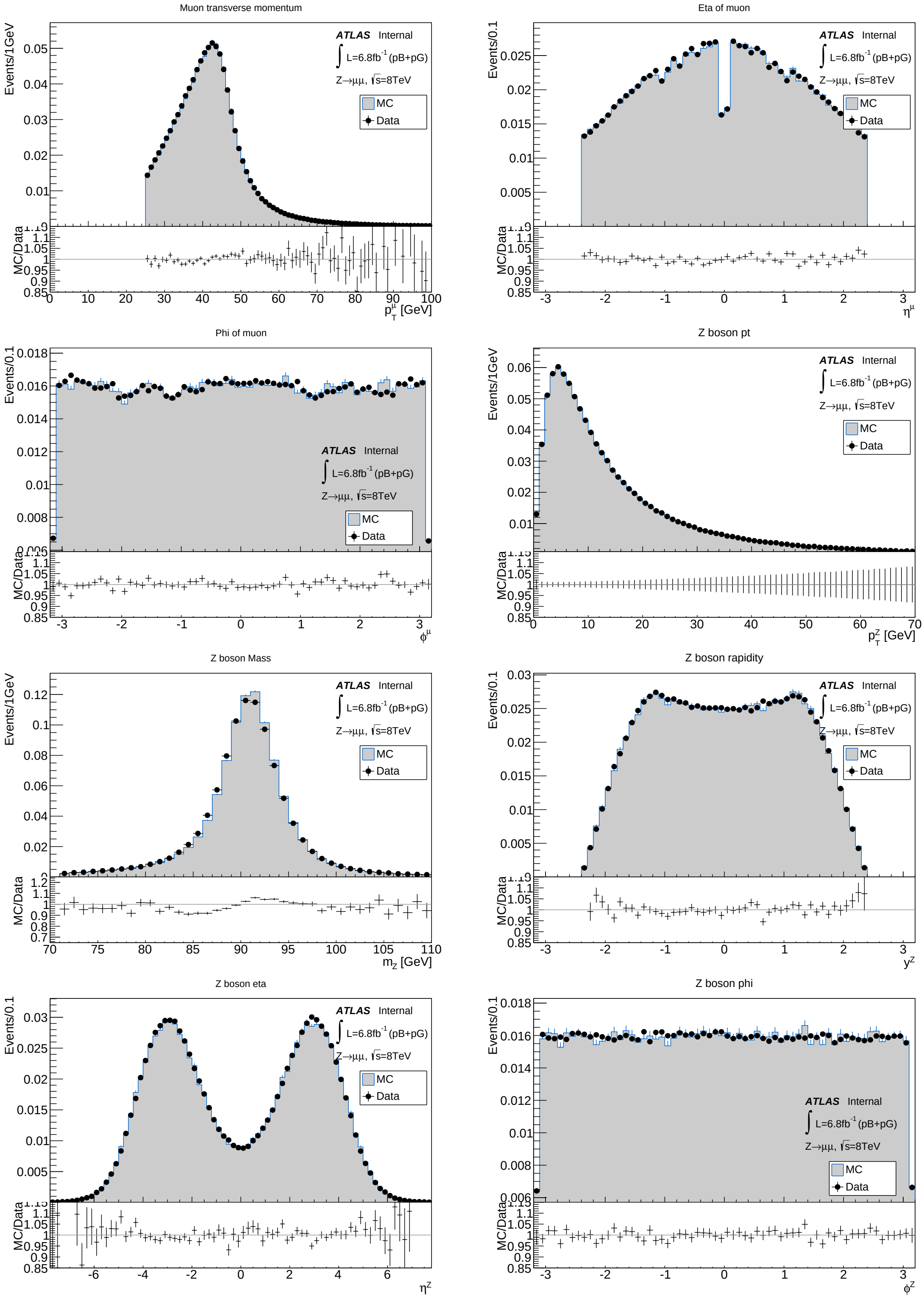

Figure 5.3.: Z boson and muon kinematic distributions for the 8 TeV analysis.

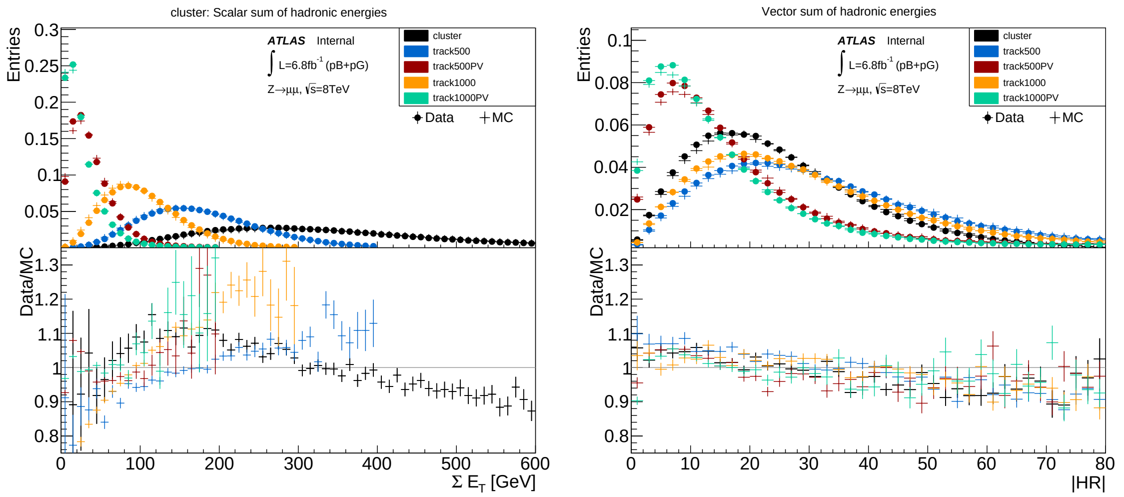

Figure 5.4.: The ΣE_T and $|HR|$ distribution of the various hadronic recoil algorithms in the 8 TeV analysis without any reweighting applied.

5.5. Unweighted hadronic recoil distributions for the different algorithms in events containing a Z boson

Before the different steps of the reweighting technique will be explained in detail, a first overview of the relevant quantities and their representation in the various algorithms as well as in the different datasets is given. The agreement between data and simulation is shown in the bottom pad of the relevant plot by the ratio of data and MC. No reweighting is applied to the simulations and the distributions are scaled to their integral being one.

5.5.1. 8 TeV analysis

Hadronic activity The various implementations of the hadronic recoil algorithms include a different amount of hadronic activity per event. The ΣE_T distribution is a good measure for the total energy considered in the calculation of the hadronic recoil and is shown in Fig. 5.4 for the 8 TeV analysis.

The cluster algorithm includes the largest fraction of particles. Since no restrictions on the vertex of these particles can be made, a lot of pileup is included here. For most events the amount of hadronic activity is as large as several hundred GeV, which can be quantified by the peak of the distribution at around 280 GeV. The track algorithms on the other hand do not consider neutral particles measured only in the calorimeter. As a consequence, less energy is considered for the algorithm calculation. The implementation with tracks of a transverse momentum of at least half a GeV (track500) have a most probable value that is found at roughly 160 GeV, and thus almost not considering half of the energy per event compared to the cluster algorithm. Since no cut on the track vertex is performed, the missing hadronic activity comes from neutral particles, tracks below the momentum threshold and energy deposits outside the inner detector volume. The latter would be picked up by the larger

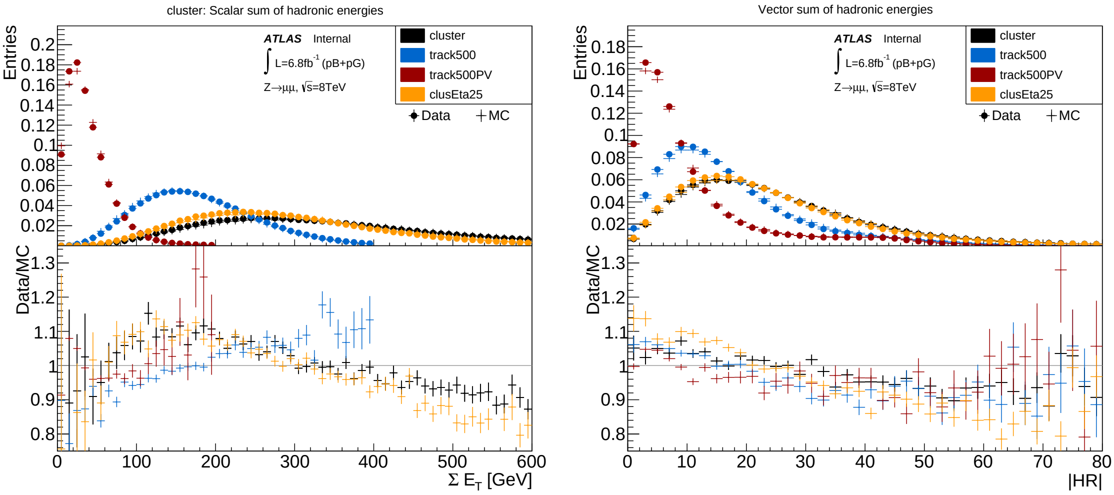

Figure 5.5.: The ΣE_T and $|HR|$ distribution cluster, clusEta25 and track500(PV) algorithms in the 8 TeV analysis without any reweighting applied. The energies are not scaled here.

coverage of the calorimeter. This effect is estimated by comparing the cluster algorithm with the implementation clusEta25, which only considers clusters that are within the coverage of the inner detector $|\eta| < 2.5$. Fig. 5.5 shows the scalar and vector sum of the hadronic activity for the cluster, clusEta25 and the two track500 algorithms. The implementation of clusEta25 shows only slightly lower ΣE_T values than the regular cluster implementation. To allow for a clearer understanding of the contribution to the recoil, the energy scaling is not applied to the $|HR|$ distribution, which is shown in the right plot of the same figure. The magnitude of the hadronic recoil vector for clusEta25 is almost as large as for the full implementation. This suggests, that the largest fraction of recoil is deposited inside the coverage of the inner detector. The effect of additional pileup in the intermediate region up to $|\eta| < 4.9$ is found to be comparably small. Thus, it can be concluded, that the missing activity in the track algorithms is almost entirely due to neutral particles, which make up around half of the hadronic activity.

The ΣE_T distribution for the track1000 algorithm with a higher momentum threshold than track500 is even narrower than the track500 distribution (see again Fig. 5.4) and peaks at a smaller value of around 85 GeV. From this it can be concluded, that tracks that have a transverse momentum between $0.5\,\text{GeV} < p_T^{track} < 1\,\text{GeV}$ contribute to half of the hadronic activity of charged particles. When again comparing the energy scale factors (see Tab. 5.6) and the energy corrected $|HR|$ distribution, it is found that track500 and track1000 give comparable results here. From this follows that the amount of recoil energy considered in the two algorithm calculations is probably not differing largely. The difference in the ΣE_T distribution is mostly due to underlying event and pileup tracks.

When placing a cut on the origin of the tracks if not coming from the primary vertex, the hadronic activity included in the calculation is reduced further. The most probable value for the track500PV implementation is found at roughly 25 GeV and at 12 GeV for track1000PV. These algorithms consider only charged particles coming from the primary vertex and thus exclude all pileup. Underlying event tracks are nevertheless taken into account. As a result,

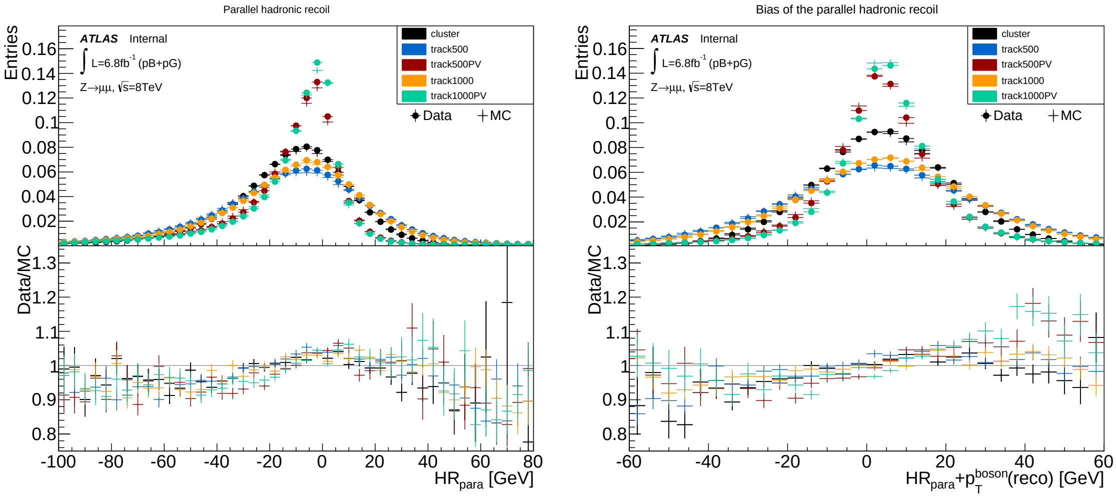

Figure 5.6.: The parallel component of the hadronic recoil HR_{par} distribution as well as the bias $HR_{par} + p_T^{boson}(reco)$ distribution. The various hadronic recoil algorithms in the 8 TeV analysis are shown without the reweighting applied.

true charged recoil particles from the hard interaction vertex are combined with charged particles coming from interactions of the remaining partons, which are not participating in the hard interaction. A distinction between the two cannot be made. But since neutral tracks are not included, around half of the recoil information is not taken into account for these implementations.

The hadronic activity included in the simulation clearly differs from the data. For the track algorithms, the scalar energy is underestimated as can be seen from the slope visible in the ratio of data and Monte Carlo. The cluster algorithm overestimates the hadronic recoil energy in the simulations. Although the ΣE_T distribution is not directly needed for the W mass measurement, it should be identical in data and the simulations nevertheless, since it influences the resolution of the hadronic recoil agreement. As part of the reweighting that is going to be applied differences in the ΣE_T distributions should be removed as thoroughly as possible.

Parallel hadronic recoil The distributions for the parallel component of the hadronic recoil are shown in Fig. 5.6. As discussed before, the algorithms do not include all particles, which carry recoil information. With the energy scaling, the average response to the transverse boson momentum can be adjusted. However, because of the non-linear response in the low-p_T^{boson} range, the recoil energy does not match the transverse boson momentum. This can be seen when looking at the distribution of the bias $HR_{par} + p_T^{boson}(reco)$[4]. The recoil is on average smaller than the transverse momentum.

---

[4] The parallel hadronic recoil component is calculated from the scalar product of the hadronic recoil vector and the transverse boson momentum vector. Usually, the recoil vector points to the opposite direction of the Z boson momentum vector and thus, HR_{par} is negative on average. The deviation between the parallel component and the magnitude of the transverse boson momentum can be calculated by the sum $HR_{par} + p_T^{boson}(reco)$

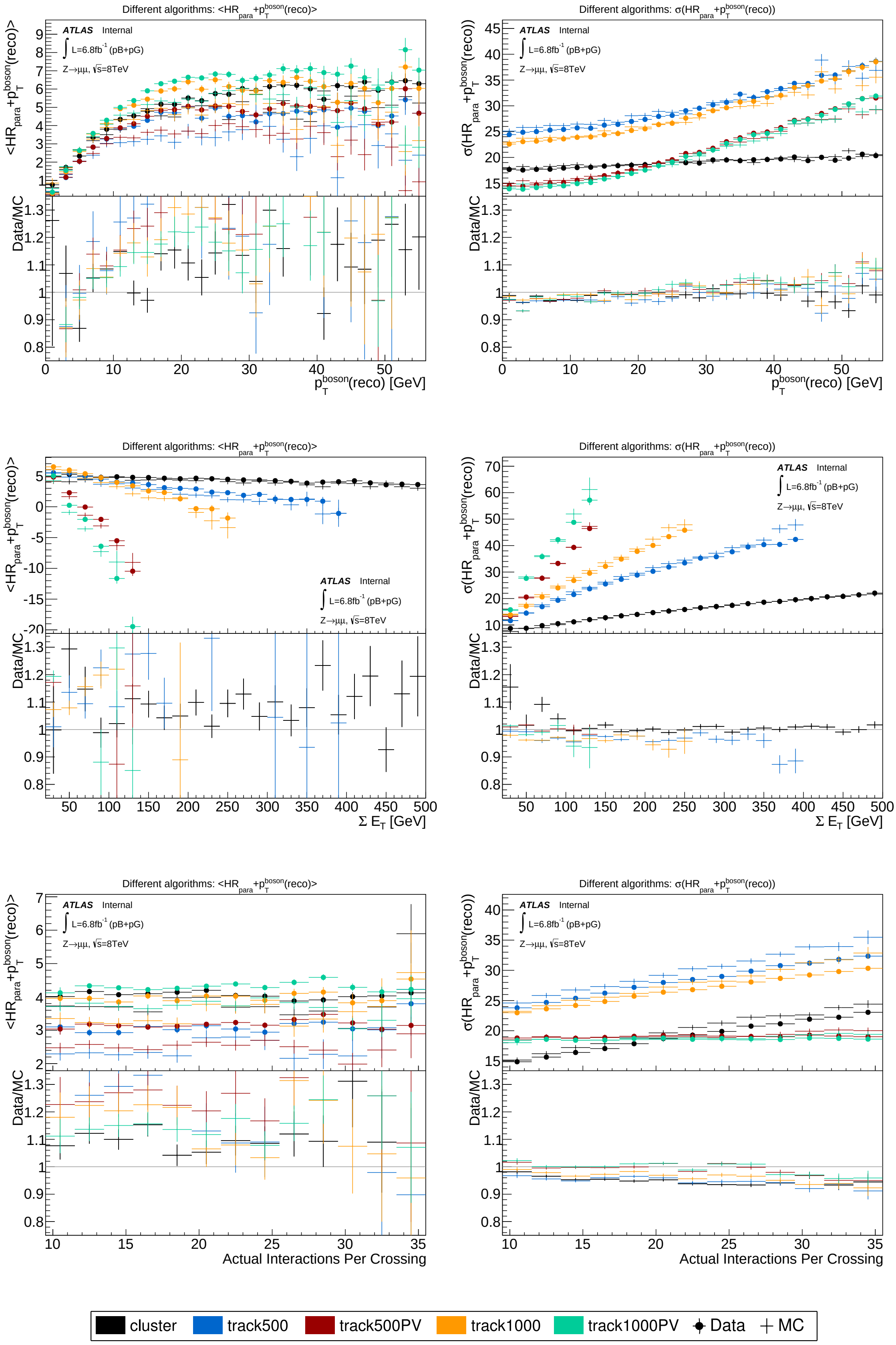

Figure 5.7.: Several mean and sigma distributions for the bias $HR_{par} + p_T^{boson}(reco)$. The various hadronic recoil algorithms (see legend below for the color coding) in the 8 TeV analysis are shown without main reweighting applied.

The bias mean $\langle HR_{par} + p_T^{boson}(reco)\rangle$ and resolution $\sigma(HR_{par} + p_T^{boson}(reco))$ as a function of the transverse boson momentum after scaling the energies is visible in the first subplots of Fig. 5.7. The mean and sigma in these plots were derived from a Gaussian fit in bins of the quantity of interest.

The bias is zero if the transverse boson momentum is zero and rises to a plateau of $4-5\,\mathrm{GeV}$ for the cluster and the track500 algorithm and to a plateau of $7\,\mathrm{GeV}$ for the track1000PV algorithm. This behavior is caused by the energy scaling applied. A remaining difference between data and simulations even with the energy scaling applied is clearly visible in a different height of the plateaus and a large discrepancy in the ratio shown in the bottom pad of the plot. This is accounted for by a dedicated bias correction, which will be introduced in the next chapter.

The resolution as a function of $p_T^{boson}(reco)$ (see top right plot of Fig. 5.7) is almost stable for the cluster algorithm and found to be $18\,\mathrm{GeV}$, it shows almost no dependency on $p_T^{boson}(reco)$. The large amount of pileup, which enters the calculations, dominates the resolution for the cluster algorithm independent of the transverse boson momentum. The resolution increases however for all track algorithms as a function of $p_T^{boson}(reco)$. Although the average resolution (see Fig. 5.6 again) of the trackPV algorithms is the smallest, the resolution strongly increases with increasing transverse boson momentum. A large transverse boson momentum is balanced by high energy tracks and more tracks in total. Jets are more likely to occur as well. The resolution can be expected to increase as a consequence. The track algorithms without a vertex cut have the worst resolution, since they are additionally influenced by pileup as will be seen below.

The amount of hadronic activity per event, visible with the quantity ΣE_T, influences the goodness of the recoil description (see central row of plots in Fig. 5.7). The bias shows a correlation with ΣE_T, generally a falling slope can be noted.

All algorithms show a resolution dependency on the ΣE_T. If more hadronic activity is included in the event, the resolution gets worse. Again, the track algorithms are much more influenced by the hadronic activity and especially track algorithms with primary vertex cut show a wide resolution for large ΣE_T values.

The same is visible for the dependency of the resolution on the actual interactions per crossing, which is a measure of the pileup. The track algorithms without a vertex cut and the cluster algorithm show a worsened resolution if more interactions are recorded simultaneously. The resolution for algorithms with a cut on the primary vertex is independent of pileup, as can be expected, when most pileup is not considered in the calculation. The mean of the bias is not influenced by pileup for any algorithm.

Perpendicular hadronic recoil The perpendicular component HR_{perp} (see Fig. 5.8) is a direct measure for the amount of noise that is picked up by the algorithm. The amount per event is randomly distributed around zero, showing no preferred direction. The mean and the resolution of the perpendicular recoil, $\langle HR_{perp}\rangle$ and $\sigma(HR_{perp})$, are given as a function of the transverse boson momentum, ΣE_T and actual interactions per crossing. The mean shows in general no dependency on any quantity, like it is visible in the central left subplot as a function of $p_T^{boson}(reco)$.

For the cluster algorithm, the resolution is again stable as a function of the transverse boson momentum and increases modestly if the hadronic activity or the pileup increases. The resolution for track algorithms without a vertex cut is more stable on $p_T^{boson}(reco)$ than for

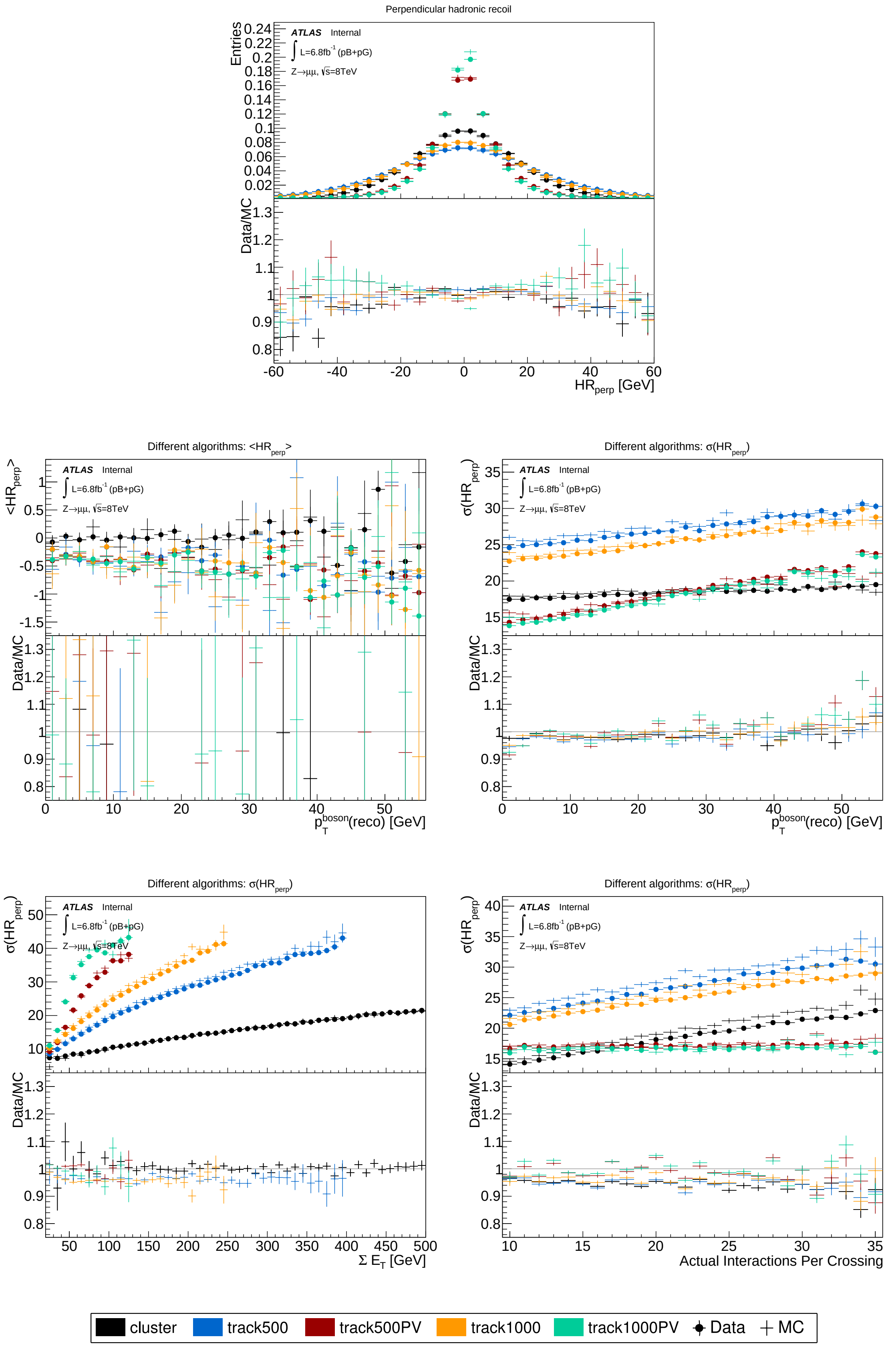

Figure 5.8.: The distribution of the perpendicular hadronic recoil component as well as several resolution distributions for HR_{perp}. The various hadronic recoil algorithms (see legend below for the color coding) in the 8 TeV analysis are shown without the main reweighting applied.

trackPV algorithms, although the overall resolution is the smallest for trackPV algorithms. The resolution of trackPV algorithms is again highly influenced by ΣE_T, but independent of pileup, while for track algorithms without a vertex cut it is again strongly correlated with ΣE_T and pileup.

5.5.2. *lowMu* analyses

A set of corresponding plots for the *lowMu* analyses at $\sqrt{s} = 5\,\text{TeV}$ and $\sqrt{s} = 13\,\text{TeV}$ are given in Fig. 5.9 to Fig. 5.11. The full set of plots is found in Appendix C. It is visible from the ΣE_T plots (top row of Fig. 5.9, left: 5 TeV, right: 13 TeV), that the amount of hadronic activity per event depends on the implementation of the algorithm but also on the center of mass energy of the collision[5]. The dataset with a higher collision energy shows larger reconstructed energies. A comparison to the 8 TeV algorithms is not very feasible, since the implementations and the collision parameters differ. In general, the particle flow algorithms are based on a purer and more complete selection of clusters and tracks with an more optimized pileup suppression compared the 8 TeV algorithms, which are either based on clusters or tracks.

In the *lowMu* setting, only two interactions happen simultaneously on average. This low pileup contamination allows for a reduction of the reconstruction threshold for clusters. With this, more recoil information is picked up at the cost of more noise. The latter is however not directional, thus the more complete recoil reconstruction should outweigh the noise disadvantage.

The different implementations differ with respect to the detailed implementation and calibration of the selected objects that enter the recoil calculation. The EM scale as implemented for pfoEM and pfoNeutralEM apply the electromagnetic weights to calibrate the individual energies of the neutral clusters. Since those weights are smaller compared to the general local cluster approach, the pfoEM ΣE_T value is on average smaller than for the pfo implementation[6]. For the pfo algorithm a most probable value of around 180 GeV for the center of mass energy of $\sqrt{s} = 13\,\text{TeV}$ is found, while pfoEM gives a value of 110 GeV.

While pfo and pfoEM use the standard configuration with all clusters and tracks, which pass the selection criteria, pfoCharged only uses tracks and pfoNeutralEM only clusters. It can be seen, when comparing the pfoCharged and pfoNeutralEM ΣE_T distributions, that the hadronic activity of tracks is much smaller than the hadronic activity of the neutral clusters. This is due to the fact, that the cluster reconstruction threshold is lowered and therefore more noise, pileup, underlying event but also more recoil energy is included in the cluster calculation. The sum of the ΣE_T pfoCharged and pfoNeutral distributions add up to the pfoEM ΣE_T distribution.

Since pfoCharged and pfoNeutralEM exclude a large fraction of particles respectively, the amount of hadronic activity included in the track-only or cluster-only calculation is smaller than for a combined algorithm and the energy of the recoil measurement would be underestimated by this, which is why the recoil energies are scaled. The effect of the scaled energies is visible in the $|HR|$ distributions (the scale factors are not applied to ΣE_T). The scale fac-

---

[5] For completeness, the hadronic activity also strongly depends on the luminosity, since this determines the number of events happening simultaneously, which are partially counted by the algorithms, but this dependency is not directly visible here.

[6] It should be noted, that the energy scaling of this analysis is not applied to ΣE_T.

tors were found to be slightly smaller for pfoCharged than for pfoNeutralEM (see Tab. 5.7 again). The tracks apparently include slightly more true recoil energy than the neutral clusters.If the parallel recoil energy is identical after scaling, the remaining difference visible in the $|HR|$ distribution must come from the larger aforementioned background contributions in the pfoNeutralEM algorithm, which are now overestimated by the scaling.

The bias $\langle HR_{par} + p_T^{boson}(reco) \rangle$ distributions (see Fig. 5.10) of the *lowMu* analyses show, that the parallel recoil with energy scaling applied is on average only slightly smaller than the reconstructed transverse boson momentum for all implementations. The discrepancy, visible in the offset of the mean value, is largest for the charged pfo algorithm and smallest for the pfoNeutralEM implementation. However, for pfoNeutralEM the dependency as a function of $p_T^{boson}(reco)$ is not flat but decreases for large transverse boson momenta. The same is found for pfoCharged, the effect is however found to go into the opposite direction and is less strong. Further studies suggest, that for the particle flow algorithms the ratio of the reconstructed amount of recoil energy in neutral clusters and tracks depend on the transverse boson momentum. In combined algorithms like pfo and pfoEM, this is not visible, but for pfoNeutralEM and pfoCharged this effect alters the $\langle HR_{par} \rangle$ to $p_T^{boson}(reco)$ dependency. The energy scale factors are derived by assuming a linear dependency, which is not fully valid for pfoNeutralEM and pfoCharged (see again Fig. B.3 in the Appendix).

The main algorithms for the *lowMu* analyses, pfo and pfoEM, are modeled well by this energy scaling.

The resolution, determined by a Gaussian fit, depends on the center of mass energy and is in general larger for the $\sqrt{s} = 13\,\text{TeV}$ analysis than for the $\sqrt{s} = 5\,\text{TeV}$ measurement. The two algorithms without either neutral clusters or charged tracks included, show the worst resolution. Pfo and pfoEM give comparable results with pfoEM having the slightly better resolution.

The same behavior is also visible for the perpendicular recoil component, see Fig. 5.11. Here, $\sigma(HR_{perp})$ is larger for the higher center of mass energy as well and pfoNeutralEM with the overestimated background contribution shows the largest resolution. The pfoEM algorithm shows the smallest resolution.

As can be seen from all distributions, the agreement between data and simulation is not ideal without any reweighting applied. The following section will discuss an approach, which adapts the hadronic activity in data by modeling its pileup dependence.

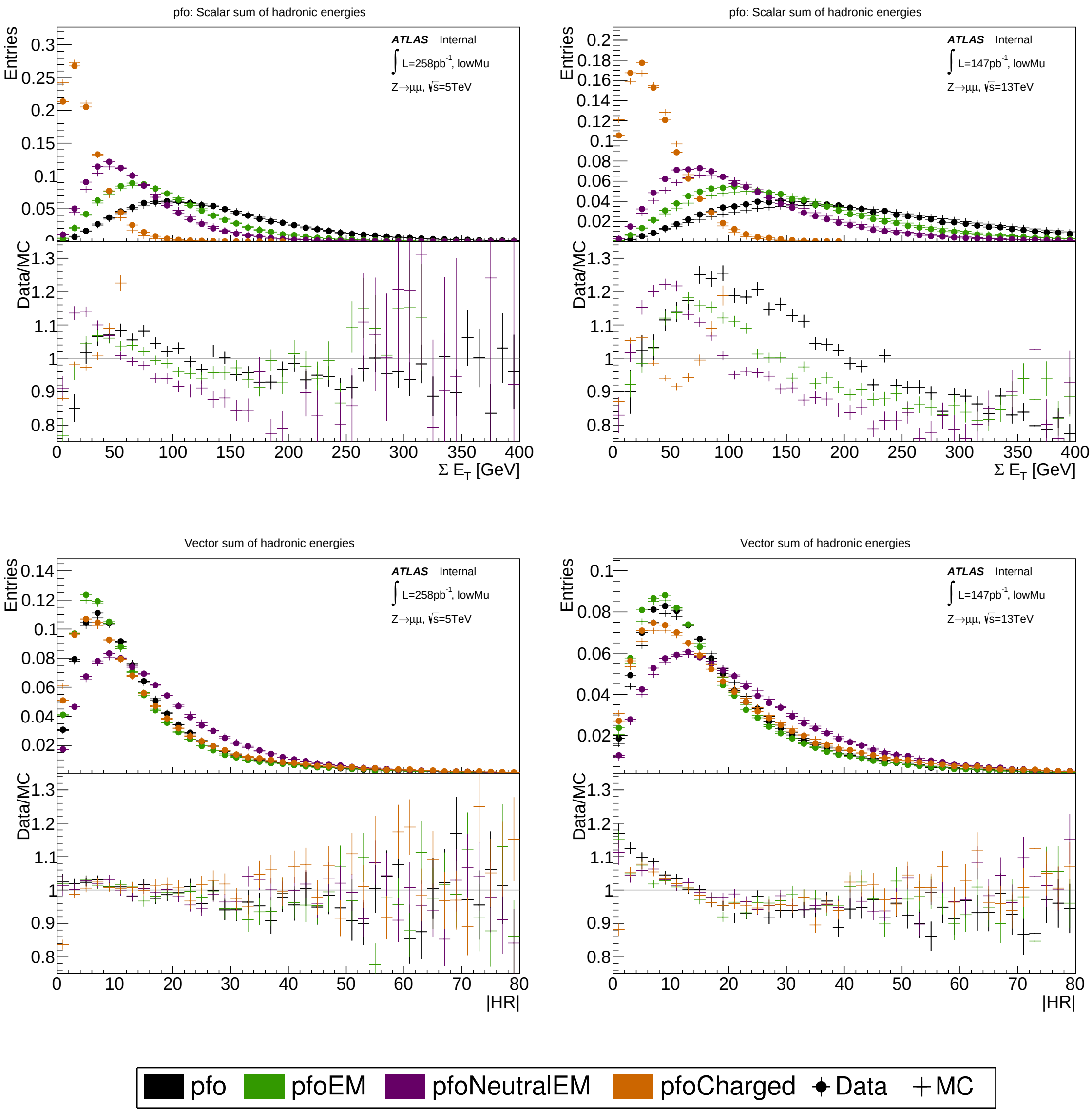

Figure 5.9.: Hadronic activity shown in the ΣE_T and $|HR|$ distribution (energy scaling applied to $|HR|$) for the *lowMu* $Z \to \mu\mu$ analysis. The various hadronic recoil algorithms (see legend below for the color coding) in the *lowMu* analysis are shown without main reweighting applied.

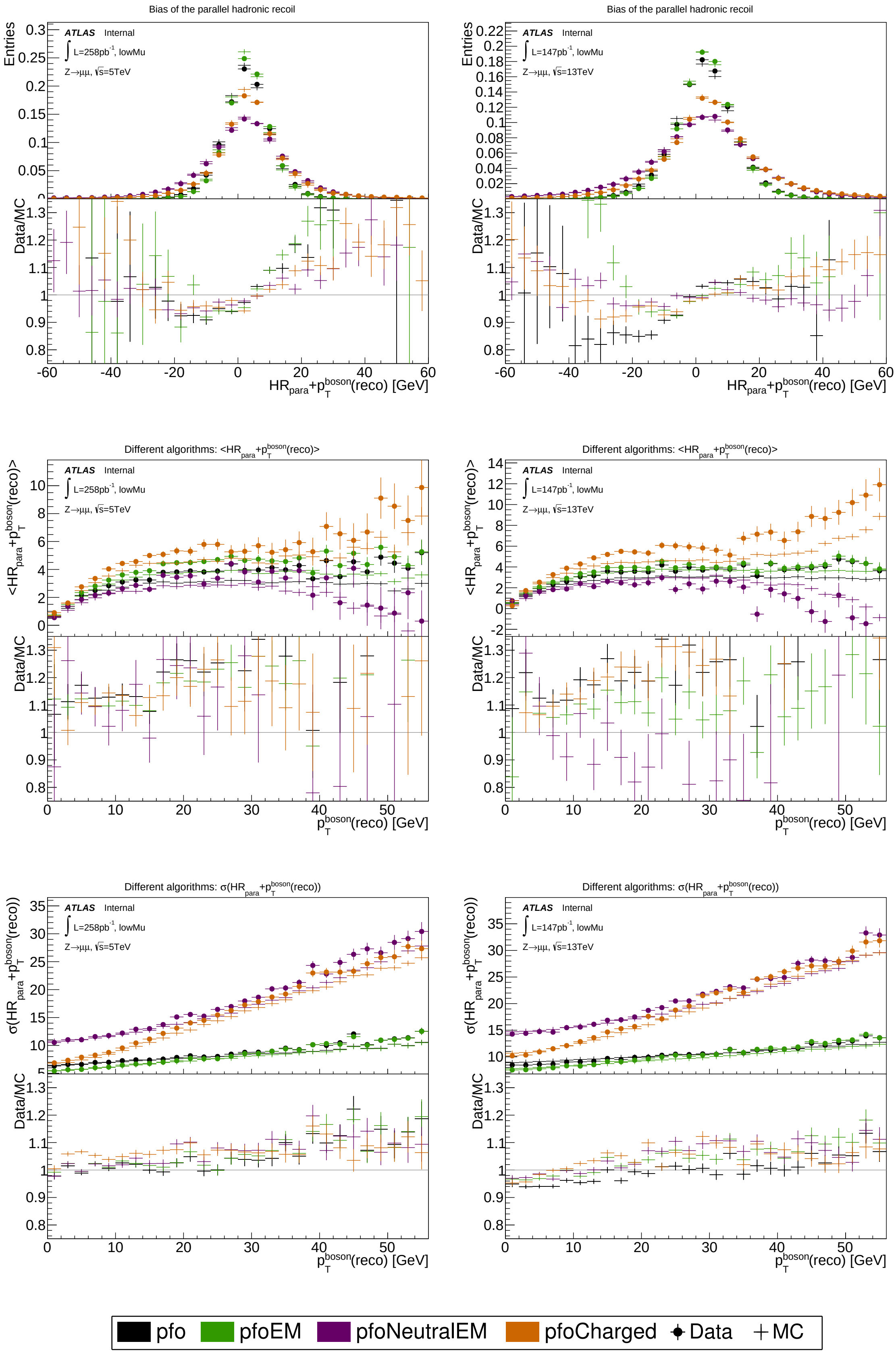

Figure 5.10.: Several hadronic recoil distributions for the corrected parallel hadronic recoil component $HR_{par} + p_T^{boson}(reco)$ for the *lowMu* $Z \to \mu\mu$ analysis. The legend below shows the color coding of the various algorithms. The recoil energy is scaled.

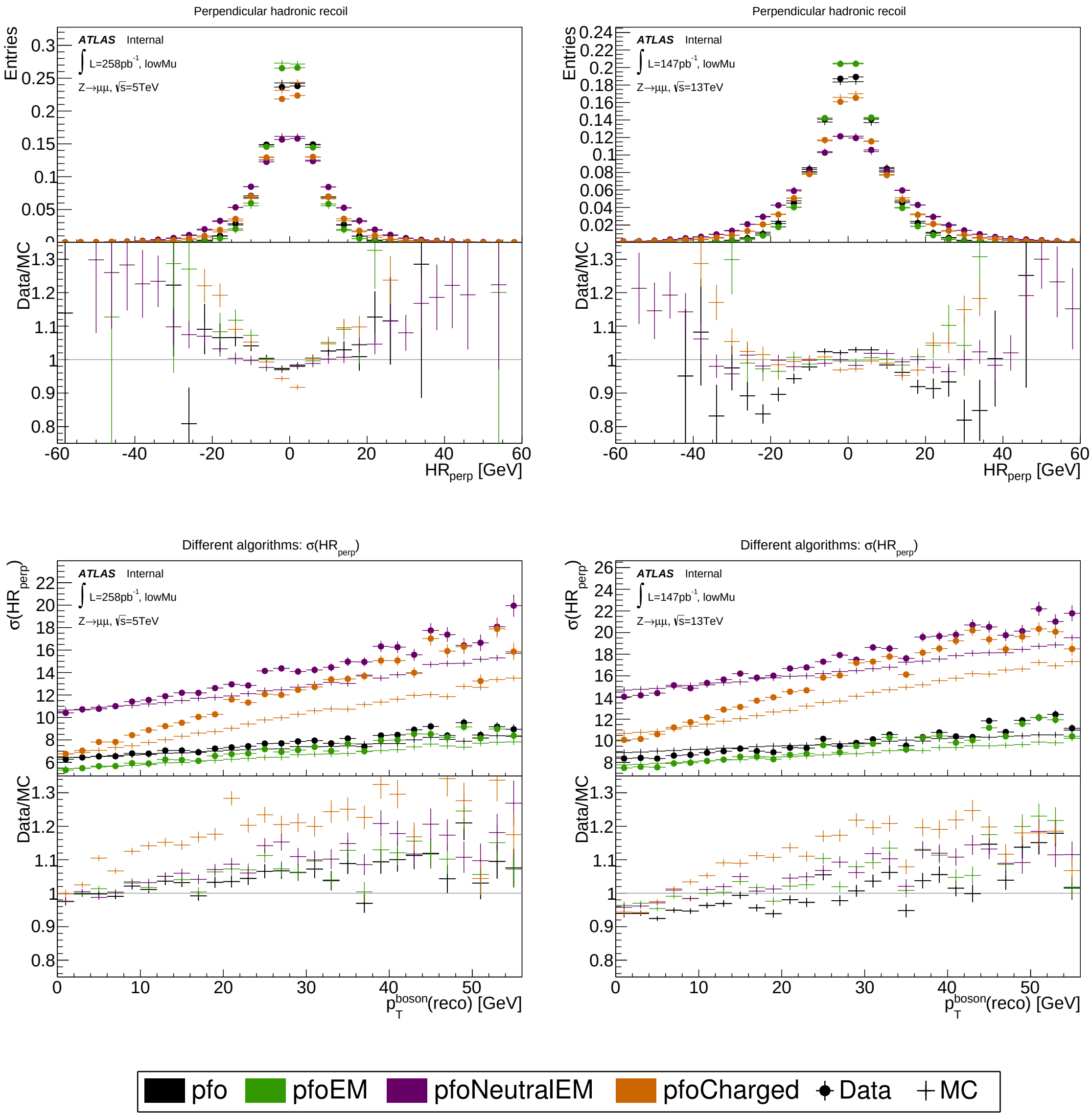

Figure 5.11.: Several hadronic recoil distributions for the perpendicular hadronic recoil component for the *lowMu* $Z \to \mu\mu$ analysis. The various hadronic recoil algorithms (see legend below for the color coding) in the *lowMu* analysis are shown without main reweighting applied. The recoil energy is scaled.

CHAPTER 6

Hadronic activity reweighting technique

6.1. The scope of the pileup and ΣE_T reweighting

Before giving a detailed description of the reweighting technique, the general concept of the reweighting will be explained briefly. The two background collision parameters pileup and underlying event and the modeling thereof influence the hadronic activity, visible in the quantities ΣE_T and HR. Not only is the pileup distribution different in simulation as in data (which can be adopted for by applying a simple weight to each event), but also the average amount of hadronic activity per pileup vertex differs. Thus, one additional interaction, happening in parallel to the hard scattering, contributes to a different amount of hadronic activity in the simulations as in data. In the 7 TeV analysis, the pileup multiplicity in data was by a factor 1.1 larger than in the simulations. The exact factor depends on the luminosity and the cross section for minimum bias interactions, which can differ for the various run campaigns, as well as the implementation of the modeling of these quantities in the MC simulation. These difference can be accounted for by the pileup reweighting.

The basic idea of the reweighting technique that is developed in this analysis is to use the relation of the mean hadronic activity measured by $\langle \Sigma E_T \rangle$ to a representation of the pileup to model the differences. First, the average activity measured by $\langle \Sigma E_T \rangle$ as a function of pileup is made uniform in data and simulations, then a set of event weights, which only depends on pileup, is derived to adjust the differences in the pileup modeling in the simulations. The shape of the simulated ΣE_T distribution itself will not be perfectly identical to data by this approach yet, since only the average activity was adapted. Remaining difference in the shape can be removed by another set of event weights. The smaller the remaining differences, the less likely is an interference with the transverse boson momentum because of its dependency to ΣE_T. After this, the resolution of the parallel and perpendicular hadronic recoil components might still differ. They will be adapted by a subsequent scaling step and a bias correction will be applied to the parallel hadronic recoil.

Especially hadronic recoil calculations that include large amounts of pileup like the cluster algorithm are expected to be modeled well by this approach. The method was first derived for the 8 TeV analysis, which is used as a reference sample for this section. The effect of the reweighting on the *lowMu* analyses will be discussed afterwards.

6.2. Pileup distribution

The pileup included in each event cannot be perfectly measured in the setting of the ATLAS detector. An estimate is given by the quantity of the number of interactions per bunch crossing, which is derived within the luminosity measurement. Several parallel strategies for the luminosity determination and its calibration are implemented in ATLAS [107]. Two variables that monitor the pileup are computed. The first is the number of actual interactions per bunch crossing μ. It is the expectation value of a Poisson distribution, that describes the number of interactions for one collision of two given bunches during one luminosity block LB. [1] It is averaged over all collisions of the same two bunches during each luminosity block. The second variable is the average interactions per bunch crossing $\langle\mu\rangle$, that averages over all bunches during one luminosity block. For the event selection applied here, the actual interactions per bunch crossing gives the more accurate pileup description. Both quantities are represented by decimal numbers rather than integer values as one might expect. The data distribution is therefore continuous. In the Monte Carlo datasets however, usually only integer numbers are simulated.

Fig. 6.1 shows the distribution of the number of actual interactions per bunch crossing for the 8 TeV analysis. The amount of simultaneous interactions strongly depends on the luminosity and center of mass energy of the collisions. The distribution is therefore different for each dataset. The double peak structure visible in the data distribution can be explained by the fact that the collision parameters were slightly changed in between the two data taking periods B and G.

The modeling in the simulations need to be finely tuned to the data distribution to which the simulations are compared to. In order to remove the larger discrepancies in the shape of the distribution, a first modeling of the simulated distribution is done by applying event weights as a function of the actual interactions per bunch crossing. The event weights are derived by the ratio of data and MC in integer bins of the number of actual interactions per bunch crossing, as shown in the bottom plot of Fig. 6.1.

The quite different pileup conditions of the *lowMu* analyses are presented in Fig. 6.2 for the $Z \to \mu\mu$ analyses. Here, only few simultaneous interactions are observed when comparing to the regular beam conditions. In the 5 TeV dataset, between 1 and 5 simultaneous interactions are registered in parallel. For the 13 TeV setup, most events consist of two simultaneous interactions per bunch crossing. These low number of collisions were achieved by separation leveling [50]. With this method, the two beams are not brought to collision head on but with an offset in the transverse plane [108].

To allow for a better scaling of the narrow pileup distribution it is simulated in a half integer stepping in the 5 TeV Monte Carlo simulations. With this, a larger handle for a reweighting is given. Unfortunately, this smaller step size is not available for the 13 TeV analyses. In addition, which is opposed to the 8 TeV datasets, the simulated *lowMu* ActIntPerXing values are provided as half integer[2] for the 13 TeV analyses and quarter integer values[3] for the 5 TeV analyses. To exploit the full width, the bins are chosen centered around this stepping.

The corresponding event weights can be subsequently used to adapt the simulated distri-

---

[1] One luminosity block usually lasts one minute and the luminosity parameters are assumed to be constant during that time. [107]

[2] analyses @13 TeV with a stepping of ~ 1: ActIntPerXing={0.5,1.5,2.49,3.5,4.5,...}

[3] analyses @5 TeV with a stepping of ~ 0.5: ActIntPerXing={0.24,0.75,1.25,1.74,2.24,2.75,...}

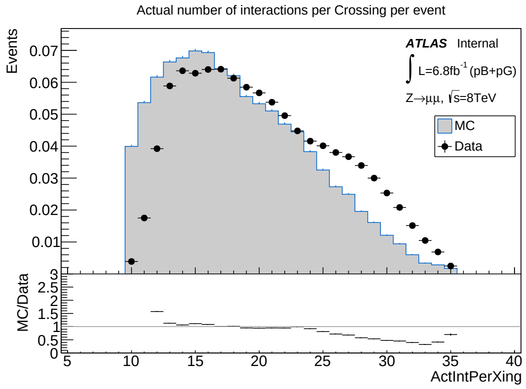

Figure 6.1.: The pileup measured by the quantity of the actual interactions per bunch crossing for the periods B and G of the 8 TeV run campaign as well as the unweighted distribution of the MC simulation. The lower section shows the event weights, which are used to adapt the simulated distribution to the data periods B and G. Note that an event cut is applied here, which rejects events with less than 10 or more than 35 simultaneous interactions.

bution and are again shown in the bottom pad of the two plots in Fig. 6.2. The distributions and event weights for the $Z \to ee$ analyses are found in Appendix E. The scale factors show small differences due to statistical fluctuations compared to the $Z \to \mu\mu$ analyses.

6.3. Dependency of ΣE_T on pileup

The correlation between ΣE_T and pileup is illustrated in Fig. 6.3 by the distribution of events as a function of the two quantities for the cluster algorithm as an example. Here, only events with a small transverse boson momentum of $p_T(Z) < 5\,\text{GeV}$ are included in the calculations. This allows to analyze the pileup dependency on the constituents of the hadronic activity that is not coming from true recoil. To illustrate the connection quantitatively, the mean ΣE_T per integer value of the actual interactions is calculated and given in the central profile plot for both data and simulation.

It can be seen that the dependency of the $\langle \Sigma E_T \rangle$ value on the actual interactions per bunch crossing follows a linear trend. The relation differs in data and simulation, as it was already visible in the unweighted plots in the previous section. This difference can be quantified by a second order polynomial fit of the form $A + B \cdot x + C \cdot x^2$. The three parameters can be interpreted in the following way: The y-intercept, determined by the parameter A, describes the hadronic activity, which is independent of the number of simultaneously happening interactions. Since true recoil is largely excluded by the $p_T(Z) < 5\,\text{GeV}$ cut, this activity is expected to come mostly from the underlying event, which are the decay particles from the collision of the same two protons as the hard interaction. The slope parameter of the linear relation B is the direct measure for the pileup dependency. The third parameter C describes the deviation from the linearity. However, the fit results for C, listed in Tab. 6.1, and especially the precision thereof indicate that this deviation is mostly consistent with zero. Since these values are small in comparison to the linear parameter anyhow, the influence of the quadratic term for the reweighting is expected to be small as well.

			8 TeV $Z \to \mu\mu$			
Algorithm	A_{MC}	A_{Data}	B_{MC}	B_{Data}	C_{MC}	C_{Data}
cluster	39.9±7.7	42.0±4.8	17.16±0.87	13.91±0.49	−0.045±0.023	0.001±0.011
track500	27.1±3.2	27.2±2.1	7.52±0.35	6.88±0.21	0.0029±0.0091	0.0057±0.0050
track500PV	23.9±1.2	22.71±0.78	0.36±0.13	0.325±0.077	−0.0007±0.0032	0.0000±0.0018
track1000	16.3±2.1	17.7±1.4	4.01±0.23	3.69±0.14	0.0043±0.0060	0.0076±0.0033
track1000PV	15.24±0.88	15.08±0.59	0.205±0.095	0.154±0.058	−0.0011±0.0024	0.0003±0.0014

Table 6.1.: Fit results of the ΣE_T-pileup dependency for the 8 TeV analysis.

			5 TeV $Z \to \mu\mu$			
Algorithm	A_{MC}	A_{Data}	B_{MC}	B_{Data}	C_{MC}	C_{Data}
pfo	56.84±0.65	58.1±2.0	33.93±0.65	30.4±2.0	−1.04±0.15	−1.14±0.49
pfoEM	40.93±0.47	41.3±1.4	21.17±0.46	19.2±1.4	−0.60±0.11	−0.74±0.34
pfoNeutralEM	25.80±0.34	25.7±1.0	20.53±0.35	18.1±1.1	−0.536±0.087	−0.61±0.27
pfoCharged	15.69±0.16	16.20±0.53	0.48±0.14	0.78±0.49	−0.033±0.030	−0.06±0.11

Table 6.2.: Fit results of the ΣE_T-pileup dependency for the 5 TeV analysis in the muon channel.

			13 TeV $Z \to \mu\mu$			
Algorithm	A_{MC}	A_{Data}	B_{MC}	B_{Data}	C_{MC}	C_{Data}
pfo	108.6±1.3	158.3±5.4	51.8±1.2	3.1±4.6	−2.44±0.27	2.69±0.99
pfoEM	79.52±0.99	127.6±4.1	32.55±0.91	−8.3±3.4	−1.10±0.21	3.35±0.72
pfoNeutralEM	52.07±0.82	100.7±3.6	31.91±0.78	−9.0±3.1	−1.06±0.18	3.55±0.66
pfoCharged	27.73±0.25	27.22±0.96	0.55±0.21	0.45±0.76	−0.000±0.045	−0.10±0.15

Table 6.3.: Fit results of the ΣE_T-pileup dependency for the 13 TeV analysis in the muon channel.

			5 TeV $Z \to ee$			
Algorithm	A_{MC}	A_{Data}	B_{MC}	B_{Data}	C_{MC}	C_{Data}
pfo	58.77±0.39	60.6±2.6	31.78±0.39	27.3±2.6	−0.714±0.093	−0.60±0.60
pfoEM	42.35±0.28	42.9±1.8	19.64±0.28	17.3±1.8	−0.368±0.065	−0.41±0.42
pfoNeutralEM	26.65±0.20	27.3±1.4	19.53±0.21	16.1±1.4	−0.396±0.053	−0.25±0.34
pfoCharged	16.099±0.096	16.06±0.68	0.115±0.086	0.92±0.62	0.022±0.018	−0.10±0.13

Table 6.4.: Fit results of the ΣE_T-pileup dependency for the 5 TeV analysis in the electron channel.

			13 TeV $Z \to ee$			
Algorithm	A_{MC}	A_{Data}	B_{MC}	B_{Data}	C_{MC}	C_{Data}
pfo	107.5±1.6	153.1±6.7	50.3±1.5	6.6±5.0	−2.11±0.35	1.74±0.92
pfoEM	78.8±1.2	107.8±5.2	31.5±1.1	2.5±4.1	−0.87±0.26	1.50±0.81
pfoNeutralEM	51.6±1.0	80.8±4.4	30.96±0.96	2.8±3.6	−0.89±0.23	1.3.±0.72
pfoCharged	27.53±0.30	27.9±1.4	0.42±0.26	−0.9±1.1	0.041±0.055	0.28±0.20

Table 6.5.: Fit results of the ΣE_T-pileup dependency for the 13 TeV analysis in the electron channel.

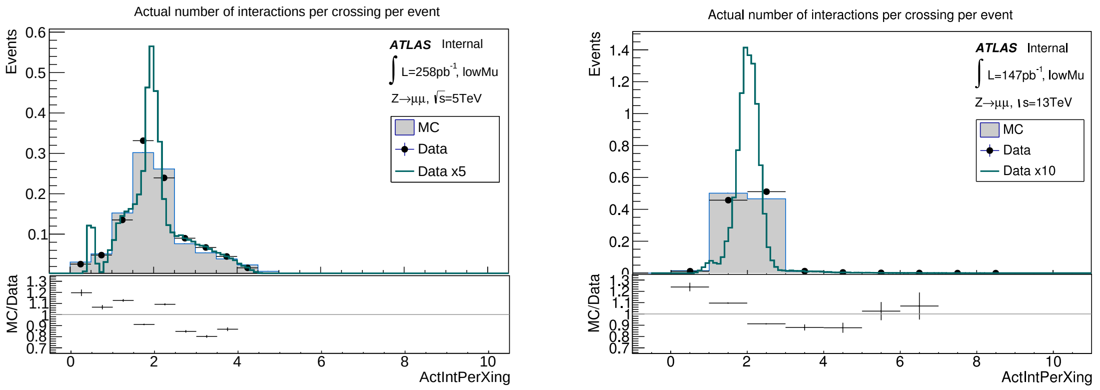

Figure 6.2.: The pileup measured by the quantity of the actual interactions per bunch crossing for the two *lowMu* run campaigns as well as the unweighted distribution of the MC simulation with the $Z \to \mu\mu$ selection. In the 5 TeV dataset, between 1 and 5 simultaneous collisions are registered, while for the 13 TeV dataset, dominantly two simultaneous interactions are observed. The lower section of each plot shows the event weights, which are used to adapt the simulated distribution to the data.

The fit parameters for the 8 TeV analysis also constitute that the pileup dependency is quite different for the various algorithms, which is expected from the varying pileup rejection capability of each algorithm. The corresponding distributions for all algorithms can be found in Appendix F. The cluster algorithm shows a large correlation to pileup with high slope values. One simultaneous interaction increases the hadronic activity by around 17 GeV in data. Here, the hadronic activity is dominated by pileup, whereas the underlying event influence is comparably small. For the track algorithms without primary vertex cut, the slope is already less steep. For trackPV algorithms the average ΣE_T values are dominated by underlying event rather than pileup, one additional interaction per bunch crossing contributes to less than half a GeV.

While the fits can be regarded as quite stable for the 8 TeV analysis, the results for the *lowMu* analyses are based on a narrow pileup distribution with a small lever arm, what are found to be less ideal conditions for this polynomial fit. An exemplary fitted distribution for the pfo algorithm is shown in Fig. 6.4 and the full set of fitted distributions for all algorithms can be found in Appendix F. The fit parameters are determined on the basis of a few data points only, thus the parameters are accompanied by large uncertainties. The results are listed in Tab. 6.2, 6.3, 6.4 and 6.5. The fit parameters for the two algorithms that include clusters as well as tracks, pfo and pfoEM, indicate a modest pileup dependency. This could give a good handle for the modeling. PfoNeutral, which is only based on clusters, also indicates a good basis for the pileup reweighting. PfoCharged however, which is only based on tracks, shows a really low pileup dependency and is dominated by underlying event. The track selection within this algorithm has a powerful pileup rejection. As a consequence, the reweighting technique is not ideal for this selection.

The 13 TeV fit results are based on an even smaller set of data points with low statistics except for the two dominant bins around $\mu = 2$. The uncertainties on the fit are even larger here. The quadratic shape is much more pronounced in data than in the simulations, visible in the fit parameters B and C. It should be noted that the reweighting technique, which is

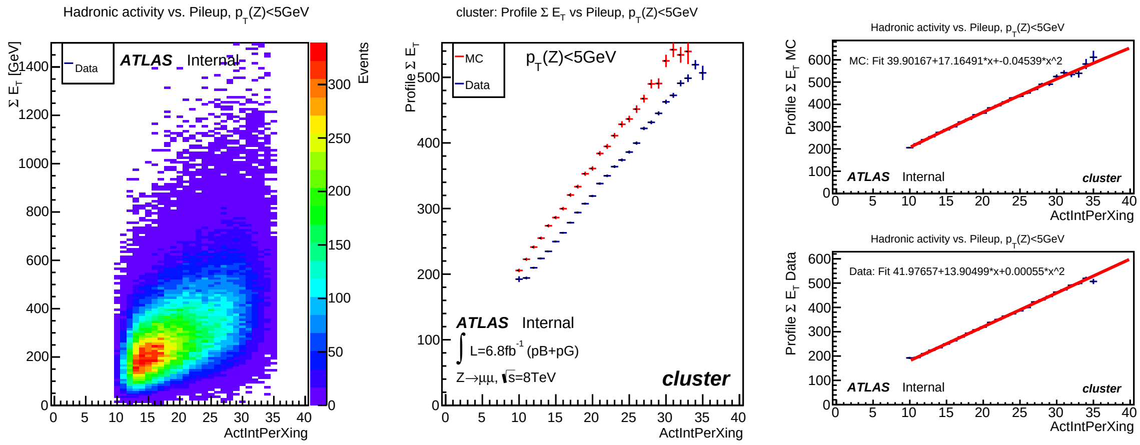

Figure 6.3.: First step of the ΣE_T reweighting: The left plot shows the distribution of the events as a function of ΣE_T and pileup (ActIntPerXing) for data. Only events where the reconstructed transverse boson momentum is small ($p_T(Z) < 5\,\text{GeV}$) are taken into account here. In the central plot, the mean ΣE_T value for every pileup bin is computed (profile ΣE_T), showing the dependence of the average ΣE_T on pileup for both data (red) and simulation (blue). The right plot shows the profile of ΣE_T again separately for data and simulation and a corresponding fit $A + B \cdot x + C \cdot x^2$ as well as the fit parameters.

based on the pileup dependency, might not be optimal for these datasets.

6.4. Pileup stretching in data

The quantified difference between the average hadronic activity measured by ΣE_T in data and simulations can be used to improve the agreement between data and simulations in all hadronic recoil variables. The choice of the $\langle \Sigma E_T \rangle$ to pileup relation as a baseline for the reweighting is somehow arbitrary, other correlations could also be used. But for analyses that are sensitive to the number of vertices[4] and that use datasets with large pileup contribution this approach is well motivated.

To obtain a pileup distribution with identically $\langle \Sigma E_T \rangle$ per pileup interaction in data and simulation, the pileup in each event needs to be modulated. This is equivalent to a stretching of the x-axis of the ActIntPerXing distribution. As already pointed out, the ActIntPerXing distribution is continuous in data while it is only represented in bins with a fixed stepping for the simulations. Thus, performing the pileup stretching only in data is the more precise choice that does not show binning effects.

In detail, the number of actual interactions per bunch crossing in data is recalculated by multiplying it with the ratio of three parameters describing the quadratic dependency. The stretching factor is defined by solving the equation that is given by the two sets of quadratic fit parameters.

$$A_{Data} + B_{Data} \cdot x + C_{Data} \cdot x^2 = A_{MC} + B_{MC} \cdot x' + C_{MC} \cdot x'^2$$

---

[4] For the W mass measurement the hadronic recoil resolution is sensitive to the number of vertices, which are measured by the reconstructed quantities of the pileup.

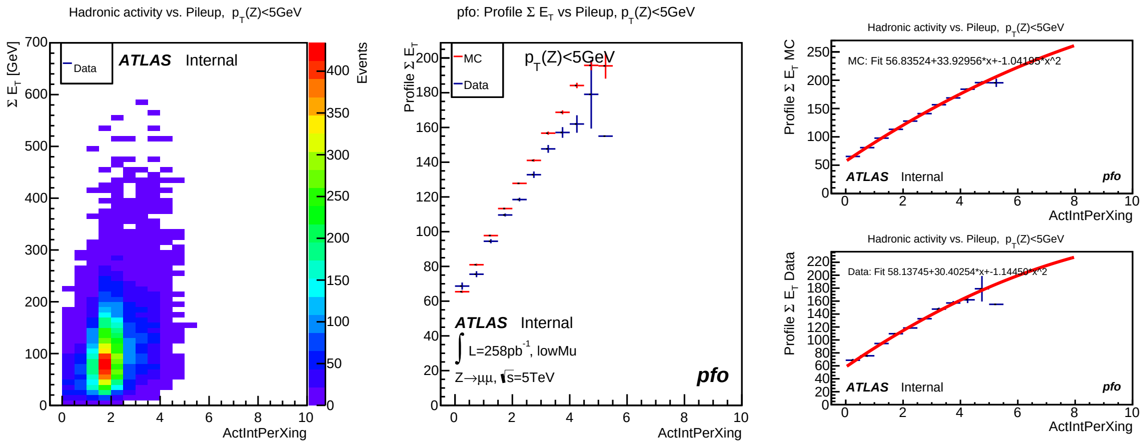

Figure 6.4.: First step of the ΣE_T reweighting for the 5 TeV *lowMu* analysis: The left plot shows the distribution of the events as a function of ΣE_T and pileup (ActIntPerXing) for data. Only events where the reconstructed transverse boson momentum is small ($p_T(Z) < 5\,\text{GeV}$) are taken into account here. In the central plot, the mean ΣE_T value for every pileup bin is computed (profile ΣE_T), showing the dependence of the average ΣE_T on pileup for both data (red) and simulation (blue). The right plot shows the profile of ΣE_T again separately for data and simulation and a corresponding fit $A + B \cdot x + C \cdot x^2$ as well as the fit parameters.

From this, a the stretched number of actual interactions per bunch crossing x_{Data}^{new} can be calculated:

$$x_{Data}^{new} = x_{Data} \pm \frac{\sqrt{A_{Data} - \frac{A_{MC}}{C_{MC}} + \frac{B_{MC}^2}{4 \cdot C_{MC}} + B_{Data} \cdot x_{Data} + C_{Data} \cdot {x_{Data}}^2}}{C_{MC}} - \frac{B_{MC}}{2 \cdot C_{MC}},$$

where the number of actual interactions per bunch crossing as measured in data is used for x_{Data}.

The stretched pileup distribution in comparison to the unstretched simulated distribution is shown in the top left plot in Fig. 6.5 for the cluster algorithm. The stretched data distribution is shifted to lower pileup values. As can be seen from the bottom left plot of the same figure, the correlation between the $\langle \Sigma E_T \rangle$ and pileup is now almost identical. The results of the quadratic fit, indicated in the bottom right plots, is good.

6.5. Pileup event weights

With the stretched data pileup distribution where the average hadronic activity per pileup interaction is now identical, a handle is given to model the remaining differences between data and simulations. A set of event weights can be derived, that equalize the contribution of simulated event at a given number of actual interactions per bunch crossing. Because of the stretching, it is guaranteed, that the $\langle \Sigma E_T \rangle$ within each categorization of the pileup is identical and thus, no bias is introduced by a differing hadronic activity. The set of event weights for the cluster algorithm is visible in the top right plot in Fig. 6.5. The event weights

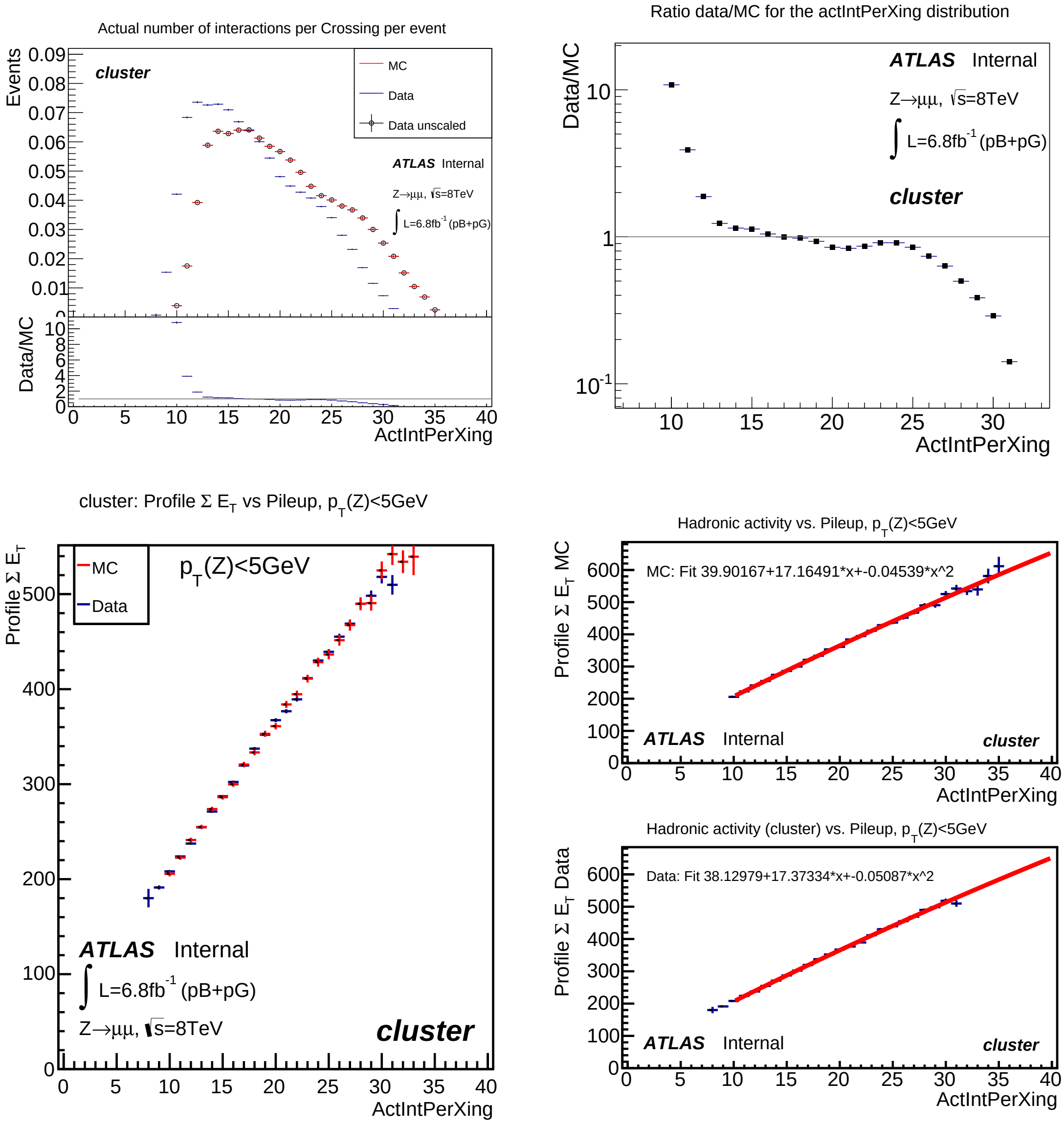

Figure 6.5.: Top row: Recalculated pileup distribution for data, where the values were stretched to give identical average hadronic activity as the simulations, in comparison to the unstretched pileup distribution in data and in the simulations (top left). Ratio of the stretched data distribution and the simulations (top right). Since event weights were applied to the simulations beforehand, the shape of the simulated distribution is equivalent to the unstretched data distribution. The bottom row plots show the agreement between the average hadronic activity measured by $\langle \Sigma E_T \rangle$ and the fit results in data and simulation after the data was stretched.

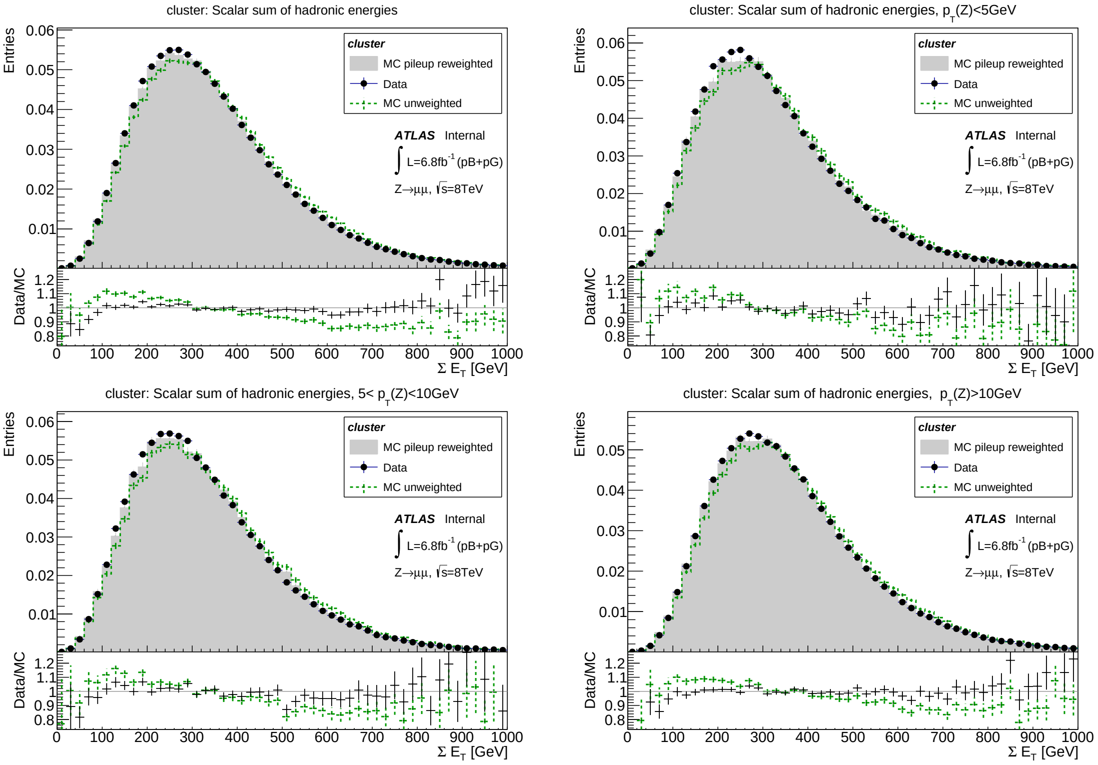

Figure 6.6.: ΣE_T distributions for the cluster algorithm for various subset of different transverse boson momentum categories of $p_T(Z) < 5\,\text{GeV}$, $5\,\text{GeV} < p_T(Z) < 10\,\text{GeV}$ and $p_T(Z) > 10\,\text{GeV}$. The reweighted Monte Carlo simulation is shown along with the unmodified MC distributions (dashed green) and are both compared to data.

are applied to simulation, while the scale factors for the stretching of the pileup distribution in data are not applied in the following analysis steps.

6.6. Results of the pileup reweighting

6.6.1. 8 TeV analysis

The ΣE_T distribution with the pileup event weights applied to the simulation is presented in Fig. 6.6. The total event selection as well as three categorizations of the transverse boson momentum are given. In general, the agreement between data and simulation is much improved by the reweighting over the full transverse boson momentum range. No major difference is visible in the three different categorizations of the transverse boson momentum except for statistical fluctuations. However, very small ΣE_T values show a disagreement of up to 20%, although the comparably large error bar on these values due to small statistics should be noted. It can be concluded, that this reweighting procedure is able to adjust the different modeling in the simulations over a wide range of ΣE_T values and even in the tails with high values of ΣE_T, although the average hadronic activity was modeled with respect to $\langle \Sigma E_T \rangle$ only.

The reweighted ΣE_T distributions for the track algorithms of the 8 TeV analysis are pre-

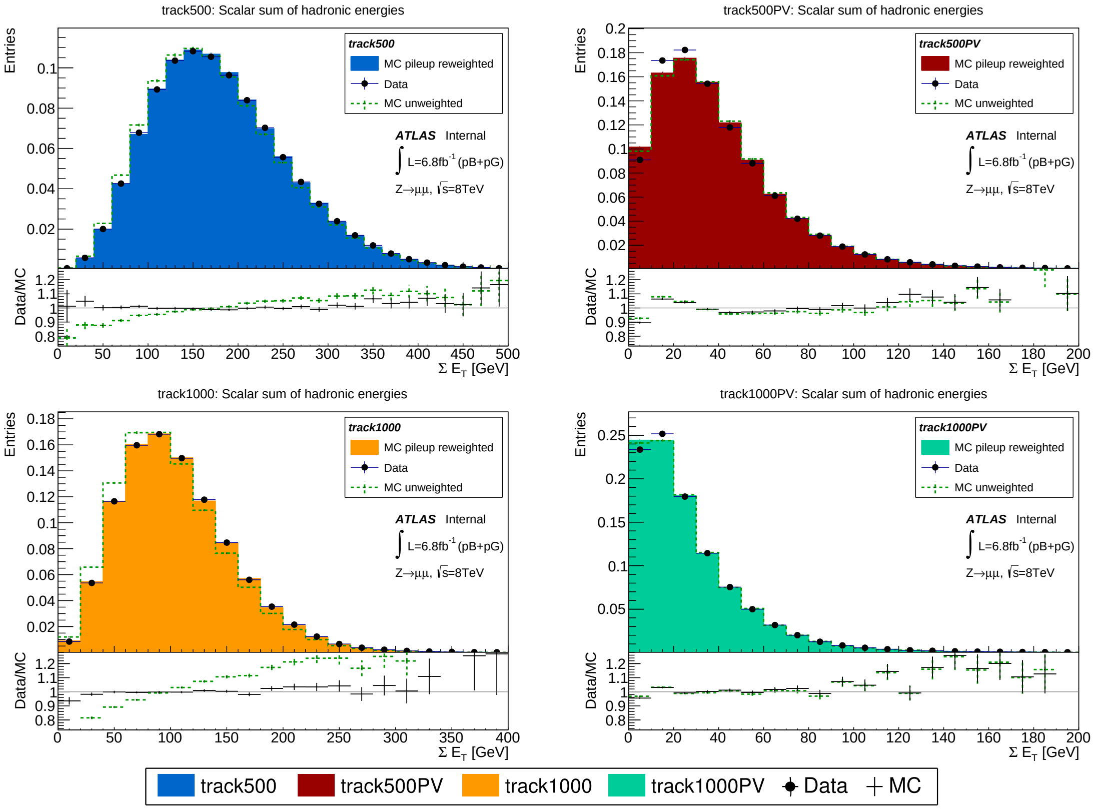

Figure 6.7.: ΣE_T distributions for the different track algorithms (see legend below for the color coding).

sented in Fig. 6.7. The two algorithms without a primary vertex cut are in good agreement between data and simulations after reweighting. The ΣE_T reweighting can successfully be applied to these algorithms as well. The same disagreement for low ΣE_T values as observed for the cluster algorithm is also visible here. The trackPV algorithms however show only little improvement after reweighting, but the agreement, especially for track100PV was comparably close to unity already before the reweighting. That the pileup reweighting did not add an effect can be explained by the high pileup rejection capability of these algorithms. As a consequence, the remaining pileup dependencies is small compared to the hadronic activity from underlying event particles. Although the underlying event contribution is included in the modeling by the parameter A, the lever arm of the pileup dependency modeled by the parameters B and C is too weak to allow for an effective modeling on this basis.

The effect of the reweighting on the parallel and perpendicular component of the hadronic recoil is shown in Fig. 6.8 for the cluster algorithm. The two quantities are barely influenced by the pileup reweighting. A small change in the resolution is visible, the slightly parabolic shape of the Data/MC ratio for the perpendicular component has been reduced. The resolution is dependent on the ΣE_T distribution and calibrations thereof have a small effect. Remaining differences in the resolution will be adapted in a following step of the reweighting.

The distribution of $|HR|$, the magnitude of the recoil vector, is also shown in the same figure. Also here, the effect of the reweighting is small, slightly decreasing the agreement. This effect might be a consequence of the decreased resolution of the parallel and perpendicular component.

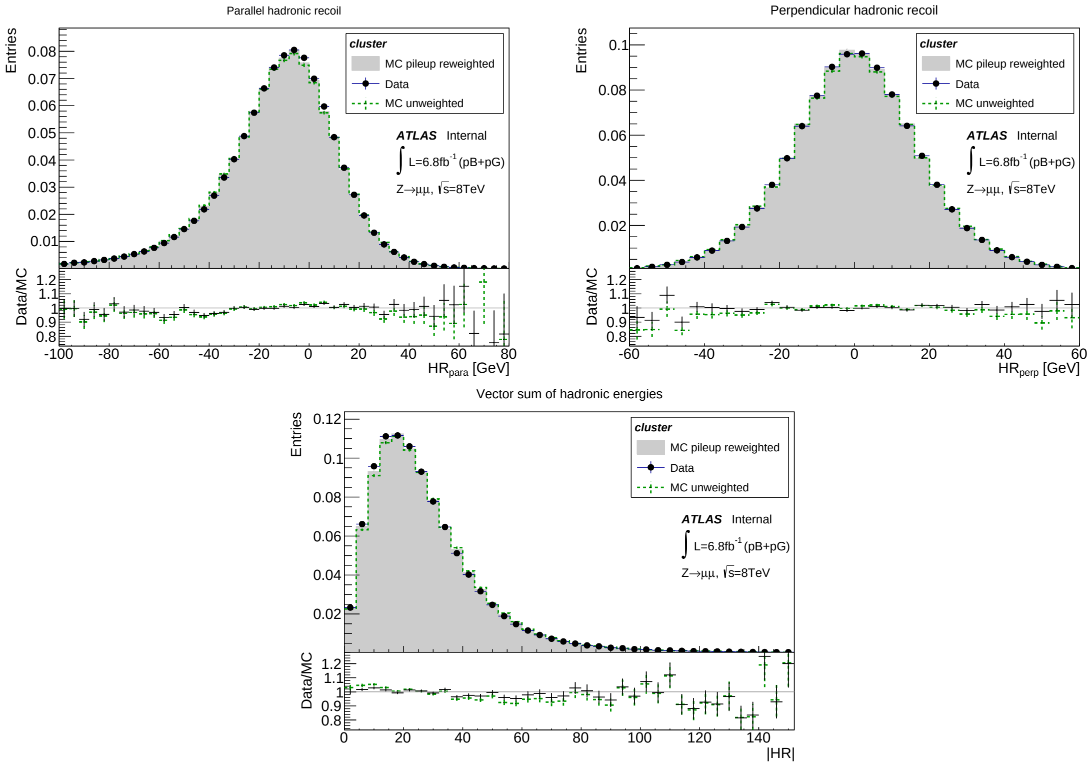

Figure 6.8.: Distributions of the parallel and perpendicular hadronic recoil component for the cluster algorithm as well as the magnitude of the recoil vector $|HR|$. The pileup reweighted Monte Carlo simulation is shown along with the unmodified MC distributions (dashed green) and are both compared to data.

6.6.2. *lowMu* analyses

The results for the ΣE_T reweighting on the *lowMu* analyses are given for the ΣE_T distribution in Fig. 6.9 for the muon channels and in Fig. 6.10 for the electron channels.

The pileup reweighting applied to the two standard algorithms pfo and pfoEM and to the implementation with only neutral clusters (pfoNeutralEM) gives good results for both center of mass energies in the muon channel. The agreement between data and the simulations can be improved in the central region and is found to be close to unity for the 5 TeV analysis. In the 13 TeV datasets a small wavy trend, which is also visible in the unweighted data to MC ratio, remains slightly. The tails are not ideally modeled. The same disagreement for low values of ΣE_T as observed for the 8 TeV analysis is also visible here. In addition, the tails with high ΣE_T values show the same trend in all distributions. The number of events in the simulations is always underestimated in the tails.

When this pileup reweighting technique is applied to the algorithm with only charged tracks included in the calculation (pfoCharged) no improvements can be found for the 5 TeV analysis. The agreement between data and the simulations is not significantly improved. This was already expected from the fits to the $\langle \Sigma E_T \rangle$ as a function of pileup. For the 13 TeV analysis the method could not even be applied to the pfoCharged algorithm. Here, the dependency of $\langle \Sigma E_T \rangle$ on pileup was too flat in data, resulting in a negative slope for the upper ActIntPerXing bins. As a consequence, the newly calculated stretched data ActIntPerXing

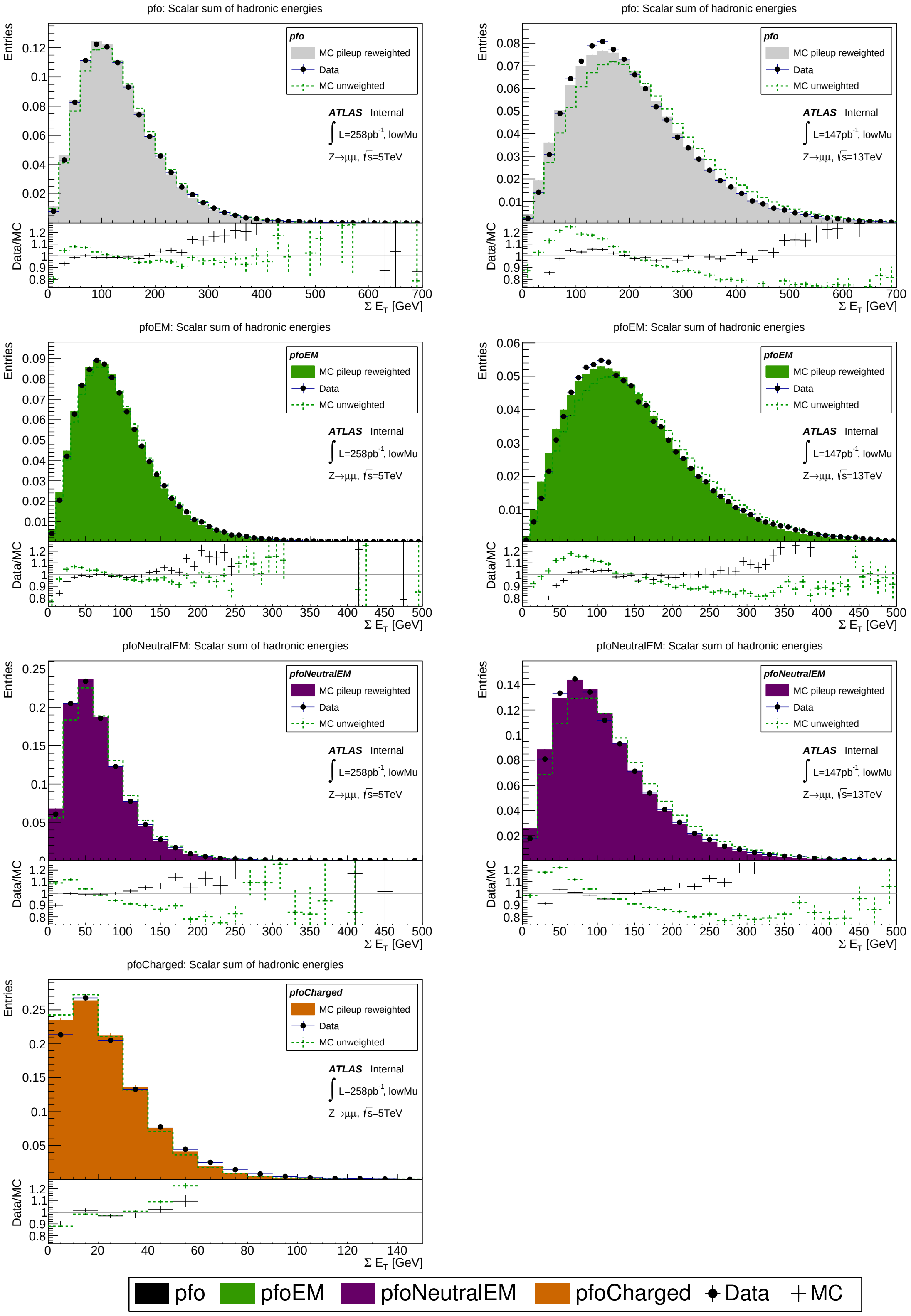

Figure 6.9.: ΣE_T distributions for the different algorithms (see legend below for the color coding) of the *lowMu* analysis in the $Z \to \mu\mu$ channel. The pileup event weights have been applied to MC. In comparison, the unweighted distributions are shown alongside (green dashed line). The left column shows the 5 TeV results, while the right column gives the 13 TeV results.

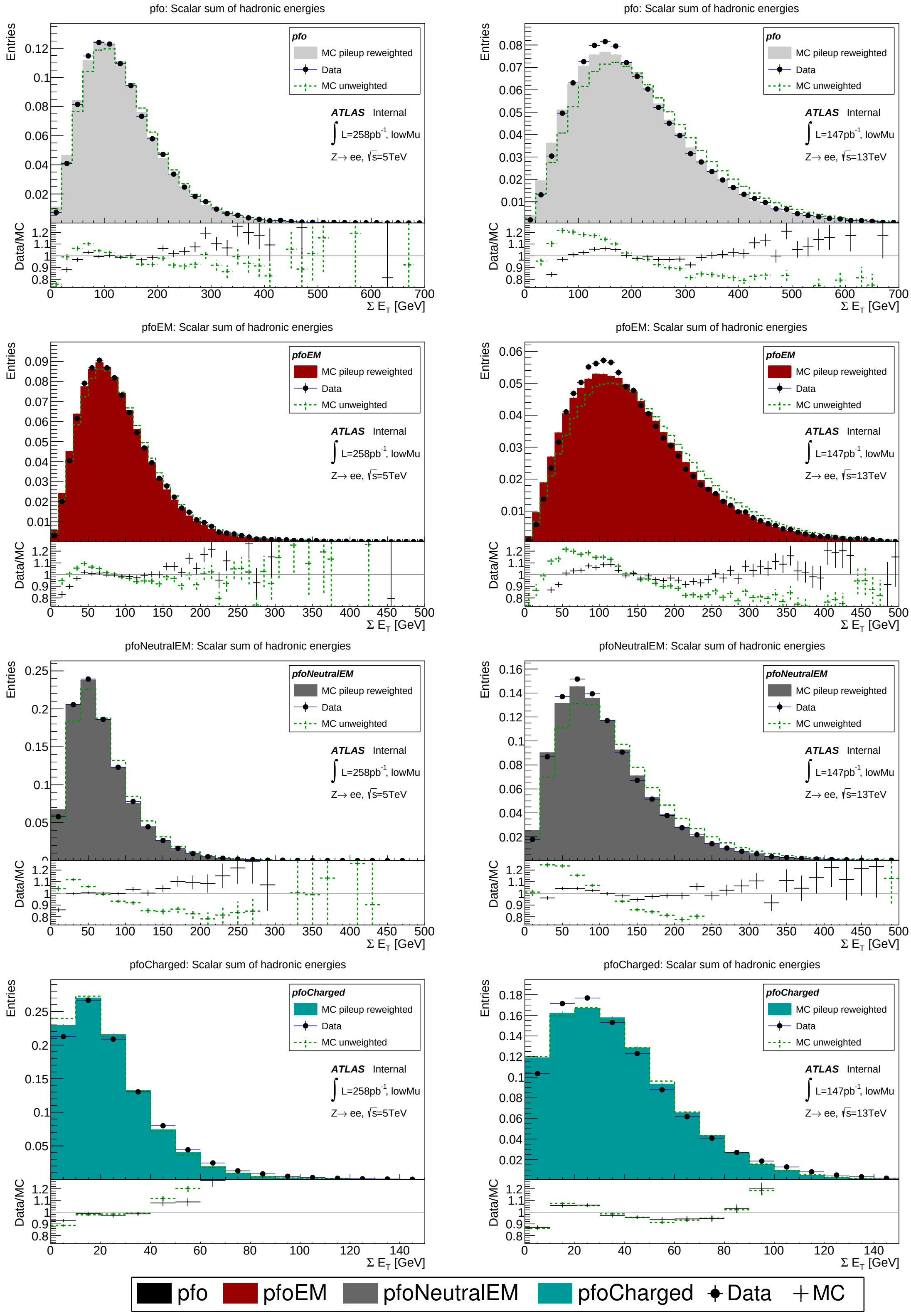

Figure 6.10.: ΣE_T distributions for the different algorithms (see legend below for the color coding) of the *lowMu* analysis in the $Z \to ee$ channel. The pileup event weights have been applied to MC. In comparison, the unweighted distributions are shown alongside (green dashed line). The left column shows the 5 TeV results, while the right column gives the 13 TeV results.

values were all shifted to the zero bin, leaving no pileup dependency. Calculating the event weights in the subsequent step could not be completed. Therefore, no distributions can be shown for the 13 TeV $Z \to \mu\mu$ pfoCharged algorithm.

The performance of the reweighting technique in the electron channel is generally good as well (see Fig. 6.10). The same effects as seen in the muon channel are also observed here. The remaining wavy effect in the 13 TeV sample might be slightly larger than for the 5 TeV sample.

Interestingly, the fit to the pileup distribution for the pfoCharged algorithm in the 13 TeV samples was acceptable for the method and the following processing steps did not crash. However, the reweighted distributions show no improvement to the data/MC ratio.

It can be concluded, that the combination of a low dependency of the hadronic activity on the number of pileup events together with a narrow pileup distribution is not ideal for the pileup reweighting as it was applied here. In contrast, the reweighting works well for algorithms that include clusters in the recoil calculation and gives comparable results for the two datasets for these algorithms.

6.7. Effect of a varied binning of the pileup distribution

During the analysis development it was found that the feasibility of this reweighting technique strongly depends on the exact pileup distribution. The binning of the ActIntPerXing distribution can be varied to investigate the effect further. This is especially relevant for the *lowMu* analyses with the narrow pileup distributions. The two runs allow for two alternative variations:

- For the 5 TeV analyses, a full integer binning is applied to increase the statistics for the outside bins. This comes at the cost of a reduced number of points available to the fit. The left plot of Fig. 6.11 shows the new ActIntPerXing distribution, which is used as a baseline for an alternative reweighting procedure.

- For the 13 TeV analyses, the unusual stepping of the simulated ActIntPerXing values, which is not exactly 1 (see again 6.2), allows to divide the entries into a different pileup distribution. This is performed by shifting the bin edges to half integer, e.g. 0.5,1.5,2.5 and so on. The newly defined ActIntPerXing distribution is shown in the right plot of Fig. 6.11. One large bin around ActIntPerXing = 2 is found, since two simulated categories are combined in one bin. The bin around 3 is empty in the simulations.

The results of the alternative pileup reweighting approaches in comparison to the pileup reweighting with the original binning is shown in Fig. 6.12 for the pfo and pfoEM algorithm. The modified binning of the 5 TeV analysis (left column) results in a similar agreement of data and MC as the first reweighting approach. Small differences can be noted. The deviation in the tails seem to be lowered and the central region is a nuance closer to unity.

From the right column of plots, which give the results for the 13 TeV analysis, it is clearly visible that the alternative binning applied here does not give as good improvements as the original binning. The single central bin of the alternative ActIntPerXing distribution along with the empty third bin seems to be a worsened handle for the polynomial fit as well as the subsequent application of the event weights.

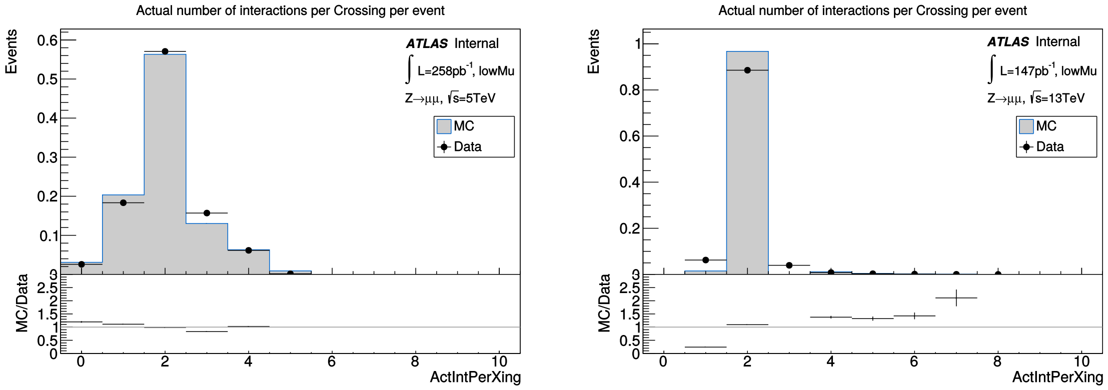

Figure 6.11.: The differently binned ActIntPerXing distributions for the *lowMu* analyses.

From this it can be concluded, that the ideal reweighting needs to be finely tuned to the pileup distribution in data. A different binning can already remove the positive effects of the reweighting for the 13 TeV analyses. The wider pileup distribution of the 5 TeV dataset seems to be more stable against binning modifications.

6.8. ΣE_T reweighting

As it was seen in the previous sections, the ΣE_T distribution in the simulations is not yet in perfect agreement with the data distributions, especially in the tails. The pileup modeling is based on a modification of the $\langle \Sigma E_T \rangle$ rather than of the full shape of the ΣE_T distribution. In addition, other effects besides the a differing average hadronic activity like an imperfect detector description, can influence the goodness of the agreement between data and the simulations. These remaining effects can be removed by a set of event weights. Because of the dependency of ΣE_T on the transverse boson momentum, this can change the distribution of the transverse boson momentum. For this reason, the differences in the ΣE_T distribution should be removed as largely as possible beforehand. As it could be seen in the previous section, the pileup reweighting could successfully be used to minimize the deviations between data and simulation. As a next step, the remaining differences in the shape of the ΣE_T distribution are modeled as a function of the transverse boson momentum.

The set of event weights, which is generated from two-dimensional $\Sigma E_T - p_T(Z)$ distribution, is shown in Fig. 6.13 for the cluster algorithm of the 8 TeV analysis. Large event weights with values >10 are removed to not introduce artificial large fluctuations in the simulations.

The effect of these event weights on the different algorithms of the 8 TeV analysis are shown in Fig. 6.14. The shape of the simulations is now identical to the data distribution in the central regions. However, deviation still arise in the tails. This can be explained by the two-dimensional binning. Empty bins are found in the tails for both data and the simulated distributions because of the limited statistics and the therefore low number of expected entries for bins in the tails. Empty bins in the simulations lead to the effect that an event weight applied to zero entries cannot adjust the number to be identical to data. Therefore, too few simulated events are found in the tails after the reweighting compared to

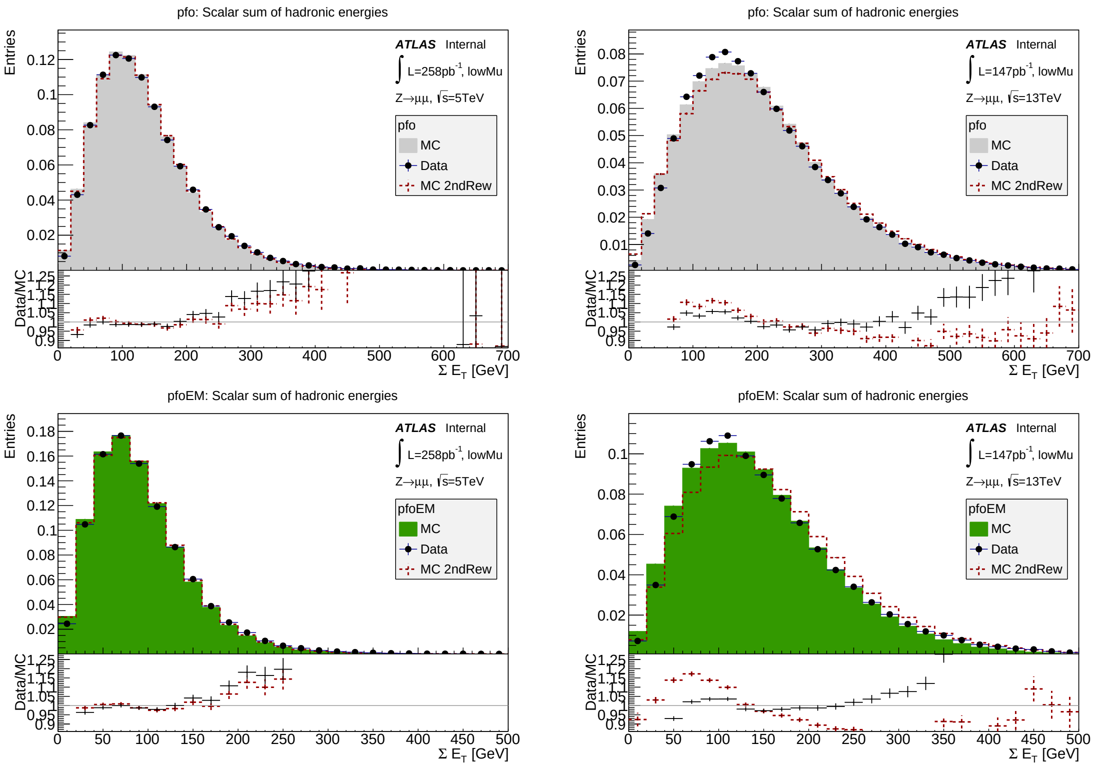

Figure 6.12.: Comparison between the original and the alternative reweighting techniques for the pfo and pfoEM ΣE_T distribution in the $Z \to \mu\mu$ *lowMu* analyses. The left column shows the effect of the new binning in the 5 TeV analysis for the two algorithms pfo and pfoEM while the right column shows the effect of the changed binning for the 13 TeV analysis. The red dashed curve indicates the alternative approach (2nd reweighting), which use a different binning of the ActIntPerXing distribution.

data[5]. The ratio of data and the simulations is therefore increasing.

The relevant figures for the *lowMu* $Z \to \mu\mu$ analyses are shown in Fig. 6.15 and in Appendix G.2 for the $Z \to ee$ analysis. The same effects are found here as well, the event weights lead to a perfect agreement between data and the simulations in the central region. The tails with high values of ΣE_T are also not modeled well by this approach for the 5 TeV analysis. However, this effect is barely visible for the 13 TeV analysis. Here, the tails show a full agreement up to the range included in the plots.

The effect of empty bins does not allow for an ideal agreement between data and the simulations in both tails - as a function of ΣE_T and of $p_T^{boson}(reco)$.

The effect visible for the transverse boson momentum is shown in Fig. 6.16. It shows the ratio between the transverse boson momentum distribution in data and in the simulations after the ΣE_T reweighting is applied (see Appendix G.3 for the *lowMu* $Z \to ee$ results).

The 13 TeV results however show no fluctuations. This can be explained by the fact, that the ΣE_T distribution is much wider for the higher center of mass energy. The range in which

---

[5] Empty bins in the data distribution cannot balance this effect, since these can easily be propagated to the simulations by applying a weight of zero.

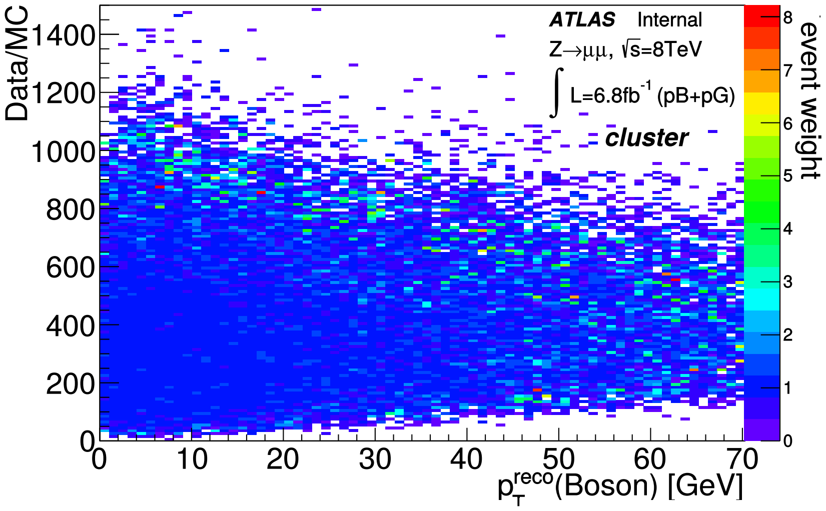

Figure 6.13.: The two-dimensional event weights for the ΣE_T reweighting are shown for the 8 TeV analysis. The weights were generated by the ratio of the ΣE_T distribution as a function of the transverse boson momentum in data and the simulations.

the scale factors are derived, is however the same. As a consequence, the statistics in the outer bins at high ΣE_T values benefit from a better statistics, thus the effect of empty bins is minimized here.

To correct for the introduced bias due to empty bins on the transverse momentum distribution, the transverse boson momentum will be corrected for a second time. The reweighting is identical to the procedure described before (see again Section 5.3.1), but the event weights are derived independently for each algorithm since the effect on $p_T^{boson}(reco)$ differs for each algorithm. With these new event weights applied in addition, the agreement between data and the simulations after all event weights were applied is again evaluated in Fig. 6.17 (see App. G.4 for the $Z \rightarrow ee$ results). As it can be seen now, no effect of the reweighting is visible any longer. This one-dimensional approach leaves the ΣE_T distributions almost unaffected, only small fluctuations are visible (see Appendix G.5 for the relevant distributions).

6.9. Conclusion on the pileup and ΣE_T reweighting

It could be noted that the pileup and ΣE_T reweighting approach shows good results for algorithms, which are at least partially based on clusters. Here, not only recoil and underlying event particles are included but also large enough amounts of pileup. This gives a good handle for a pileup based reweighting. The agreement between data and simulation for track based algorithms with a primary vertex selection cannot be improved well by this approach because of the missing pileup link.

The capability for an improvement by this reweighting technique also depends on the dataset itself. The event weights for modeling the average hadronic activity by means of its pileup dependency can only be determined well if more than one pileup bin is present in the dataset. The configuration of the 8 TeV dataset included a large pileup contribution. This technique was generally effective for the cluster and track algorithms without primary

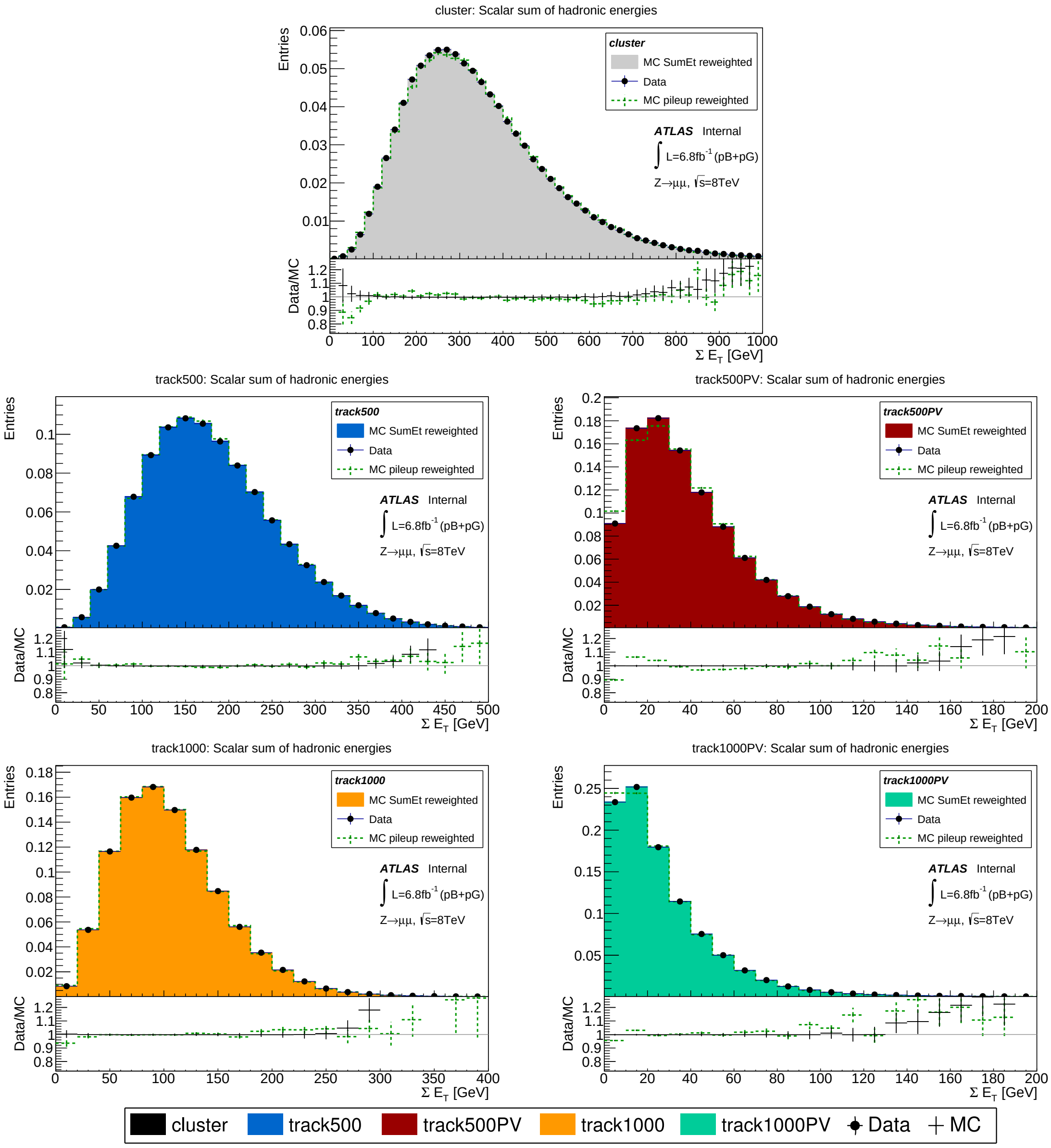

Figure 6.14.: ΣE_T distributions with the pileup and ΣE_T reweightings applied for the different algorithms (see legend below for the color coding) of the 8 TeV analysis. In addition, the distributions with only the pileup weights applied are shown alongside (green dashed line).

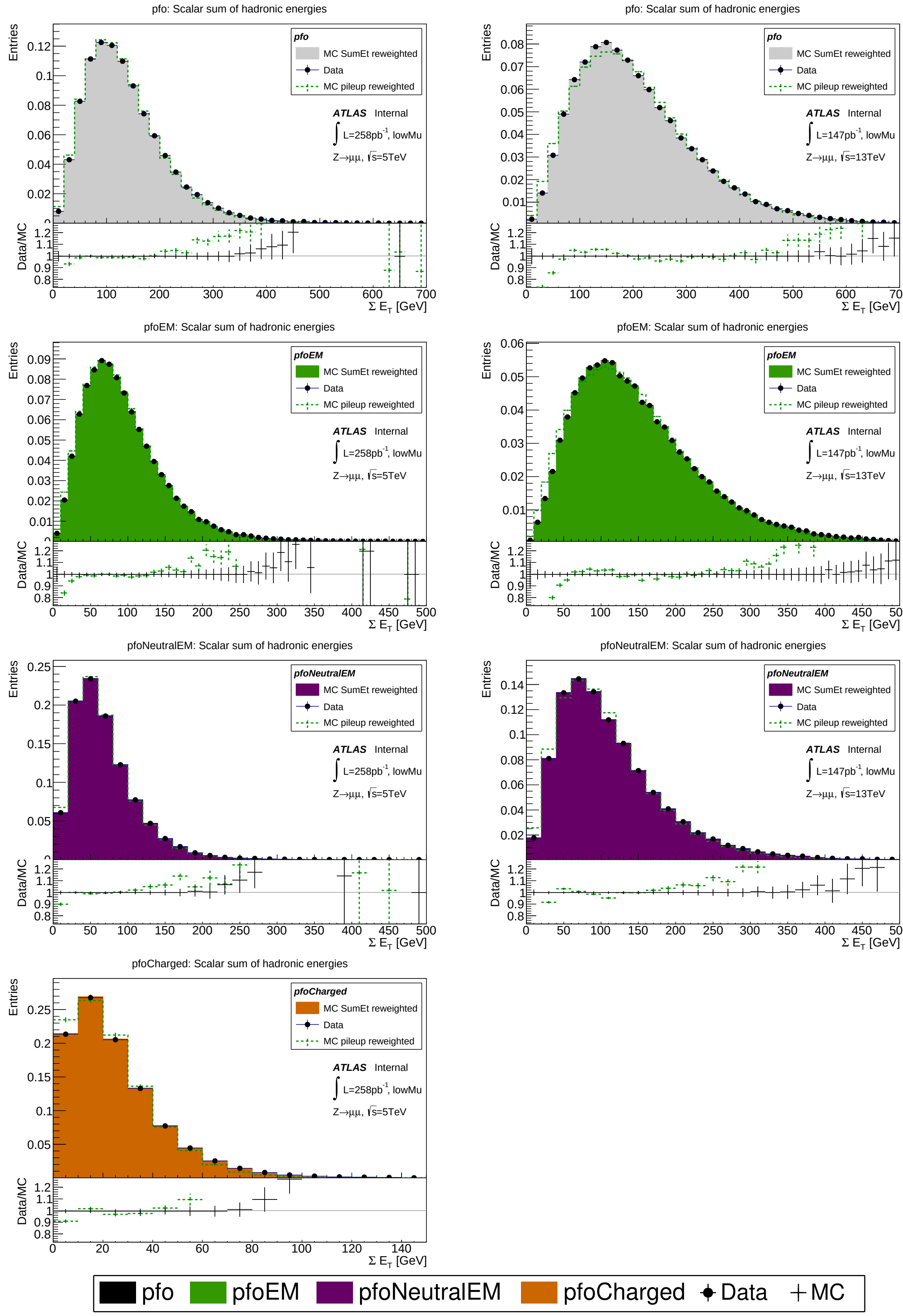

Figure 6.15.: ΣE_T distributions with the pileup and ΣE_T reweightings applied for the different algorithms (see legend below for the color coding) of the *lowMu* analysis. In addition, the distributions with only the pileup weights applied are shown alongside (green dashed line).

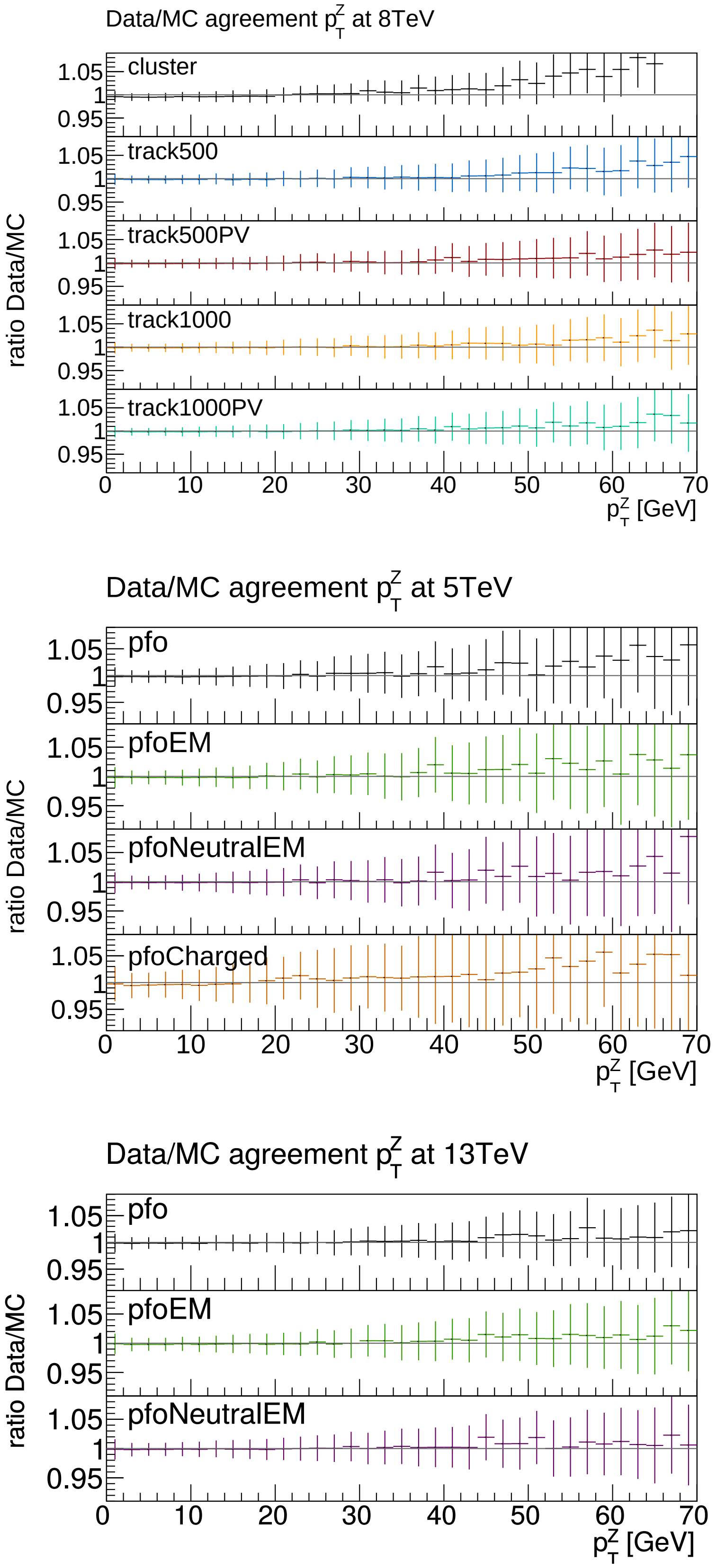

Figure 6.16.: Data to Monte Carlo agreement after the ΣE_T and pileup reweighting are applied to the simulations as a function of the transverse boson momentum $p_T^{boson}(reco)$ for the 8 TeV analysis as well as for the muon channels of the *lowMu* analysis.

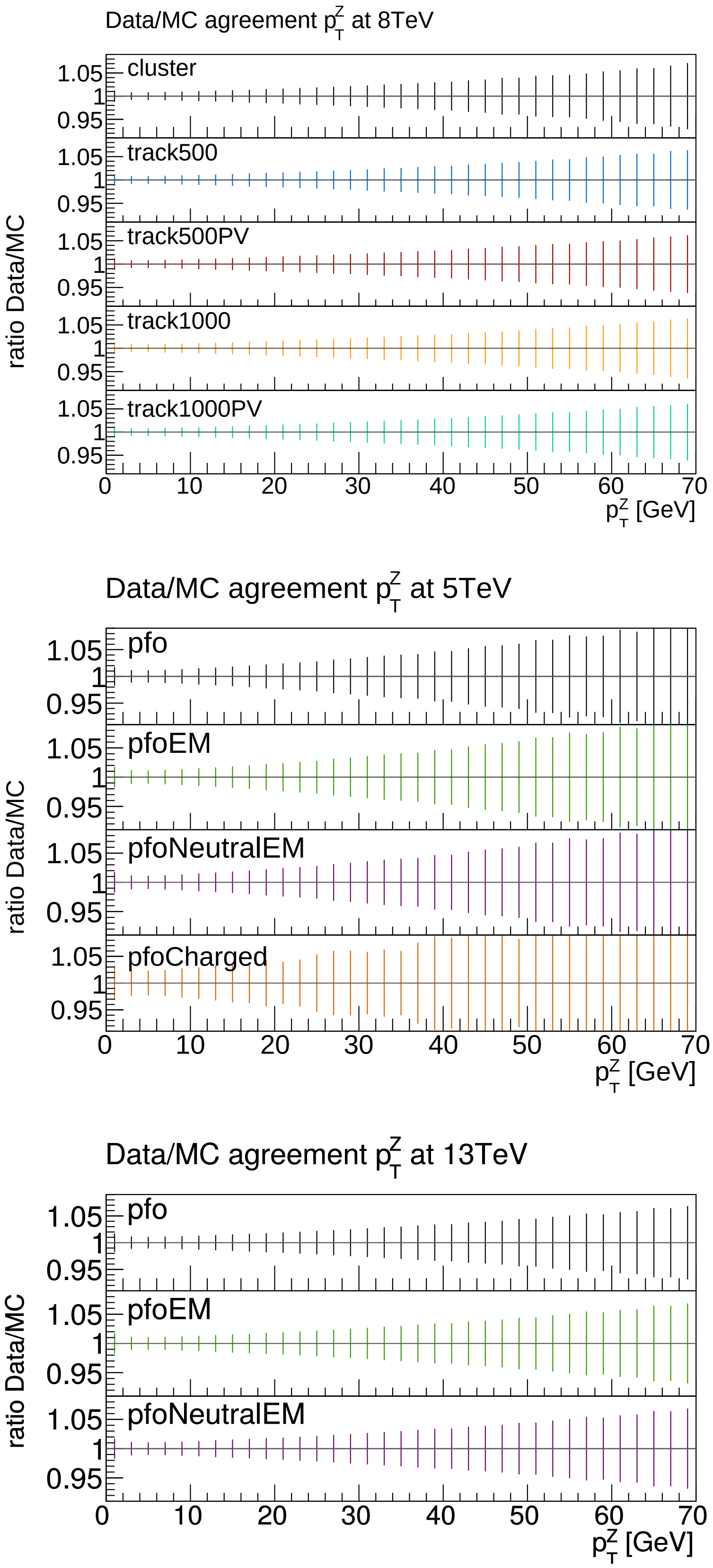

Figure 6.17.: Data to Monte Carlo agreement after the ΣE_T and pileup reweighting as well as a boson $p_T^{boson}(reco)$ reweighting are applied to the simulations as a function of the transverse boson momentum $p_T^{boson}(reco)$ for the 8 TeV analysis as well as for the muon channels of the *lowMu* analysis.

vertex cut and showed large improvements there. TrackPV algorithms showed only small improvements by this approach.

Applying this reweighting approach to the two *lowMu* datasets might be counter intuitive, since the pileup influence is supposed to be largely removed by the run configurations for these datasets. However, it its not the absolute number of simultaneous interactions but rather the width of a distribution thereof, which influence the goodness of the effect. Both *lowMu* analyses offered a wide enough base for a reliable $\langle \Sigma E_T \rangle$ fit and the effect of the reweighting was found to be well for the standard pfo algorithms. The different binning approach of 13 TeV analysis showed that the effect is strongly dependent on the exact shape of the distribution and that less ideal starting conditions can already remove the effectiveness of this approach. A fine tuning for each dataset is therefore necessary.

The ΣE_T event weights could remove the remaining differences in the ΣE_T distributions. Discrepancies in the tails remained for the 8 TeV and the 5 TeV analysis, where the reweighting also introduced a small mismodeling of the transverse boson momentum distribution, which was again corrected for afterwards. The 13 TeV analysis was however found to be stable.

6.10. Resolution scaling technique

The final steps of the reweighting approach focus on the mismodeling in the parallel and perpendicular hadronic recoil components due to a different resolution and a different bias.

The resolution of the hadronic recoil components depend on the resolution of the individual tracks and clusters included in the recoil calculation. The measured resolution in the simulations differs inevitably from the real detector conditions. In addition, the pileup event weights had a small effect on the resolution, especially for the perpendicular hadronic recoil. It is therefore necessary to adjust the resolution in both components. This can be done by scaling the recoil vector in each event. It is advisable to handle the parallel and the perpendicular component separately, since the disagreement is not necessarily identical here. For the resolution of the parallel component the bias, i.e. $\langle HR_{para} + p_T^{boson}(reco) \rangle$, is used. Because of the strong dependence of the resolution on the transverse boson momentum the scaling should be performed as a function of $p_T^{boson}(reco)$.

The resolution is determined by a Gaussian fit in the central region, which is defined within the limits mean $\pm 2.5 \cdot$ RMS. The mean and RMS are determined over the full $p_T(Z)$ range. The fit is performed in slices of $p_T^{boson}(reco)$, which are non-linearly defined to give comparable statistics in each bin. The resolution is compared in data and simulations and scale factors are computed by the ratio of the two values. Fig. 6.18 shows the fit results as well as the resulting scale factors $\alpha^{res} = \frac{\sigma_{Data}}{\sigma_{MC}}$ for the parallel and perpendicular fit for the cluster algorithm. Here, the scale factors are found to correct for a disagreement of the order of a few percent. See Appendix G.6 for the full set of scale factors for all datasets and algorithms.

The scale factors are applied to the simulation in a next step. The perpendicular resolution is scaled for each event by recalculating the value of the perpendicular hadronic recoil:

$$HR_{perp}^{res} = \alpha_{perp}^{res} \cdot HR_{perp}.$$

Since the parallel resolution is not distributed around a mean of zero, the scaling is done by adjusting the deviation of the sum of the parallel hadronic recoil and the transverse boson

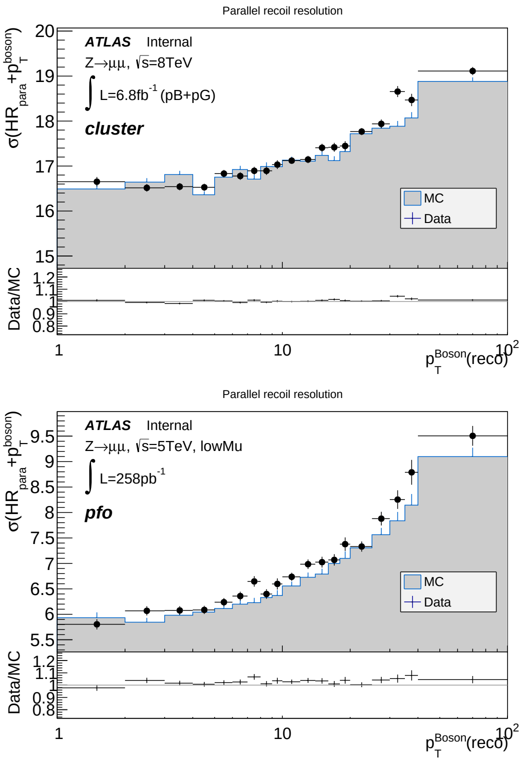

Figure 6.18.: Parallel and perpendicular resolution obtained in Gaussian fits within 2.5 · RMS around the mean for the cluster algorithm in the 8 TeV analysis and the pfo algorithm of the 5 TeV $Z \to \mu\mu$ *lowMu* analysis. The bottom pad of each plot shows the corresponding scale factors α_{res} in the ratio of data and MC.

momentum in each event from the average sum, calculated for a given $p_T^{boson}(reco)$ bin:

$$HR^{res}_{par} + p_T^{boson} - \langle HR_{par} + p_T^{boson} \rangle = \alpha^{res}_{par} \cdot (HR_{par} + p_T^{boson} - \langle HR_{par} + p_T^{boson} \rangle).$$

This can be rewritten to:

$$HR^{res}_{par} = \alpha^{res}_{par} \cdot (HR_{par} + p_T^{boson} - \langle HR_{par} + p_T^{boson} \rangle) - p_T^{boson} + \langle HR_{par} + p_T^{boson} \rangle.$$

With the two scaled components, a scaled hadronic recoil vector is formed. Since the scale factors are not necessarily identical for the parallel and perpendicular component, the direction of the recoil vector is slightly corrected.

The results of the resolution scaling will be discussed after the bias correction has been introduced.

6.11. Bias correction

In addition to a slightly different resolution, the bias $\langle HR_{para} + p_T^{boson}(reco) \rangle$ is also not identically modeled in the simulations. Small deviations, usually less than one GeV, are visible in the mean value of the bias in data and the simulations. This effect was clearly visible in top left plot of Fig. 5.7 for the 8 TeV analysis. The energy scaling corrected for the

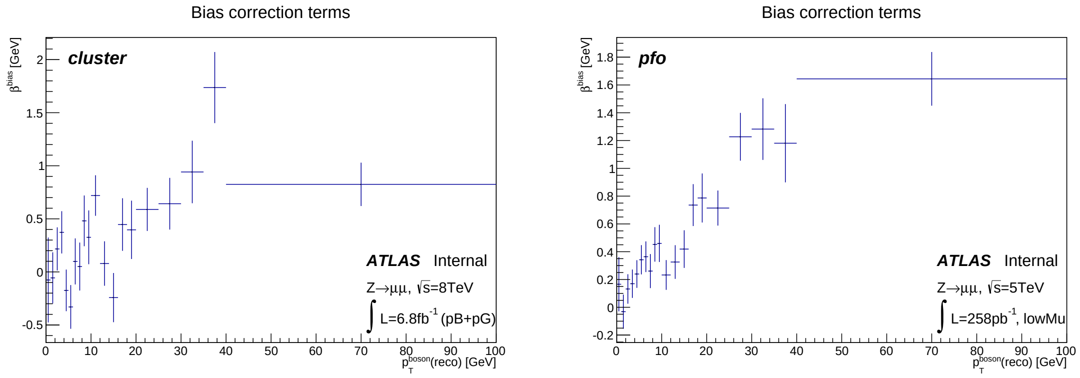

Figure 6.19.: Correction terms for the bias correction for the cluster algorithm in the 8 TeV analysis and the pfo algorithm of the 5 TeV $Z \to \mu\mu$ *lowMu* analysis.

response of the parallel hadronic recoil to the transverse momentum and the bias reached a plateau with the scaling applied. The difference between data and the simulations in bins of $p_T^{boson}(reco)$ is now corrected for by this bias correction.

A set of correction terms $\beta^{bias} = \langle HR_{para} + p_T^{boson}(reco)\rangle_{Data} - \langle HR_{para} + p_T^{boson}(reco)\rangle_{MC}$ is generated as a function of the transverse boson momentum and applied to the parallel hadronic recoil component:

$$HR_{par}^{biasCorr} = HR_{par} + \beta^{bias}$$

The resulting set of correction terms for the 8 TeV analysis is shown for the cluster algorithm of the 8 TeV analysis and for the pfo algorithm of the 5 TeV *lowMu* analysis in Fig. 6.19. The full set of correction terms can be found in Appendix G.7.

6.12. Results for the full reweighting and resolution scaling

6.12.1. Hadronic recoil distributions for the 8 TeV analysis

The effect of the pileup and ΣE_T reweighting as well as of the resolution scaling and bias correction of the hadronic recoil vector will be discussed in this section. Since the first two reweightings, on pileup and ΣE_T, showed almost no effect for the hadronic recoil components, the changes observed here are largely due to the resolution scaling and bias correction.

Parallel hadronic recoil component The parallel hadronic recoil component is shown in Fig. 6.20 for the different algorithms of the 8 TeV analysis. The agreement of data and simulation is best for the cluster algorithm after the reweighting is applied, the ratio of data and MC is in full agreement with unity. In the tails, statistical fluctuations become slightly larger.

The track algorithms show a less flat agreement between data and the simulations for the parallel hadronic recoil component. The track500 algorithm calculation is improved with the full reweighting applied, although the simulations still do not model the data perfectly,

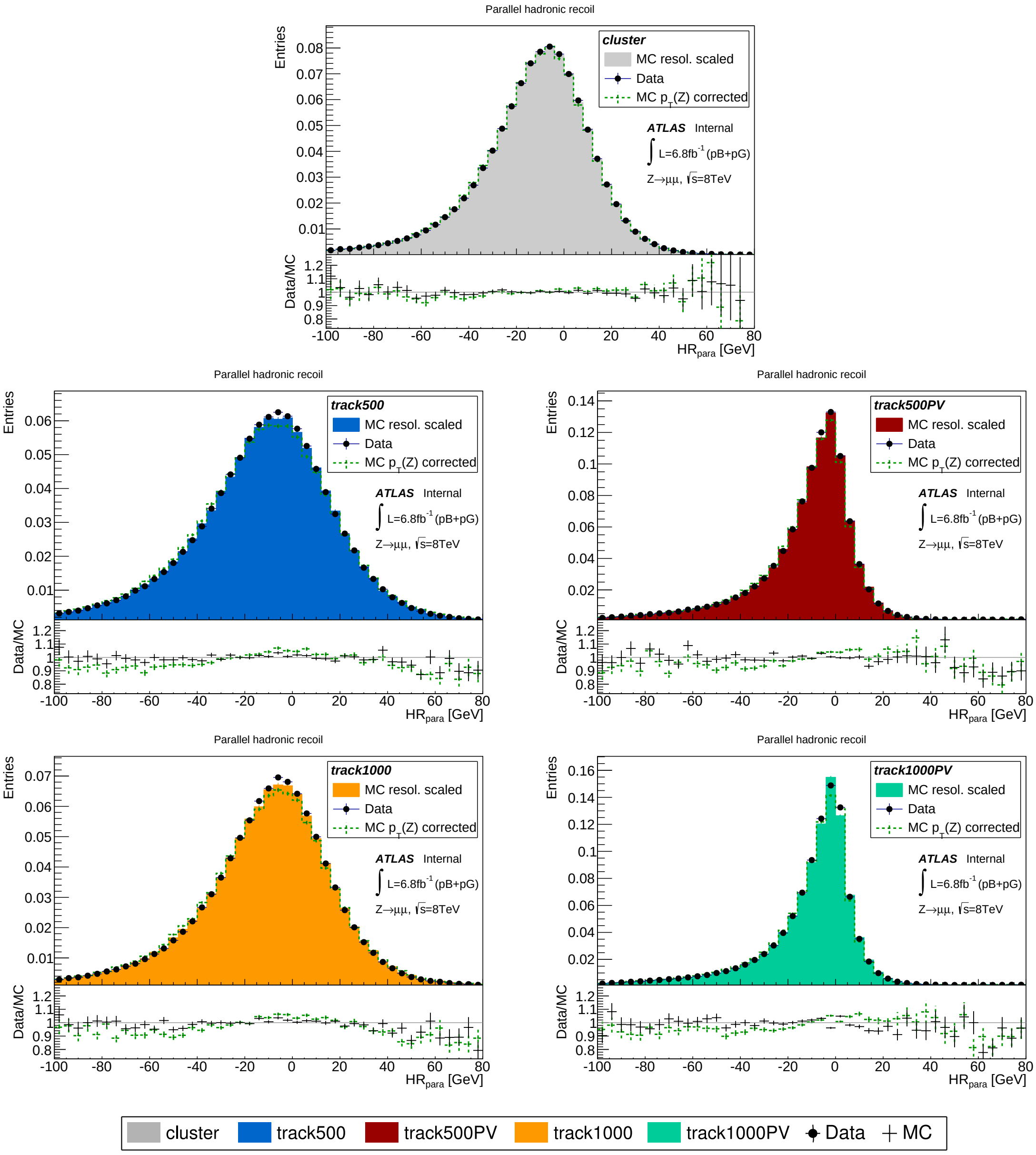

Figure 6.20.: Parallel hadronic recoil distributions with the reweighting and scaling techniques applied to the Monte Carlo simulations for various algorithms (see legend below for the color coding) of the 8 TeV analysis. Also shown are the MC distributions (dashed green) with only the previous reweighting steps applied, i.e. pileup and ΣE_T weights as well as renewed transverse boson momentum weights.

especially in the tail with positive values. The reweighting and resolution scaling applied to the parallel recoil calculated by the track500PV algorithm gives an improvement in the ratio of data and MC. Especially the central region with most events is modeled well. Also here, the tail with positive values shows unchanged fluctuations.

The track1000 algorithm seems to be not altered much by the full reweighting. Here, the small difference between simulations and data cannot be described by a simple Gaussian distribution only, which is the basis for the resolution scale factors. But it should be noted that the unweighted distribution in the simulations did not deviate much from the data distribution in the first place.

The distribution for the track1000PV algorithms after the scaling was applied deviates from the unweighted distribution. The data/MC ratio in the negative tails shows a better agreement with unity, while the disagreement was increased for the positive tails. A real effect cannot be found for this algorithm.

The bias $HR_{par} + p_T^{boson}(reco)$ distributions are shown in Fig. 6.21. The effect of the bias correction will be largest here.

For the cluster algorithm a good agreement over the full range is also visible. The combination of the resolution scaling with the bias corrections resulted in a flat ratio of data and MC. This can be seen from the fact that the unweighted ratio followed an asymmetric curve, the negative tail showed a larger disagreement than the positive tail. The scaling adjusts the resolution symmetrically but cannot adapt asymmetries in the tails. The bias correction however added this effect. With both, a flat agreement is achieved.

The agreement of the track algorithms is in general almost identical to the observed agreement for the parallel component without the added transverse momentum. A more detailed comparison of the mean and resolution plots is available in Fig. 6.22. The left column shows the mean bias distributions as a function of the transverse boson momentum, ΣE_T and pileup. Before the reweighting, a disagreement of the bias $\langle HR_{par} + p_T^{boson}(reco)\rangle$ between data and simulation as a function of the transverse boson momentum was clearly visible (see again Fig. 5.7 for the unweighted distributions). This disagreement is now mostly removed by the bias correction. Thus, it is valid to use a bias correction as introduced here.

The distributions for the bias as a function of the other quantities, ΣE_T and pileup, shows improvements in the ratio compared to the unweighted distributions, but fluctuations are still visible. This is not unexpected, since the bias modeling was not performed with respect to these quantities. However, an improvement is clearly visible, especially as a function of pileup .

The agreement between the resolution, shown in the right column, of data and the simulations is significantly improved when the full reweighting is applied. For the $p_T(Z)$ dependency (top right plot) the improvement is largest for the pileup sensitive algorithms cluster and track500. The ratio of the resolution is well in agreement with unity here. Since the scaling was performed in bins of $p_T(Z)$, the functionality of the approach is validated by this plot.

The resolution as a function of ΣE_T (central right plot) is also modeled well by the simulations. The ratio of data to MC is found to be agreeing with unity withing the uncertainties for the relevant ranges where most events are found. Fluctuations but no trends are observed in the tails.

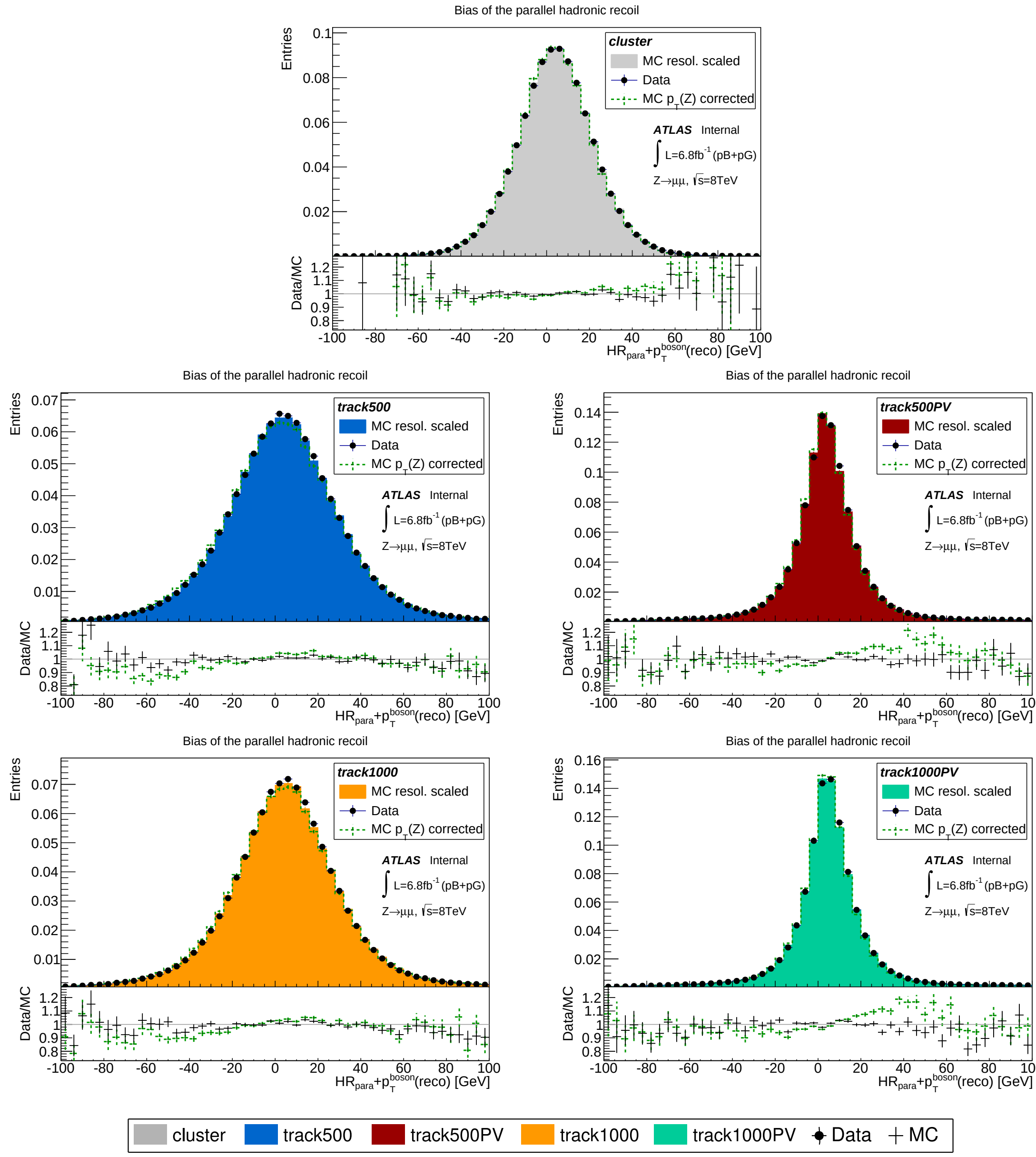

Figure 6.21.: Bias of the parallel hadronic recoil distributions with the reweighting and scaling techniques applied to the Monte Carlo simulations for various algorithms (see legend below for the color coding) of the 8 TeV analysis. Also shown are the MC distributions (dashed green) with only the previous reweighting steps applied, i.e. pileup and ΣE_T weights as well as renewed transverse boson momentum weights.

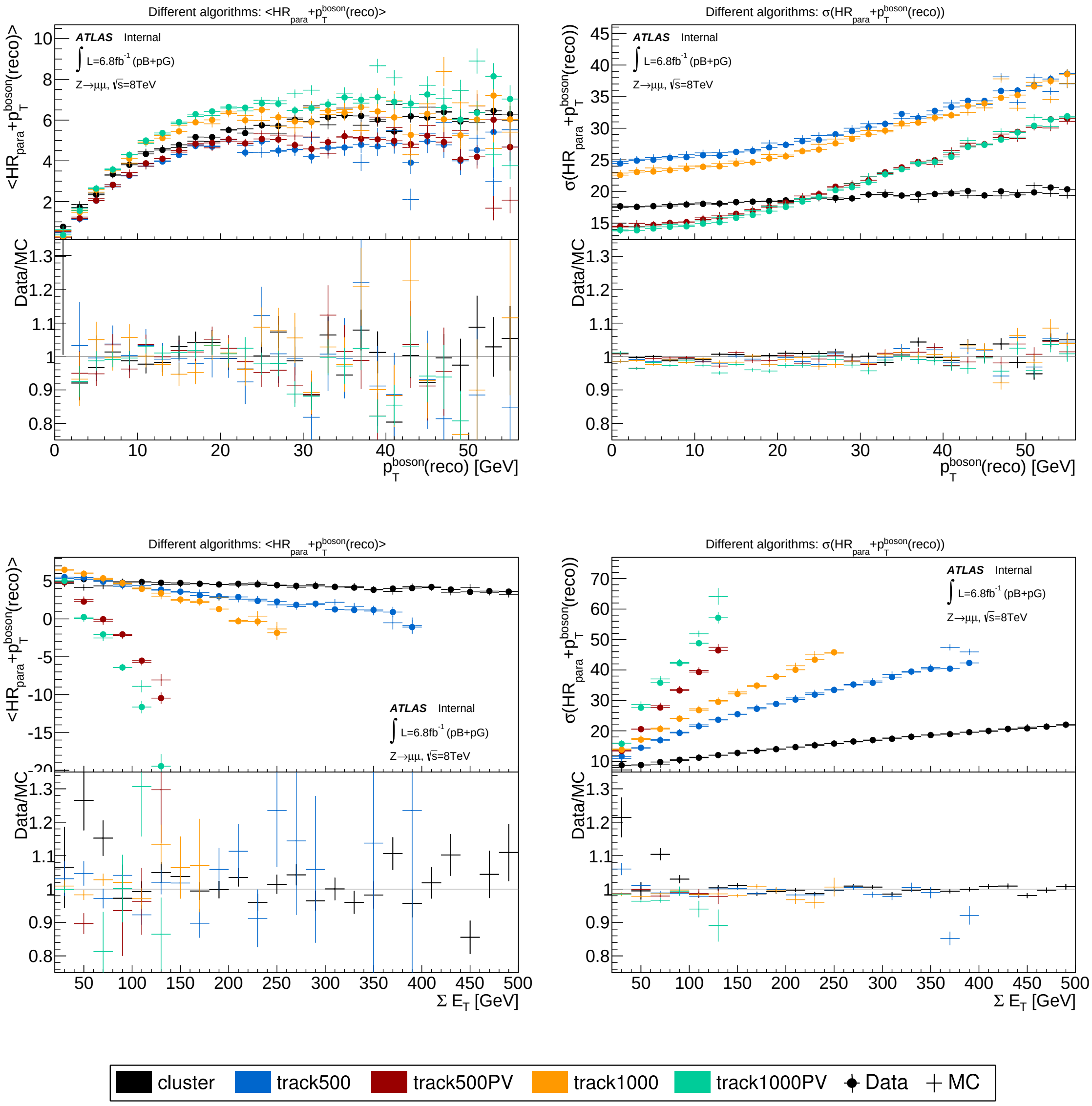

Figure 6.22.: Several mean and sigma distributions for the bias $HR_{par} + p_T^{boson}(reco)$ of the parallel hadronic recoil component for the 8 TeV analysis. The distributions are shown for the different algorithms (see legend below for the color coding) with the full reweighting applied.

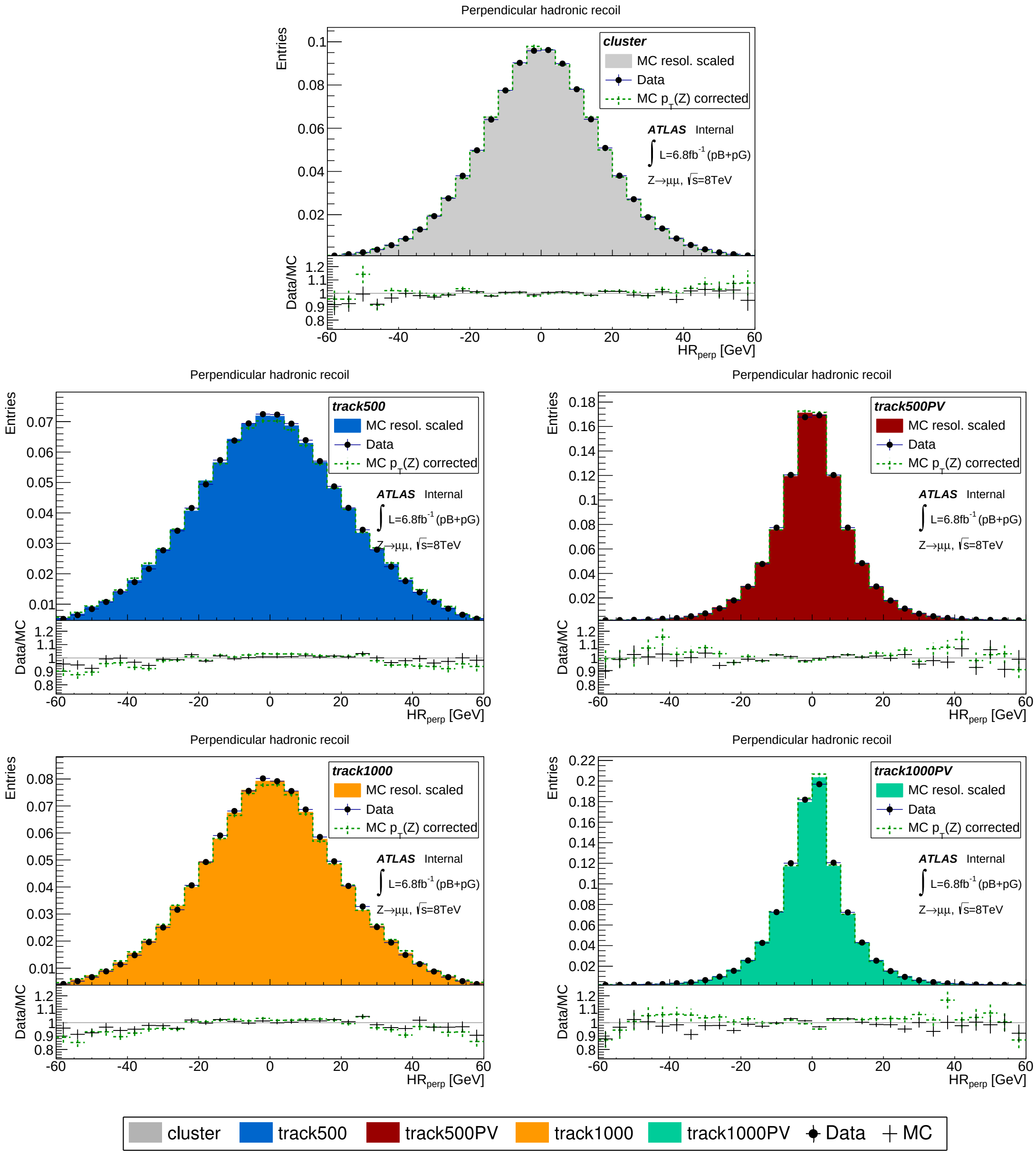

Figure 6.23.: Perpendicular hadronic recoil distributions with the reweighting and scaling techniques applied to the Monte Carlo simulations for the various algorithms (see legend below for the color coding) for the 8 TeV analysis. Also shown are the MC distributions (dashed green) with only the previous reweighting steps applied, i.e. pileup and ΣE_T weights as well as renewed transverse boson momentum weights.

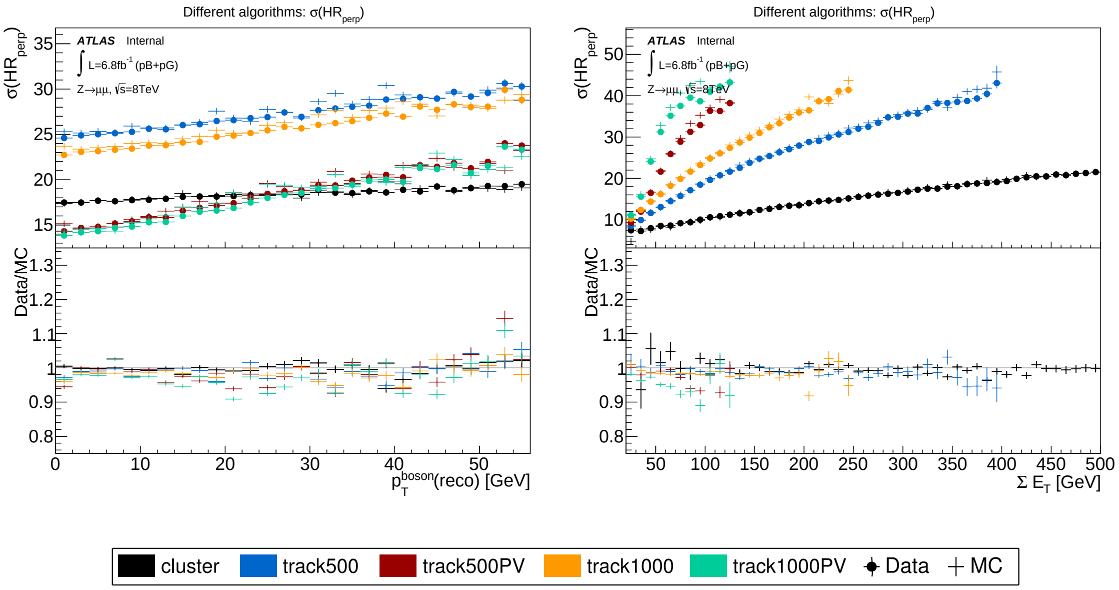

Figure 6.24.: Distributions of the resolution of the perpendicular hadronic recoil component for the 8 TeV analysis. The distributions are shown for the different algorithms (see legend below for the color coding) with the full reweighting applied. Also shown are the MC distributions (dashed green) with only the previous reweighting steps applied, i.e. pileup and ΣE_T weights as well as renewed transverse boson momentum weights.

Perpendicular hadronic recoil component When looking at the effect of the full reweighting on the perpendicular component (see Fig. 6.23), the largest improvement is again registered for the cluster algorithm. The MC/data ratio is almost flat after the reweighting and found to be compatible with unity within the uncertainties. The tails show deviations of up to a few percent.

The perpendicular resolution of the track500 algorithm is improved as well and also showing an agreement close to unity over the full range of the distribution. The reweighting and scaling caused almost no effect for the track500PV algorithm implementation. The agreement was already good before. The same is true for the track1000 algorithm. The reweighting altered small mismodelings to be in agreement afterwards, visible in the central region. The agreement in the tails is slightly reduced however. Track1000PV showed a differing resolution in the unweighted ratio, which was partially removed by the reweighting. Compared to the other algorithms, larger fluctuations are still visible.

A detailed analysis of the behavior of the perpendicular resolution as a function of $p_T(Z)$, ΣE_T and pileup is given in Fig. 6.24. The same effects as observed for the parallel resolution are again visible here: The ratio of data and MC is agreeing with unity for most of the visible range. Fluctuations are observed in the tails with low statistics.

The magnitude of the hadronic recoil vector, $|HR|$, is a measure for the combined effect of the parallel and perpendicular resolution scaling. When only the ΣE_T reweighting was applied no large effect on $|HR|$ were observed, except for the change in resolution for the two components. The results for the full reweighting are indicated in Fig. 6.25. With the scaling and bias correction applied, the agreement between data and simulation is improved for the cluster and the two track500(PV) algorithms. Track500 stills shows a linear trend

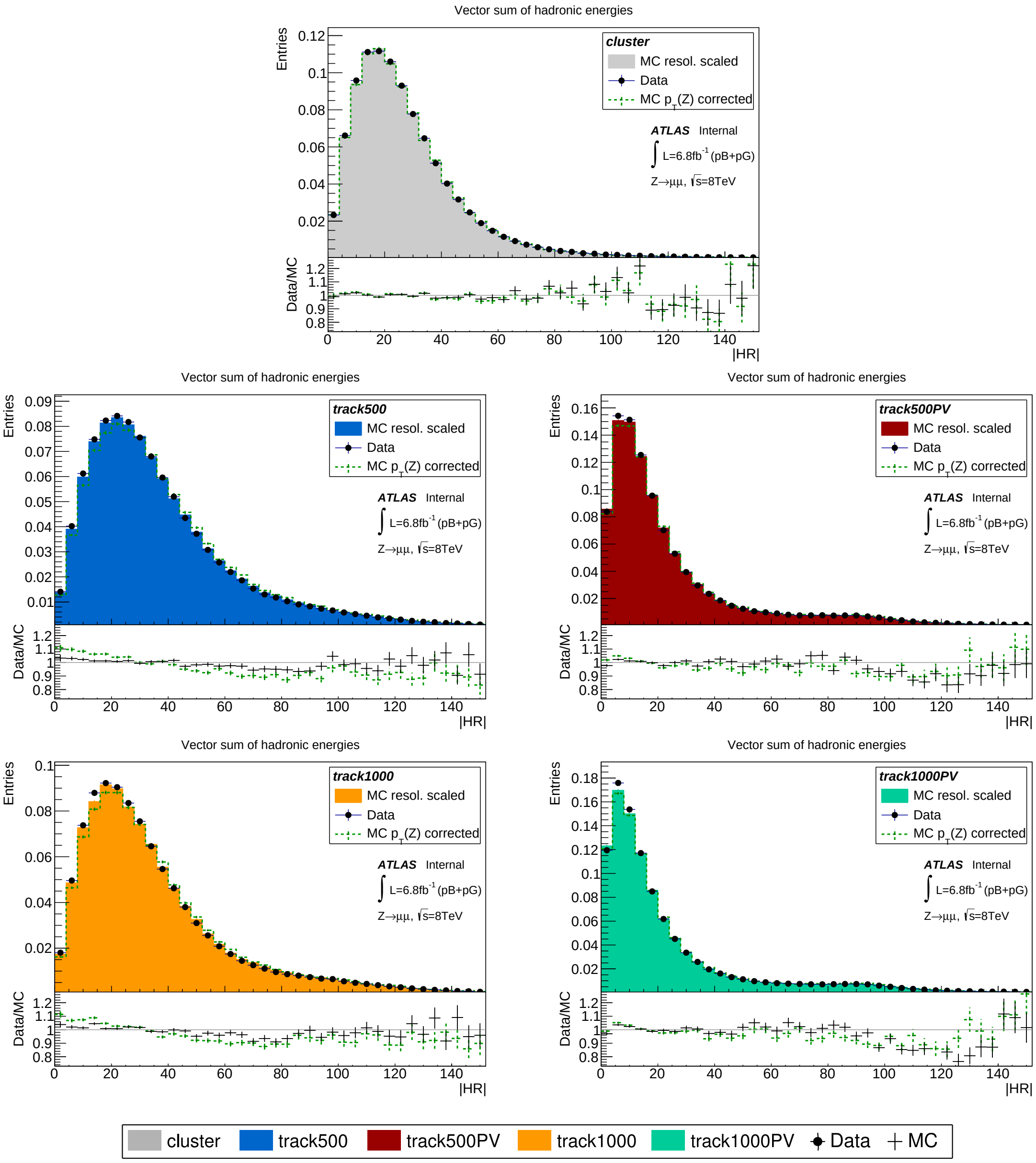

Figure 6.25.: Distribution of the magnitude of the hadronic recoil vector with the reweighting and scaling techniques applied to the Monte Carlo simulations for the various algorithms (see legend below for the color coding) of the 8 TeV analysis. Also shown are the MC distributions (dashed green) with only the previous reweighting steps applied, i.e. pileup and ΣE_T weights as well as renewed transverse boson momentum weights.

in the ratio data/MC. The track1000 and track1000PV algorithms show small changes, but the ratio of data and MC was already acceptably good before the reweighting for these two algorithms.

6.12.2. Hadronic recoil distributions for the *lowMu* analyses

The same reweighting and resolution scaling procedure is applied to the data of the two *lowMu* datasets. The results of the full reweighting on the parallel hadronic recoil is given in Fig. 6.26 for the muon channel of the 5 TeV (left column) and 13 TeV (right column) analyses. The results for the electron channel are presented in Fig. 6.27 and the corresponding bias distributions are shown in Fig. 6.28 and 6.29

The agreement between the simulations and data for the parallel hadronic recoil component and bias distributions was not much deviating from unity without any reweighting applied. The full reweighting shows small improvements for the ratio data/MC in the 13 TeV dataset (right column), where larger deviations were visible before the reweighting. Generally, an improvement is found for the tail with positive values. Here, larger deviations could be removed by the bias correction. The pfoNeutralEM algorithm, which showed an odd data to MC ratio before the reweighting in the 5 TeV dataset, now shows a good agreement between the simulations and data. A change is also visible for the pfoCharged distribution. However, the changes do not indicate a general improvement.

The results for the electron channel, see Fig. 6.27, confirm the findings for the muon analysis. The small discrepancies in the 13 TeV dataset were reduced by the reweighting. The agreement between data and the simulations is generally compatible with unity and an effect in the positive tails is visible here as well. The pfoCharged algorithms shows and improved ratio of data and MC.

When analyzing the bias distributions (see Fig. 6.28 and 6.29), a good improvement to the ratio is generally visible. Asymmetric differences between the positive and negative tails could mostly be removed, if present. The narrow central region is now modeled well for all algorithms, datasets and lepton channels. Deviations in the tails, especially in ranges with decreasing statistics, can still be observed. The resolution for the *lowMu* datasets is not dominated by pileup like for the 8 TeV datasets. Non-Gaussian effects are much stronger pronounced here. As a consequence, the shape of these distributions cannot be fully described by a Gaussian curve and the resolution cannot be fully adapted by this approach.

The mean and resolution as a function of the transverse boson momentum and ΣE_T is shown in Fig. 6.30 for the muon channel and in Fig. 6.31 for the electron channel. The disagreement in the mean (top row) between data and simulation could be largely removed by the bias correction (For a comparison to the unweighted distributions see again Fig. 5.10). In addition, the agreement of the resolution (central row) has also been improved by the resolution scaling, but is slightly larger than unity for all algorithms. This effect is related to small remaining differences in the resolution between data and the simulations as a function of ΣE_T. When looking at the agreement as a function of $p_T^{boson}(reco)$, a sum over the full ΣE_T range is performed per $p_T^{boson}(reco)$ bin. Disagreements in the ΣE_T dependency add up to a ratio slightly larger than one.

The larger disagreements in the resolution of the bias as a function of ΣE_T (bottom row) could be reduced with the resolution scaling and bias correction applied. However, small

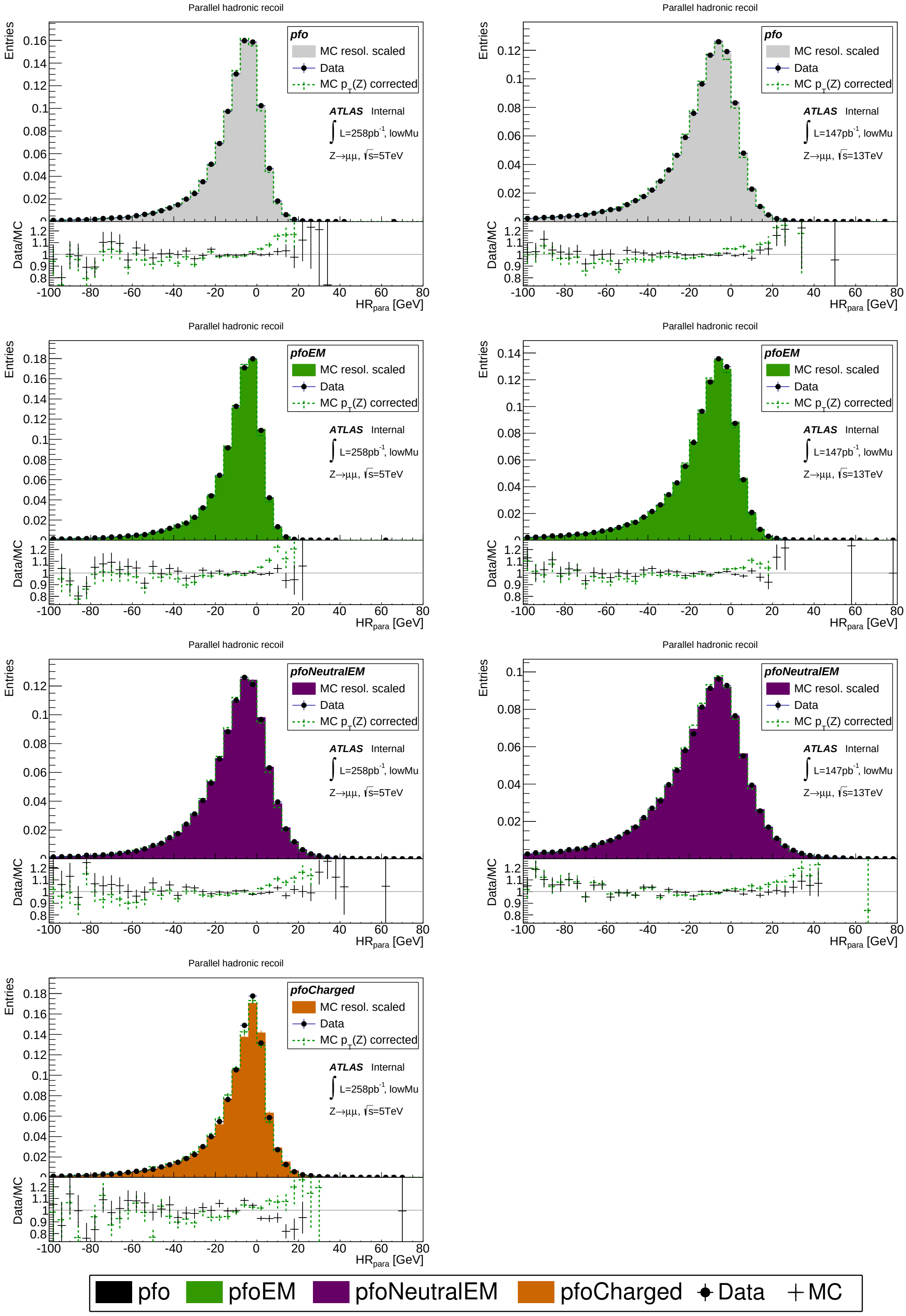

Figure 6.26.: Distributions of the parallel hadronic recoil component for the different algorithms of the 5 TeV and 13 TeV *lowMu* analyses in the muon channel. The full reweighting and resolution scaling has been applied. The left column shows the 5 TeV results, while the right column gives the 13 TeV results. The distribution for the reweighted pfoCharged algorithm are not available for the 13 TeV dataset, because the method could not be applied here.

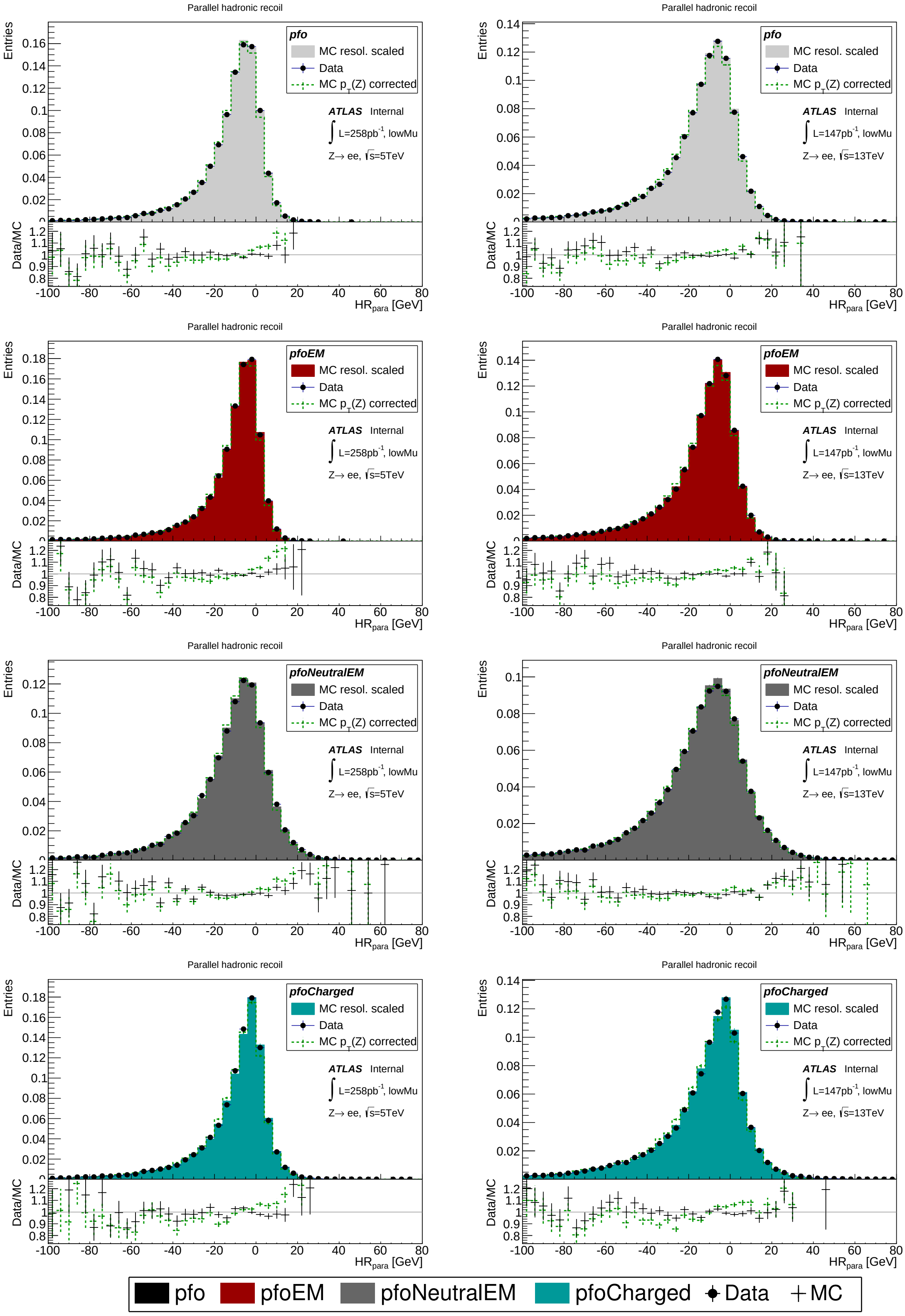

Figure 6.27.: Distributions of the bias for the different algorithms of the 5 TeV and 13 TeV *lowMu* analyses in the muon channel. The full reweighting and resolution scaling has been applied. The left column shows the 5 TeV results, while the right column gives the 13 TeV results. The color coding for the algorithm distinction is again given below.

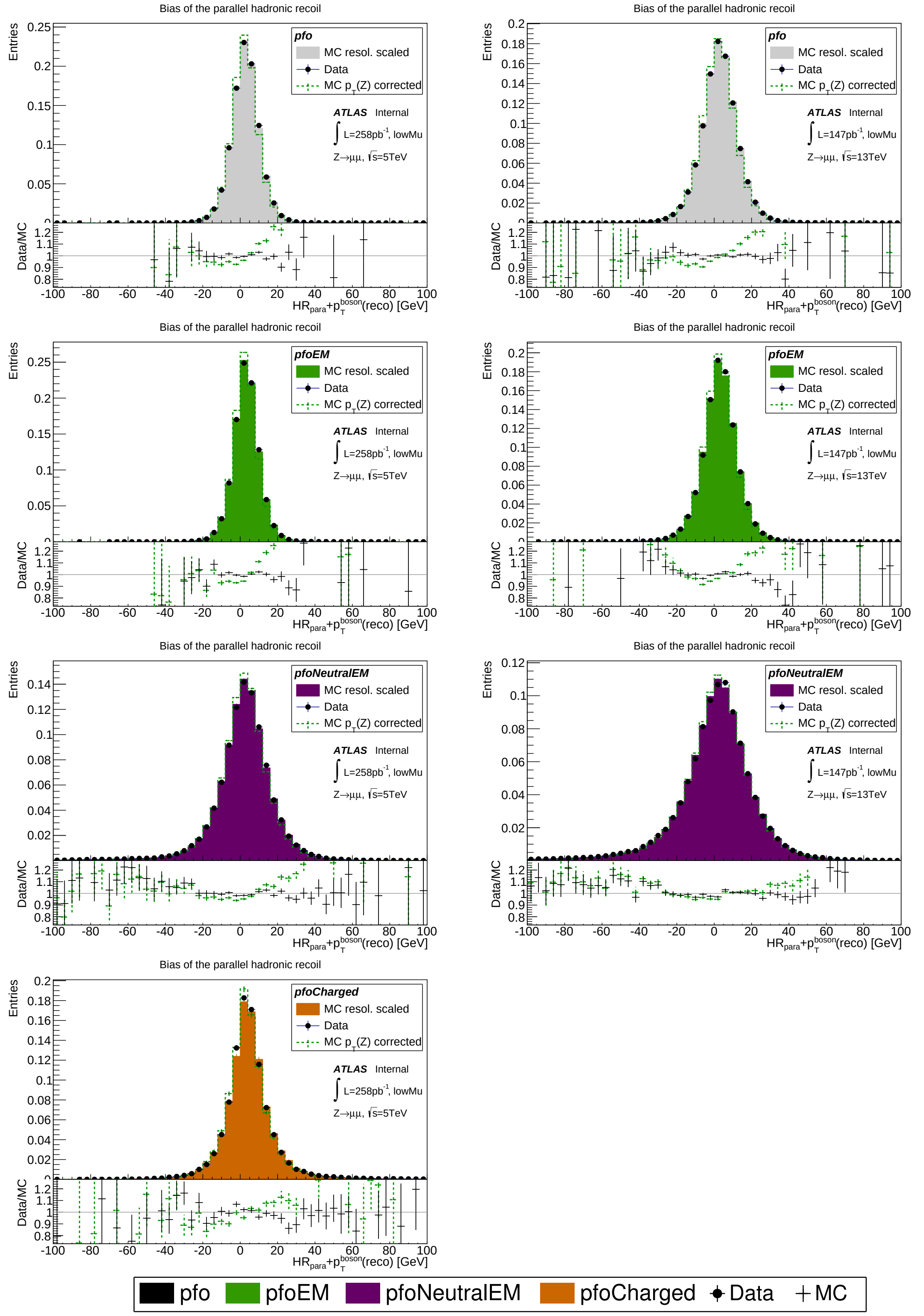

Figure 6.28.: Distributions of the bias for the different algorithms of the 5 TeV and 13 TeV *lowMu* analyses in the muon channel. The full reweighting and resolution scaling has been applied. The left column shows the 5 TeV results, while the right column gives the 13 TeV results. The distribution for the reweighted pfoCharged algorithm are not available for the 13 TeV dataset, because the method could not be applied here.

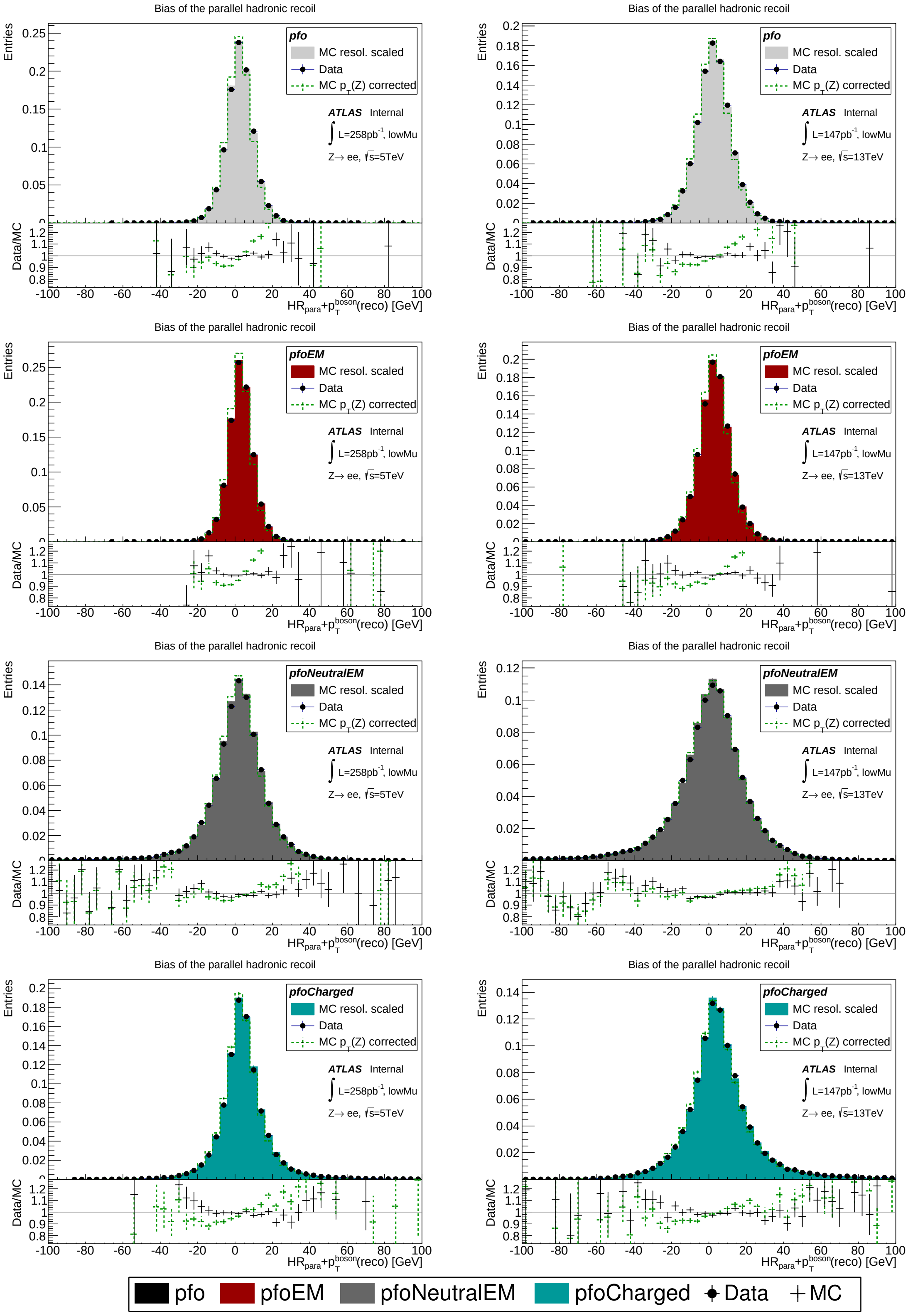

Figure 6.29.: Distributions of the parallel hadronic recoil component for the different algorithms of the 5 TeV and 13 TeV *lowMu* analyses in the electron channel. The full reweighting and resolution scaling has been applied. The left column shows the 5 TeV results, while the right column gives the 13 TeV results. The color coding for the algorithm distinction is again given below.

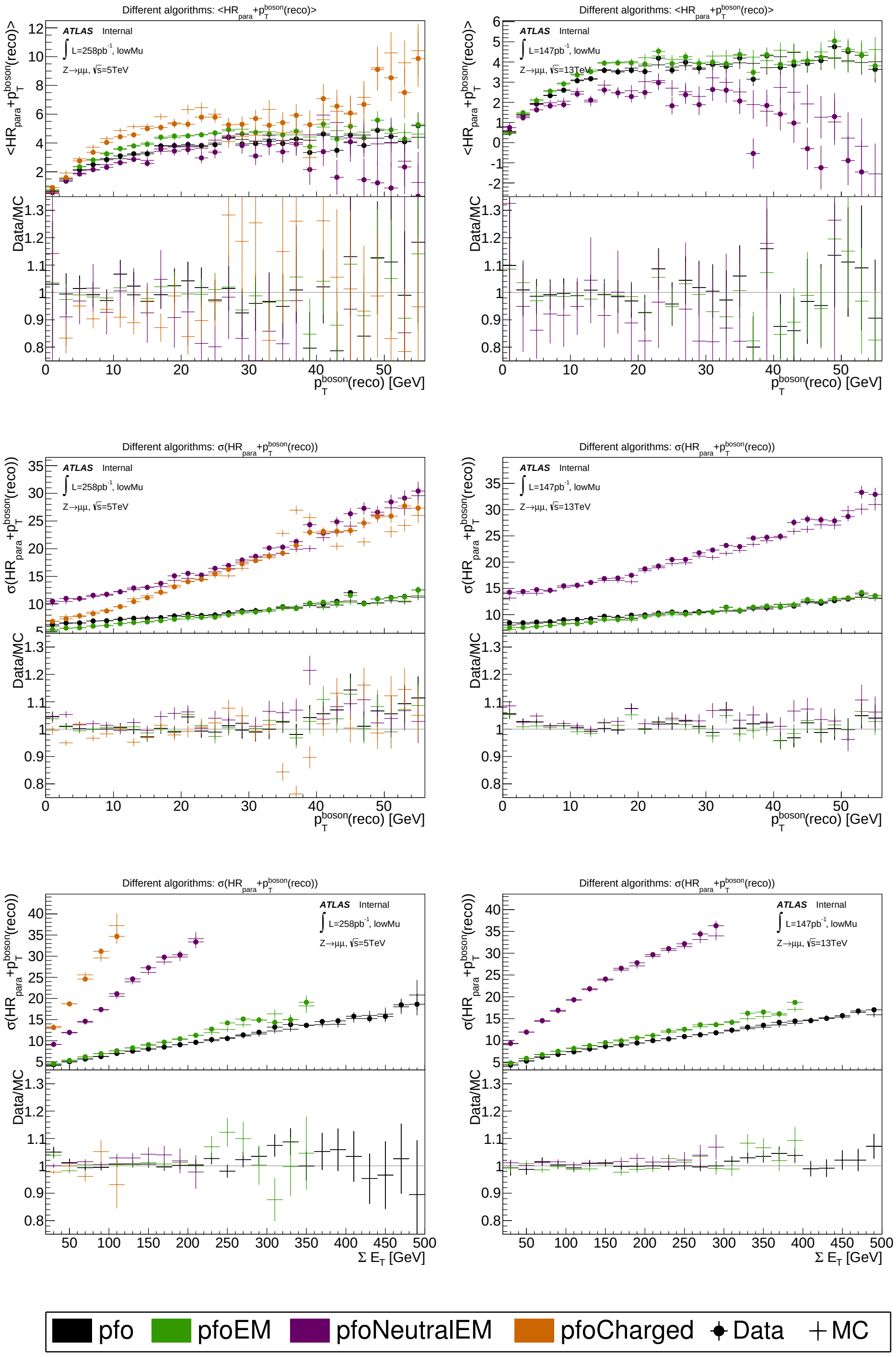

Figure 6.30.: Distributions of the resolution of the sum of the parallel hadronic recoil component and the transverse boson momentum for the muon channel in the 5 TeV and 13 TeV dataset of the *lowMu* analyses. The distributions are shown for the different algorithms with the full reweighting applied (see legend below for the color coding).

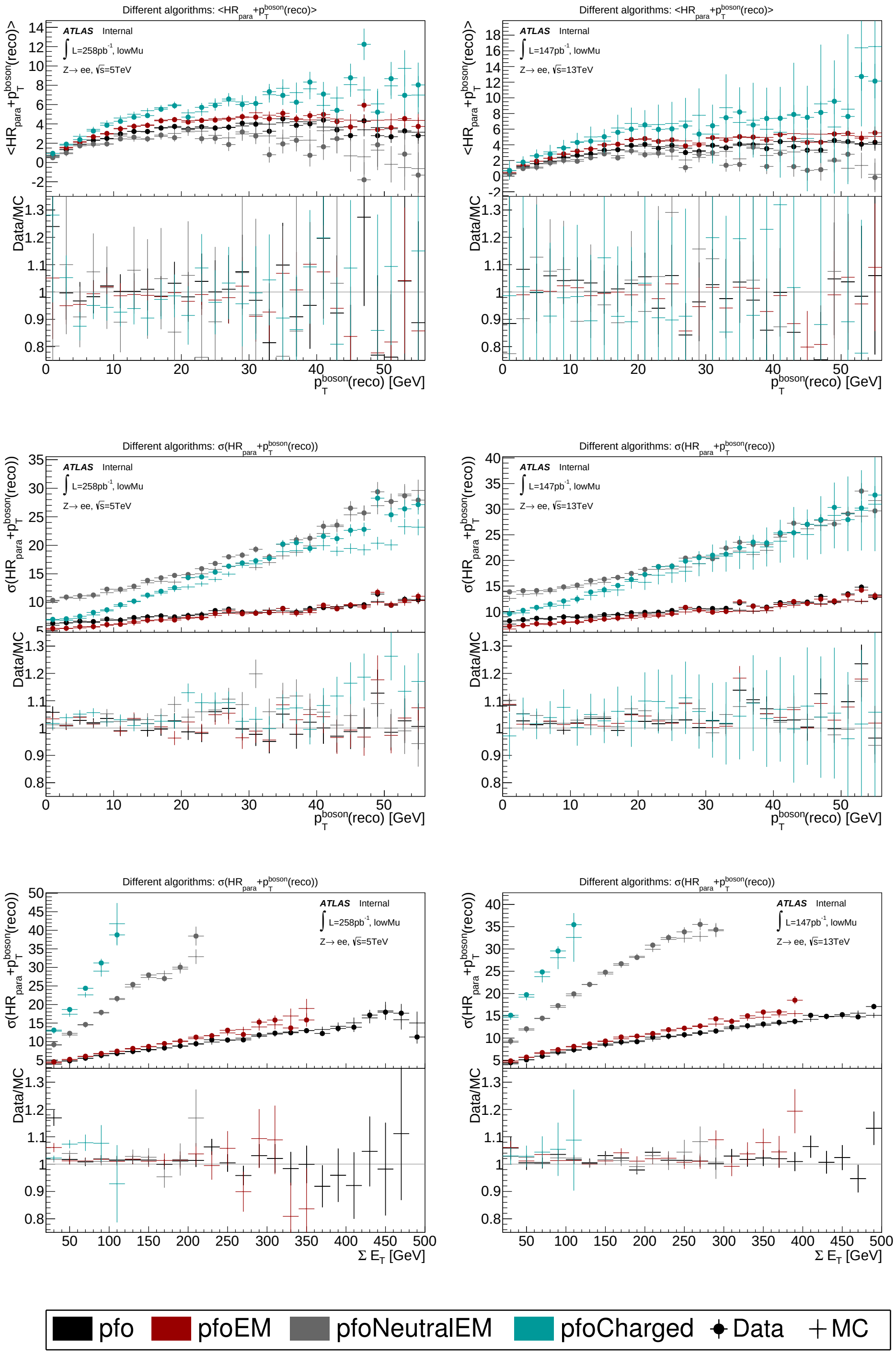

Figure 6.31.: Distributions of the resolution of the sum of the parallel hadronic recoil component and the transverse boson momentum for the electron channel in the 5 TeV and 13 TeV dataset of the *lowMu* analyses. The distributions are shown for the different algorithms with the full reweighting applied (see legend below for the color coding).

disagreements remain, since the scaling was not performed as a function of ΣE_T.

The perpendicular hadronic recoil component shows a good agreement between data and simulations in the central region with the resolution scaling applied (see Fig. 6.26 and 6.27). Likewise, the tails are also not in full agreement here and a Gaussian width cannot describe the resolution of the perpendicular component fully. This behavior is seen in all algorithms in both datasets and also for muons as well as electrons.

The set of plots in Fig. 6.34 and Fig. 6.35 shows the perpendicular resolution as a function of $p_T(Z)$ and ΣE_T for both the muon and the electron analyses in the two datasets. Bin to bin deviations can still be observed here. The resolution was adapted in coarse steps of $p_T(Z)$. The deviations of the smaller stepping visible here cannot be removed by this. The general agreement is however good. For the resolution as a function of ΣE_T it can be seen from the 13 TeV analysis in the $Z \to \mu\mu$ and $Z \to ee$ channel, that the scaled simulated resolution slightly deviates from data as a function of ΣE_T. This dependency is not mapped in the one dimensional scale factors. If the statistics would allow to perform the Gaussian fits as a function of two components, like $p_T^{boson}(reco)$ and ΣE_T, this effect might be removed. However, this is not feasible within the statistical limitations of the current dataset.

6.13. Non-Gaussian tails

The resolution scaling technique applied to the perpendicular hadronic recoil showed good results for the central region. Remaining discrepancies can be observed in the tails. Usually the shape of the resolution only follows a Gaussian function in the central region. Interestingly, the deviation from the central shape is larger in data than observed in the simulations. This section will investigate those differences.

Fig. 6.36 shows the perpendicular hadronic recoil component with the focus on the tails for the cluster algorithm of the 8 TeV analysis and the pfoEM algorithm for the 5 TeV as well as the 13 TeV $Z \to \mu\mu$ analysis as an example. The red line indicates the expected curve for a pure Gaussian distribution.

The effect is larger with a looser set of lepton cuts: Muons are not required to be isolated and the impact parameter cuts are less tight. With this selection, the effect of the tails becomes much more visible. The plots with a looser selection applied are shown in Fig. 6.37. The following analysis is performed with this looser selection.

From the definition of the width σ for a Gaussian distribution follows that around 0.27 % of events are found in the tails outside $\pm 3 \cdot \sigma$. Generally this fraction is increased in data as well as in the simulations. The numbers are shown in Tab. 6.6 for the loose lepton selection. In all datasets it is also found that the tails include more events in data than in the simulations. These two effects are however comparably small for the 8 TeV analysis in contrast to the *lowMu* analyses. The resolution in the 8 TeV analysis is dominated by pileup, resulting in a wide central Gaussian distribution. This probably shadows the effect of the non-Gaussian tails largely.

The 5 TeV analysis shows the largest fraction of events inside the tails. These numbers generally depend on the boundary of the tails, which is determined by the fit of the central region. Small changes here can change the fraction of events in the tail drastically. Since the same boundary is applied to data and simulations, the numbers are at least comparable with each other. In addition to this, the deviation between data and simulation is smaller for the

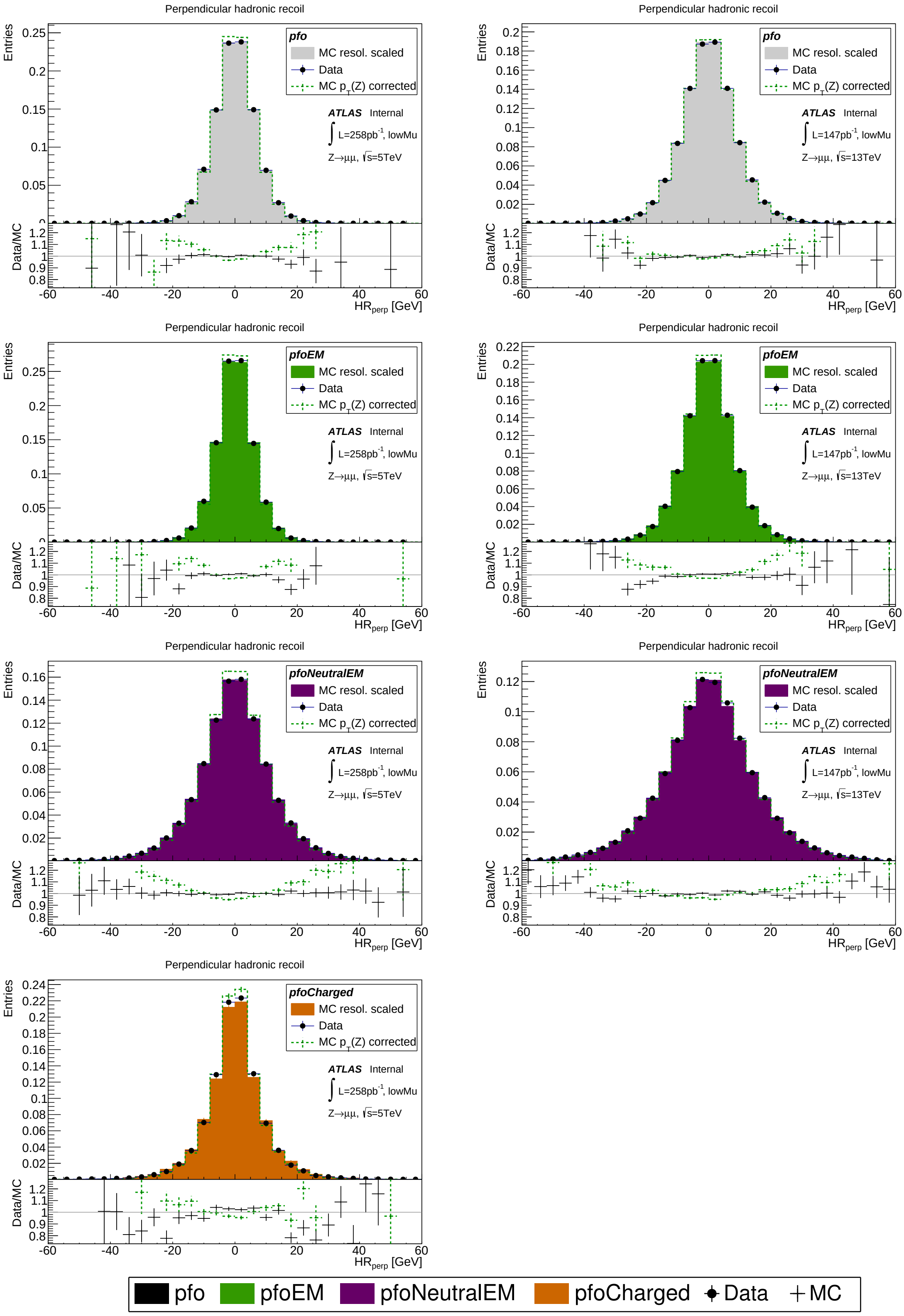

Figure 6.32.: Distributions of the perpendicular hadronic recoil component for the different algorithms of the 5 TeV and 13 TeV *lowMu* analyses in the muon channel. The left column shows the 5 TeV results, while the right column gives the 13 TeV results. The color coding for the algorithm distinction is again given below.

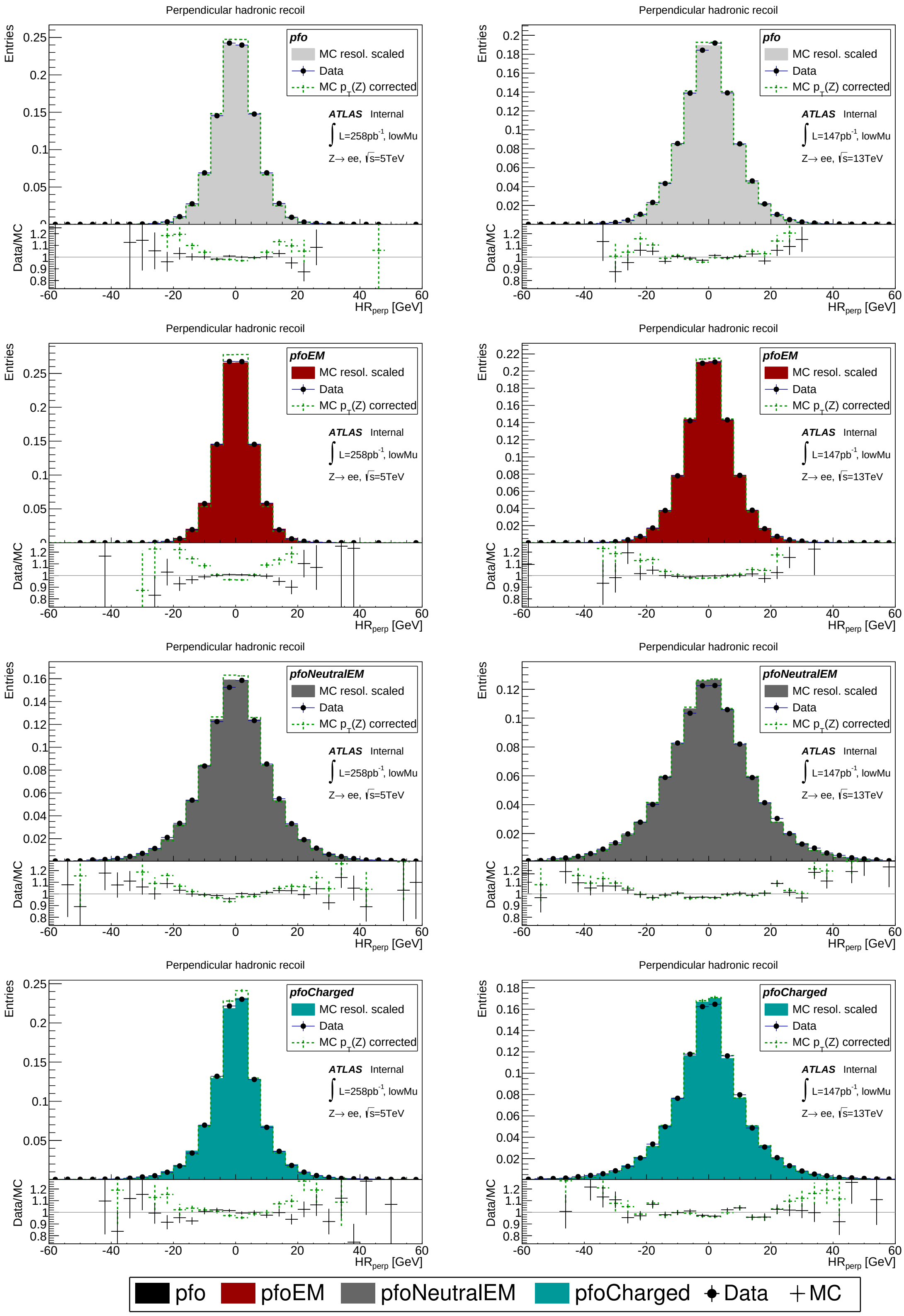

Figure 6.33.: Distributions of the perpendicular hadronic recoil component for the different algorithms of the 5 TeV and 13 TeV *lowMu* analyses in the electron channel. The left column shows the 5 TeV results, while the right column gives the 13 TeV results. The color coding for the algorithm distinction is again given below.

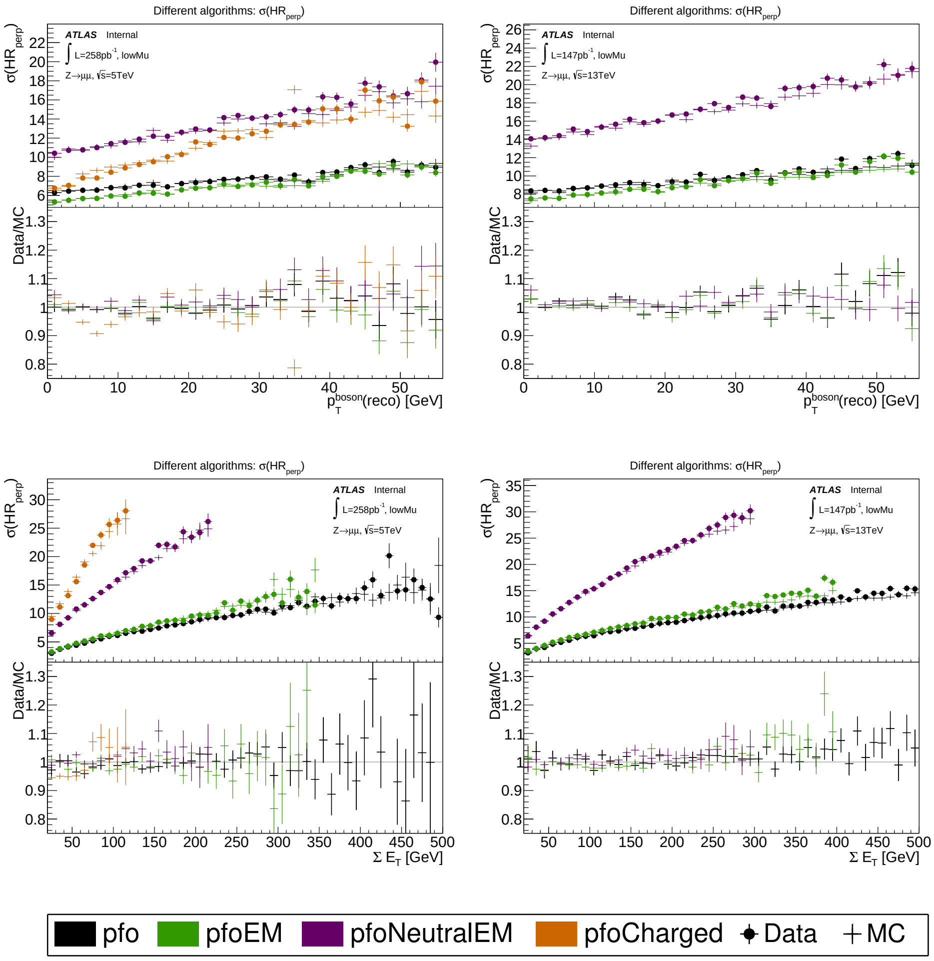

Figure 6.34.: Distributions of the resolution of the perpendicular hadronic recoil component for the muon channel in the 5 TeV and 13 TeV dataset of the *lowMu* analyses. The distributions are shown for the different algorithms (see legend below for the color codings) with the full reweighting applied.

Dataset selection	*Data*	*Simulation*
cluster $Z \to \mu\mu$ 8 TeV	1.13 %	1.05 %
pfoEM $Z \to \mu\mu$ 5 TeV	3.33 %	3.14 %
pfoEM $Z \to \mu\mu$ 13 TeV	2.36 %	1.60 %

Table 6.6.: Event numbers in the tails outside $\pm 3 \cdot \sigma$ of the HR_{perp} distribution for the 8 TeV and for the two *lowMu* $Z \to \mu\mu$ analyses. A loose lepton selection is applied here.

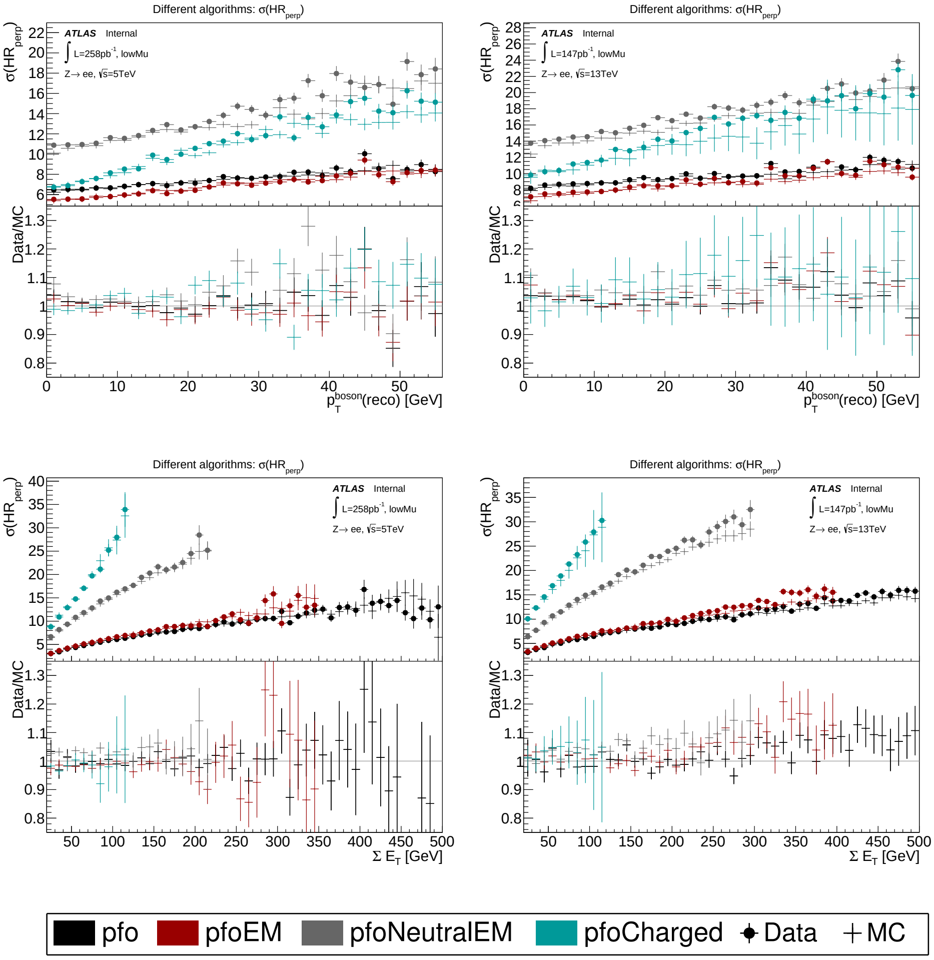

Figure 6.35.: Distributions of the resolution of the perpendicular hadronic recoil component for the electron channel in the 5 TeV and 13 TeV dataset of the *lowMu* analyses. The distributions are shown for the different algorithms (see legend below for the color codings) with the full reweighting applied.

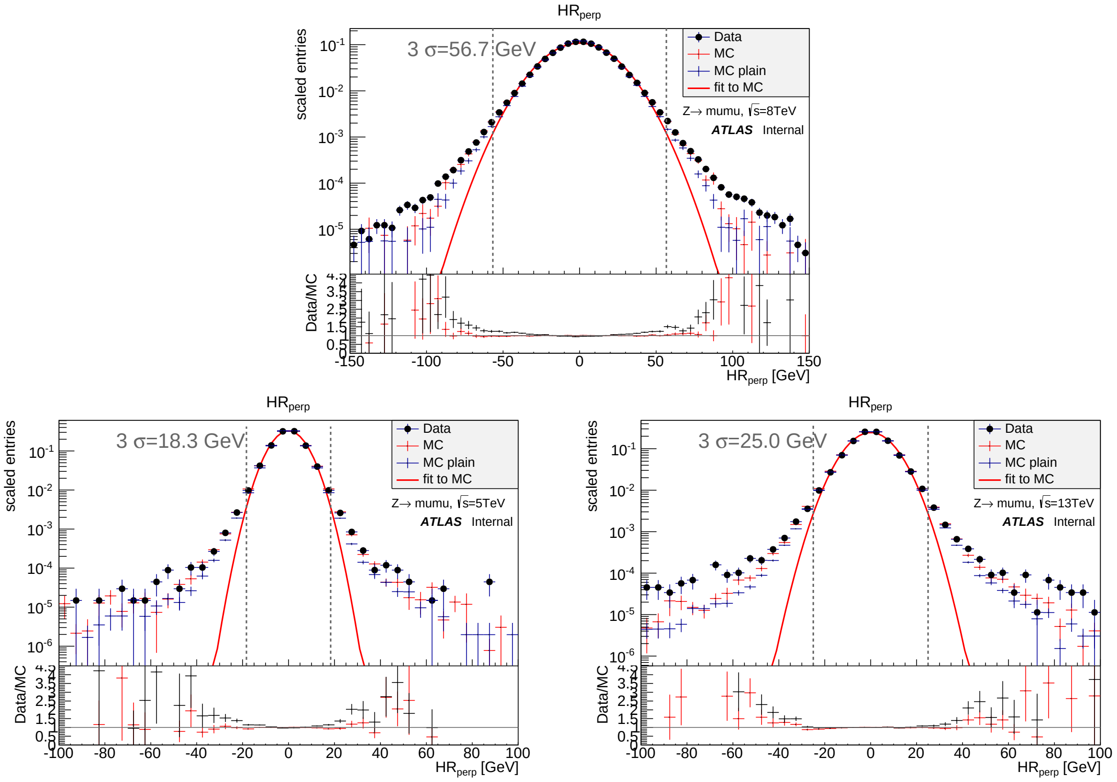

Figure 6.36.: Perpendicular hadronic recoil component in a logarithmic representation for the cluster algorithm of the 8 TeV analysis as well as for the pfoEM algorithm for the *lowMu* $Z \rightarrow \mu\mu$ analyses. The tails visible in the data distribution are shown along with the unweighted and fully reweighted MC distributions. A Gaussian fit to the scaled MC simulation is shown in red

5 TeV dataset than for the 13 TeV analysis. The main difference between the two datasets, that is the smaller amount of energy available in the 5 TeV collision compared to the 13 TeV collision, might be the cause of this difference.

The difference between data and simulation can depend on several factors. For once, data includes the signal of interest as well as background processes that pass the selection criteria. The simulations only include the $Z \rightarrow \mu\mu$ signal. In addition, the exact modeling in the simulations can play a role. Detector effects, which are not modeled correctly in the simulations, can make a difference.

The parameters of the events in the tails are investigated further for the *lowMu* analyses to shed some light on the origin of the differing number of events in the tails. A correlation of the events in the tail with recoil parameters is tested and shown in Fig. 6.38. The number of events in the tail in bins of ΣE_T and $p_T(Z)$ is given as a fraction to all events. While the ratio of the tail events to all events shows little to no dependency on either ΣE_T or $p_T(z)$ for the simulations (except statistical fluctuations), a clear trend is visible for data. The larger the ΣE_T value, the larger is also the contribution to tail events. Events with a $p_T(Z) > 30\,\text{GeV}$ seem to play a role as well, since the contribution of tail events is enlarged here as well.

The effects are much more pronounced in the 13 TeV sample than in the 5 TeV sample, although the same trend is visible as far as the statistical limits allow to draw a conclusion for the latter sample. The ΣE_T distribution for the 5 TeV analysis is located at much lower

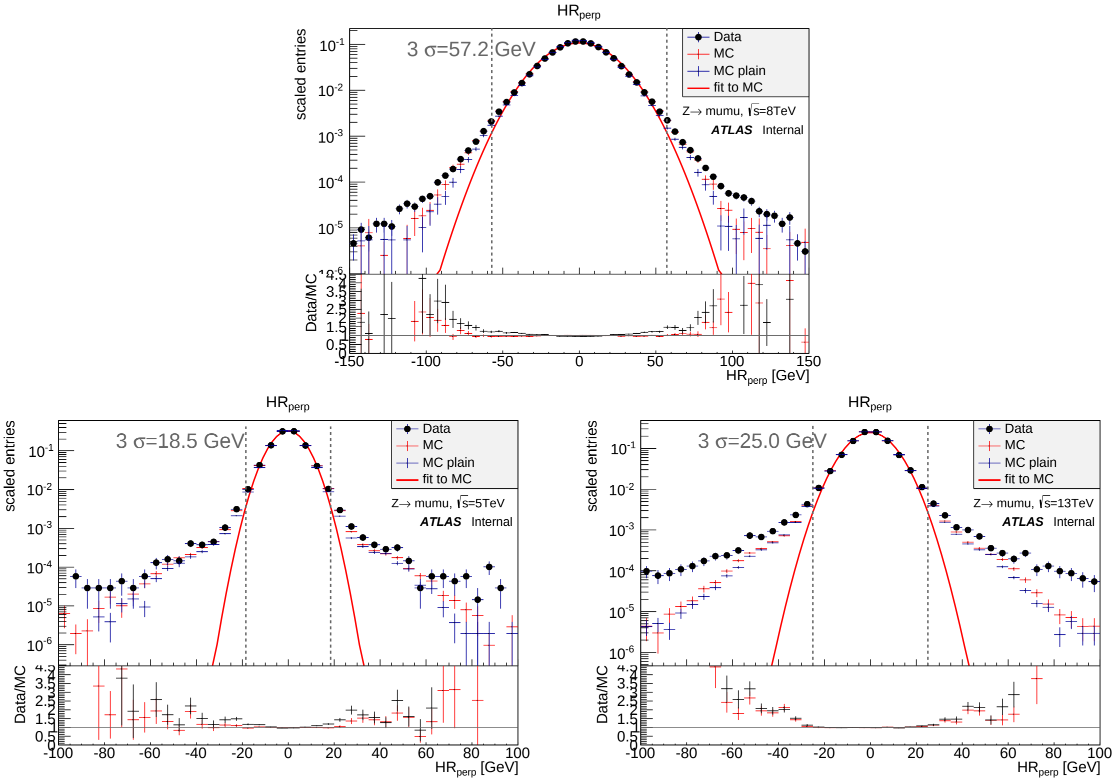

Figure 6.37.: Perpendicular hadronic recoil component in a logarithmic representation for the cluster algorithm of the 8 TeV analysis as well as for the pfoEM algorithm of the *lowMu* $Z \to \mu\mu$ analyses with a loose lepton selection. The tails visible in the data distribution are shown along with the unweighted and fully reweighted MC distributions. A Gaussian fit to the scaled MC simulation is shown in red

values and even the tails are mostly vanished above energies of 400 GeV. If the effect is triggered in events with enormous amounts of hadronic activity, a smaller fraction of events falls into this category for the lower center of mass energy. This would explain the lower discrepancy between data and simulation in the 5 TeV sample.

The invariant mass distribution of the events in the tail, shown in Fig. 6.39 for the 13 TeV analysis, gives a hint on the origin of these extra events in the tails. The left plot shows the invariant mass for all events in the tail, while the left plot only shows events with large hadronic activity ($\Sigma E_T > 300\,\mathrm{GeV}$) in the tails.

While the simulated events follow a typical mass peak, the data events show a mass peak on top of a flat offset. When the simulated events are subtracted from data, the remaining events (red curve) show the origin of the excess in data. A fraction of these excess events is visible in the peak, but the flat baseline is clearly visible here. This suggests, that at least a part of the difference comes from events which are not coming from a Z boson decay.

When again comparing the largeness of the tails with a tighter lepton selection as shown at the beginning of this section, the number of events in the tails could be effectively reduced. Small differences remain however. With a carefully chosen set of selection cuts, the differences could be further reduced. Especially the selection criteria for events containing a W boson should be considered with care, since background events passing the selection are

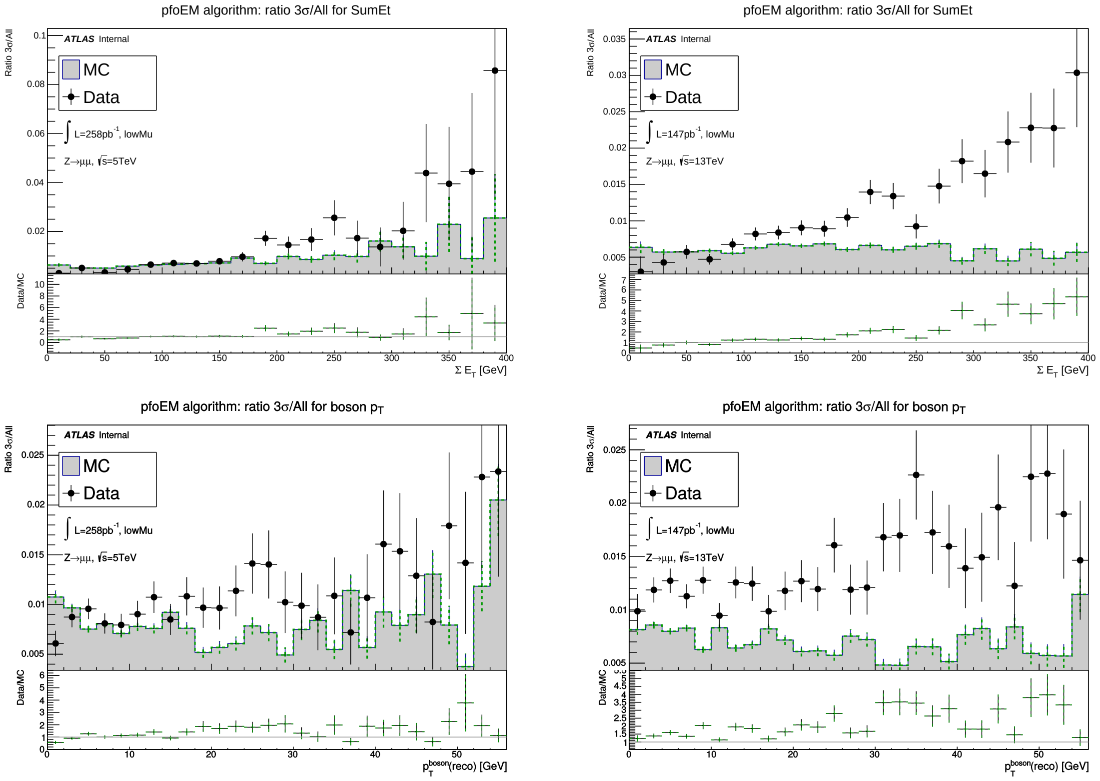

Figure 6.38.: Fraction of the events in the $3 \cdot \sigma$ tails to all events as a function of ΣE_T and the transverse boson momentum for the pfoEM algorithm in the 5 TeV and 13 TeV $Z \to \mu\mu$ analysis for data and the simulations. A loose lepton selection is applied here.

more relevant. The Z boson samples show smaller background contributions because of the effective cut on the invariant mass of the lepton system.

6.14. Conclusion on the resolution scaling and bias correction technique

It was found that this resolution scaling approach works well if the resolution in data and the simulations is largely based on a Gaussian shape. Discrepancies can be modeled by adjusting the resolution in the simulations with the use of scale factors. Especially the HR_{perp} distributions, where the differences were the largest in general, showed good results after the resolution scales were applied for all analyses. HR_{para} distributions benefited from a bias correction in the form of a correction term, which models the absolute difference between the mean bias in data and the simulations.

In general, non-Gaussian tails are not adjusted ideally with this simple technique. With large enough statistics a multi-dependent modeling as a function of ΣE_T could be implemented for the resolution scaling. However, this is not very feasible for the current *lowMu* datasets.

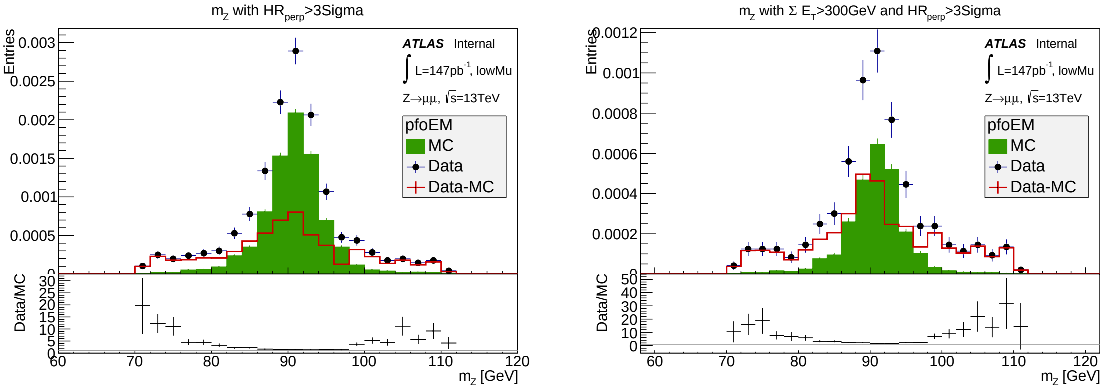

Figure 6.39.: Invariant mass distribution of the events in the $3 \cdot \sigma$ tails for the pfoEM algorithm of the 13 TeV analysis with the muon selection. Shown are the data as well as simulation events and the difference of the two (red line). A loose lepton selection is applied here.

CHAPTER 7

Estimation of the effect of the reweighting technique on the W mass analysis

For the measurement of the mass of the W boson, the calibrations obtained for the Z boson are extrapolated to a W boson selection. The set of event weights and scale factors were determined by comparing simulated events to real data. When working with real data, only reconstructed quantities are available. For the Z boson, both charged leptons can easily be measured and thus, a full reconstruction of the Z boson is possible here.

For the extrapolation to events containing a W boson, a full reconstruction of the decay kinematics is not directly available because of the undetectable neutrino. As a consequence, the simulations can only be calibrated by using truth information, which is stored in simulated events as well. Thus, all relevant kinematic quantities of the boson, its direction of motion and momentum, are taken from truth information. The measured hadronic recoil vector is now divided into a parallel and perpendicular component with respect to the truth boson direction.

A validation of the extrapolation method can be done by applying the set of scale factors and event weights as a function of the corresponding truth variables with a Z boson selection first. This approach will be presented first in this chapter. Afterwards, the method is applied to the W boson analysis. The effect of the various steps of the reweighting and resolution scaling on a W mass measurement is estimated. In addition, the statistical uncertainty is calculated for the two algorithms pfo and pfoEM for the different *lowMu* datasets.

7.1. Validation of the transfer procedure

7.1.1. Scale factors and event weights

The calibration procedure for the hadronic recoil consist of three main steps: First, the pileup distribution is adjusted in the simulations to match the average ΣE_T value per pileup bin in data. Secondly, remaining differences in the full ΣE_T distributions are removed by event weights as a function of the transverse boson momentum. Finally, the resolution of the parallel and perpendicular hadronic recoil components are scaled to be identical to real data.

The pileup event weights, which were generated as a function of ActIntPerXing, can be applied unchanged. The set of event weights, which models the ΣE_T, will be applied as a function of the truth transverse boson momentum $p_T^{boson}(truth)$ instead of the reconstructed quantity. As discussed before, the intrinsic transverse boson momentum description is not ideally described in the simulations. By applying the event weights that model the transverse boson momentum, the differences observed in Z events are removed. However, differences between the transverse momentum of W bosons and Z bosons are not modeled by this. In the full ATLAS W mass analysis, this will be accounted for by a systematic uncertainty, which is an estimate for this difference.

The scaling of the resolution also needs to be slightly adapted. The scale factors are now applied to the simulated truth components of the recoil. Afterwards, the recoil vector is rebuilt from the scaled components.

In addition to the calibration of the hadronic recoil, the energy response of each algorithm will be corrected as well. The energy scale factors, described in Sec. 5.3.2, adjusted the energy response for the algorithms by a set of energy scale factors. This was especially relevant for those algorithms that only included part of the recoil information, like pfoCharged. The hadronic energy measured by the parallel hadronic recoil component was compared to the reconstructed momentum of the Z boson. The parallel hadronic recoil component is not available for W boson events in data. Thus, they are now derived by fitting the parallel hadronic recoil distribution with respect to the truth boson in the simulations. The energy scale factors are applied to the magnitude of the hadronic recoil vector in data and simulations.

7.1.2. Results for the Z boson selection

The adapted full reweighting approach is applied to the Z boson selection and compared to the results of the original full reweighting. The procedure is studied for the pfoEM algorithm. The results for the other algorithm relevant to the W mass measurement, pfo, are comparable and are found in the Appendix H.1 along with the results for the 13 TeV analysis. The 5 TeV $Z \to \mu\mu$ dataset is used as the main example here.

To give an impression between the differences of the approach using truth information instead of reconstructed quantities (reco), a comparison between the reconstructed and truth transverse boson momentum is shown in the top left plot of Fig. 7.1. The difference between these two quantities $p_T^{boson}(reco) - p_T^{boson}(truth)$ is indicated in the top right plot. The difference between reco and truth for the vector components p_x and p_y is given in the bottom plots. It can be seen that the reconstructed momentum is not identical to the truth momentum. When looking at the x and y difference, the values are distributed around zero. The reconstructed components are smeared randomly around the truth components. As a result, the magnitude of the vector p_T built from the (smeared) x and y components, is found to be on average larger for the reconstructed Z boson than for the truth boson. The average difference of the vector magnitudes is slightly larger than zero.

The top row of plots in Fig. 7.2 shows the distributions for ΣE_T and $|HR|$ after the reweighting is applied to truth (red) and to reconstructed quantities. The ΣE_T distribution is only sensitive to the effect of the pileup and ΣE_T reweighting but not to the resolution scaling. Since the ΣE_T event weights are applied as a function of the transverse boson mo-

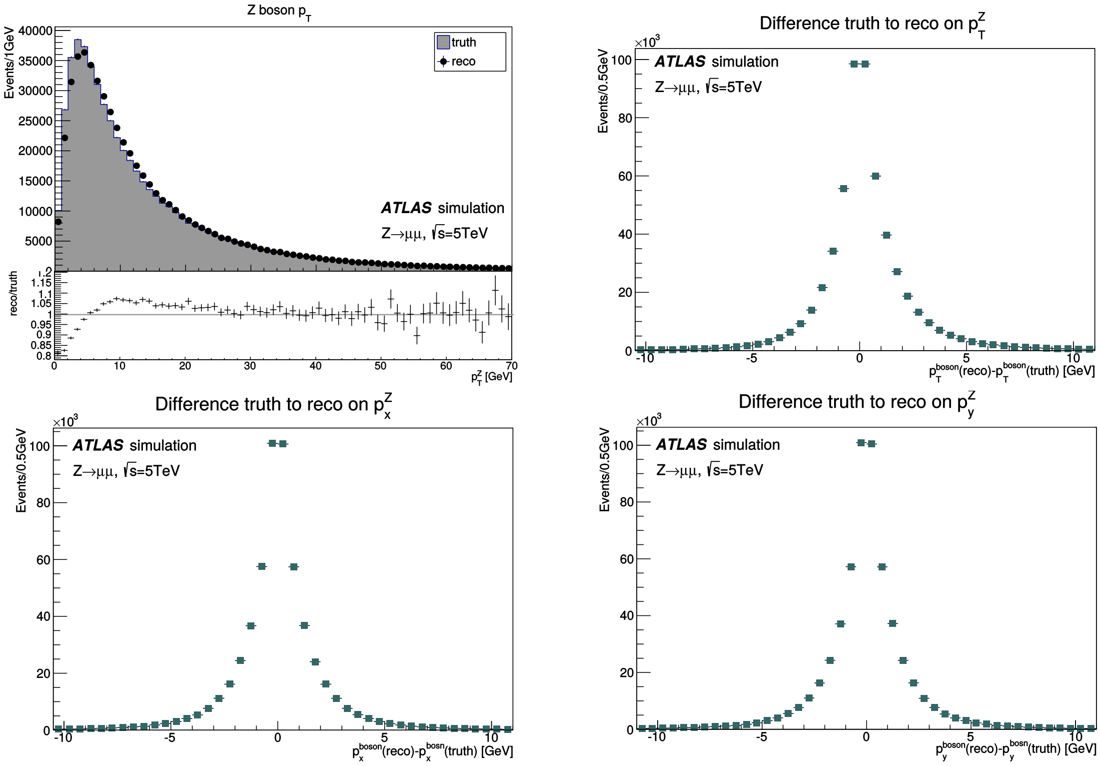

Figure 7.1.: Comparison between the transverse boson momentum obtained from reconstructed quantities as well as truth. The difference between the reconstructed and truth vector and their components is shown as well. The $Z \to \mu\mu$ 5 TeV analysis is used as an example here. No reweighting or scaling is applied.

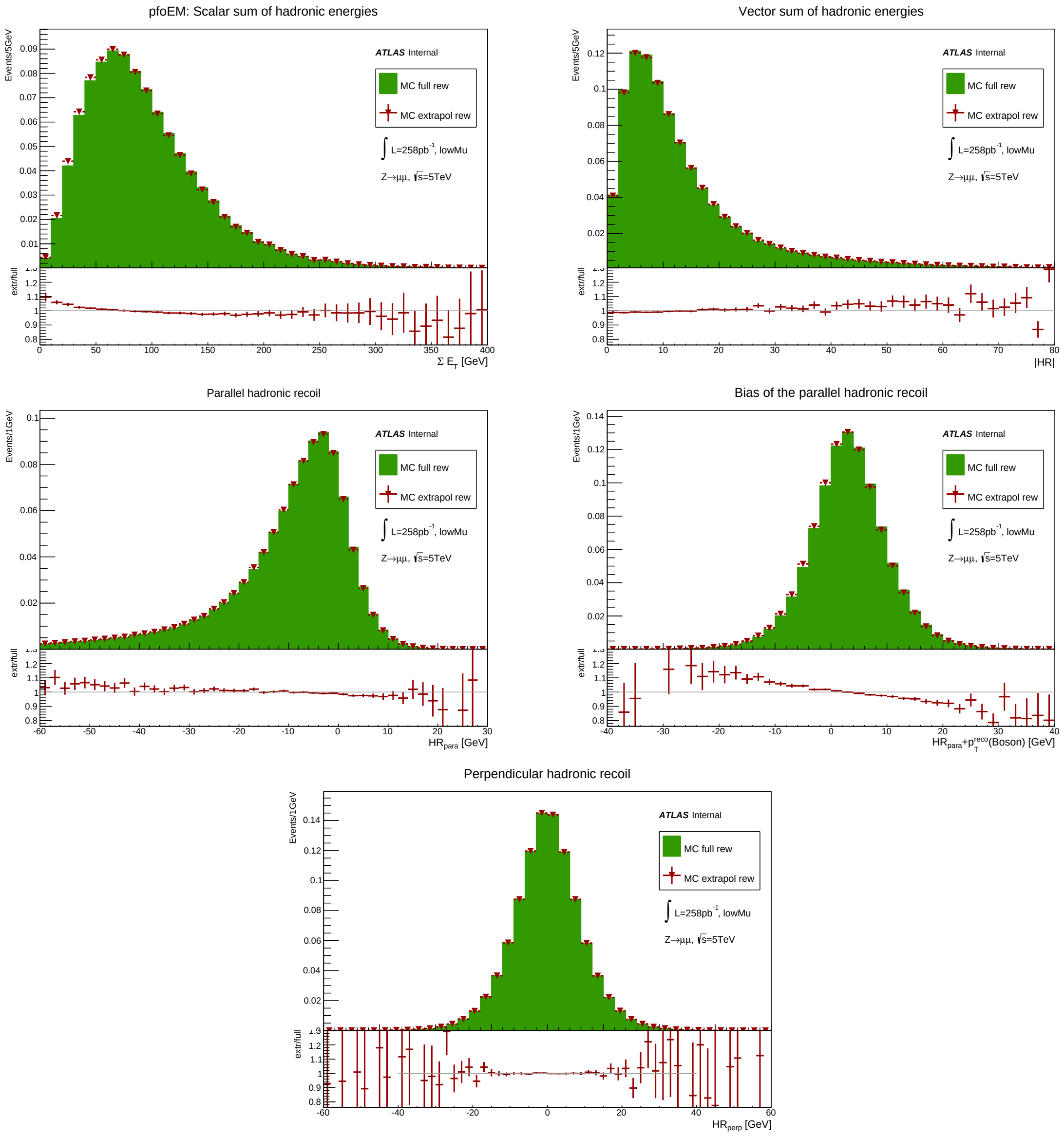
pfoEM: Scalar sum of hadronic energies

Vector sum of hadronic energies

Parallel hadronic recoil

Bias of the parallel hadronic recoil

Perpendicular hadronic recoil

Figure 7.2.: Results of the extrapolated reweighting for the ΣE_T and hadronic recoil distributions in comparison to the original approach for the 5 TeV $Z \rightarrow \mu\mu$ analysis with the pfo algorithm. The red curve shows the extrapolated reweighting with the use of truth quantities, while the green area gives the full reweighting results. The unreweighted distribution (green dashed curve) is a reference for the overall effect. All varieties are compared to data.

mentum, differences between *truth* and *reco* can influence the extrapolated reweighting as well. The effect of the original reweighting and the extrapolated reweighting is different. The ratio plot shows the difference between the two approaches. The agreement is close to unity in the central region, but the extrapolated reweighting procedure shows a trend. The deviation is the largest for small ΣE_T values. This difference is related to the description of the transverse boson momentum. The distribution of the transverse boson momentum based on truth information p_T^{truth} could not be modeled to be identical to data. Thus, the event weights as a function of the transverse boson momentum can give different results.

The vector sum of the hadronic recoil is displayed in the top right plot of Fig. 7.2. The extrapolated reweighting gives a slightly deviating agreement between reconstructed and truth quantities. The effect of the reweighting and scaling depends on the effect on the parallel and perpendicular components. Differences between truth and reconstructed splitting play a role here. The parallel and perpendicular components as well as the bias are shown in central and bottom row of Fig. 7.2.

Here only reconstructed quantities are displayed to allow for an easier comparison to the previous studies. Nevertheless, the extrapolated reweighting was applied to truth quantities, the reconstructed quantities were calculated afterwards and are depicted (red curve). The parallel component has a good conformity in the central region. The deviations increase for the tails and are of the order of a few percent. The bias, calculated from the parallel component and the boson transverse momentum, differs between the two reweighting approaches. This is due to the fact that the transverse momentum distribution is not identical. Deviation are therefore unavoidable for the bias.

The perpendicular hadronic recoil component, shown in the bottom row of Fig. 7.2, indicates no visible differences between the original and the extrapolated method. The deviations are only larger in the tails, where low statistics play a role.

It can be summarized, that the extrapolated reweighting approach gives reasonable results for the pileup reweighting and good results for the resolution scaling approach.

7.2. General distributions of the W boson selection

Before the influence of the full reweighting technique on the W mass measurement in the form of systematic uncertainties will be estimated, the general behavior of the full reweighting applied to events with a reconstructed W boson candidate in comparison to data will be presented shortly. It should be noted beforehand, that the data contains W boson events along with other background processes passing the signal selection, which are mostly coming from QCD interactions as well as from Z boson with one misidentified lepton. The simulations on the other hand only include the signal processes $W^\pm \rightarrow \mu^\pm \nu$. Because of this, differences in the performance can be expected.

Fig. 7.3 shows the relevant distributions of the hadronic recoil for the 5 TeV and the 13 TeV dataset (see Appendix H.2 for the set of distributions for the pfo algorithm). The ΣE_T distribution (top row plots) shows a good agreement between data and the simulations with the reweighting applied. The disagreement without the reweighting is comparable to the Z boson selection discussed in the previous chapter. With the reweighting, most differences are removed. It can be seen, that the reweighting technique can be successfully applied to the W boson selection.

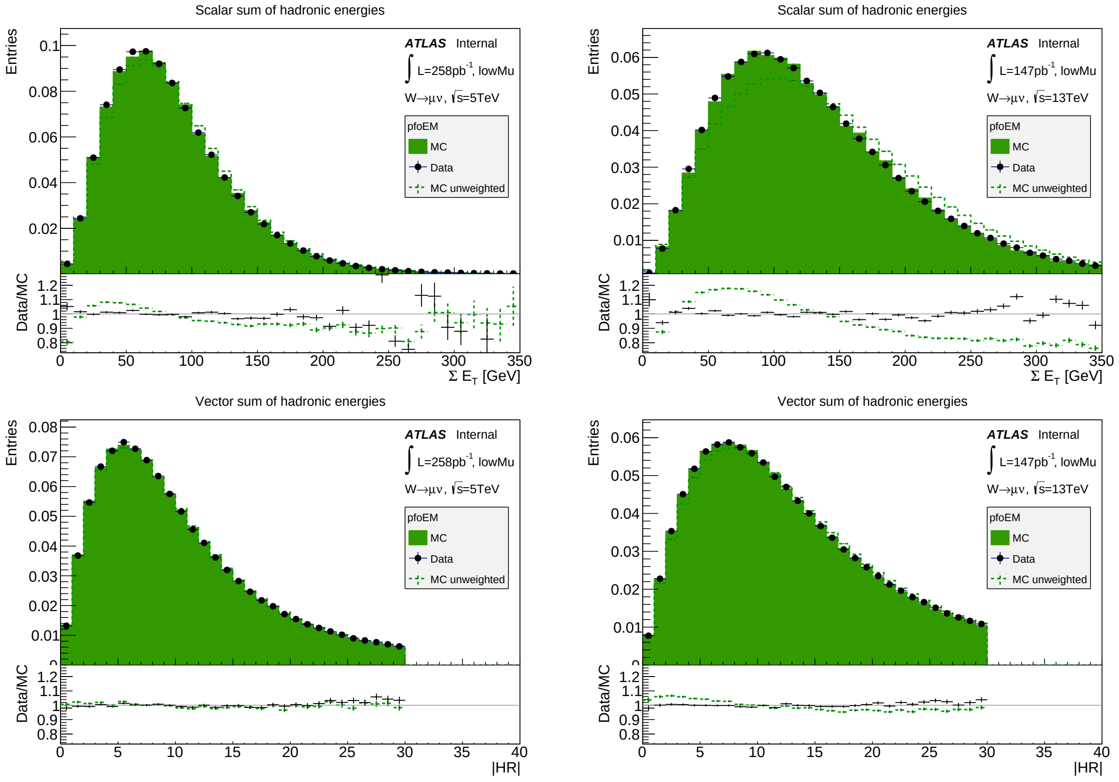

Figure 7.3.: Fully reweighted hadronic recoil distributions for the pfoEM algorithm with the $W \to \mu\nu$ selection in the 5 TeV and in the 13 TeV dataset.

The bottom plots show the magnitude of the hadronic recoil vector. The intrinsic differences between data and the simulations are comparably small. The full reweighting with the resolution scaling applied creates small improvements, especially for the 13 TeV dataset, where the intrinsic deviations are larger.

The division of the hadronic recoil vector into a component parallel and a component perpendicular to the reconstructed transverse boson momentum is not possible for the W selection, where the boson kinematics cannot be reconstructed. To nevertheless estimate the contribution of signal and of pileup at least partially, the hadronic recoil vector can be divided with respect to the charged lepton track. In this thesis, the quantities are called u_{para} and u_{perp} respectively. The two distributions are shown in Fig. 7.4. The intrinsic agreement between data and the simulations is already quite good for all distributions and is found to be close to unity in the central regions. Small deviations in the resolution of the perpendicular component are found to be more pronounced in the 13 TeV plots and can be reduced by the resolution scaling.

Finally, the transverse mass M_T of the W boson is shown in Fig. 7.5. The agreement between data and the simulations is already close to unity for the lower range. The falling edge and the tails are not ideally modeled. The reweighting however decreased this disagreement. The distribution at the higher center of mass energy is slightly better described in the simulations than at 5 TeV, before and after the reweighting. Especially the tail shows smaller deviations. The shape of the falling edge and the tail depend on the resolution of the hadronic recoil and on the transverse boson momentum. Both quantities depend on the

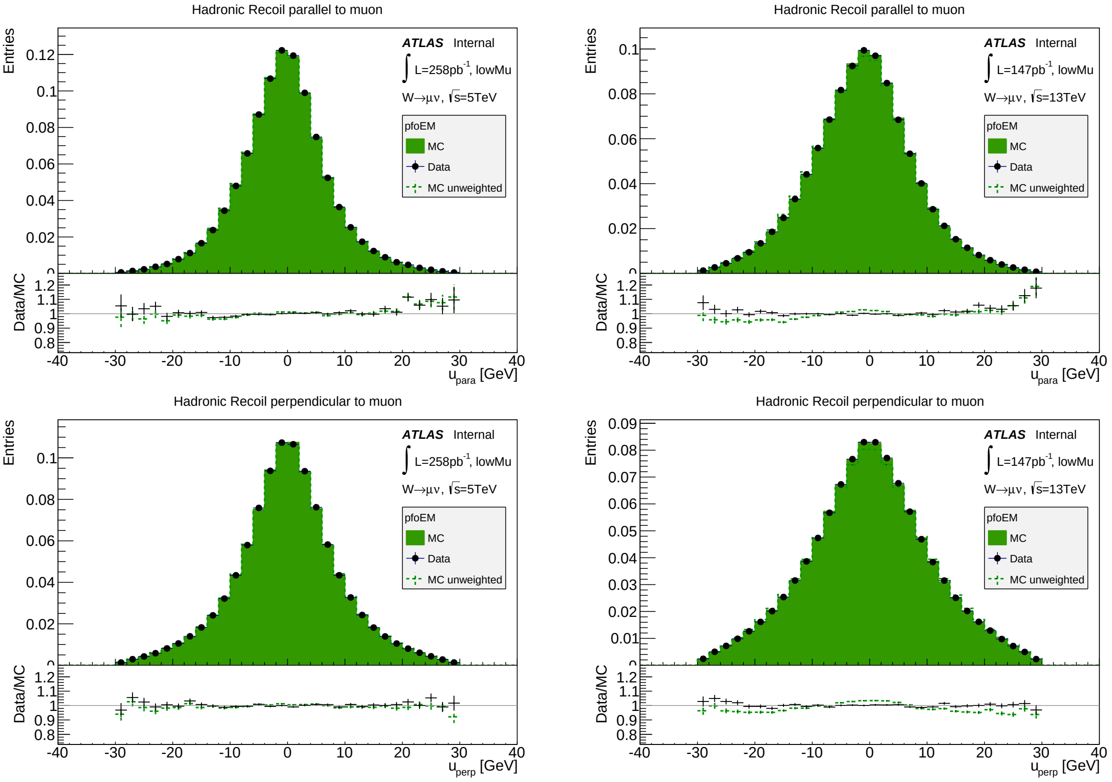

Figure 7.4.: Fully reweighted hadronic recoil distributions u_{para} and u_{perp} for the pfoEM algorithm with the $W \rightarrow \mu\nu$ selection in the 5 TeV dataset.

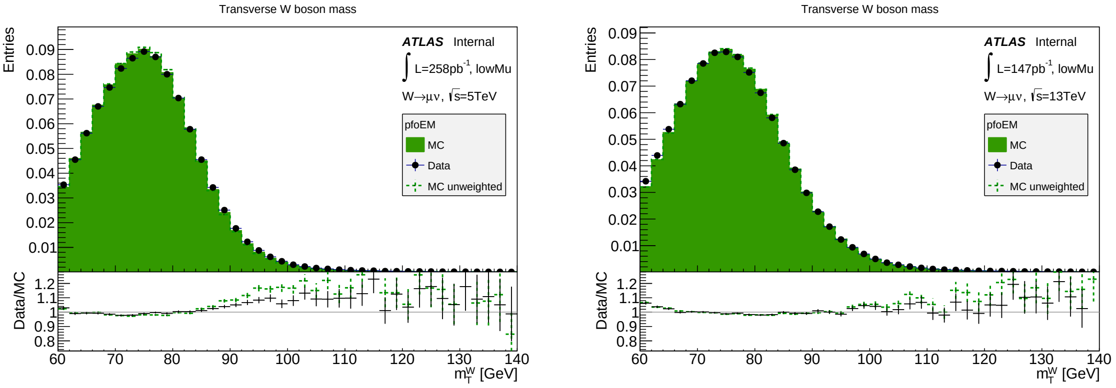

Figure 7.5.: Fully reweighted hadronic recoil distributions for the pfoEM algorithm with the $W \rightarrow \mu\nu$ selection in the 13 TeV dataset.

center of mass energy and it was shown in the previous chapters, that the resolution is found to be larger for the 13 TeV dataset. The intrinsic modeling seems to be better for the 13 TeV dataset. Together with the reweighting, the transverse mass distribution is modeled best for the 13 TeV dataset and reasonably well for the 5 TeV dataset.

7.3. Estimation of the uncertainty on the W mass measurement: Statistical error

The statistical uncertainties will be estimated for the analyses of the *lowMu* dataset in this section. This can be done in the framework of the W mass measurement. With the template fit approach, the transverse mass distribution measured in data is compared to the simulations with different mass hypotheses, the templates. By this, the value of the W boson mass is determined that describes the given data best. Since the data can only be taken with finite statistics, the measured value is accompanied by a statistical uncertainty. For this reason, different sets of pseudodata are generated. They represent statistical fluctuations of the data. By comparing the transverse mass distributions of the pseudodata to the templates, a mass value for each fluctuation is obtained. The spread of these new mass values is an estimate for the statistical uncertainty on the W boson mass.

In this thesis, the optimal value for the W boson mass will not be determined with real data. Since the development of the hadronic recoil calibration was performed quite early within the overall W mass analysis of the ATLAS group. Using real data would already reveal parts of the results of the whole analysis before all parts of the calibration are finalized. The effect of statistical fluctuations can also be determined by only using pseudodata generated from the simulations.

Therefore, the templates as well as the pseudodata are generated from the simulations. The relevant aspects of this procedure will be introduced in this section. The $W \rightarrow \mu\nu$ Monte Carlo sample for the 5 TeV analysis is used as an example.

7.3.1. Template generation

The distribution of the transverse mass M_T is generated with the pileup and ΣE_T event weights and scale factors applied as described in the previous section for the original mass point of the simulations. In addition, copies of the original transverse mass distribution are modified with specific template weights to obtain transverse mass distributions for each template.

The templates are generated for several mass points from the full simulation directly by making use of the the relativistic Breit Wigner parametrization as described in Sec. 4.3.2. The simplification of a fixed-width formula is sufficient for a first estimate of the uncertainties like it is done in this chapter. A full W mass measurement should however be performed with the precise template reweighting with a running decay width.

The effect of the template reweighting is shown in Fig. 7.6 by the weighted truth distribution of the W boson mass for the mass point at $M_W^{templ} = M_W^{MC} + 200\,\mathrm{MeV}$. As a reference, the distribution for the unweighted truth mass, as it was generated in the Monte Carlo sample production, is shown alongside. The input value used in the Monte Carlo generation is $M_W^{MC} = 80.399\,\mathrm{GeV}$ with a width of $\Gamma_W^{MC} = 2.085\,\mathrm{GeV}$.

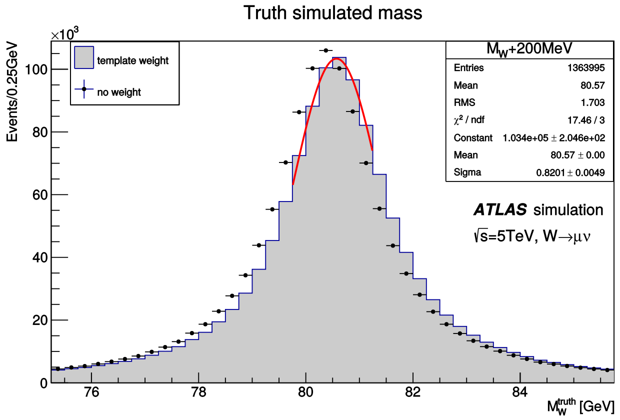

Figure 7.6.: Comparison between the unweighted distribution of the truth W boson mass and the weighted distribution, which was obtained by applying the template weights for the mass point $M_W^{MC} + 200\,\text{MeV}$. In addition, a fit to the weighted distribution is shown and the fit results are indicated in the box. The 5 TeV $W \to \mu\nu$ Monte Carlo dataset was used to generate this distribution.

The mean of the weighted distribution and the reference distribution is fitted with a Gaussian distribution in the central region. Despite the fact that the shape of the distribution cannot be ideally described by Gaussian curve, this approximation is sufficient to test the shift introduced by the template reweighting approach. A mean of $M_{W,templ}^{gauss} = 80.572\,\text{GeV}$ is found for the weighted template distribution and of $M_{W,ref}^{gauss} = 80.381\,\text{GeV}$ for the reference distribution. This corresponds to a shift of $\Delta M^{gauss} = 191\,\text{MeV}$, which is in agreement with the expected shift of 200 GeV within the limitations of the approximation by a Gaussian distribution.

In order to reduce the computing time, only a few mass points were generated like this. Additional mass values are extrapolated by assuming a linear progression of the mass points in close proximity. The principle is as follows: First, the transverse mass distribution of the original mass point $M_T(M_W)$ is calculated in the full Monte Carlo simulation. The transverse mass distribution for a second mass point $M_T(M_W + \Delta m)$ is generated in parallel, obtained by the Breit-Wigner template parametrization. This mass point is at a distance of Δm from the original mass point. Both mass points are run through the full reweighting procedure as just described. Then, the distribution of a new mass point $M_T + \kappa \cdot \Delta m$ is calculated by making the following assumption: The difference between the transverse mass distribution of the original mass point $M_T(M_W)$ and the distribution of the new mass point $M_T(M_W + \kappa \cdot \Delta m)$ is approximated to be as large as κ times the difference between the distributions of the original and the second mass point:

$$M_T(M_W) - M_T(M_W + \kappa \cdot \Delta m) \simeq \kappa \cdot (M_T(M_W) - M_T(M_W + \Delta m))\,.$$

With the given transverse mass distributions of the original and the second mass point, the distribution for the new mass point can be calculated. This approximation is valid for small values of κ, where the mass shifts are smaller than the given resolution. It is sufficient to use the linear term only, higher orders are negligible.

By the combination of the two template methods, 36 mass points are simulated around the

Monte Carlo value of $M_W = 80.399\,\mathrm{GeV}$ in steps of $\pm 0.02\,\mathrm{GeV}$. The values at $\pm 0.01\,\mathrm{GeV}$, $\pm 0.04\,\mathrm{GeV}$, $\pm 0.1\,\mathrm{GeV}$ and $\pm 0.2\,\mathrm{GeV}$ were calculated by the direct Breit-Wigner reweighting, while the other mass points are generated from the approximation with the second mass point being at $\Delta m = 0.01\,\mathrm{GeV}$. The validity of this approach is tested by a χ^2 test, described in the next section.

7.3.2. χ^2 test

The mass measurement as well as the validation of the template generation is performed by a χ^2 test, that calculates the squared deviation of each mass point from a reference distribution by [109]:

$$\chi^2 = \sum_i \frac{(x_i^{temp} - x_i^{ref})^2}{\sigma_i^2}$$

The summation is done within a categorization i of the quantity of interest, for example in bins of the transverse mass distribution M_T[1]. The values for x_i^{temp} and x_i^{ref} represent the number of entries in category i of the template and the reference distribution respectively. In the full measurement the reference distribution is taken from data or pseudodata, while the templates are generated from the simulations. The uncertainty per bin σ_i is the uncertainty per bin of the data (pseudodata) distribution to reflect the precision in data.

For the validation of the template generation, the original Monte Carlo mass point is used as the reference. The tests proofs, if the extrapolated templates deviate from the original mass point in the same way the regular templates do. Fig. 7.7 shows the result of the χ^2 tests performed for each mass point. It can be seen that the results nicely follow a parabolic shape. The χ^2 values of the extrapolate templates (blue markers) seem to follow the same parabola as the regular templates (black markers).

The minimum and the width of this behavior are fitted by a parabola $A + B \cdot (M_W - C)^2$. The minimum is found to be at $M_W^{fit} = 80.399\,\mathrm{GeV}$, which is determined by the fit parameter C. This result exactly agrees with the original mass point from the Monte Carlo simulation. The uncertainty of the minimum is defined at the point M_W^{+1} at which the χ^2 value of the minimum is increased by 1. From the fit results this point can easily be calculated:

$$f(M_W^{+1}) = A + B \cdot (M_W^{+1} - C)^2 \equiv A + 1.$$

The difference of M_W^{+1} to the minimum at C is:

$$\Delta M_W^{fit} = M_W^{+1} - C = \frac{1}{\sqrt{B}}$$

For this validation, a value of $\Delta M_W^{fit} = 15\,\mathrm{MeV}$ is found. It reflects the statistics of the reference distribution. In this case this is the statistics of the Monte Carlo $W \to \mu\nu$ sample[2].

It can be concluded, that it is valid to generate a set of extrapolated template distributions by the simplified approach in comparison to a full template calculation. This setup will be used for the uncertainty estimation in the analysis presented here.

---

[1] For all χ^2 tests performed in this thesis, the transverse mass distributions are normalized and compared in the range $60\,\mathrm{GeV} < M_T < 110\,\mathrm{GeV}$.

[2] The statistics used for the 5 TeV Monte Carlo set are around 60 % larger than the statistics available in data.

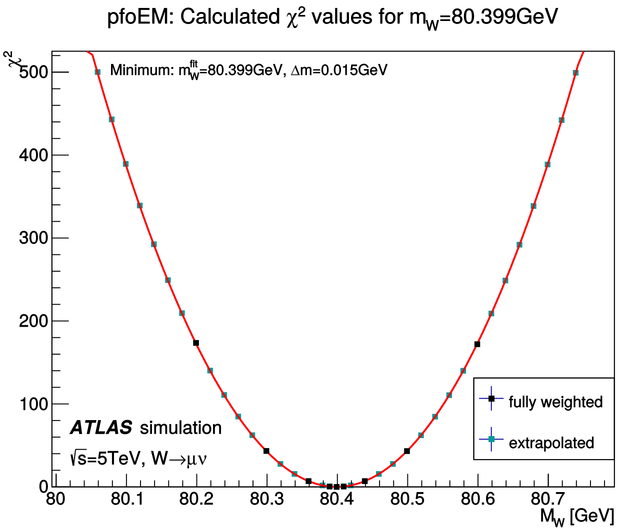

Figure 7.7.: χ^2 test performed with the set of templates for this exemplary pseudodata experiment. The 5 TeV $W \to \mu\nu$ Monte Carlo dataset with the pfoEM algorithm is used.

7.3.3. Pseudodata calculation with the bootstrap method

As explained before, the uncertainties presented in this chapter are not calculated using real data to not bias the full ATLAS W mass measurement. Thus, pseudodata is used in the bootstrap method instead, which is generated from the simulations [109].

The bootstrap method is widely used to estimate the measurement of a theoretically known quantity with finite statistics. In this case, the transverse mass distribution of the data sample is estimated on the basis of the same number of events as seen in data. The observed data distribution is a representation of a true unknown distribution, which fluctuates around the true values within its statistics. These fluctuations can be described by the discrete Poisson distribution. The pseudodata samples will mimic these fluctuations. Each pseudodata experiment represents a set of random results obtained from an input distribution, where each new bin content is calculated randomly from the input bin content by applying Poisson statistics. This procedure is performed repeatedly, for example around 10 000 times, giving a large set of pseudodata experiments.

A typical transverse mass distribution for one random pseudodata experiment is shown in the left plot of Fig. 7.8 along with the reference distribution that is used as input to the bootstrap method. The integral over the reference distribution has been scaled to the total number of data events in a $W \to \mu\nu$ selection of the 5 TeV dataset. The number of entries of the pseudodata experiments naturally fluctuates around the number of data events N_{data}. From the right plot of the same figure it can be seen, that the number of generated entries for all pseudodata experiments is scattered with an RMS of 733 around $N_{data} = 534\,127$ which is well comparable to the expectation of $\sqrt{N_{data}} = 730$.

Each pseudodata experiment is then used as the reference distribution in a χ^2 test and compared to the template distributions. The χ^2 results for one pseudodata experiment are given in Fig. 7.9. The corresponding W mass value of each pseudodata experiment is determined by a subsequent parabolic fit. The values will fluctuate within the statistical uncertainty used

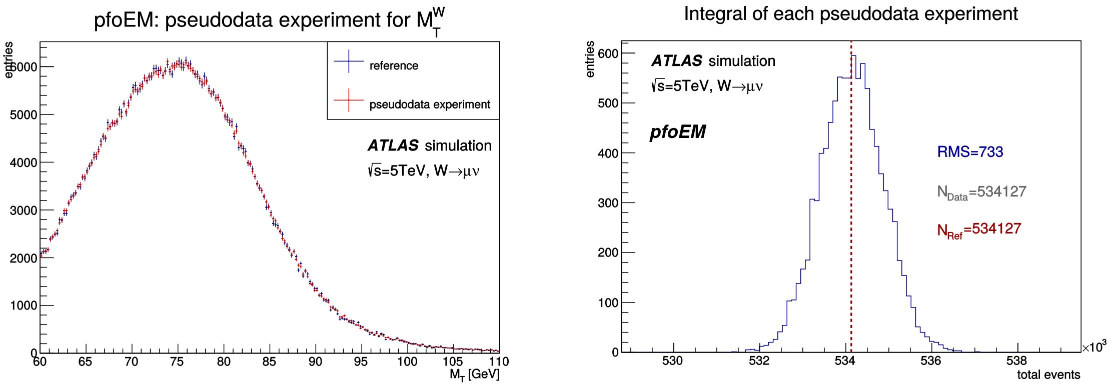

Figure 7.8.: Transverse mass distribution for one exemplary pseudodata experiment (blue) along with the reference distribution (red) used to generate the pseudodata distribution. The 5 TeV $W \rightarrow \mu\nu$ Monte Carlo dataset with the pfoEM algorithm is used.

for the pseudodata generation. For example for the pseudodata distribution shown here, a value of $M_W^{fit} = 80.407\,\text{GeV}$ is found.

Finally, the statistical uncertainty σ_{stat} of the data can be inferred from the width of the distribution of these fitted mass values. By using the simulated distributions as input to the bootstrap procedure, the information on the true mass of the W boson will not be revealed by this, but only the statistical and experimental uncertainties.

7.3.4. Results for the statistical uncertainties

With the bootstrap method, 10 000 pseudodata experiments were performed and analyzed with the χ^2 test method. Since the simulations were scaled to the number of entries of the data distribution with the same W boson selection applied, the statistical variations in the pseudodata experiments reflect the true statistical uncertainty of the dataset of interest.

The fit values M_T^{fit} obtained for each pseudodata experiment is shown in the left plot of Fig. 7.10 together with a Gaussian fit to determine the width of the fluctuation. The fit results are indicated in the plot as well. With this, a statistical uncertainty for a W mass measurement in the muon channel of the 5 TeV *lowMu* analysis is found to be $\sigma_{stat}^{5\,\text{TeV},pfo} = 18\,\text{MeV}$ for the pfo algorithm . The according W mass value obtained from the two fit as well is found to be $M_W^{stat} = 80.399\,\text{GeV}$ for both algorithms. This value is in exact agreement with input value of the Monte Carlo production used for the pseudodata generation. The results for the second algorithm and the 13 TeV *lowMu* dataset, which were analyzed in the same way, are given in Tab. 7.1. In addition to the uncertainty obtained in the Gauss fit to the spread of the χ^2 fit mass values, the mean error ΔM_{stat} on these values from the χ^2 fit is also indicated. Here, each pseudodata experiment provides a separate fit error and the mean of all pseudodata results is stated in the table. The deviation is however comparably small. For a reference see also the right plot of Fig. 7.10.

When comparing the two results for the uncertainty, once from the spread of the values and once from the mean uncertainty of each fit value, the two numbers are generally found to be well comparable. With the high number of pseudodata experiments the error on the uncertainty σ_{stat} is small, i.e. this value is very precise. From the compatibility of the two

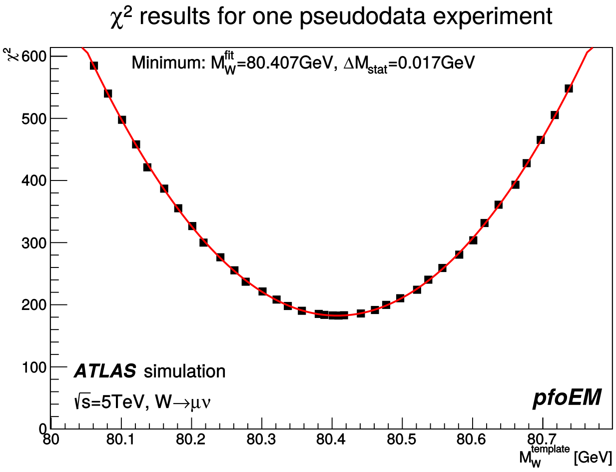

Figure 7.9.: χ^2 test performed with the set of templates for one exemplary pseudodata experiment. The 5 TeV $W \to \mu\nu$ Monte Carlo dataset with the pfoEM algorithm is used for both the templates and the pseudodata.

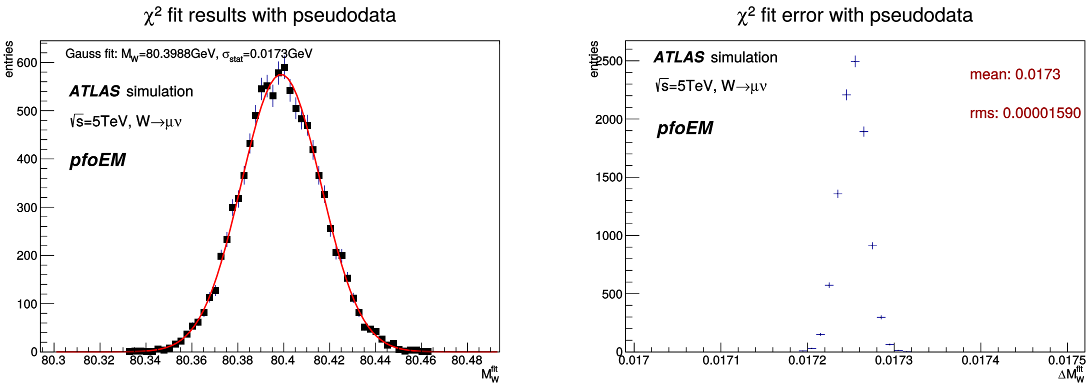

Figure 7.10.: Resulting distribution of the mass values M_W^{fit} and uncertainties ΔM_W^{fit} obtained from the fit to the χ^2 tests of the pseudodata experiments. The 5 TeV $W \to \mu\nu$ Monte Carlo dataset with the pfoEM algorithm is used.

numbers and the small error on the χ^2 fit uncertainty, it can be concluded, that the uncertainty obtained from the χ^2 fit parabola is valid. This could further be used to estimate the effect of a change in the statistics or to estimate the error due to algorithm and selection optimizations directly from the fit to the χ^2 parabola.

When comparing the results for the two datasets, the uncertainties per algorithm are found to be of the same order. The integrated luminosity of 5 TeV dataset was larger, but because of the dependency of the W production cross section on the center of mass energy, the 13 TeV sample includes a slightly larger amount of reconstructed W boson candidates compared to the 5 TeV sample. However, the error is nevertheless slightly larger for both algorithms in the 13 TeV sample. This can be explained by the fact that the dataset at the larger center of mass energy showed a worser resolution when comparing the general performance of the various algorithms in the two datasets. A higher resolution allows for a better reconstruction of the transverse mass, which is less susceptible to fluctuations.

Algorithm	$\sigma_{stat}^{5\,\text{TeV}}$ [MeV]	$\Delta M_{stat}^{5\,\text{TeV}}$ [MeV]	$\sigma_{stat}^{13\,\text{TeV}}$ [MeV]	$\Delta M_{stat}^{13\,\text{TeV}}$ [MeV]
pfo	18.2	18.2	18.6	18.7
pfoEM	17.3	17.3	18.0	18.1

Table 7.1.: Statistical uncertainties for the two algorithms pfo and pfoEM for the muon channel of the two *lowMu* datasets at 5 TeV and 13 TeV. The uncertainty obtained from the spread of the mass values for each pseudodata experiment σ_{stat} is given along with the mean uncertainty of the χ^2 parabola fits ΔM_{stat}.

When comparing the two algorithms, it can be also seen that the pfoEM implementation performs slightly better. pfoEM shows the smallest resolution of the hadronic recoil for all implementations. By this, a better description of the transverse mass is possible, resulting in slightly smaller uncertainties.

7.4. Estimation of the uncertainty on the W mass measurement: Systematic error

The precision of the scale factors and event weights applied here is defined by uncertainties as well, which mainly depend on the statistics of the data and simulation distributions that were used to generate the scale factors and event weights in the first place. These systematic uncertainties need to be included in the overall error estimation for the mass measurement.

Within the template framework, this can easily be done by testing slightly varied calibrations against the original set of scale factors and event weights. For this purpose, the χ^2 test is performed by comparing the original calibrations to a slightly varied copy. Again, templates are used to determine the optimal value of the W boson mass for each variation.

Both templates and the reference distribution (pseudodata) are generated from the simulations with the calibrations applied and there is no general preference which one should be varied. Here, the reference distribution is varied to slightly simplify the procedure.

The effect of the systematic variations is estimated for each set of event weights and scale factors separately. The approach slightly differs for each set by making use of some exploits to reduce the overall computing time. The general procedure is however identical and can be summarized as:

- The original set of scale factors and event weights are generated from the comparison of data and simulation in Z boson events.
- The original calibration is applied to a W boson selection in the Monte Carlo simulations.
- The set of templates is generated from these calibrated simulations.
- New sets of scale factors and event weights are obtained by varying each set of scale factors and event weights within its uncertainties (separately for each type of calibration: pileup reweighting, ΣE_T reweighting and resolution scaling). Different approaches exist here, which will be described below.

- All varied calibrations for one set of scale factors/event weights are applied to the simulations, giving a new set of differently calibrated distributions.
- For each variation a χ^2 test is done by comparing this differently calibrated distribution to all templates. A value for the W mass is determined from the minimized χ^2 curve.
- The varied results are combined to one average deviation, the details of the combination depend on the approach of the variation.

7.4.1. Uncertainty on the resolution scale factors

First approach One approach to determine the uncertainty for the scale factors and event weights is to analyze the effect of the uncertainty of each value one by one and sum the resulting uncertainties. This can be done by taking the full set of scale factors and changing only one value (one bin) within its uncertainty, leaving the rest unchanged. For example, for the scale factors used to scale the resolution this corresponds to three sets (one for the parallel resolution, one for the perpendicular resolution and one for the bias correction term) containing each 20 scale factors. By each time varying only one of the 60 values up or down $w^{new} = w \pm \sigma$, in total 120 new sets of scale factors are obtained and applied to the reference distribution. For each new reference distribution, the effect on the W mass is calculated by comparing to the original templates (no variations applied here). The difference $\Delta M_{res}^{i\pm} = M_T^{orig} - M_T^{i\pm}$ gives the deviation of one variation i to the original mass value calculated with the ideal scale factors applied. The deviations are assumed to be uncorrelated and all 60 plus and all 60 minus variations are each combined by the two squared sums, separately for the plus and minus variation:

$$\Delta M_{res}^{\Sigma\pm} = \sqrt{\sum_i \left(\Delta M_{res}^{i\pm}\right)^2}.$$

	5 TeV			13 TeV		
Algorithm	$\Delta M_{res}^{\Sigma-}$ [MeV]	$\Delta M_{res}^{\Sigma+}$ [MeV]	ΔM_{res}^{ave} [MeV]	$\Delta M_{res}^{\Sigma-}$ [MeV]	$\Delta M_{res}^{\Sigma+}$ [MeV]	ΔM_{res}^{ave} [MeV]
pfo	15.8	15.1	15.4	18.4	16.3	17.3
pfoEM	13.6	10.6	12.1	16.3	15.1	15.7

Table 7.2.: Systematic uncertainties for the resolution calibration for the two algorithms pfo and pfoEM in the muon channel at 5 TeV and 13 TeV. The uncertainty $\Delta M_{res}^{\Sigma\pm}$ are obtained separately for the plus and the minus variation.

Tab. 7.2 shows the results for the two algorithms in both datasets. It can be seen that the minus variations result in slightly larger uncertainties compared to the plus variations. Further investigations showed, that these asymmetries can arise, if comparing small variations around the best value. Since the same simulations are used for the templates and for the varied reference distribution, the χ^2 comparison between the two is done close to the optimum. In each test only one scale factor is slightly changed and the modifications as well as the effect of one changed scale factor is small. Thus, the test and reference distributions that are used in the χ^2 test are almost identical. However, the combination of all plus or minus variations to $\Delta M_{res}^{\Sigma\pm}$ amplifies the small asymmetric effects to a larger difference. In

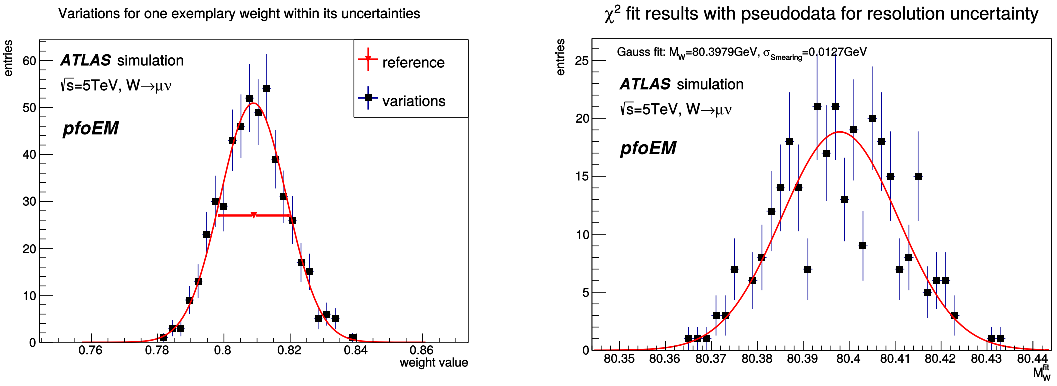

Figure 7.11.: Left plot: Variation of one event weight within its uncertainty. The 500 randomly calculated variations are distributed around the original event weight. The uncertainty of the original measurement is shown by the red horizontal bar in the center. A Gaussian fit to distribution of the new event weights is shown by the red curve. Right plot: Distribution of the fit values for all variations obtained by a fit to the χ^2 test results of the template comparisons.

this case, the resolution is either always improved or always worsened and these variations to one side lead to asymmetric shift values $\Delta M_{res}^{i\pm}$. These asymmetries between plus and minus variations vanish, if less identical distributions are compared. The full W mass measurement will compare the templates to real data, which is by definition not identical to the simulations. This means, that the asymmetries are artificially introduced by this approach. Other approaches to determine the effect of systematic variations, which use random variations or introduce much larger changes will not be affected by this anomaly.

The average values listed in the same table $\Delta M_{res}^{ave} = \frac{1}{2} \cdot (\Delta M_{res}^{\Sigma+} + \Delta M_{res}^{\Sigma-})$ give a more realistic combination of the plus and minus variations by averaging the asymmetric uncertainties.

When comparing the two algorithms, the uncertainties for the pfo algorithm are again found to be consistently larger than for the second algorithm pfoEM. The same is true for the 13 TeV dataset compared to the 5 TeV dataset.

Second approach Another approach to obtain the same uncertainty is to vary the 60 different scale factors randomly within their uncertainties, all at the same time. The new resolution scale factors are calculated by a Gaussian fluctuation around the original scale factor within the given uncertainty. An example of the variations is given in the left plot of Fig. 7.11 for one weight.

This process needs to be repeated, 500 different sets are obtained for this analysis. The 500 distributions generated with theses sets are each compared to the templates and the resulting W mass values for each set are are fitted by a Gaussian distribution as it was done for the statistical uncertainty.

The right plot of Fig. 7.11 shows the distribution of the fit values for M_W^{fit} obtained for 500 random variations for the pfoEM algorithm in the 5 TeV dataset. The spread is described by a Gaussian fit. By this, an uncertainty of $\sigma_{res}^{5\,\mathrm{TeV},pfoEM} = 13\,\mathrm{MeV}$ is found. Tab. 7.3 shows the results for both algorithms in both datasets.

Algorithm	$\sigma_{res}^{5\,\mathrm{TeV}}$ [MeV]	$\sigma_{res}^{13\,\mathrm{TeV}}$ [MeV]
pfo	15.4	17.4
pfoEM	12.7	15.4

Table 7.3.: Systematic uncertainties for the resolution calibration for the two algorithms pfo and pfoEM in the muon channel at 5 TeV and 13 TeV. The uncertainty σ_{res} is obtained by a Gaussian fit to the spread of the mass fit results of all variations.

The values of the uncertainty are found to be well comparable to the average uncertainty obtained by the first approach.

7.4.2. Uncertainty on the pileup event weights

The calibrations presented in this thesis were done in a sequence of steps. The first step, the pileup reweighting, improved the agreement of the simulations with the data vastly so that the following calibration steps only needed to remove the remaining differences. When varying the pileup event weights, the effect needs to be propagated to the other event weights and scale factors. A new pileup event weight influences the other weights, which are generated after the pileup weights have been applied. When varying the pileup event weights the full calibration needs to be rerun. Negative effects by varied event weights will be balanced to some extent by the subsequent calibration steps.

If a full variation of each scale factor/event weight is applied like introduced for the resolution scaling uncertainty, the propagation through the analysis comes at an enormous computational cost. Therefore a simplified approach is used here.

For the estimate on the uncertainty introduced by the pileup weights, the following variations are examined: The data pileup distribution has been stretched to give the same average ΣE_T distribution as a function of pileup as the simulations. In addition to this, the distribution is now shifted within the uncertainty of the average pileup to account for possible effects in the mismeasurement of the pileup distribution. Here, the precision of the mean pileup is taken as a measure for the fluctuation of the pileup entries. The error on the mean is computed by the standard deviation divided by the square root of the number of entries: $\Delta\mu = \frac{\sqrt{\frac{1}{N}\sum_i (x_i - \bar{x})^2}}{\sqrt{N}}$ with x_i being the entry per ActIntPerXing bin i, $\bar{x}$ the arithmetic mean and N the total number of entries.

In two separate variations, the ActIntPerXing axis in data is shifted by $\pm\Delta\mu$. For the 5 TeV dataset with the pfoEM algorithm the uncertainty on the mean and thus the shift is $\Delta\mu = 0.00065$. Because of the smallness of this value, only small effects on the mass measurement can be expected.

By comparing the shifted data distribution to the Monte Carlo distribution, new event weights are generated and applied. All following event weights and scale factors are recalculated. These two new set of scale factors and event weights are applied to a W boson selection. By comparing the varied distributions to the original reference templates (no variations applied here), two W mass value for the pileup variation can be calculated and can be compared to the mass value obtained for the ideal reweighting without variations. Tab. 7.4 shows the results for the two datasets.

It can be seen that the numbers obtained from this estimate are all below 1 MeV and it

Algorithm	$\Delta M^{5\,\mathrm{TeV}+}_{pileup}$ [MeV]	$\Delta M^{5\,\mathrm{TeV}-}_{pileup}$ [MeV]	$\Delta M^{13\,\mathrm{TeV}+}_{pileup}$[MeV]	$\Delta M^{5\,\mathrm{TeV}-}_{pileup}$ [MeV]
pfo	−0.48	0.54	−0.53	0.075
pfoEM	−0.62	−0.84	0.11	0.21

Table 7.4.: Systematic uncertainties for the pileup calibration for the two algorithms pfo and pfoEM in the muon channel at 5 TeV and 13 TeV. The uncertainty ΔM_{pileup} is the difference in the mass value from the parabolic fit to the χ^2 distribution for the original and the varied distribution.

can be concluded, that the effect by a variation of the pileup event weights is small. For these low uncertainties, statistical fluctuations in the variations can play a larger role than the variation of the event weights. The exact numbers would need to be derived from a full error analysis, like it was done for the resolution scale factors described in the previous section. However, the errors will be much smaller than the uncertainty introduced by the other steps of the reweighting and this step will not be performed in this thesis.

7.4.3. Uncertainty on the ΣE_T event weights

The final uncertainty, which is going to be estimated is the error introduced by the event weights, which scale the remaining differences in the ΣE_T distribution as a function of the transverse boson momentum. Before deriving the uncertainty, the overall effect of these event weights is estimated. For this purpose, the original reweighting is compared to a reweighting, where the ΣE_T event weights are not applied. Consequently, the resolution scale factors are recalculated. The difference between the mass obtained when the ΣE_T event weights are applied and when they are removed from the calibration is shown in Tab. 7.5. The mass shift introduced by this is not small enough to be negligible. This can be explained by the fact, that the ΣE_T event weights remove real differences (included in the non-Gaussian behavior) of the parallel and perpendicular hadronic recoil distributions. If the ΣE_T event weights are not applied, the resolution calibration step, if it is only performed as a function of the transverse boson momentum as described here (see Sec. 6.8), cannot account for the differences as a function of ΣE_T.

It was chosen to perform the resolution calibration only in one dimension, as a function of $p_T^{boson}(reco)$, to allow for a good precision in the tails. The statistics would be too limited in the tails to derive the scale factor as function of an additional second quantity like ΣE_T. In this case, it can be seen from the mass shifts estimated here, that the ΣE_T reweighting step is crucial and cannot be removed if a high precision on the mass value for the W boson is aimed at.

Algorithm	$\Delta M^{5\,\mathrm{TeV}}_{SumEt}$ [MeV]	$\Delta M^{13\,\mathrm{TeV}}_{SumEt}$ [MeV]
pfo	34	10
pfoEM	35	52

Table 7.5.: Effect of the ΣE_T calibration on the mass measurement for the two algorithms pfo and pfoEM in the muon channel at 5 TeV and 13 TeV.

Because of the relevance of this reweighting step, its uncertainty is estimated. The large number of event weights for the ΣE_T reweighting[3] suggest to derive the uncertainty by randomly varying the event weights simultaneously within their Gaussian uncertainty (second approach for the resolution uncertainty) rather than shifting them separately like it was done in the first approach of the resolution uncertainties. Again, the subsequent calibration steps (resolution scaling) need to be recalculated in accordance to the new values.

For this analysis, 300 variations were performed and analyzed by comparing to the reference templates. The W mass values obtained for each variation fluctuate around the original mean. The uncertainty σ_{SumEt} is again given by a Gaussian fit to this mass distribution.

Algorithm	$\sigma_{SumEt}^{5\,\mathrm{TeV}}$ [MeV]	$\sigma_{SumEt}^{13\,\mathrm{TeV}}$ [MeV]
pfo	5.3	7.3
pfoEM	5.7	5.9

Table 7.6.: Systematic uncertainties for the ΣE_T calibration for the two algorithms pfo and pfoEM in the muon channel at 5 TeV and 13 TeV. The uncertainty σ_{SumEt} is obtained by a Gaussian fit to the spread of the mass fit results of all variations.

The results, listed in Tab. 7.6 are found to be around $5-7$ MeV for the both datasets. The error on these numbers is of the order of $1/\sqrt{2N} = 4\,\%$, where $N = 300$ is the number of variations. These results suggest that the calibration of the ΣE_T distribution is a relevant source of uncertainty and that this reweighting step is important for a precise calibration of the hadronic recoil.

7.4.4. Conclusion

In this chapter, the effect of systematic uncertainties of the hadronic recoil calibration on a W mass measurement has been estimated for the muon channel in the *lowMu* analyses. The calibration for which the uncertainties were derived consist of three main steps: The pileup reweighting is applied first, then ΣE_T event weights correct the remaining differences in the ΣE_T distribution and thirdly, the resolution of the hadronic recoil vector is scaled.

The largest effect of systematic variations is found for the third step, the resolution scaling. For the pfoEM algorithm an uncertainty value of $\sigma_{res}^{5\,\mathrm{TeV}} = 13$ MeV is estimated for the 5 TeV analysis and of $\sigma_{res}^{13\,\mathrm{TeV}} = 15$ MeV for the 13 TeV analysis. The second step, the ΣE_T event weights, are accompanied by an error of $\sigma_{SumEt}^{5/13\,\mathrm{TeV}} = 6$ MeV for both datasets. The uncertainty of the event weights of the first calibration step is found to be negligible, since any effects are balanced by the following calibration steps.

With the given data statistics, the systematic errors of the recoil calibration are currently exceeded by the statistical errors, which are estimated to be $\sigma_{stat}^{5\,\mathrm{TeV}} = 17$ MeV ($\sigma_{stat}^{13\,\mathrm{TeV}} = 18$ MeV) for the 5 TeV analysis (13 TeV analysis). With the new data taking in 2018, the statistics will be improved for the 13 TeV dataset, which will reduce this statistical uncertainty.

The second algorithm, which was analyzed here, pfo, introduces consistently larger uncertainties compared to pfoEM. The difference is around 1 MeV for all systematic as well

---

[3] In total up to 3000 event weights were derived by using 150 bins along the ΣE_T axis and 20 bins on the $p_T^{boson}(reco)$ axis. However, many values thereof are set to zero because of the low statistics in the tails.

as statistical uncertainties analyzed here. Therefore it is recommended to use pfoEM as the main algorithm for a full W mass measurement.

The statistical and systematic uncertainties for the electron channel are not estimated in this thesis. However, they are expected to be comparable. The data statistics available is alike and the calibration procedure and its performance were found to be similar for the electron channel in the previous chapter. A differing effect of systematic variations is therefore not expected. A combination of the electron and muon channel in the full measurement of the W boson mass will therefore lead to smaller overall errors.

CHAPTER 8

Summary

A novel approach for the calibration of the hadronic recoil was presented in this thesis. The main aspect of this reweighting technique is the modeling of the average hadronic activity with regard to an identical $\langle \Sigma E_T \rangle$ value per pileup interaction. The calibrations were derived with a Z boson selection. They were tested first for the dataset at a center of mass energy of 8 TeV recorded by the ATLAS experiment and applied to the recent *lowMu* datasets with a reduced number of interactions per bunch crossing. For the general configurations, the main difference in the modeling of the ΣE_T distribution in the Monte Carlo simulations could be removed by a set of pileup-dependent event weights. With additional ΣE_T dependent event weights and scale factors to adjust the resolution and the bias of the parallel and the perpendicular hadronic recoil components, an overall good agreement between data and the simulations in events containing a Z boson could be achieved.

In general it can be concluded, that the effectiveness of this reweighting technique depends on two factors: the algorithm implementation and the collision parameters of the dataset. Pileup events need to play at least a small role in order to allow for a modest effectiveness. This approach is suited well for the 8 TeV analysis, where large amounts of pileup are present. But also the *lowMu* analyses, where the data taking aimed on the opposite effect of a low pileup contribution, showed good results. It could be shown, that a small lever arm with a narrow pileup distribution can already be used for this reweighting approach.

The second influencing factor which was observed is the composition of the hadronic activity included in the recoil calculation of the individual algorithms. All implementations that were at least partially based on clusters measured in the calorimeter showed good results. All reconstructed clusters are affected by pileup, although the influence can be reduced as it was done in the particle flow algorithms in the *lowMu* datasets. The vertex reconstruction of tracks on the other hand allows to distinguish particles of the hard interaction from pileup. The necessary lever arm for the reweighting is thus hardly given, when a strict primary vertex track selection is applied.

In the 8 TeV analysis, the cluster algorithm was modeled very well by the pileup and ΣE_T reweighting. Track algorithms without a primary vertex cut included large amounts of pileup and thus showed a good agreement between data and simulations after the reweighting was applied. Implementations that only use tracks from the primary vertex are not calibrated well with this method. Nevertheless, even if only a small effect from the pileup is present, data and the simulations can differ because of the underlying event modeling.

The overall performance of the cluster algorithm with respect to resolution and the modeling of the transverse boson momentum dependency was found to be good. This implementation gives a conclusive description of the hadronic recoil. Track algorithms without a cut on the primary vertex performed poorly in the recoil description and are not a suitable candidate for the W mass measurement. The two trackPV algorithms show a good resolution, but the average hadronic activity needs to be modeled by a different reweighting approach.

The main algorithms for the *lowMu* analysis are based on a combination of clusters and tracks. It was shown that the reweighting approach could successfully be applied to the pfo algorithms in these datasets despite the narrow pileup range available here. The fact, that the standard pfo algorithms contain neutral clusters allows for a positive effect of this reweighting approach. However, if only tracks are considered for the recoil calculation, the performance of the reweighting is not good. When using only neutral clusters it can be seen, that the recoil description is not perfectly balanced and as a consequence, the reweighting is not ideal.

It was found that the reweighting is sensitive to the fine tuning of the pileup distributions if working with a narrow pileup distribution. An adverse choice of binning can already remove a large amount of the effect. The best results can be obtained with the discrete values for which the pileup is generated in the simulations. However, if a finer binning were available in the simulations the results could be improved further. In general it can be noted, that this approach needs to be cautiously applied to datasets with a fixed number of simultaneous interactions per collision.

The effect of the resolution scaling, which adapts differences in the simulated Gaussian widths of the parallel and perpendicular component, is positive for all datasets analyzed here. The scale factors were derived as a function of the transverse boson momentum. The central regions of these distribution largely follow a Gaussian shape and the modeling in the simulations can thus be optimized to be almost identical to data here. The tails can show discrepancies, which however seem to be dependent on the exact lepton selection criteria. A two-dimensional approach, as a function on the transverse boson momentum and of ΣE_T, could improve the description in the tails of the simulations. However, high enough statistics are needed when determining the resolution as a function of two parameters.

The set of event weights and scale factors could successfully be extrapolated to a $W \to \mu\nu$ selection. The relevant quantities were calculated with respect to the truth information available in the simulations. The data to Monte Carlo agreement could be improved by the reweighting. Since no background contributions were considered in the simulations, remaining disagreements are not unexpected.

The influence of finite statistics and of the reweighting approach on a measurement of the mass of the W boson with the transverse mass distribution was estimated for the muon channel. The measurement was done by comparing a set of simulated templates to pseudodata and fitting a parabola to the χ^2 test results. The minimum of this curve reveals the mass point that fits data best. By applying systematic variations, the effect thereof can be estimated. The real data taken by ATLAS was only used to derive the calibrations with a Z boson selection and used to scale the pseudodata to reflect the available statistics in data. By this, the value of the W mass of the ATLAS datasets were not revealed by this uncertainty estimation.

For the statistical uncertainty a value of $\sigma_{stat}^{5\,\mathrm{TeV}} = 17\,\mathrm{MeV}$ was found for the pfoEM algorithm in the muon channel of the 5 TeV dataset and of $\sigma_{stat}^{13\,\mathrm{TeV}} = 18\,\mathrm{MeV}$ for the 13 TeV dataset. The pfo algorithm gives up to 1 MeV larger values.

The systematic variations of the reweighting event weights and scale factors result in an uncertainty of $\sigma_{res}^{5\,\mathrm{TeV}} = 13\,\mathrm{MeV}$ and $\sigma_{res}^{13\,\mathrm{TeV}} = 15\,\mathrm{MeV}$ for the resolution scale factors with the pfoEM algorithm in the muon channel of the 5 TeV and 13 TeV analysis respectively. The effect of systematic variations of the ΣE_T event weights were estimated to be around $\sigma_{SumEt}^{5/13\,\mathrm{TeV}} = 6\,\mathrm{MeV}$ (both datasets). The pileup event weights are found to have a negligible systematic uncertainty, since any effect can be balanced by the subsequent calibration steps.

The statistical as well as systematic uncertainties can be reduced, when more data becomes available for the 13 TeV analysis with the 2018 *lowMu* data taking. In addition, the combination of the uncertainties for the muon selection with the results of the electron selection will reduce the overall uncertainty. With this, a full measurement of the W boson mass in the *lowMu* datasets can be well comparable to the previous measurements and be able to improve the precision on the world average further.

Appendices

APPENDIX A

The datasets used in the analysis

The various datasets used for the analysis are listed in this section. In the first table, the references for the data samples are given along with the corresponding tags, which indicate the details of the applied processing. Since the hadronic recoil algorithm calculation was expanded to include a wider variety of algorithms to study its performance, the last processing step was performed on AODs and the typical run 1 format, D3PDs, were generated from them in a private transform job. The officially produced AOD input to this last step is listed here.

The *lowMu* analysis in done in the run 2 framework, where the overall analysis framework including the file format was updated, yielding first xAODs and subsequently derivations (DAODs), which have a reduced size and several common analysis steps already applied. In this case STDM4, a version of standard model derivations, is used. In addition, the data was further processed into minitrees, that removed unnecessary variables to decrease the size of the tuple further.

The second table lists the signal simulations used in the analysis along with the corresponding calculated cross section for each sample. Each simulation is tagged with the production year, center of mass energy, a 6-digit signal process identifier, the name and tunes of the generators, an easy to understand name of the process, the data format and the list of processing tags.

Data		
Full Name	period	events
data12_8TeV.periodB.physics_Muons.PhysCont.AOD.repro14_v01 (r4065_p1278)	B	40 984 045
data12_8TeV.periodG.physics_Muons.PhysCont.AOD.repro14_v01 (r4065_p1278)	G	2 148 000
data17_5TeV.00340644.physics_Main.deriv.DAOD_STDM4.f895_m1902_p3372	M1	311 251
data17_5TeV.00340683.physics_Main.deriv.DAOD_STDM4.f896_m1902_p3372	M2	198 361
data17_5TeV.00340697.physics_Main.deriv.DAOD_STDM4.f896_m1902_p3372	M2	1 791 775
data17_5TeV.00340718.physics_Main.deriv.DAOD_STDM4.f896_m1902_p3372	M2	4 403 595
data17_5TeV.00340814.physics_Main.deriv.DAOD_STDM4.f897_m1902_p3372	M2	2 689 795
data17_5TeV.00340850.physics_Main.deriv.DAOD_STDM4.f897_m1907_p3372	M3	1 238 606
data17_5TeV.00340910.physics_Main.deriv.DAOD_STDM4.f898_m1907_p3372	M3	1 385 254
data17_5TeV.00340918.physics_Main.deriv.DAOD_STDM4.f898_m1907_p3372	M3	446 645
data17_5TeV.00340925.physics_Main.deriv.DAOD_STDM4.f898_m1907_p3372	M3	543 446
data17_5TeV.00340973.physics_Main.deriv.DAOD_STDM4.f899_m1912_p3372	M4	1 426 339
data17_5TeV.00341027.physics_Main.deriv.DAOD_STDM4.f902_m1912_p3372	M5	3 475 353
data17_5TeV.00341123.physics_Main.deriv.DAOD_STDM4.f902_m1912_p3372	M5	1 799 816
data17_5TeV.00341184.physics_Main.deriv.DAOD_STDM4.f903_m1912_p3372	M5	2 320 714
data17_13TeV.00341294.physics_Main.deriv.DAOD_STDM4.f907_m1912_p3267	N1	300 962
data17_13TeV.00341312.physics_Main.deriv.DAOD_STDM4.f903_m1912_p3267	N2	5 683 301
data17_13TeV.00341419.physics_Main.deriv.DAOD_STDM4.f903_m1912_p3267	N2	9 402 807
data17_13TeV.00341534.physics_Main.deriv.DAOD_STDM4.f903_m1912_p3267	N4	15 902 552
data17_13TeV.00341615.physics_Main.deriv.DAOD_STDM4.f903_m1912_p3267	N4	9 583 287
data17_13TeV.00341649.physics_Main.deriv.DAOD_STDM4.f903_m1917_p3267	N4	3 614 519

Table A.1.: The datasets used in the analysis.

Monte Carlo Simulations		
Process	Name	$\sigma[pb]$
$Z \rightarrow \mu\mu$	mc12_8TeV.207309.PowhegPythia8_CT14nnlo_Zjmumu.merge.AOD.e5347_s2801_r8543_r4540	967.78
$Z \rightarrow \mu\mu$	mc12_8TeV.129681.PowhegPythia8_AU2CT10_Zmumu_DiLeptonFilter.merge.AOD.e2095_s1581_s1586_r4650_r4540	1 110.0
$Z \rightarrow \mu\mu$	mc16_5TeV.361107.PowhegPythia8EvtGen_AZNLOCTEQ6L1_Zmumu.deriv.DAOD_STDM4.e4916_s3238_r10243_r10210_p3374	642.8
$Z \rightarrow ee$	mc16_5TeV.361106.PowhegPythia8EvtGen_AZNLOCTEQ6L1_Zee.deriv.DAOD_STDM4.e4916_s3238_r10243_r10210_p3374	642.8
$W^+ \rightarrow e\nu$	mc16_5TeV.361100.PowhegPythia8EvtGen_AZNLOCTEQ6L1_Wplusenu.deriv.DAOD_STDM4.e4916_s3238_r10243_r10210_p3374	4 190.5
$W^- \rightarrow e\nu$	mc16_5TeV.361103.PowhegPythia8EvtGen_AZNLOCTEQ6L1_Wminusenu.deriv.DAOD_STDM4.e4916_s3238_r10243_r10210_p3374	2 736.8
$W^+ \rightarrow \mu\nu$	mc16_5TeV.361101.PowhegPythia8EvtGen_AZNLOCTEQ6L1_Wplusmunu.deriv.DAOD_STDM4.e4916_s3238_r10243_r10210_p3374	4 190.5
$W^- \rightarrow \mu\nu$	mc16_5TeV.361104.PowhegPythia8EvtGen_AZNLOCTEQ6L1_Wminusmunu.deriv.DAOD_STDM4.e4916_s3238_r10243_r10210_p3374	2 737
$Z \rightarrow \mu\mu$	mc16_13TeV.361107.PowhegPythia8EvtGen_AZNLOCTEQ6L1_Zmumu.deriv.DAOD_STDM4.e4916_s3238_r10243_r10210_p3374	1 911
$Z \rightarrow ee$	mc16_13TeV.361106.PowhegPythia8EvtGen_AZNLOCTEQ6L1_Zee.deriv.DAOD_STDM4.e4916_s3238_r10243_r10210_p3374	1 911
$W^+ \rightarrow e\nu$	mc16_13TeV.361100.PowhegPythia8EvtGen_AZNLOCTEQ6L1_Wplusenu.deriv.DAOD_STDM4.e4916_s3238_r10243_r10210_p3374	11 306
$W^- \rightarrow e\nu$	mc16_13TeV.361103.PowhegPythia8EvtGen_AZNLOCTEQ6L1_Wminusenu.deriv.DAOD_STDM4.e4916_s3238_r10243_r10210_p3374	8 291
$W^+ \rightarrow \mu\nu$	mc16_13TeV.361101.PowhegPythia8EvtGen_AZNLOCTEQ6L1_Wplusmunu.deriv.DAOD_STDM4.e4916_s3238_r10243_r10210_p3374	11 299
$W^- \rightarrow \mu\nu$	mc16_13TeV.361104.PowhegPythia8EvtGen_AZNLOCTEQ6L1_Wminusmunu.deriv.DAOD_STDM4.e4916_s3238_r10243_r10210_p3374	8 287

Table A.2.: The simulated datasets used in the analysis. For the 8 TeV analysis, the first sample (identifier 207309) is the main Z boson simulation used for the performance studies.

APPENDIX B

Basic event weights and scale factors for all datasets

B.1. Event weights to correct the transverse boson momentum in the simulations

This section lists the full set of event weights for all datasets in Fig. B.1, which are used to correct the transverse boson momentum distribution in the simulations.

B.2. Reference plots for the energy scale factors

The following figures (B.2 to B.4) show the dependency of the parallel hadronic recoil component on the transverse boson momentum, separately for each algorithm in the various datasets. The slope obtained in the linear fit is used as a scale factor to adjust the hadronic recoil vector accordingly.

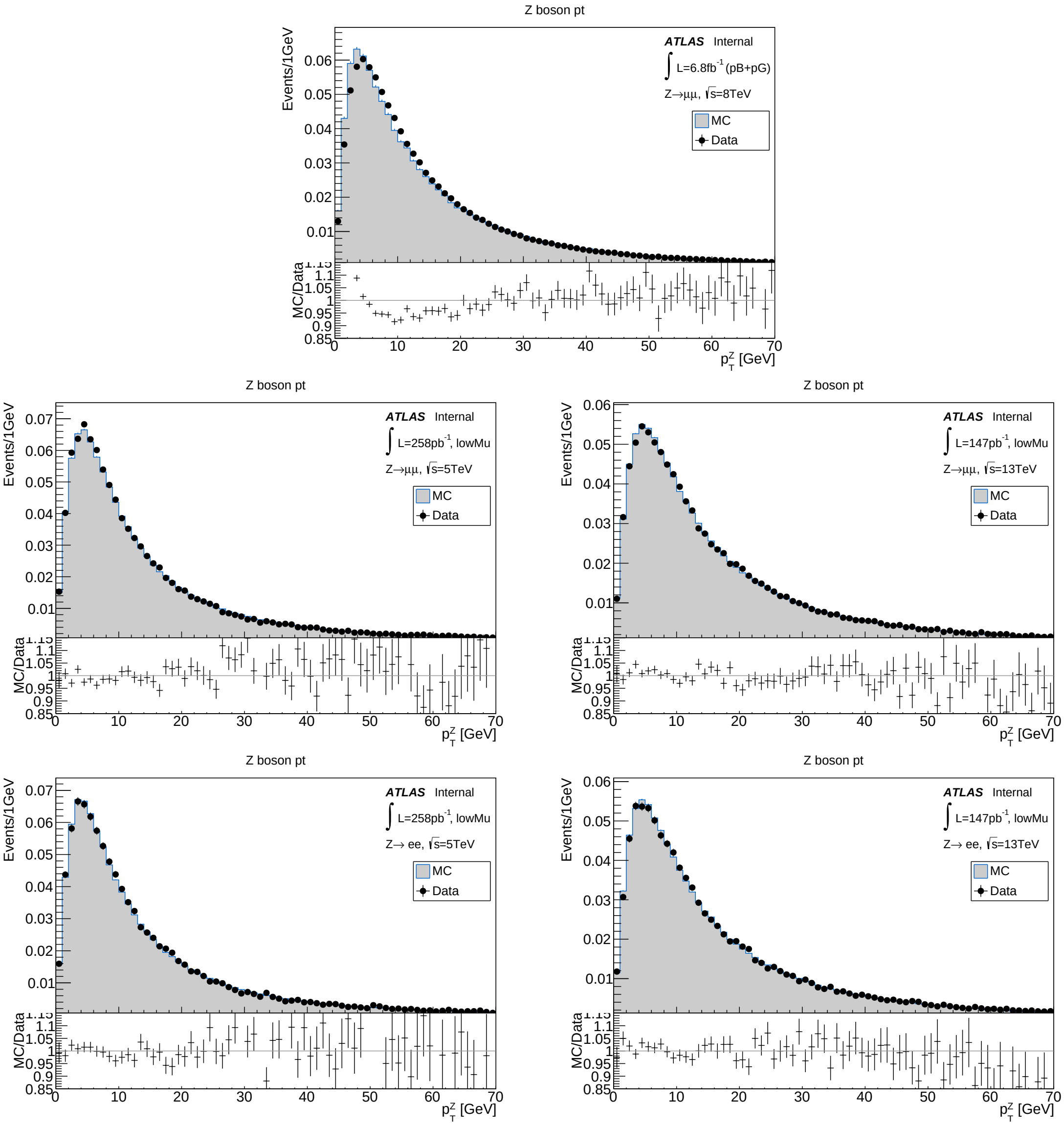

Figure B.1.: Event weights for p_T^{boson} modeling for all datasets.

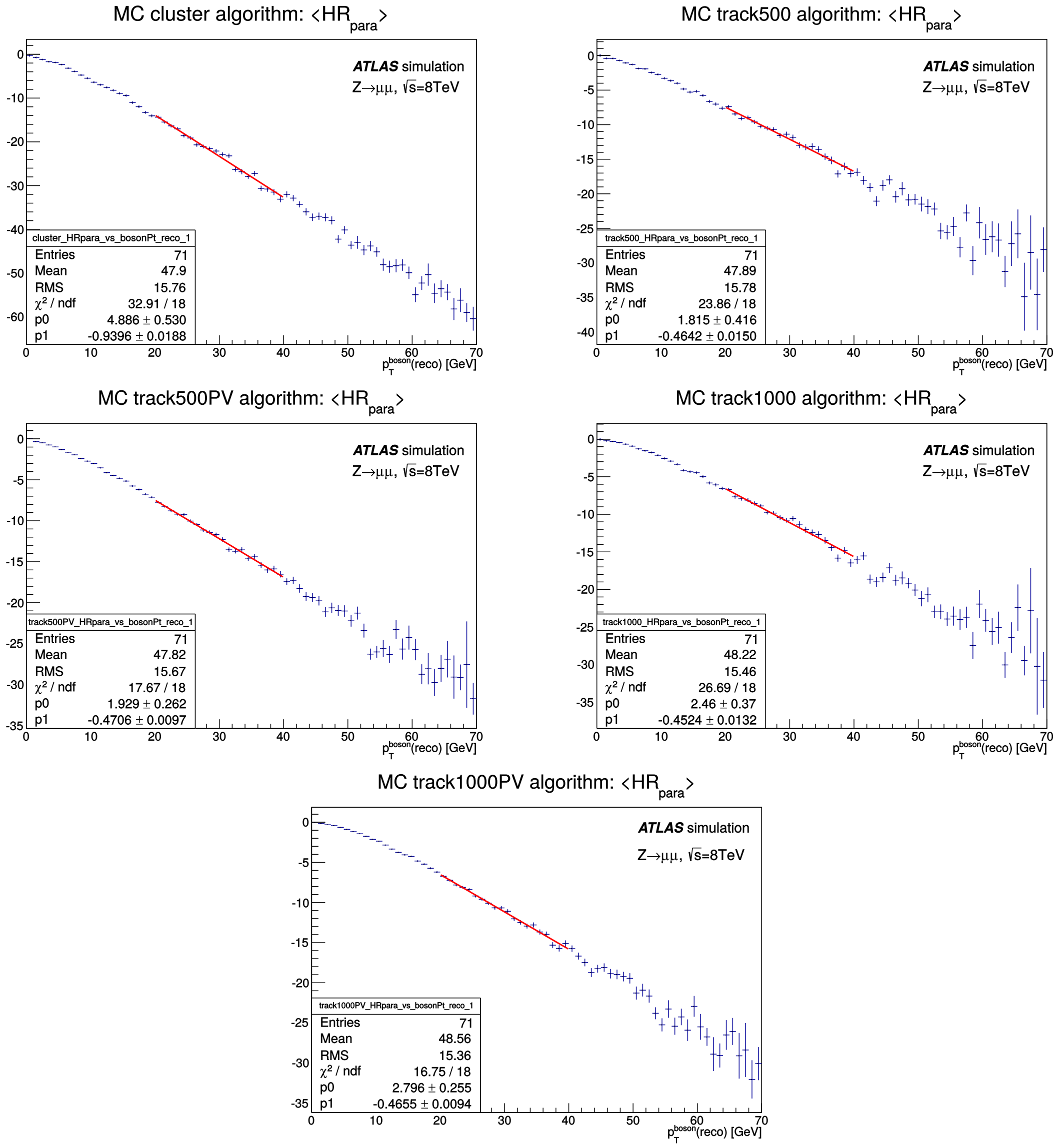

Figure B.2.: Reference plots for determining the energy scale factors for all algorithms for the 8 TeV analysis.

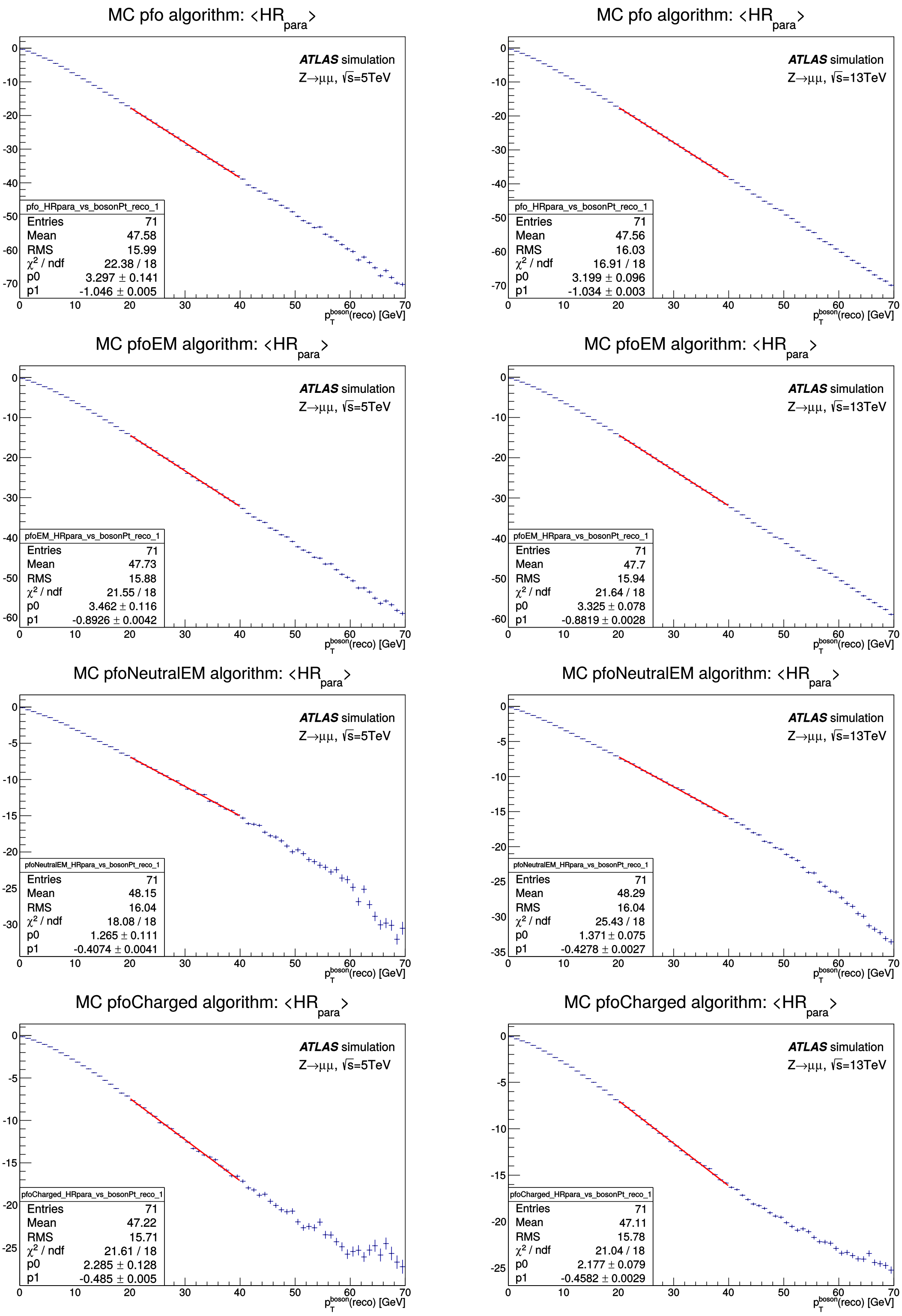

Figure B.3.: Reference plots for determining the energy scale factors for all algorithms for the $Z \to \mu\mu$ *lowMu* analysis.

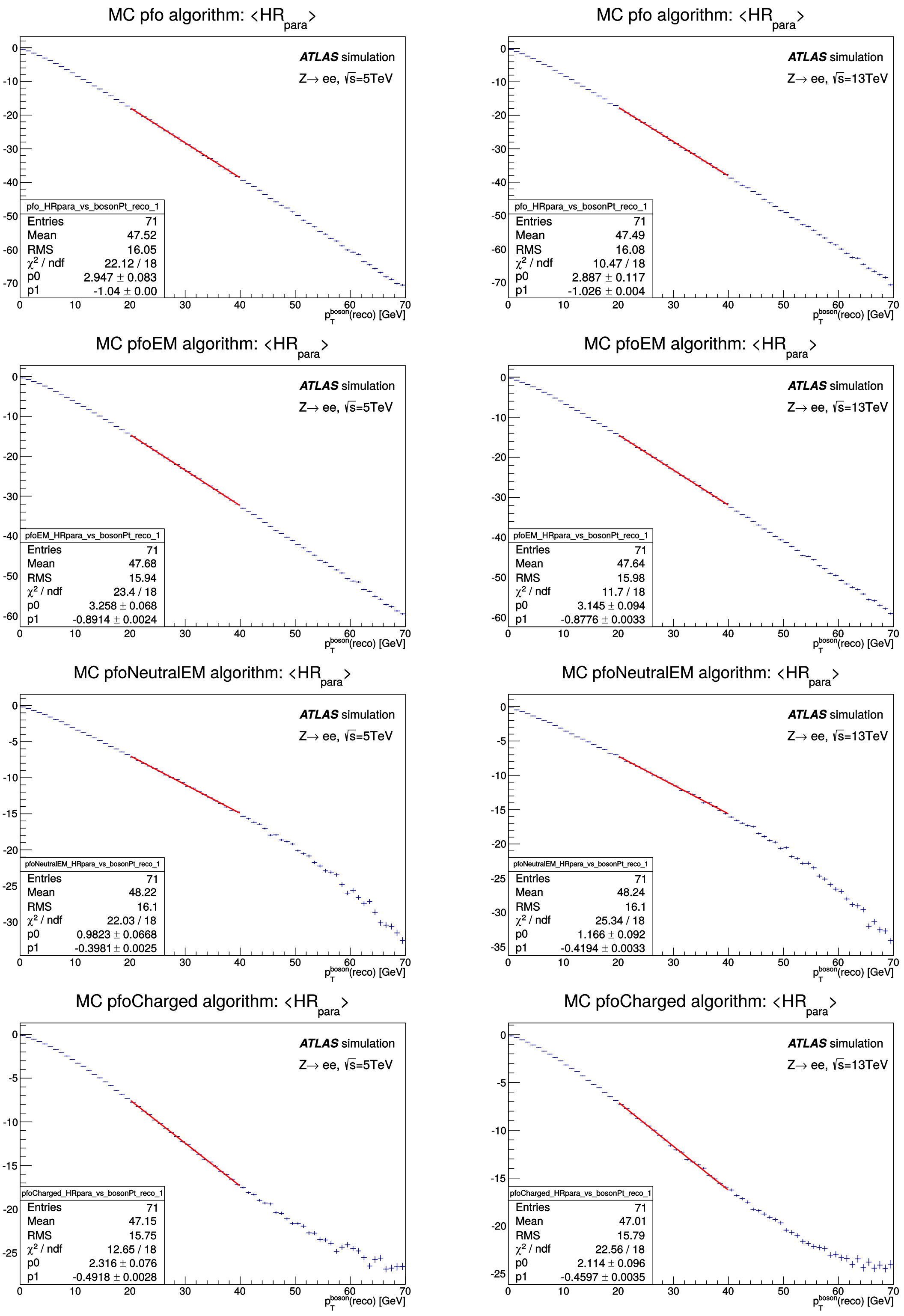

Figure B.4.: Reference plots for determining the energy scale factors for all algorithms for the $Z \to ee$ *lowMu* analysis.

APPENDIX C

Control plots for the *lowMu* analyses

This section includes the set of general control plots showing the muon and Z boson kinematics in the two *lowMu* analyses with the muon channel (Fig. C.1 and Fig. C.2) and the electron channel (Fig. C.3 and Fig. C.4).

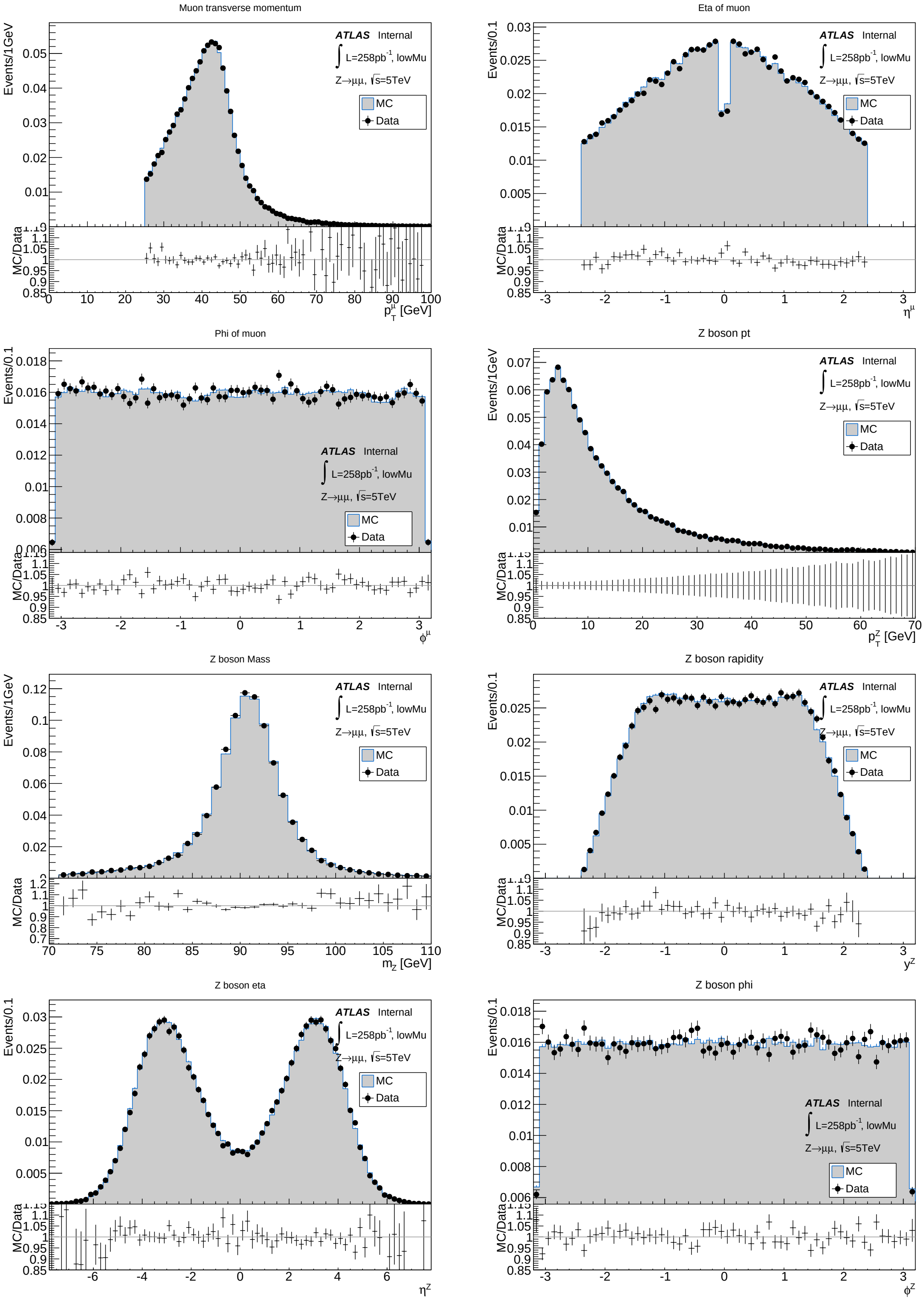

Figure C.1.: Z boson and muon kinematic distributions for the *lowMu* 5 TeV muon analysis.

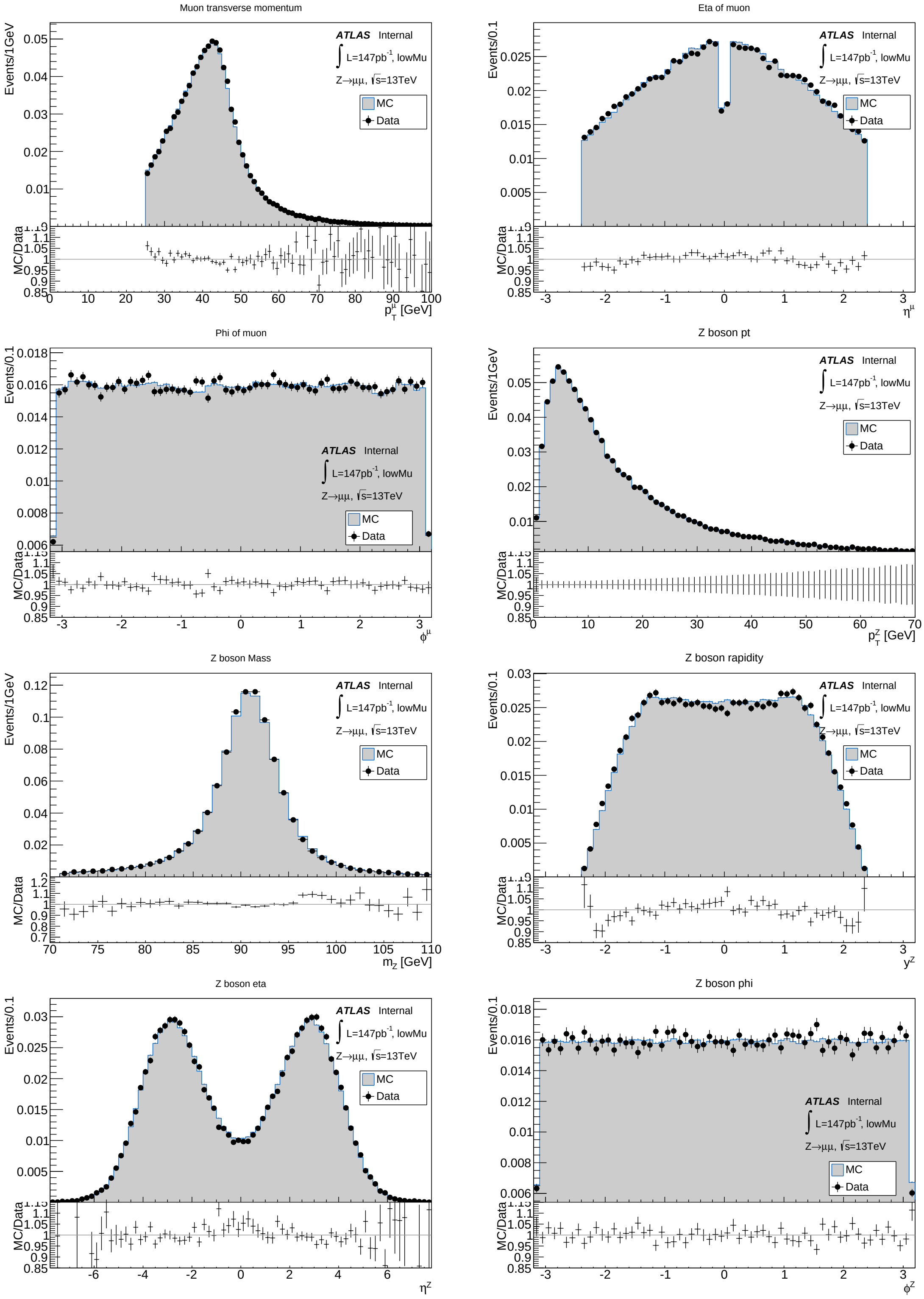

Muon transverse momentum

Eta of muon

Phi of muon

Z boson pt

Z boson Mass

Z boson rapidity

Z boson eta

Z boson phi

Figure C.2.: *Z* boson and muon kinematic distributions for the *lowMu* 13 TeV muon analysis.

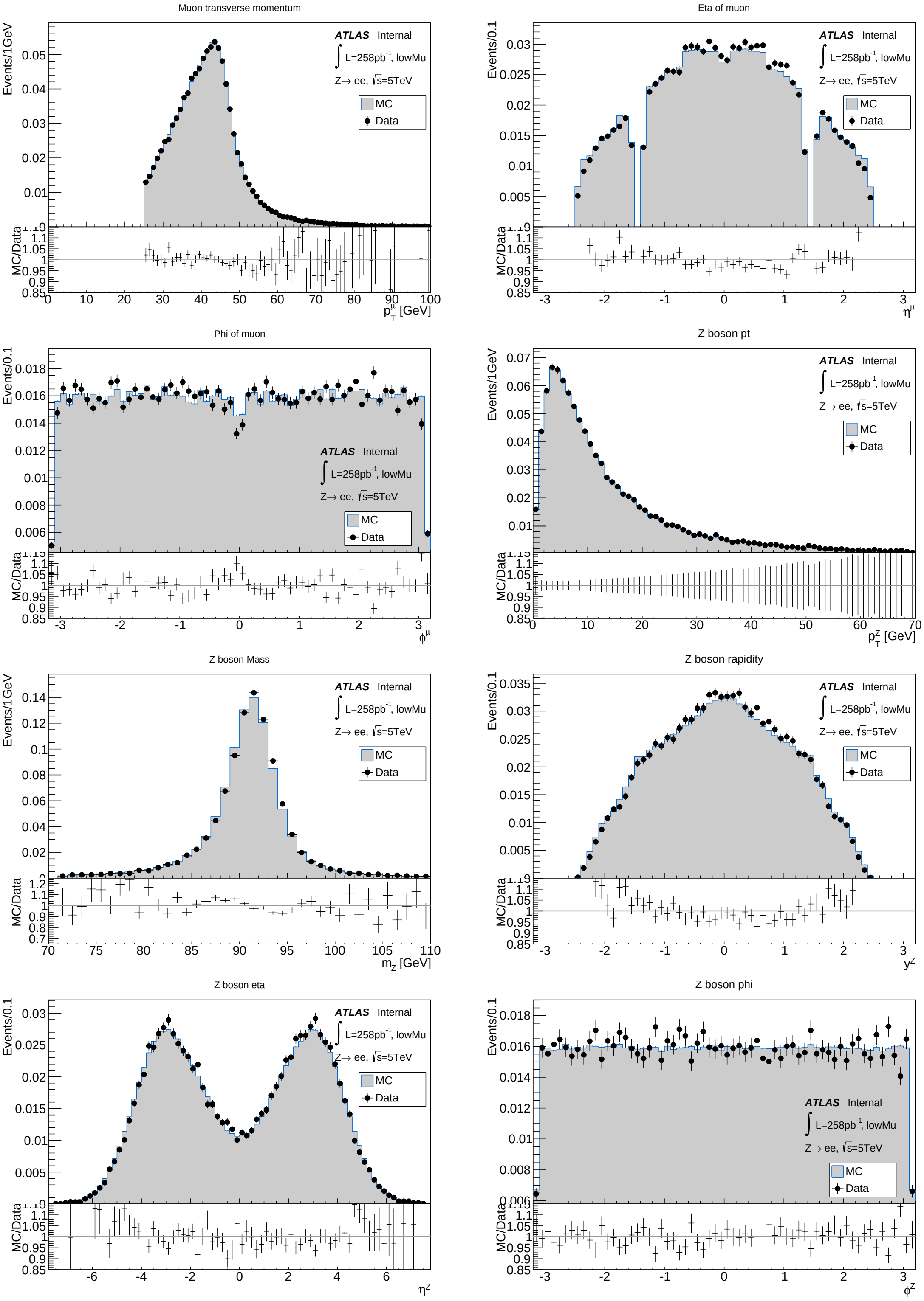

Figure C.3.: Z boson and electron kinematic distributions for the *lowMu* 5 TeV electron analysis.

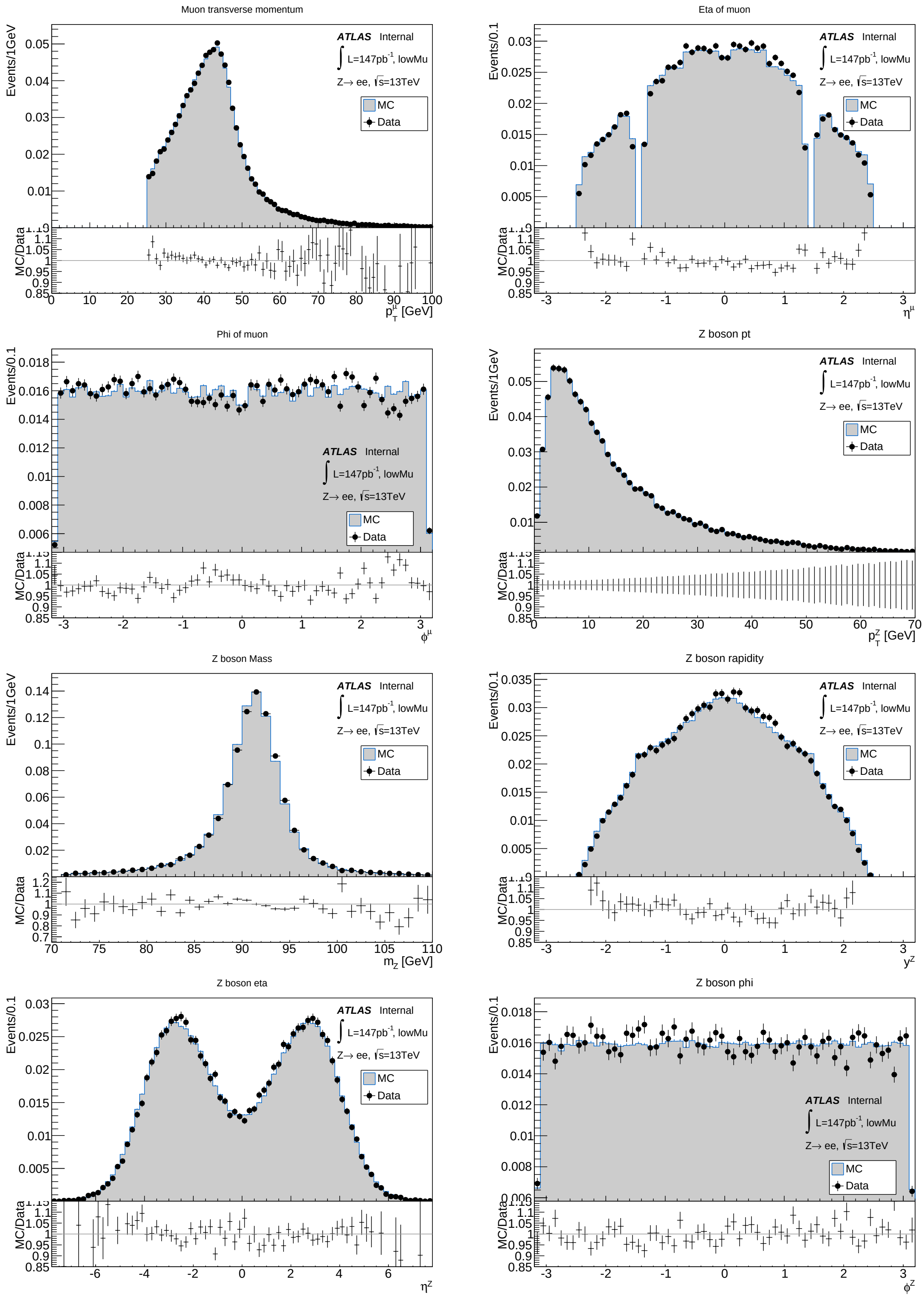
Muon transverse momentum

Eta of muon

Phi of muon

Z boson pt

Z boson Mass

Z boson rapidity

Z boson eta

Z boson phi

Figure C.4.: Z boson and electron kinematic distributions for the *lowMu* 13 TeV electron analysis.

APPENDIX D

Unweighted hadronic recoil plots for the *lowMu* analyses

The full set of plots that show the performance of the unweighted hadronic recoil for the various algorithms in the two *lowMu* datasets are given separately for the $Z \to \mu\mu$ (Fig. D.1 and D.2) and $Z \to ee$ selection (Fig. D.3 and D.4).

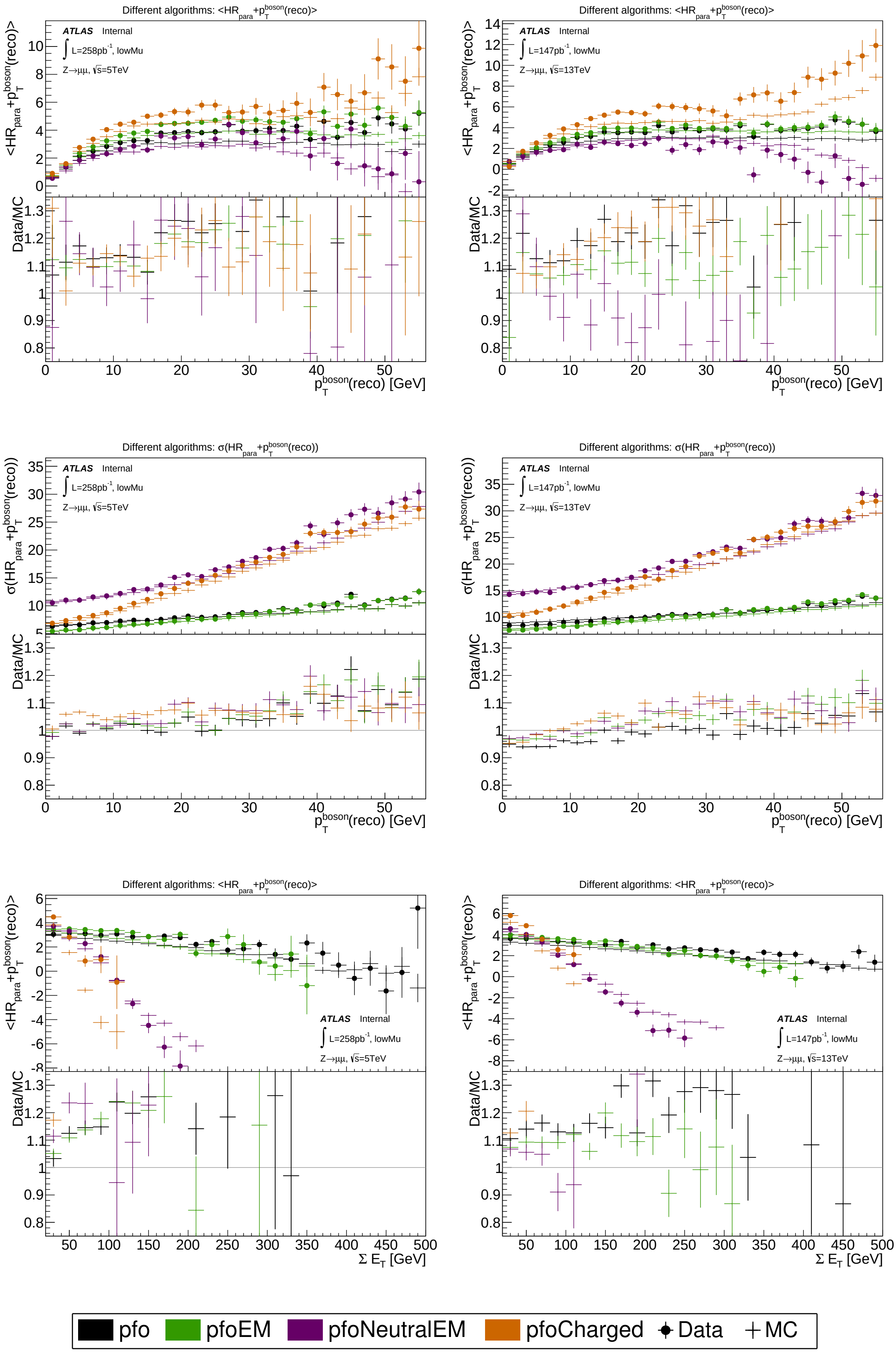

Figure D.1.: Several mean and resolution distributions for the bias $HR_{par} + p_T^{boson}(reco)$. The various hadronic recoil algorithms in the $Z \rightarrow \mu\mu$ *lowMu* analysis are shown without main reweighting applied.

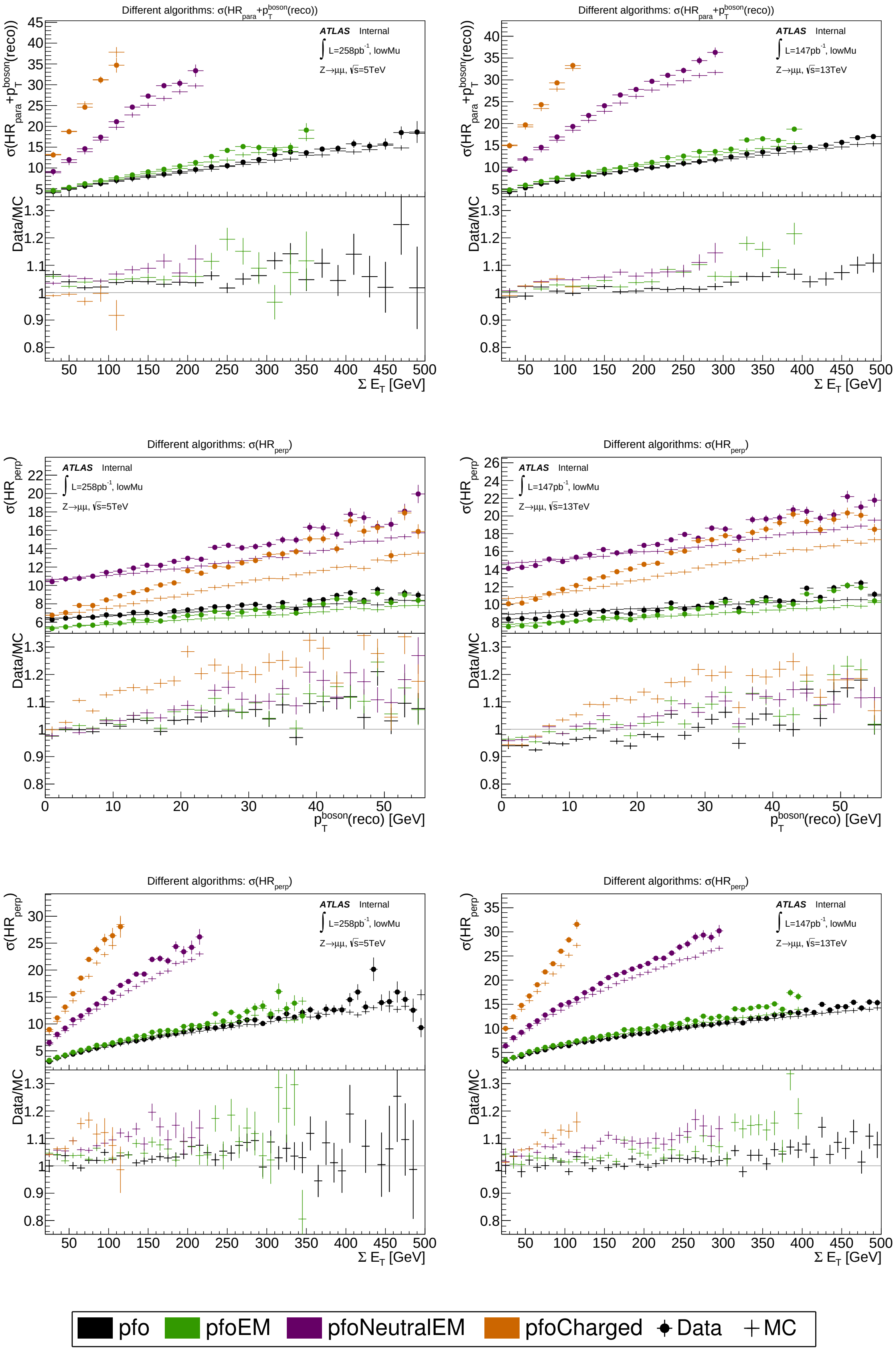

Figure D.2.: Resolution distributions of the parallel and perpendicular component. The various hadronic recoil algorithms in the $Z \to \mu\mu$ *lowMu* analysis are shown without main reweighting applied.

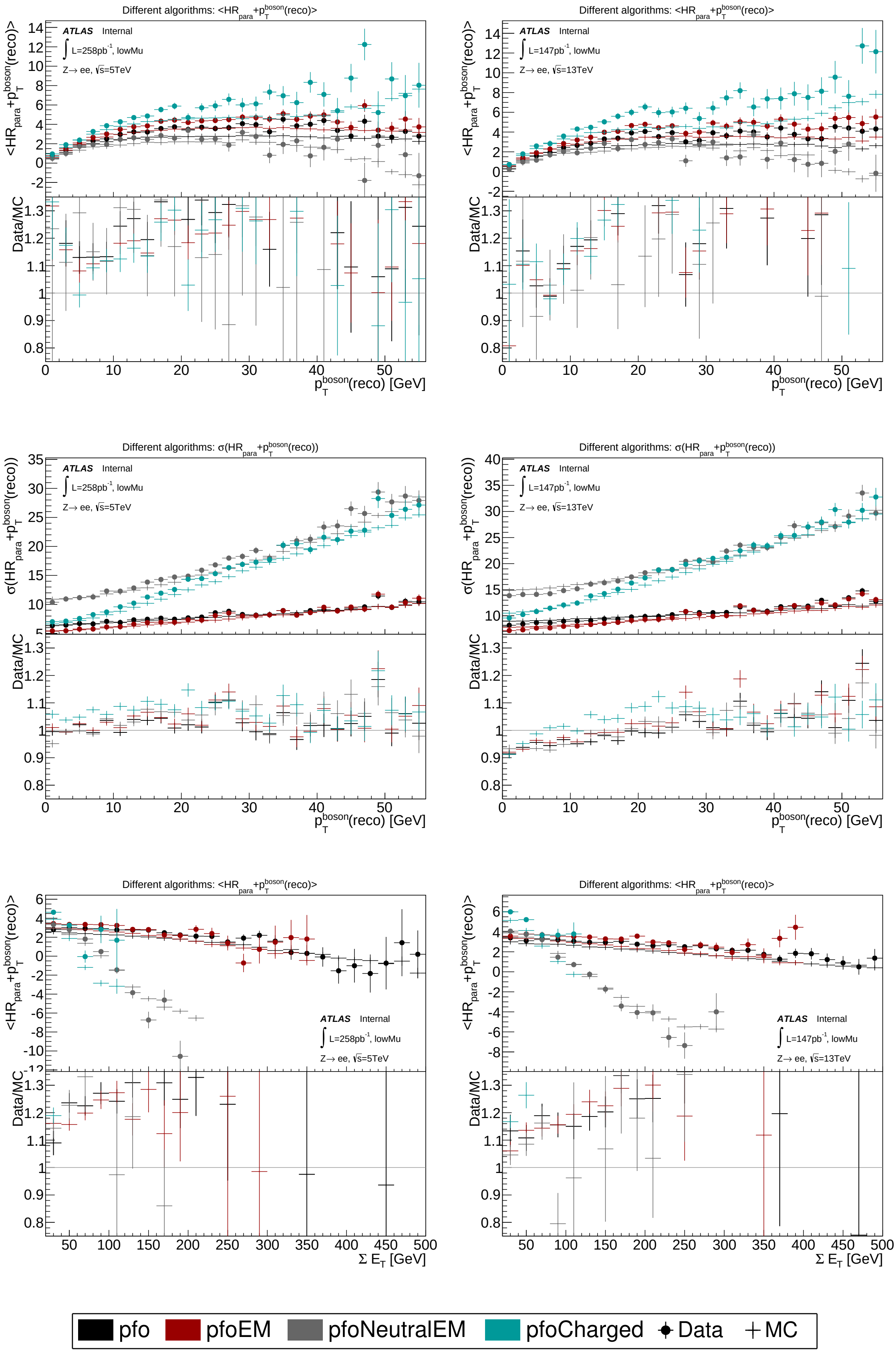

Figure D.3.: Several mean and resolution distributions for the bias $HR_{par} + p_T^{boson}(reco)$. The various hadronic recoil algorithms in the $Z \to ee$ *lowMu* analysis are shown without main reweighting applied.

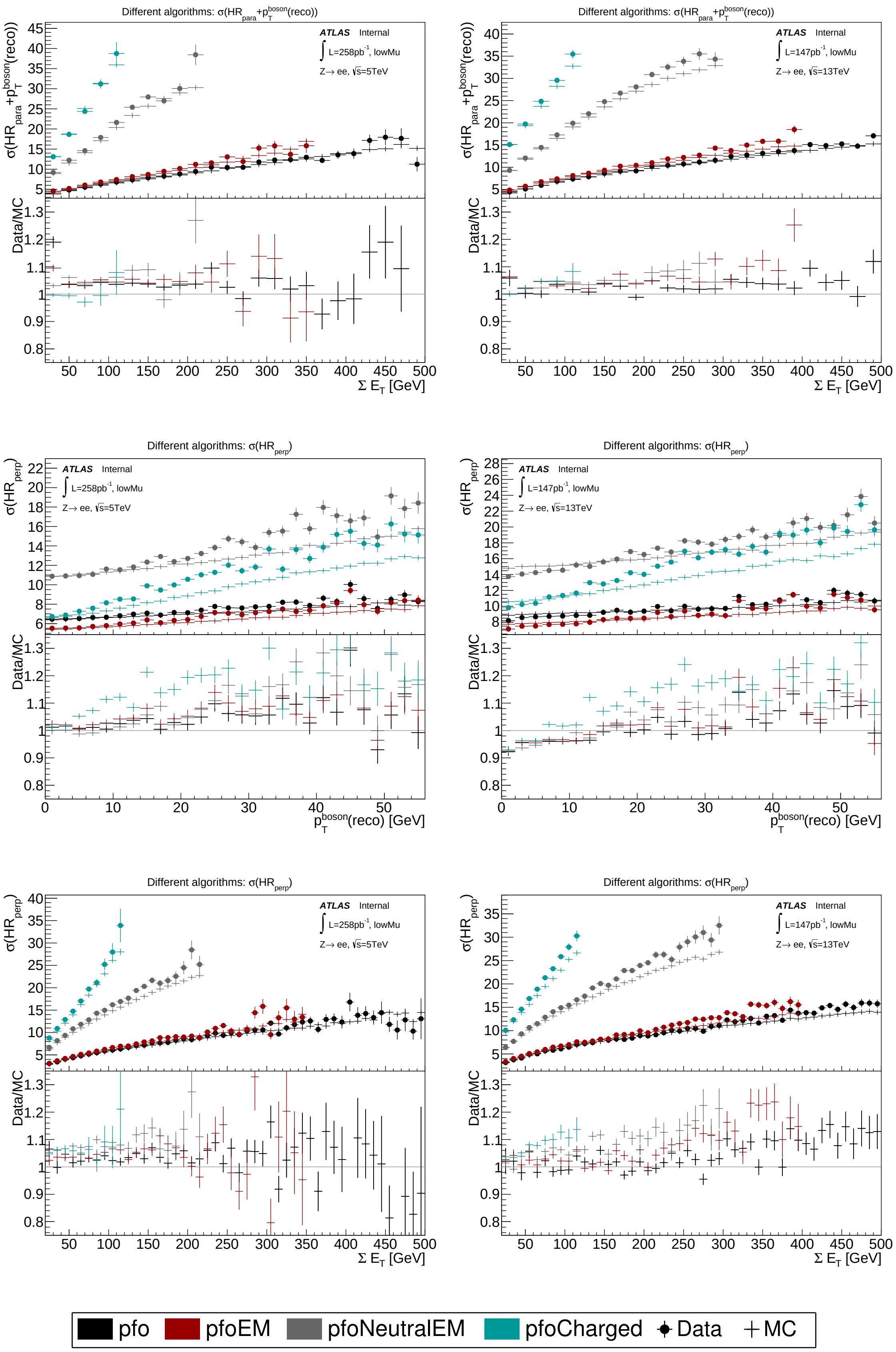

Figure D.4.: Resolution distributions of the parallel and perpendicular component. The various hadronic recoil algorithms in the $Z \rightarrow ee$ *lowMu* analysis are shown without main reweighting applied.

APPENDIX E

Pileup distribution for the *lowMu* $Z \to ee$ analyses

The general distribution of the pileup is shown in Fig. E.1 for the two datasets of the *lowMu* analysis for the electron selection.

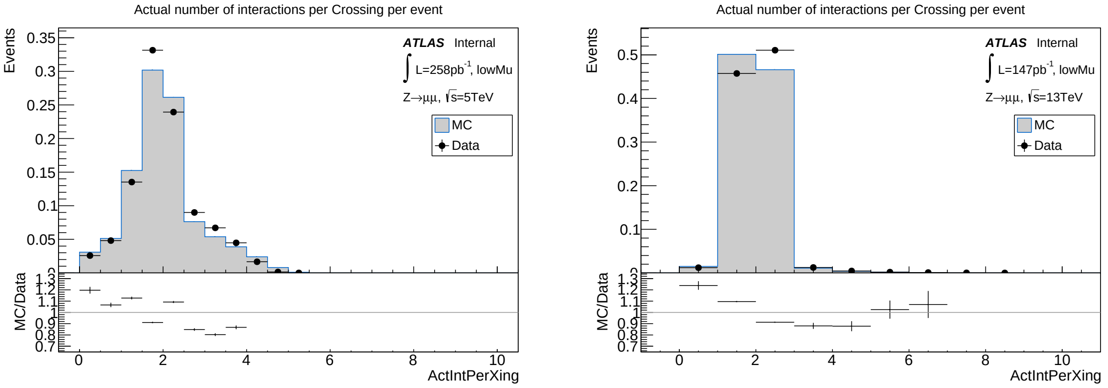

Figure E.1.: The pileup measured by the quantity of the actual interactions per bunch crossing for the two *lowMu* run campaigns as well as the unweighted distribution of the MC simulation for the $Z \to ee$ analyses. The number of simultaneous collisions was reduced by separation leveling of the colliding beams. In the 5 TeV dataset, between 1 and 5 simultaneous collisions are registered, while for the 13 TeV dataset, dominantly two simultaneous interactions are observed. The lower section of each plot shows the event weights, which are used to adapt the simulated distribution to the data.

APPENDIX F

ΣE_T vs. pileup distributions and fits

F.1. 8 **TeV** analysis

This section shows the full set of plots, which were used to fit the dependency of $\langle \Sigma E_T \rangle$ as a function of pileup for the various algorithms of the 8 TeV dataset in Fig. F.1 and F.2.

F.2. *lowMu* analyses

The corresponding set of plots is given for the different algorithms of the two *lowMu* datasets. The plots are shown for the muon selection in Fig. F.3 and F.4 and for the electron selection in Fig. F.5 and F.6.

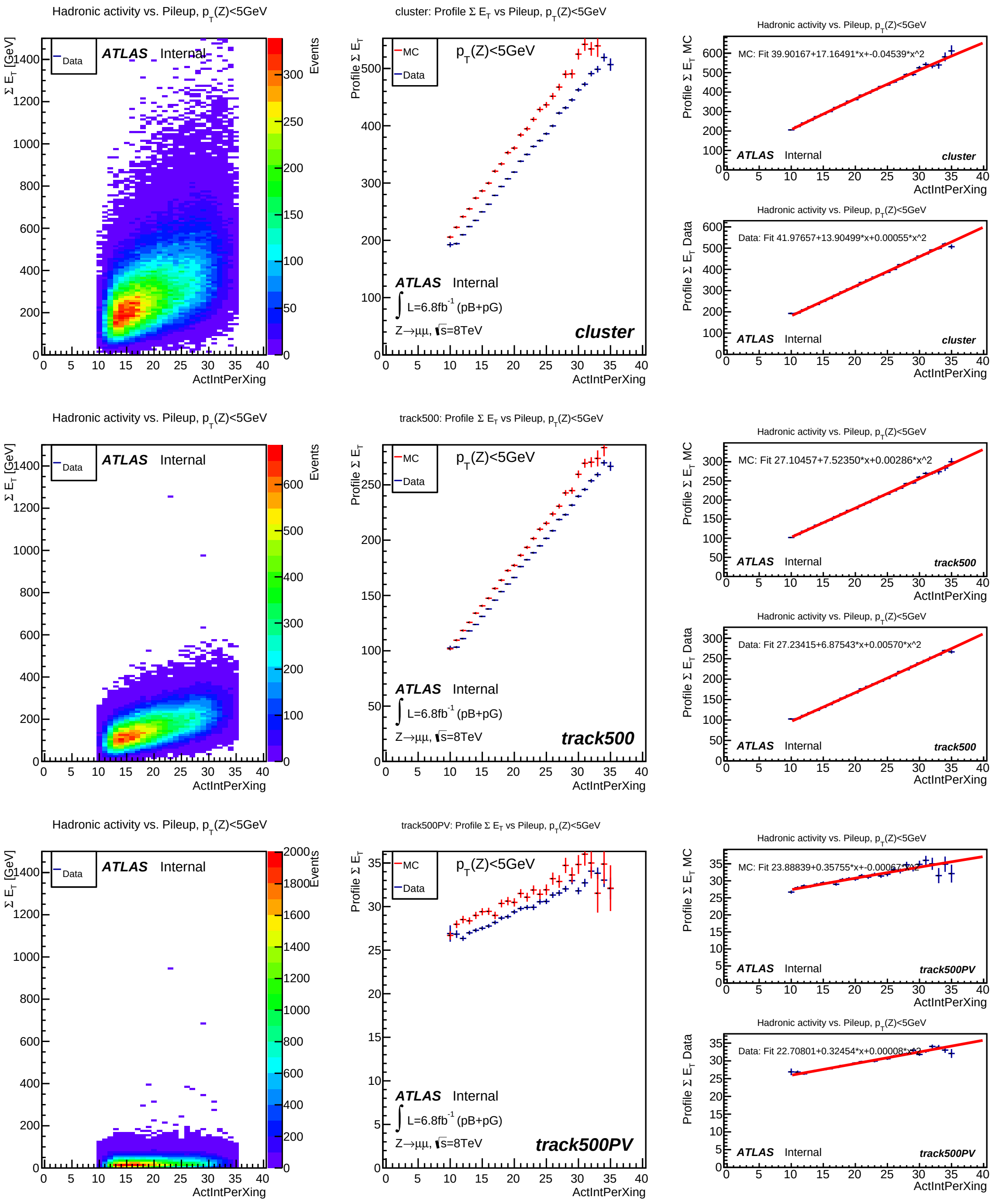

Figure F.1.: First step of the ΣE_T reweighting: The left plot shows the distribution of the events as a function of ΣE_T and pileup (ActIntPerXing) for data. Only events where the reconstructed transverse boson momentum is small ($p_T(Z) < 5\,\text{GeV}$) are taken into account here. In the central plot, the mean ΣE_T value for every pileup bin is computed (profile ΣE_T), showing the dependence of the average ΣE_T on pileup for both data (red) and simulation (blue). The right plot shows the profile of ΣE_T again separately for data and simulation and a corresponding fit $A + B \cdot x + C \cdot x^2$ as well as the fit parameters.

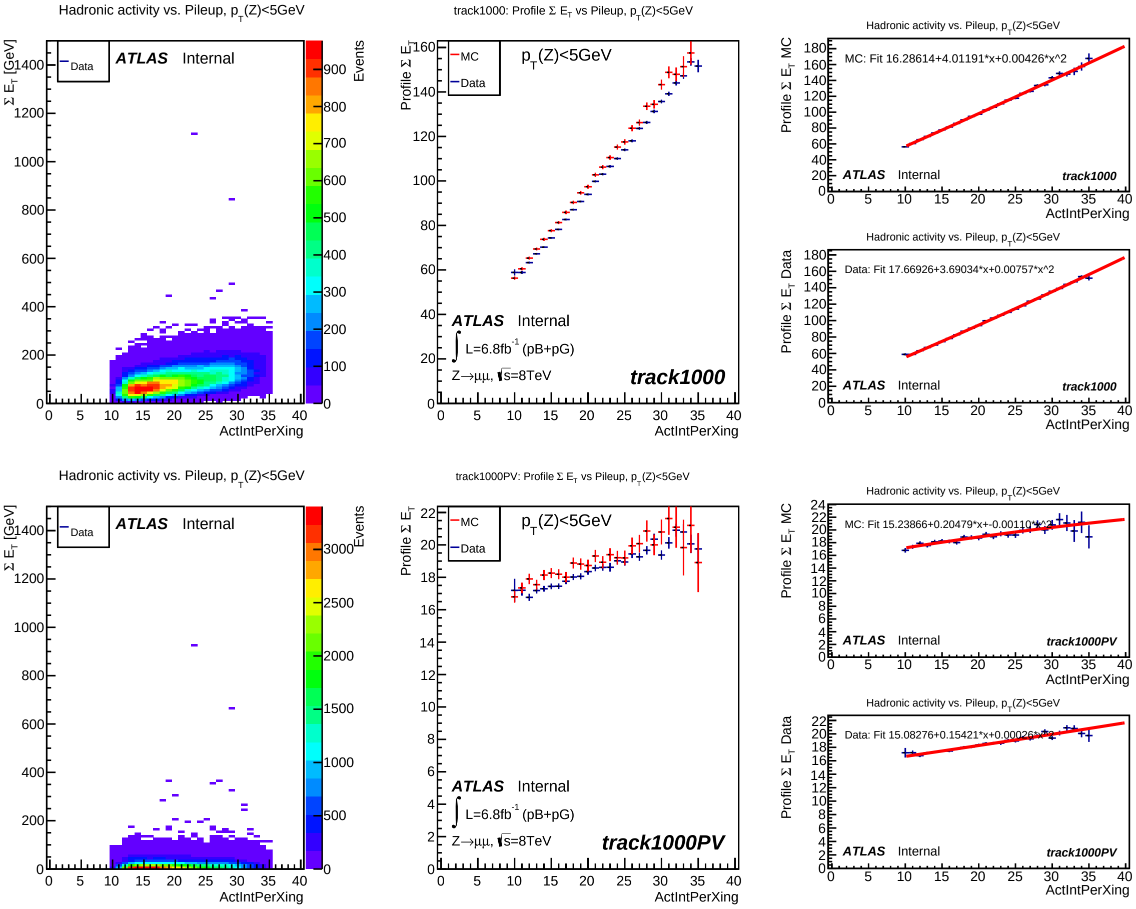

Figure F.2.: ΣE_T vs. pileup distributions and fits for the track1000 and track1000PV algorithms of the 8 TeV analysis.

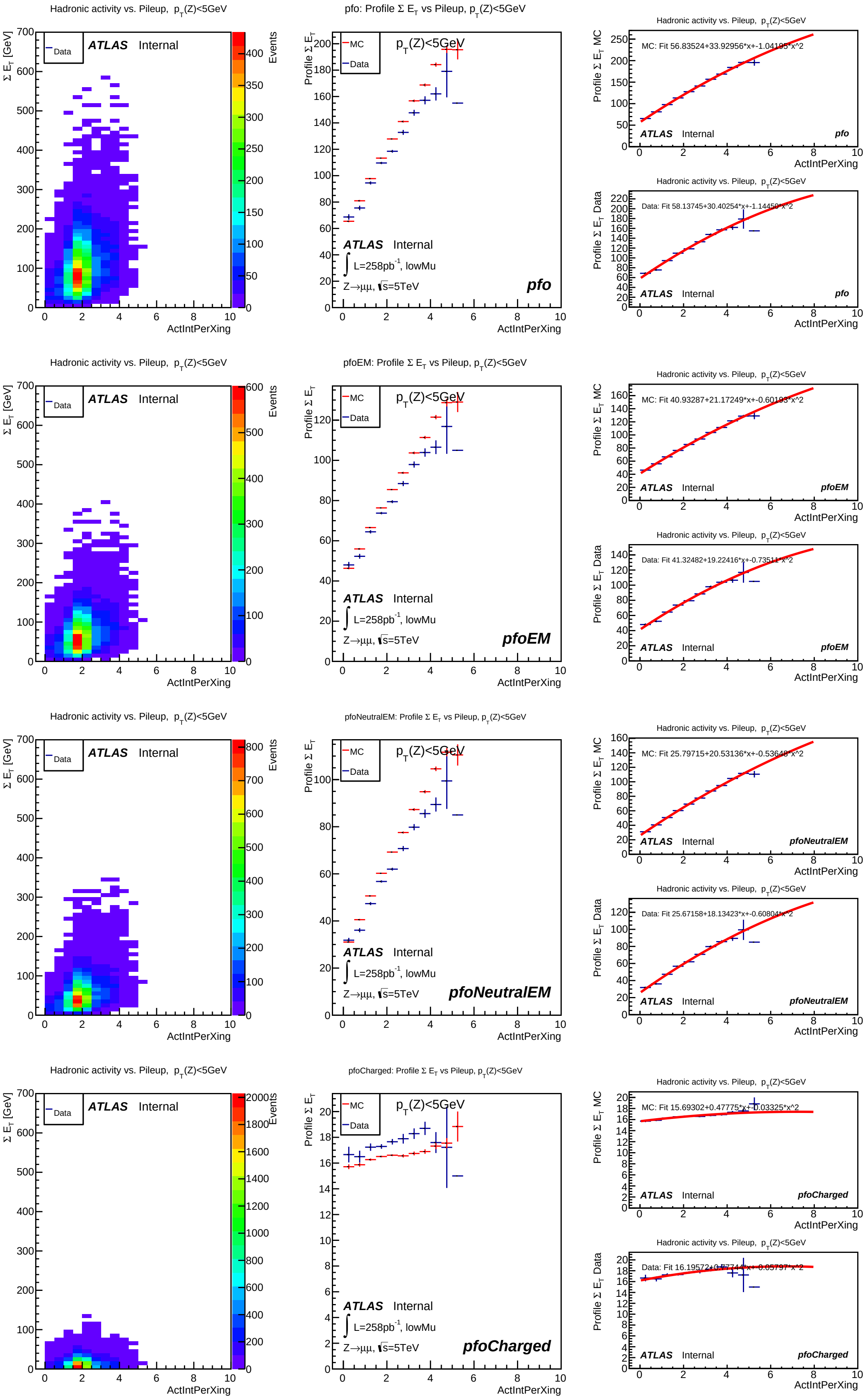

Figure F.3.: ΣE_T vs. pileup distributions and fits for the 5 TeV $Z \to \mu\mu$ analysis.

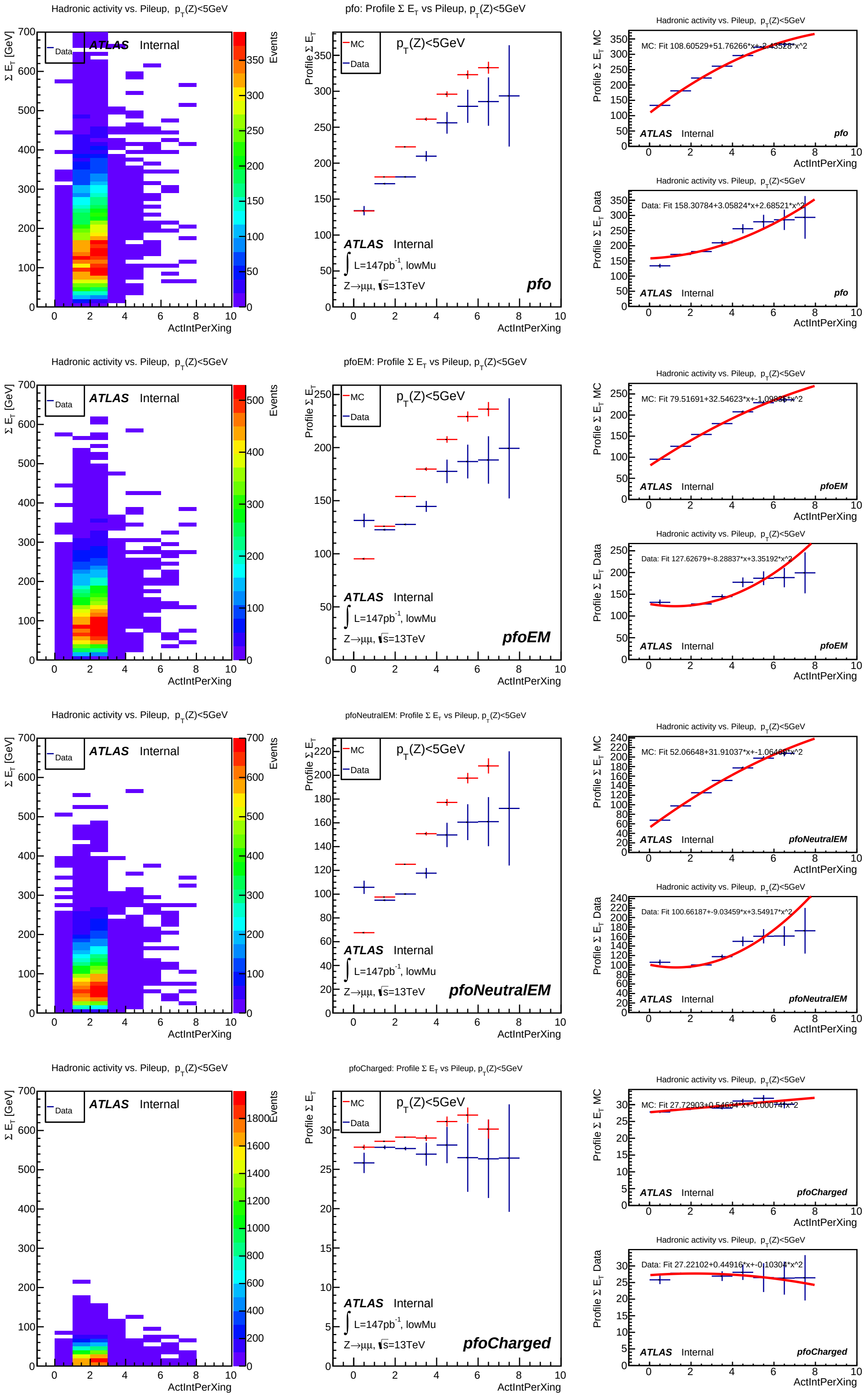

Figure F.4.: ΣE_T vs. pileup distributions and fits for the 13 TeV $Z \to \mu\mu$ analysis.

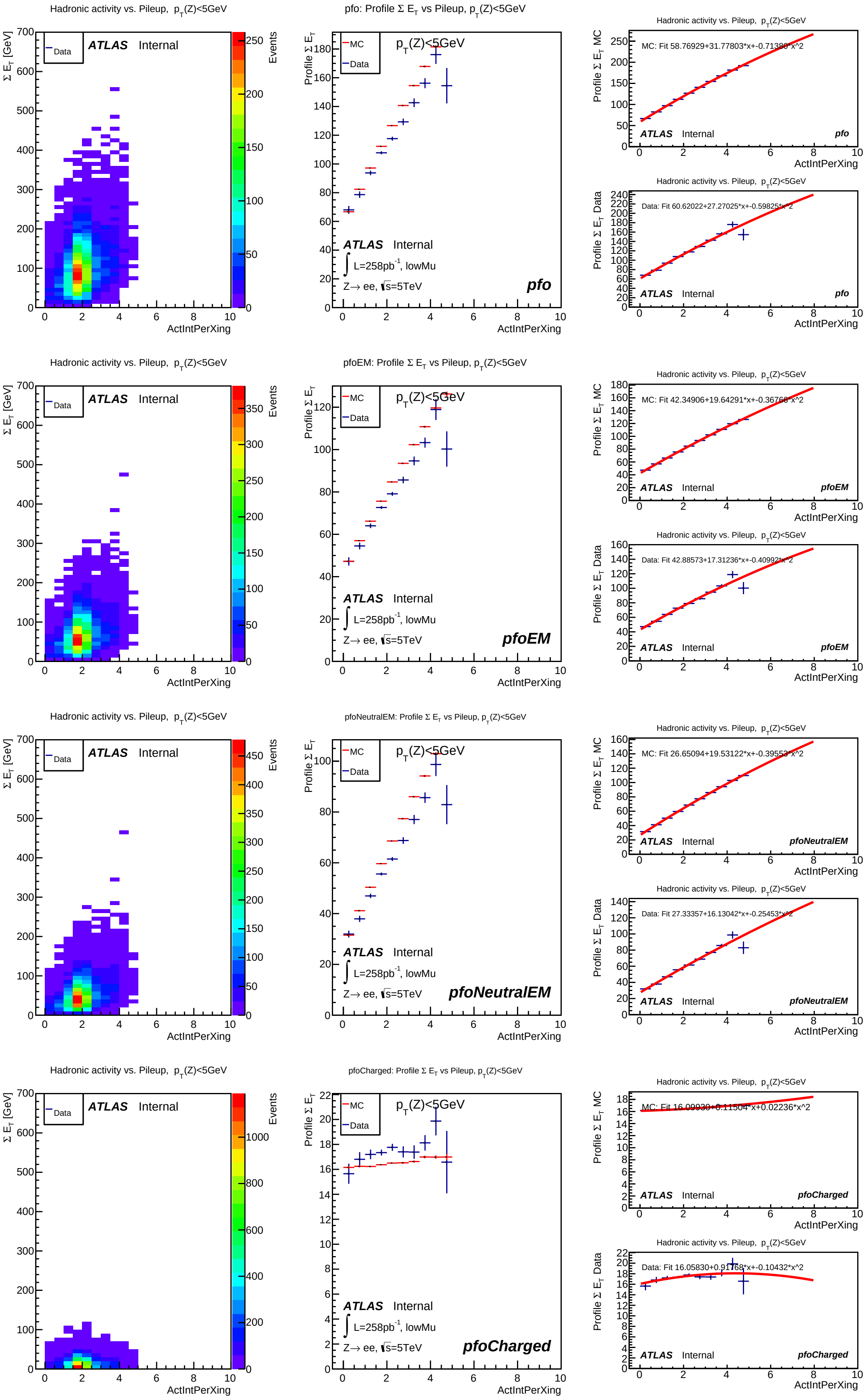

Figure F.5.: ΣE_T vs. pileup distributions and fits for the 5 TeV $Z \to ee$ analysis.

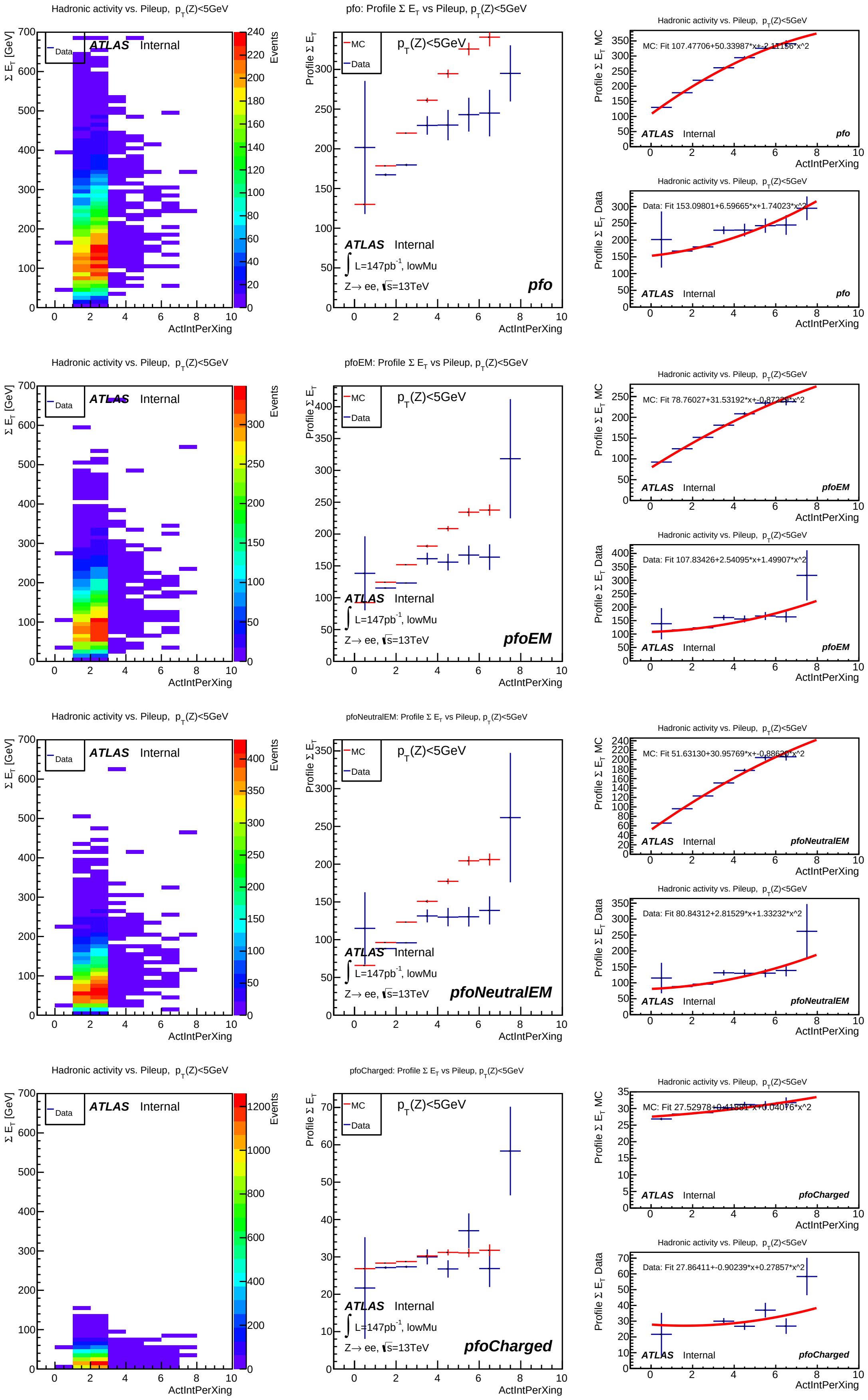

Figure F.6.: ΣE_T vs. pileup distributions and fits for the 13 TeV $Z \to ee$ analysis.

APPENDIX G

Event weights and scale factors

G.1. Pileup event weights

Listed here are the pileup event weights obtained for all algorithms. The results for the 8 TeV analysis are shown first (Fig. G.1), followed by sets for the 5 TeV and 13 TeV muon (Fig. G.2) as well as electron analysis (Fig. G.3).

G.2. Results for the ΣE_T reweighting in the $Z \rightarrow ee$ *lowMu* analyses

The effect of the ΣE_T event weights on the ΣE_T distribution is shown in this section for the various datasets in Fig. G.4.

G.3. Transverse boson momentum differences after the ΣE_T reweighting in the $Z \rightarrow ee$ *lowMu* analyses

Remaining differences between data and the simulations are shown in Fig. G.5 for the transverse boson momentum distribution for the electron selection of the two *lowMu* analyses.

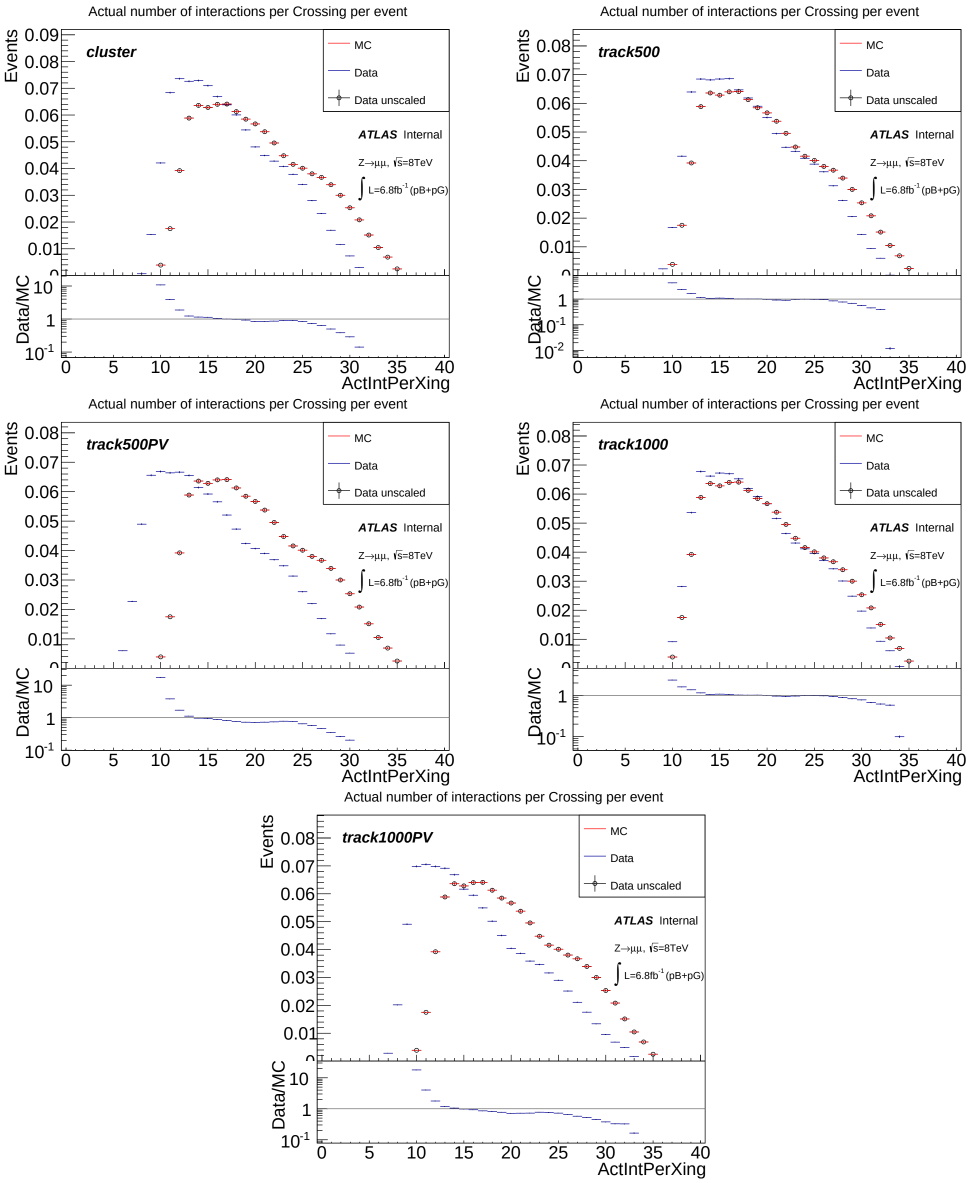

Figure G.1.: Pileup event weights for the different algorithms of the 8 TeV analysis.

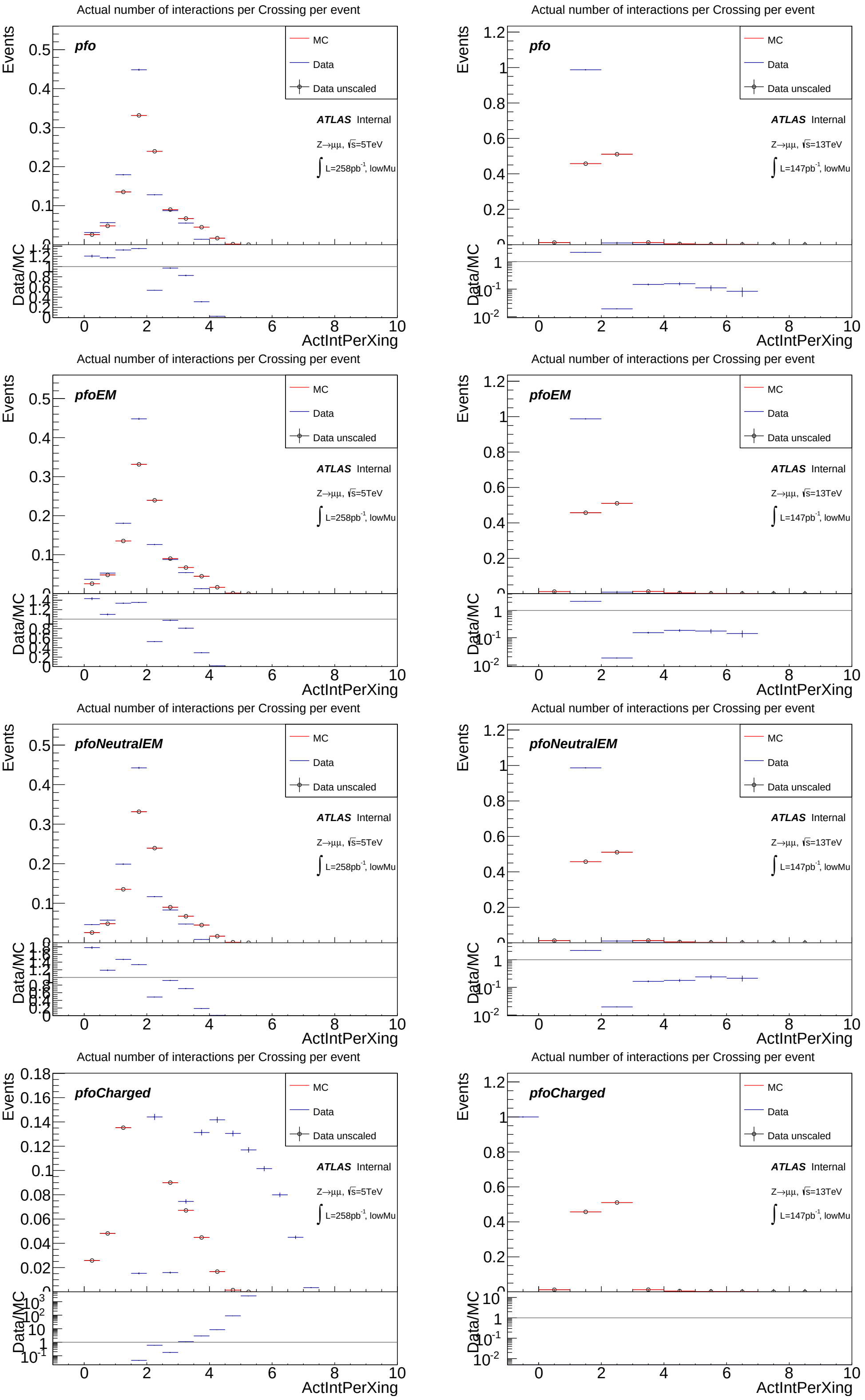

Figure G.2.: Pileup event weights for the different algorithms of the 5 TeV and 13 TeV $Z \rightarrow \mu\mu$ analysis.

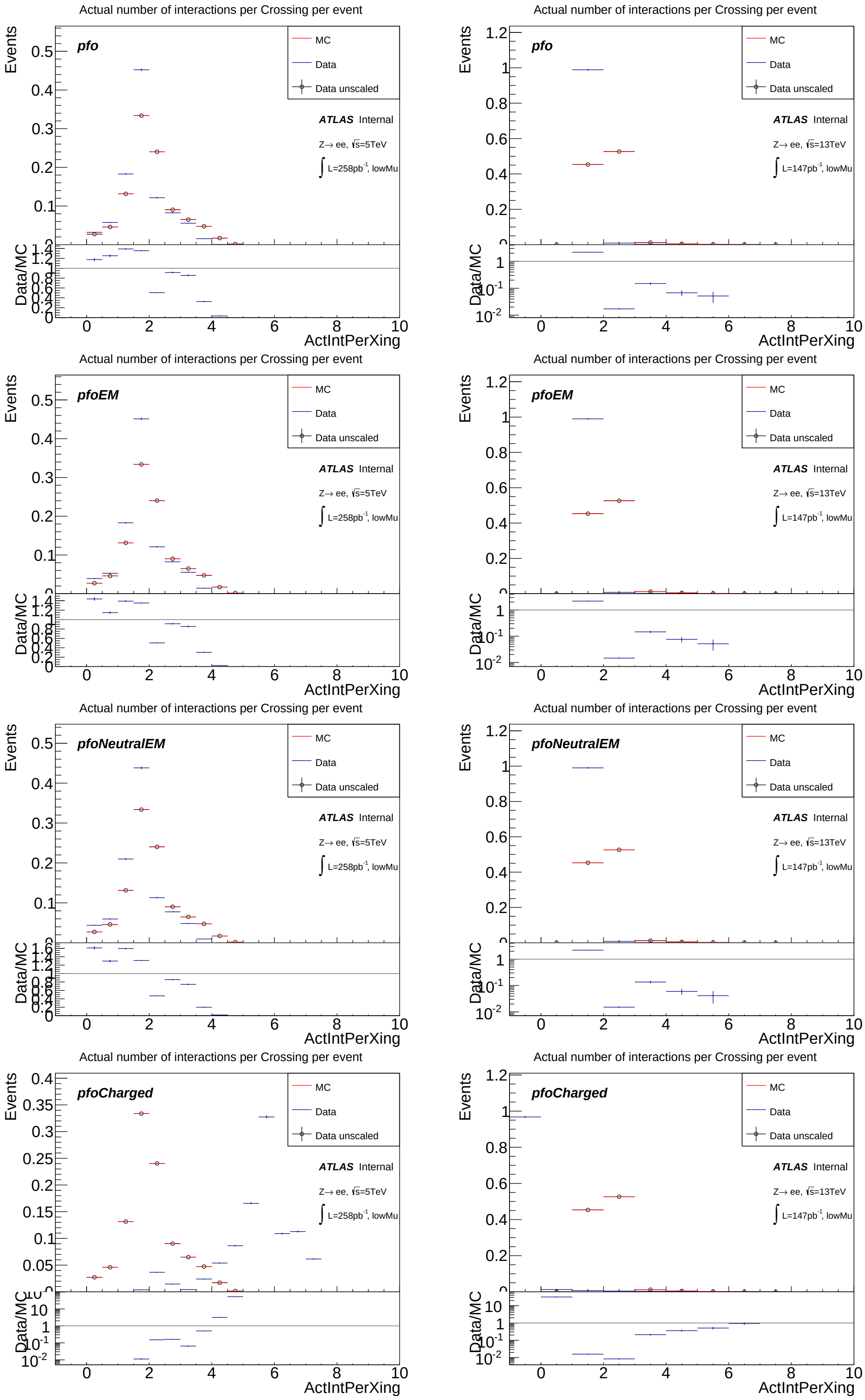

Figure G.3.: Pileup event weights for the different algorithms of the 5 TeV and 13 TeV $Z \to ee$ analysis.

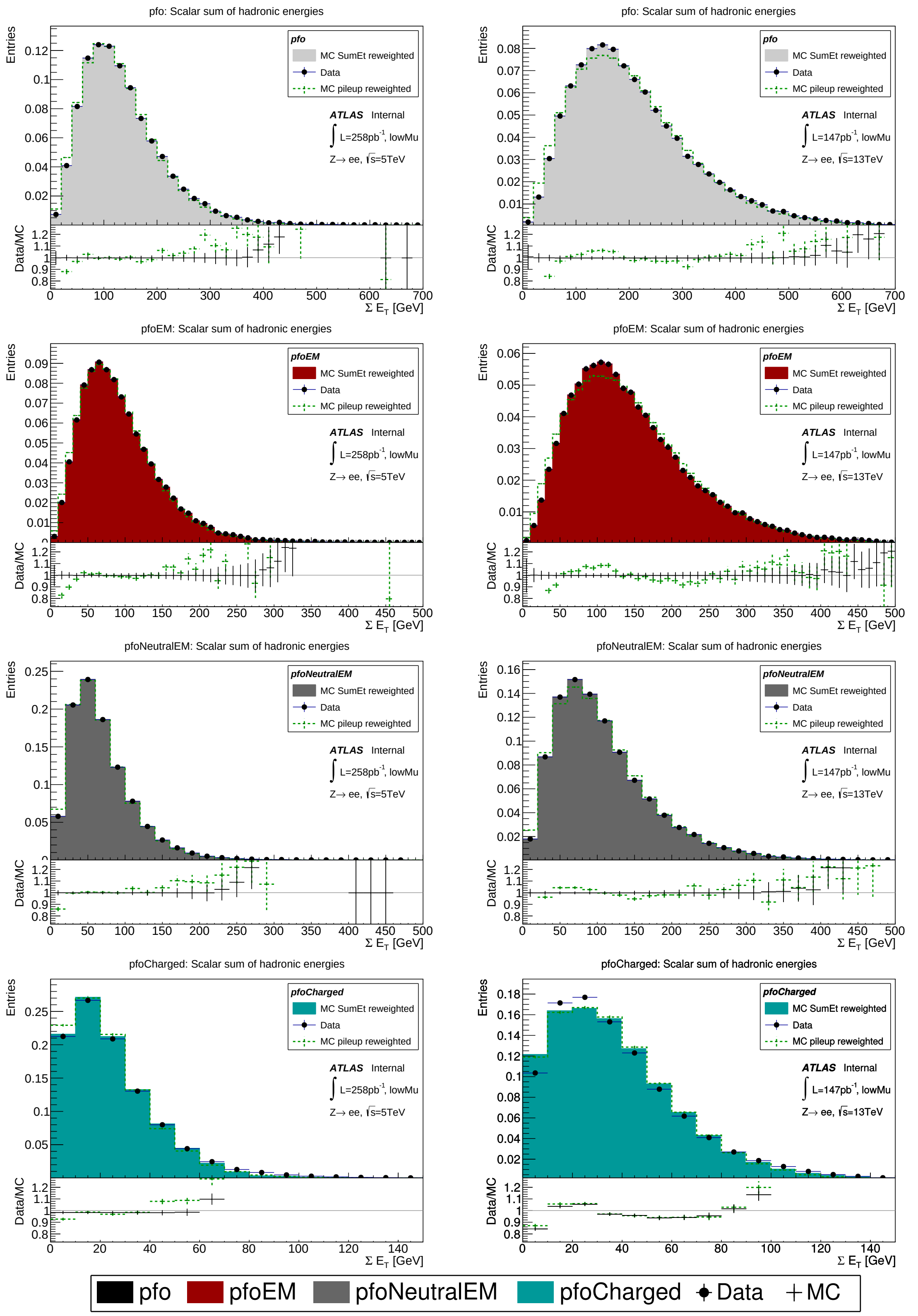

Figure G.4.: ΣE_T distributions with the pileup and ΣE_T reweightings applied for the different algorithms (see legend below for the color coding) of the $Z \to ee$ *lowMu* analyses. The MC distributions with only the pileup weights applied are shown alongside.

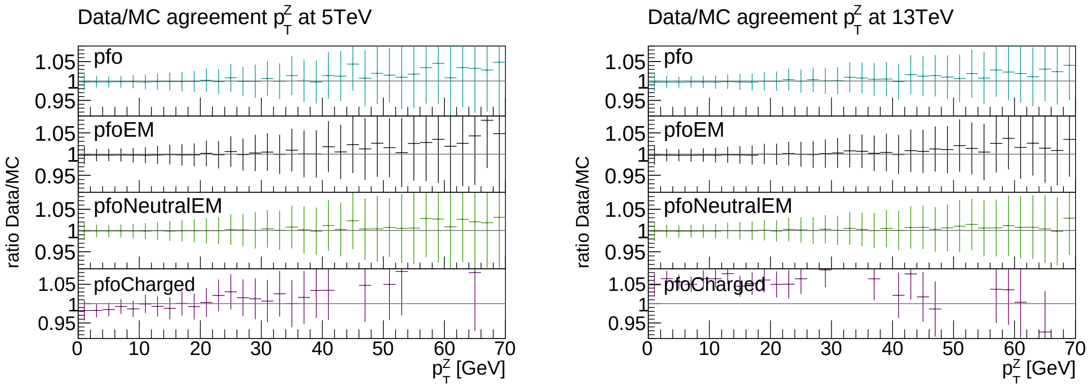

Figure G.5.: Ratio of data and MC for the $p_T(Z)$ distribution after the ΣE_T reweighting has been applied in the 5 TeV and 13 TeV $Z \to ee$ analysis. The second reweighting of the transverse boson momentum is not applied yet.

G.4. Effect of the second transverse boson momentum reweighting on the $p_T^{boson}(reco)$ distribution in the $Z \to ee$ *lowMu* analyses

This section shows the agreement between data and the simulations for the transverse boson momentum distribution after the transverse boson momentum event weights adjusted the remaining differences. Shown are the results for the $Z \to ee$ selection of the *lowMu* datasets in Fig. G.6.

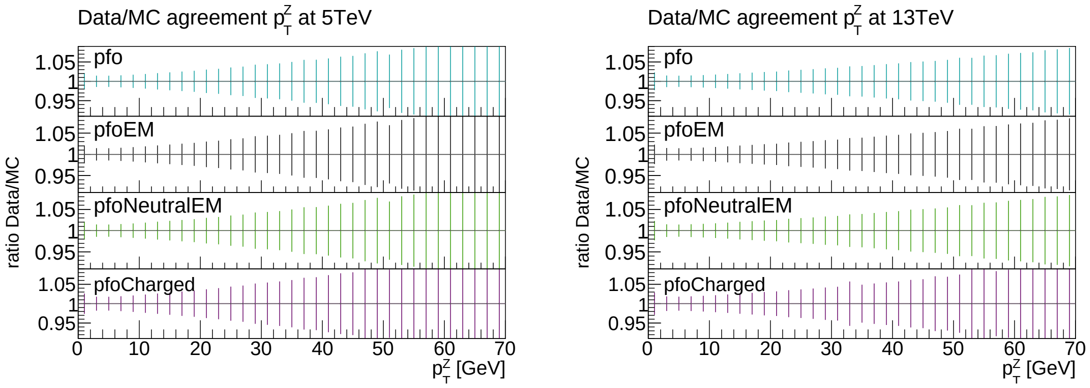

Figure G.6.: Data to Monte Carlo agreement after the ΣE_T and pileup reweighting as well as a boson $p_T^{boson}(reco)$ reweighting are applied to the simulations as a function of the transverse boson momentum $p_T^{boson}(reco)$ for the electron channels of the *lowMu* analyses.

G.5. Effect of the second $p_T^{boson}(reco)$ reweighting on the ΣE_T distribution

After the ΣE_T reweighting, the transverse boson momentum has been corrected by updated transverse boson momentum weights. The effect of these weights on the ΣE_T and $p_T^{boson}(reco)$ distribution is shown in this section. First, the results for the 8 TeV analysis are shown (see Fig. G.7), then the *lowMu* results follow with the muon and the electron selection in Fig. G.8 and in Fig. G.9 respectively.

G.6. Resolution scale factors

The scale factors, which adjust the resolution in the simulations for the parallel and perpendicular component of the hadronic recoil are indicated in this section. The first figure (G.10) shows the parallel and perpendicular scale factors for the 8 TeV dataset. In Fig. G.11 to G.14 the corresponding sets are shown for the two *lowMu* datasets with first the muon and then the electron selection.

G.7. Bias correction terms

The last section of this chapter presents the set of terms, which correct the bias differences between data and the simulations. Fig. G.15 shows the numbers for the 8 TeV dataset, while Fig. G.16 shows the results for the muon selection with both the 5 TeV and 13 TeV dataset. The results for the electron channel are given in Fig. G.17.

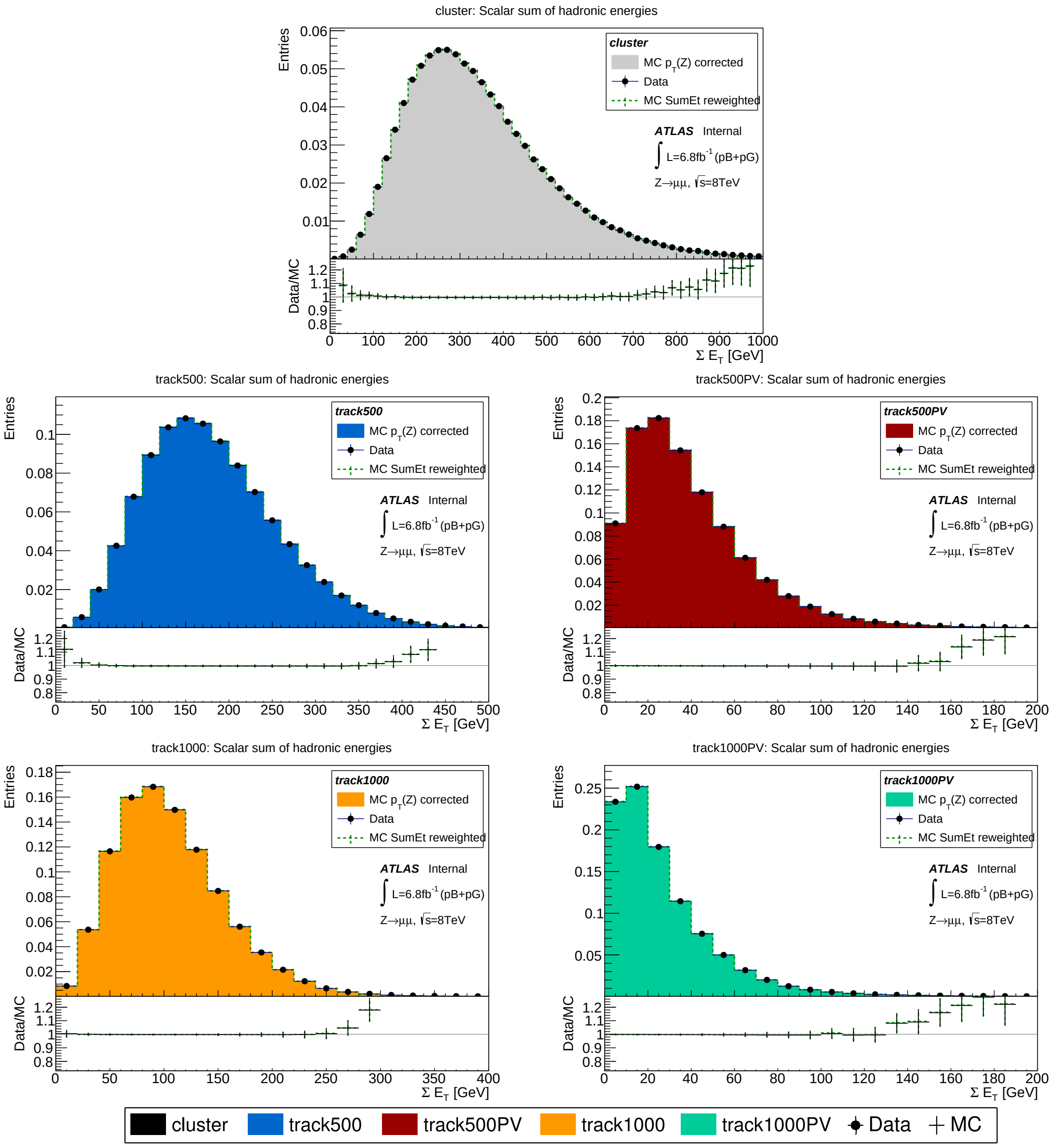

Figure G.7.: ΣE_T distributions with the ΣE_T reweighting as well as second reweighting of the transverse boson momentum applied for the different algorithms (see legend below for the color coding) of the 8 TeV analysis. The MC distribution without this second transverse boson momentum reweighting applied is shown alongside (green dashed line).

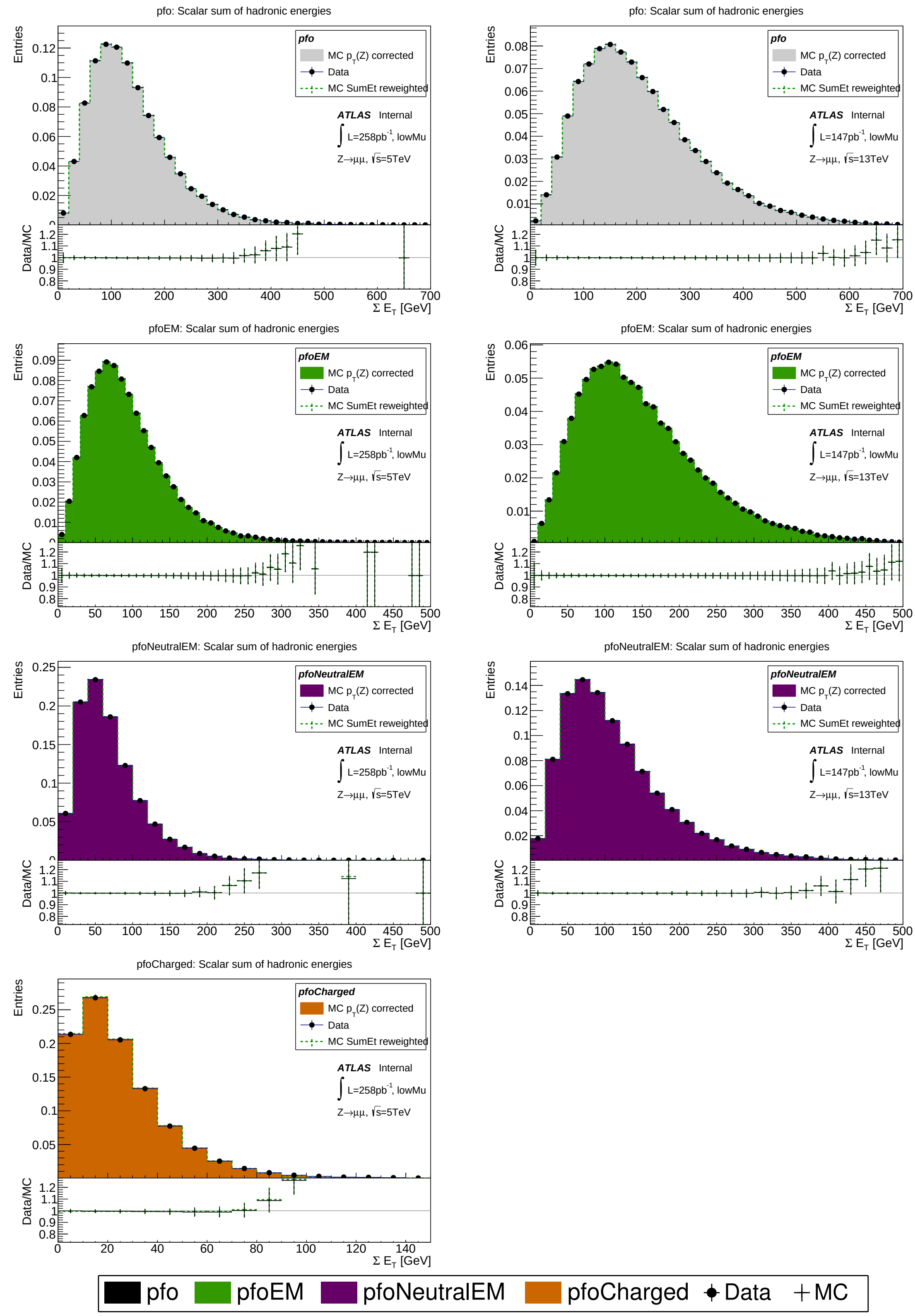

Figure G.8.: ΣE_T distributions with the ΣE_T and $p_T^{boson}(reco)$ reweightings applied for the different algorithms (see legend below for the color coding) of the $Z \to \mu\mu$ *lowMu* analysis. The MC distribution without this second transverse boson momentum reweighting applied is shown alongside (green dashed line).

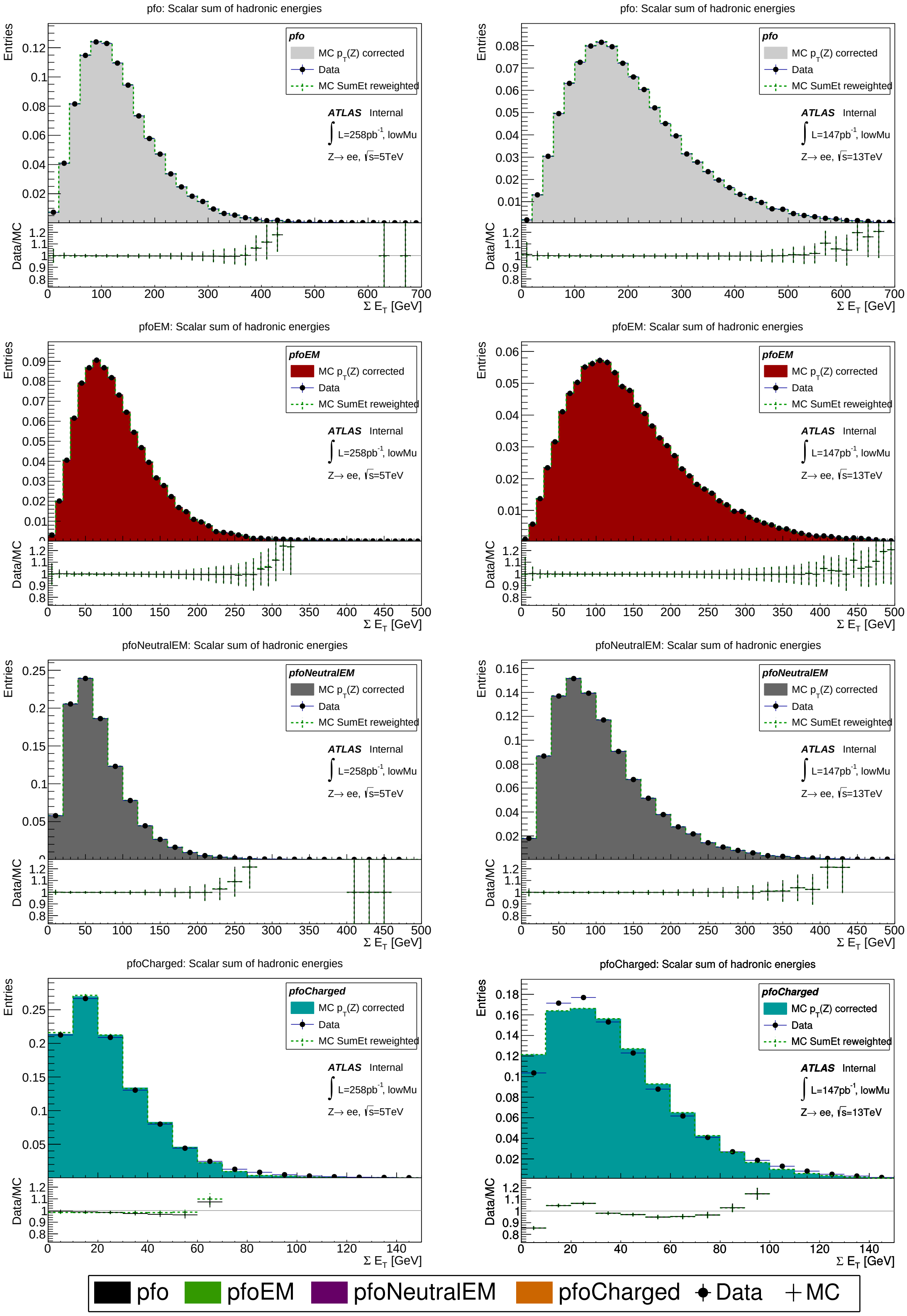

Figure G.9.: ΣE_T distributions with the ΣE_T and $p_T^{boson}(reco)$ reweightings applied for the different algorithms (see legend below for the color coding) of the $Z \to ee$ *lowMu* analysis. The MC distribution without this second transverse boson momentum reweighting applied is shown alongside (green dashed line).

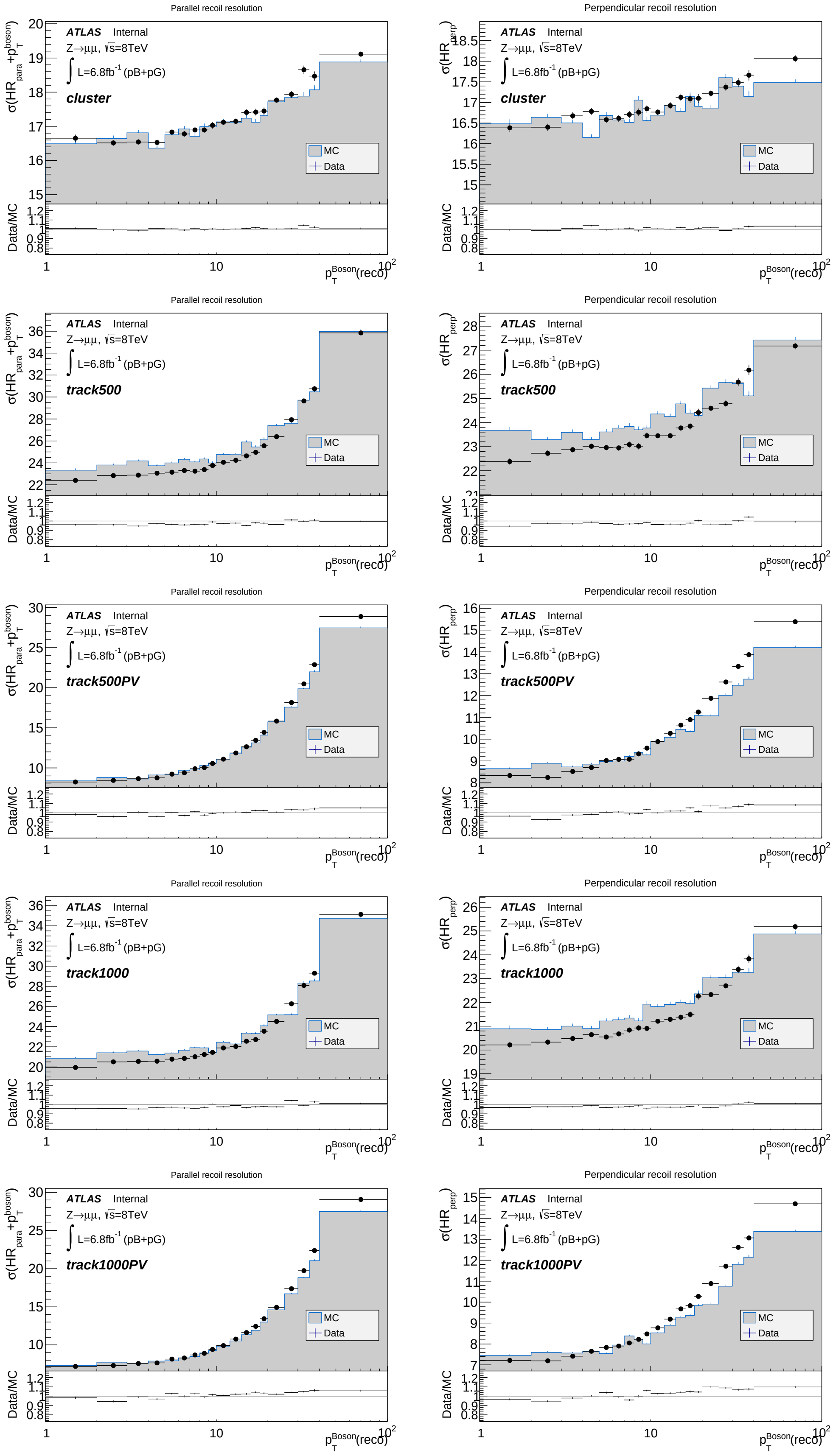

Figure G.10.: Parallel and perpendicular resolution obtained in Gaussian fits (mean $\pm 2.5 \cdot$ RMS) for the different algorithms in the 8 TeV analysis. The bottom pad shows the corresponding scale factors α_{res} in the ratio Data/MC.

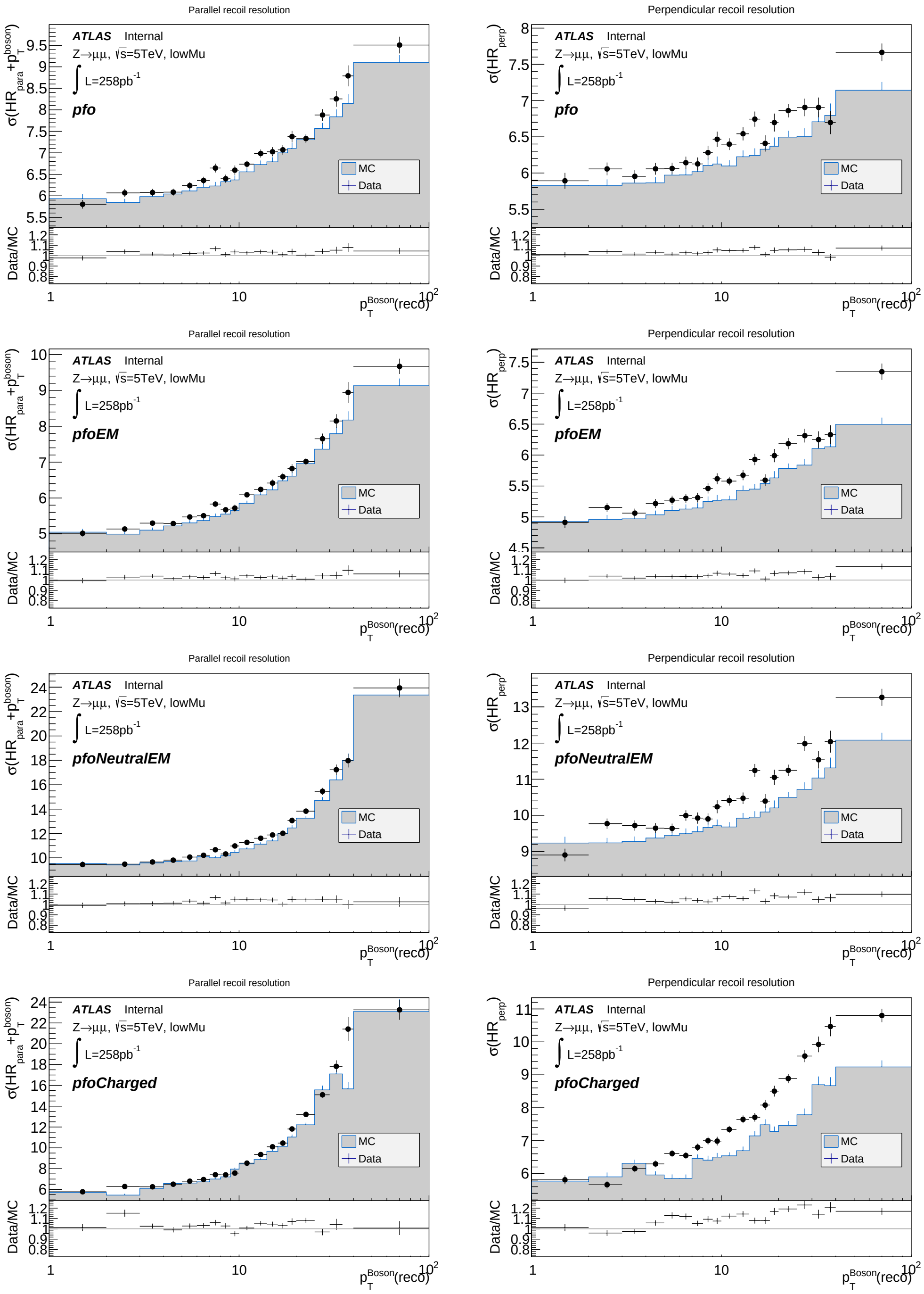

Figure G.11.: Parallel and perpendicular resolution obtained in Gaussian fits within $2.5 \cdot$ RMS around the mean for the different algorithms in the 5 TeV $Z \to \mu\mu$ analysis. The bottom pad shows the corresponding scale factors α_{res} in the ratio Data/MC.

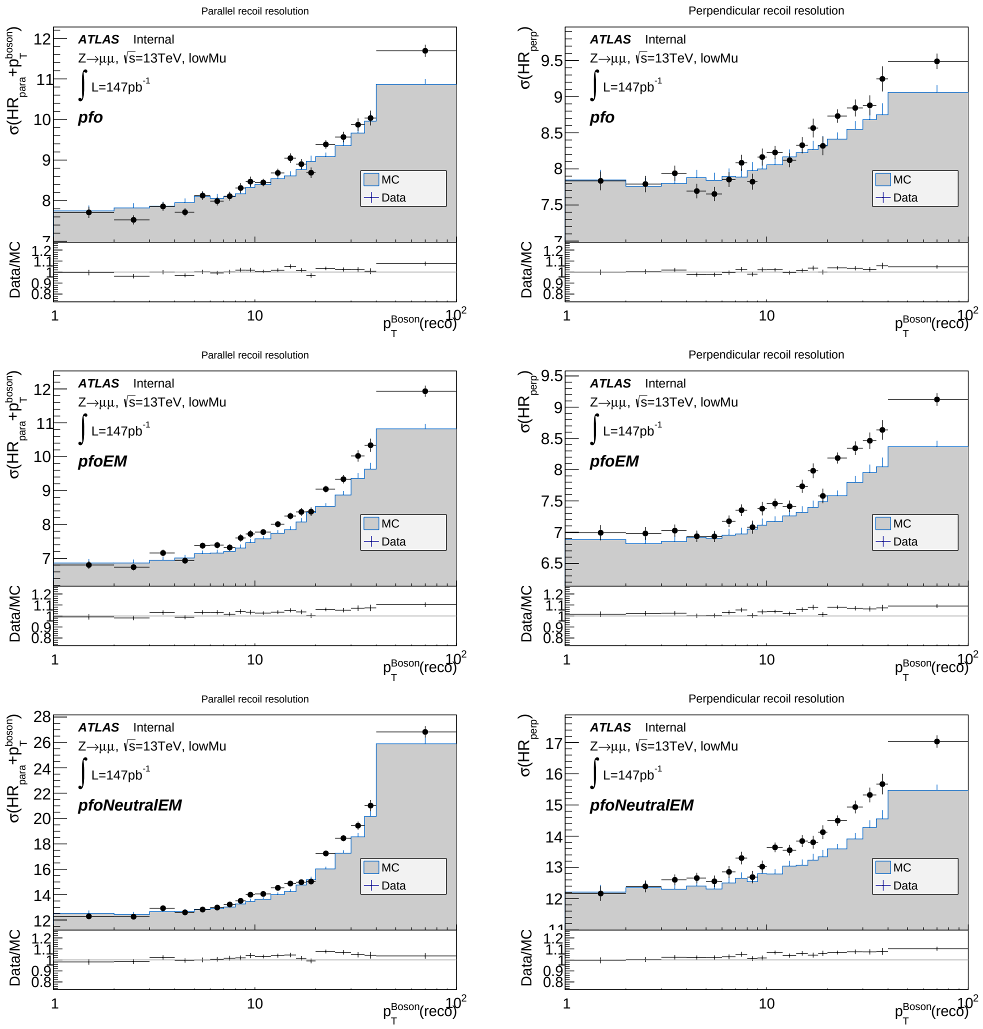

Figure G.12.: Parallel and perpendicular resolution obtained in Gaussian fits within $2.5 \cdot$ RMS around the mean for the different algorithms in the 13 TeV $Z \to \mu\mu$ analysis. The bottom pad shows the corresponding scale factors α_{res} in the ratio Data/MC.

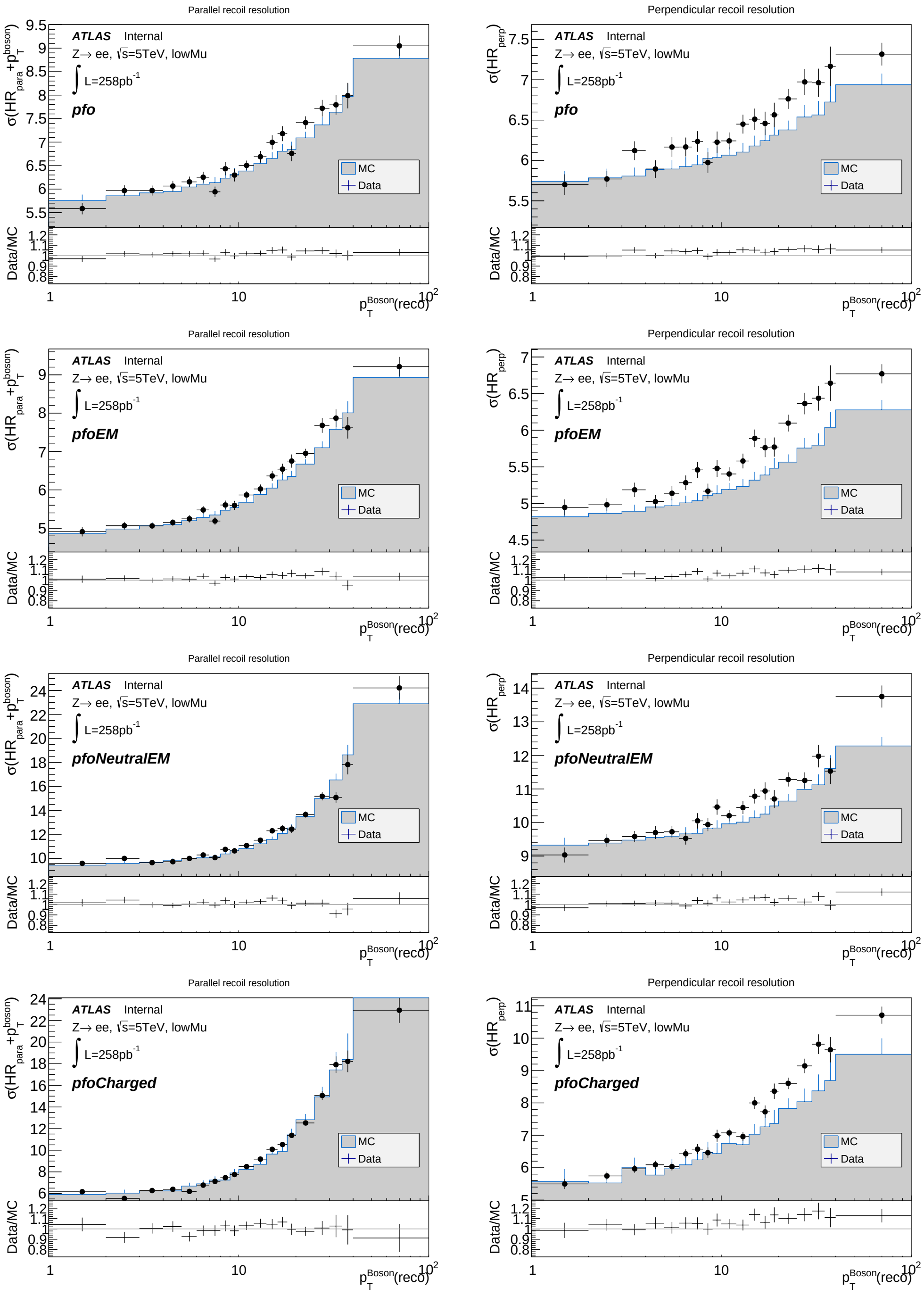

Figure G.13.: Parallel and perpendicular resolution obtained in Gaussian fits within $2.5 \cdot$ RMS around the mean for the different algorithms in the 5 TeV $Z \rightarrow ee$ analysis. The bottom pad shows the corresponding scale factors α_{res} in the ratio Data/MC.

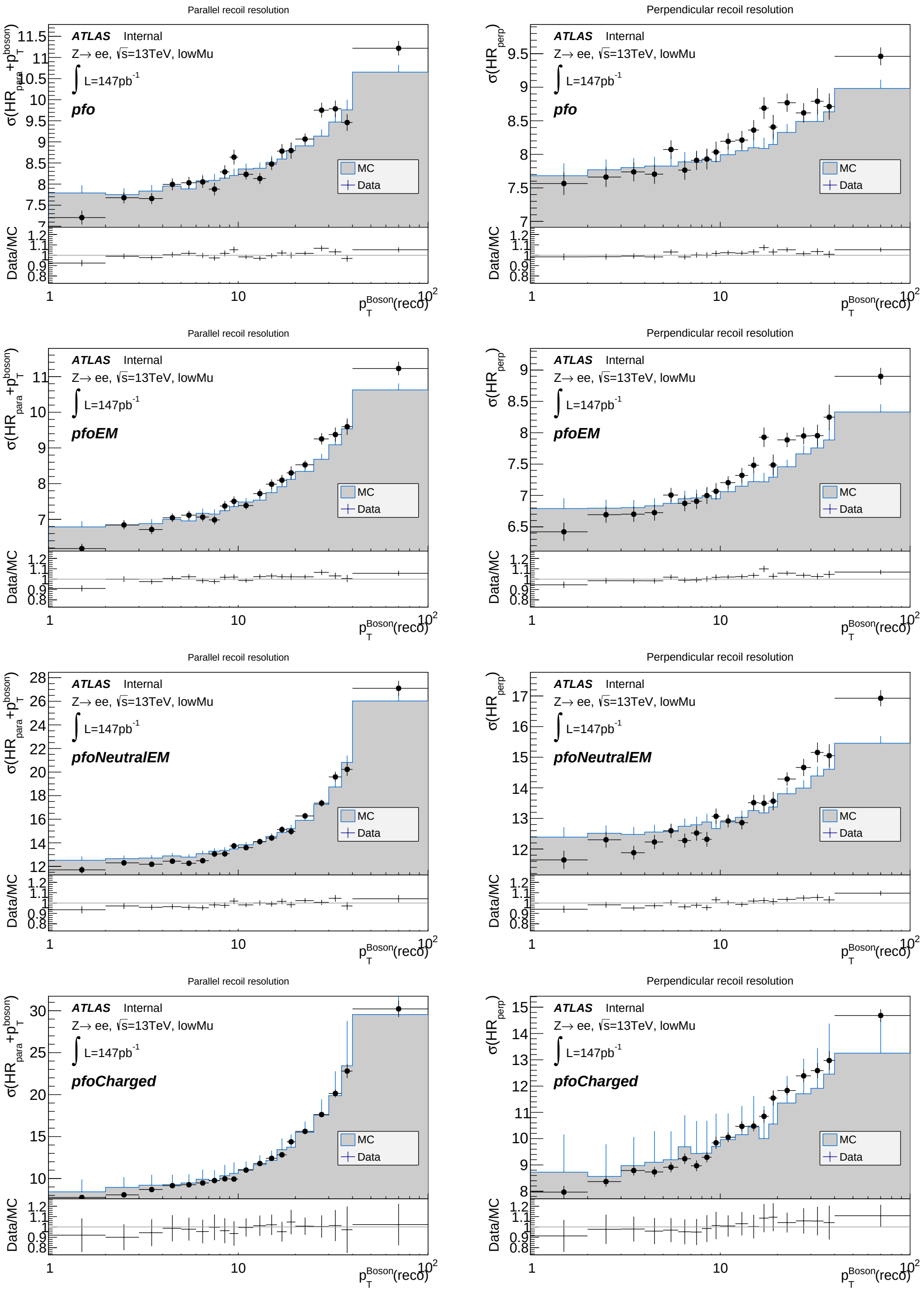

Figure G.14.: Parallel and perpendicular resolution obtained in Gaussian fits within $2.5 \cdot$ RMS around the mean for the different algorithms in the 13 TeV $Z \to ee$ analysis. The bottom pad shows the corresponding scale factors α_{res} in the ratio Data/MC.

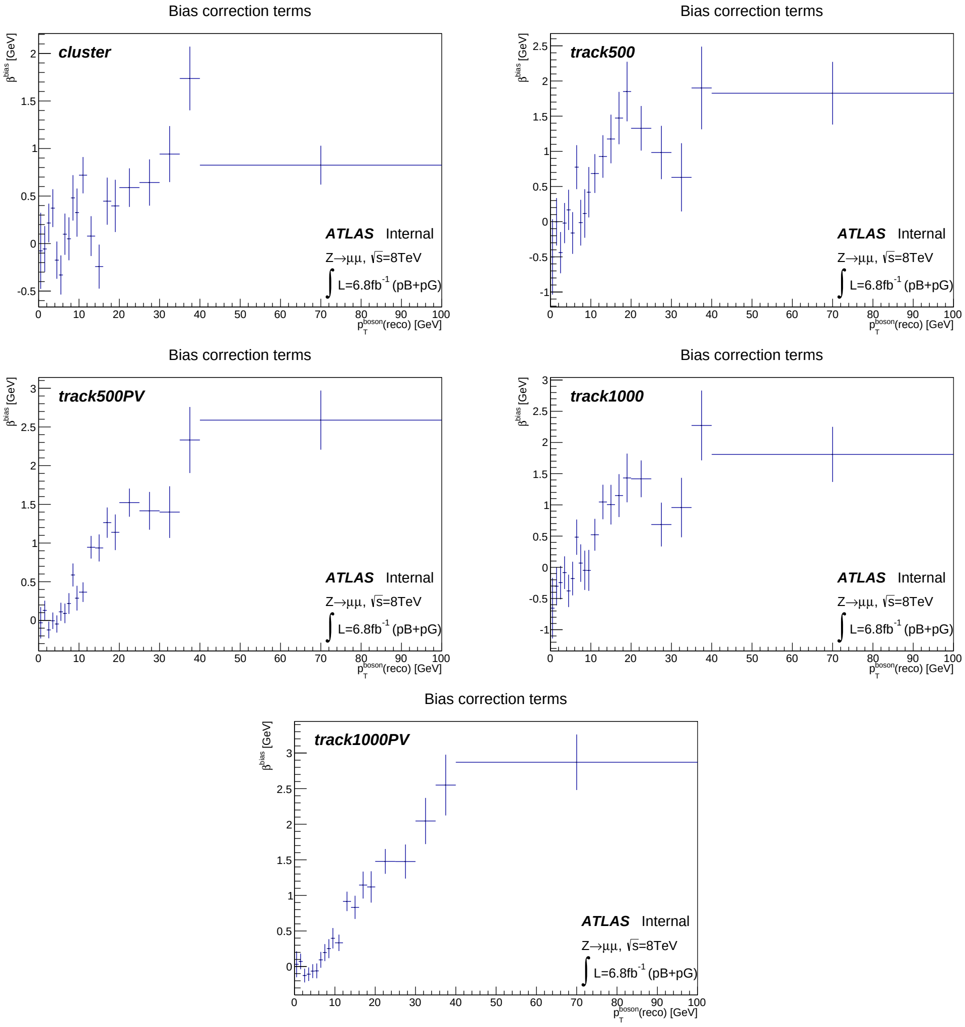

Figure G.15.: Bias correction terms β^{bias} for the different algorithms in the 8 TeV analysis.

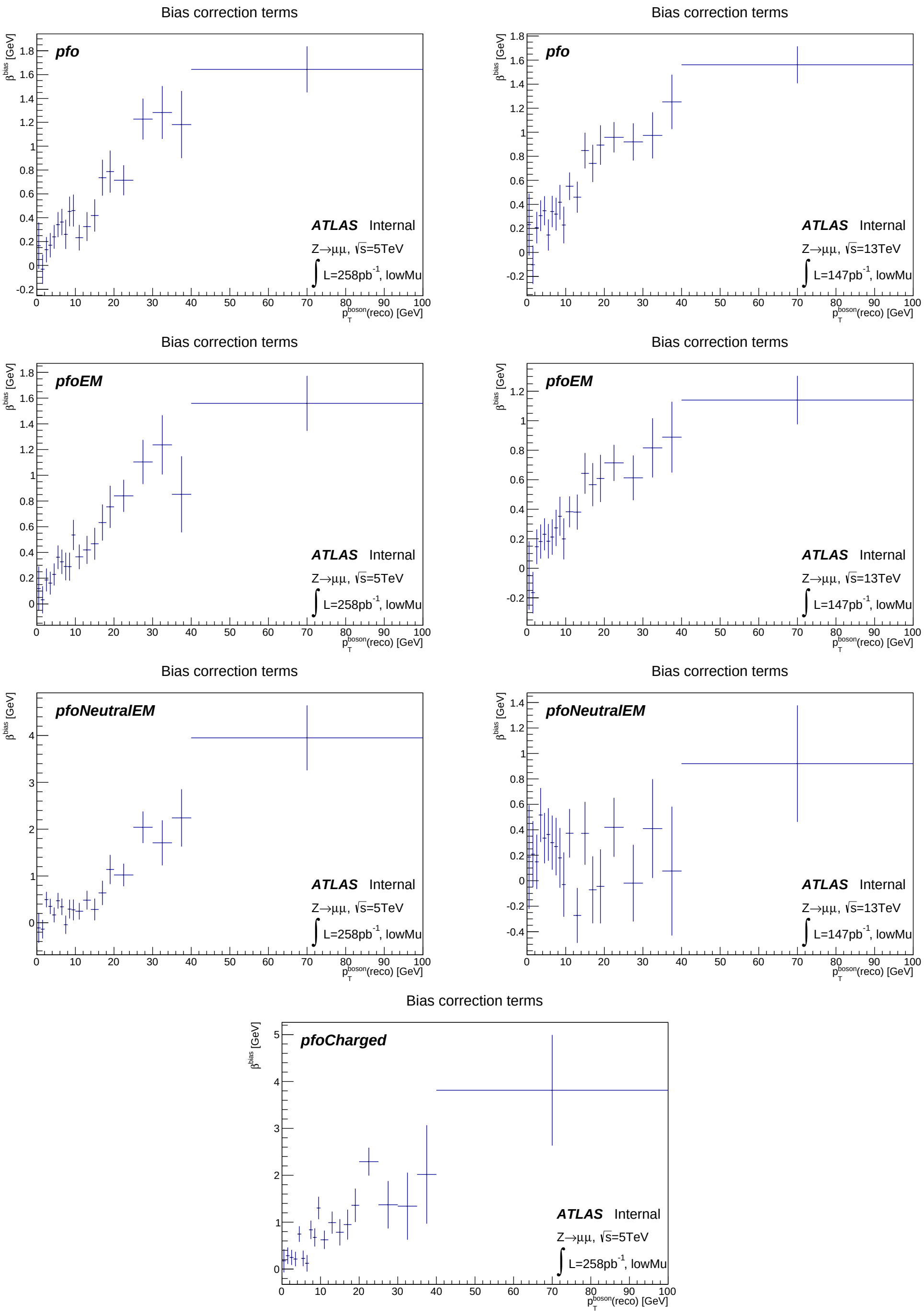

Figure G.16.: Bias correction terms β^{bias} for the different algorithms in the $Z \to \mu\mu$ 5 TeV and 13 TeV analysis.

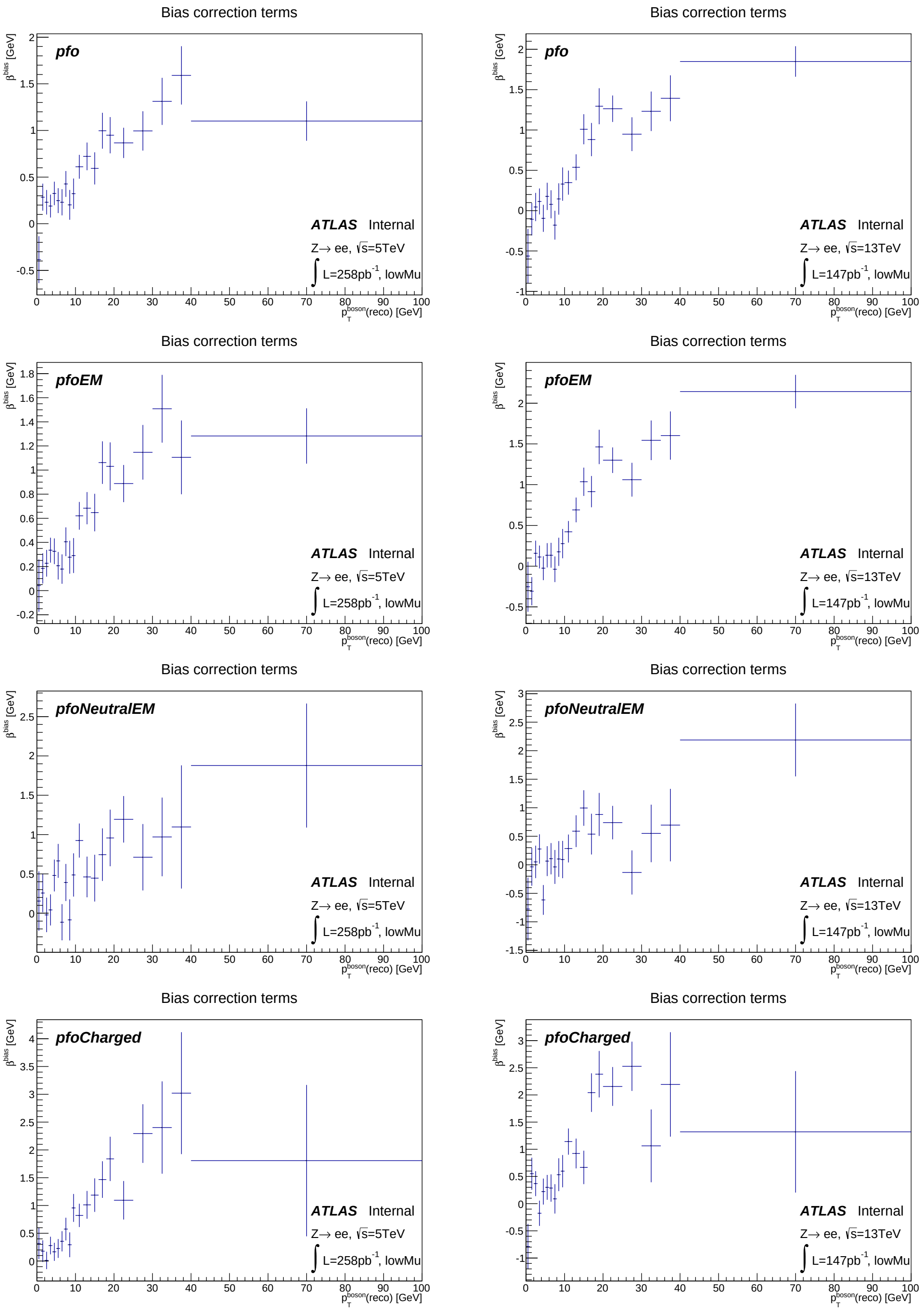

Figure G.17.: Bias correction terms β^{bias} for the different algorithms in the $Z \to ee$ 5 TeV and 13 TeV analysis.

APPENDIX H

Additional plots for the extrapolated reweighting

H.1. Distributions for the Z boson selection

The comparison between the original reweighting and the extrapolation of the event weights and scale factors by using truth quantities are shown for the pfo algorithm in the 5 TeV dataset with the muon selection in Fig. H.1. The corresponding plots for the 13 TeV dataset are given in Fig. H.2 for the pfo algorithm and in Fig. H.3 for the pfoEM algorihthm.

H.2. Distributions for the W boson selection

The resulting distributions for the extrapolationn of the event weights and scale factors to a W boson selection are shown in this section. Fig. H.4 indicates the distributions for the pfo algorithm in the 5 TeV analysis. The results for the two algorithms for the 13 TeV dataset are presented in Fig. H.5 and Fig. H.6.

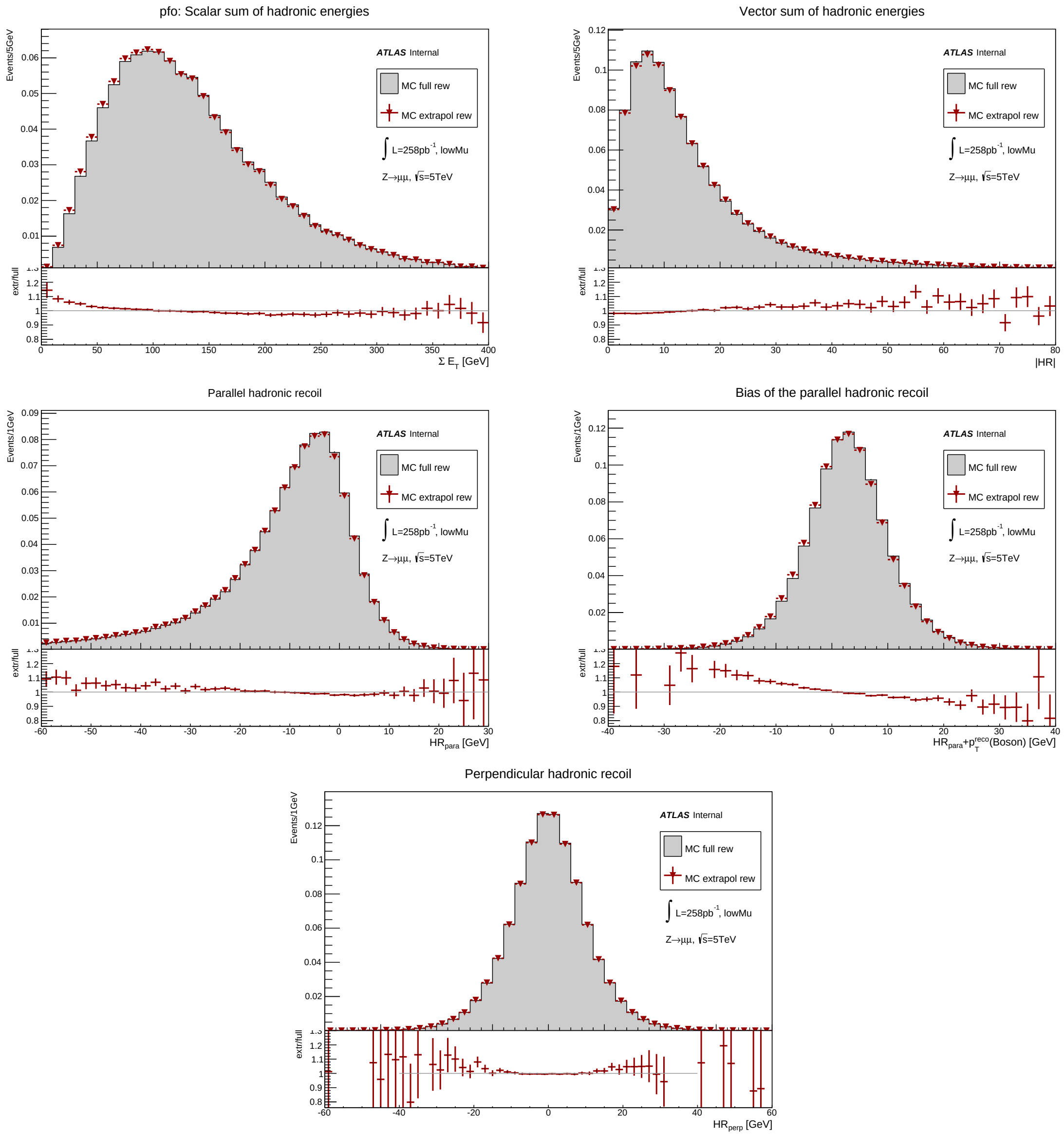

Figure H.1.: Results of the extrapolated reweighting for the ΣE_T and hadronic recoil distributions in comparison to the original approach for the 5 TeV $Z \rightarrow \mu\mu$ analysis with the pfo algorithm. The red curve shows the extrapolated reweighting with the use of truth quantities, while the green area gives the full reweighting results. The unreweighted distribution (green dashed curve) is a reference for the overall effect. All varieties are compared to data.

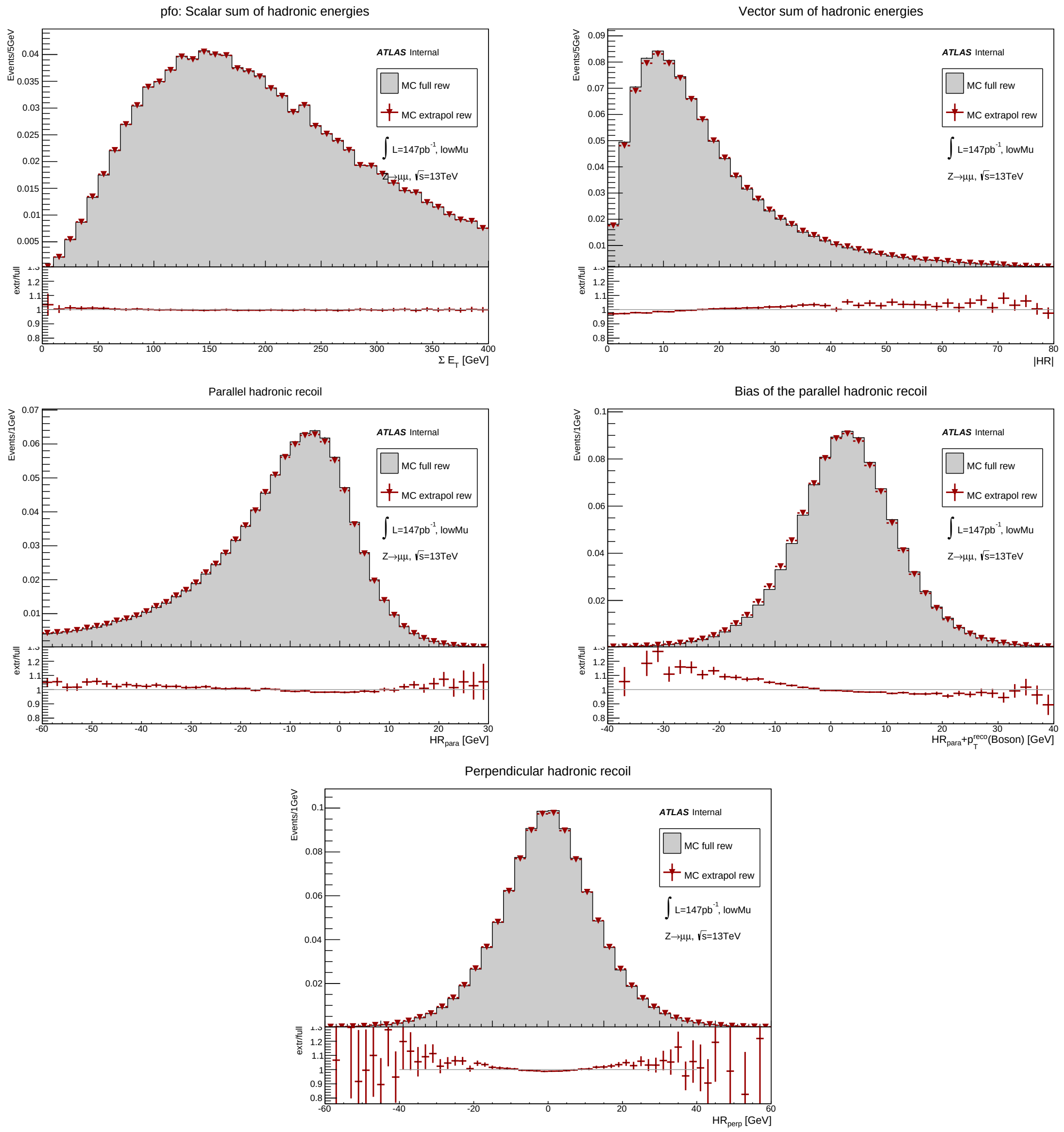

Figure H.2.: Results of the extrapolated reweighting for the ΣE_T and hadronic recoil distributions in comparison to the original approach for the 13 TeV $Z \rightarrow \mu\mu$ analysis with the pfo algorithm. The red curve shows the extrapolated reweighting with the use of truth quantities, while the green area gives the full reweighting results. The unreweighted distribution (green dashed curve) is a reference for the overall effect. All varieties are compared to data.

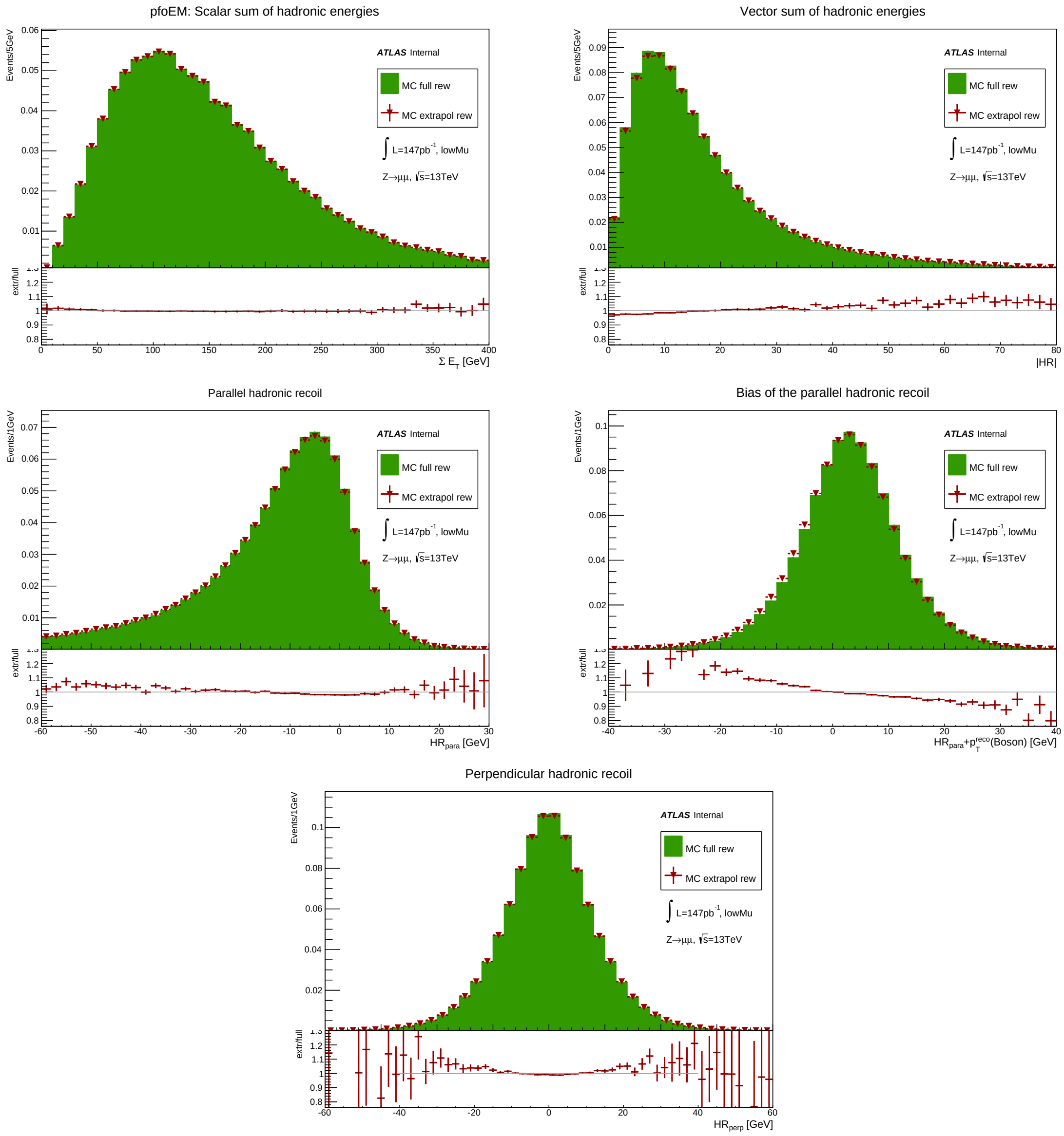

Figure H.3.: Results of the extrapolated reweighting for the ΣE_T and hadronic recoil distributions in comparison to the original approach for the 13 TeV $Z \to \mu\mu$ analysis with the pfoEM algorithm. The red curve shows the extrapolated reweighting with the use of truth quantities, while the green area gives the full reweighting results. The unreweighted distribution (green dashed curve) is a reference for the overall effect. All varieties are compared to data.

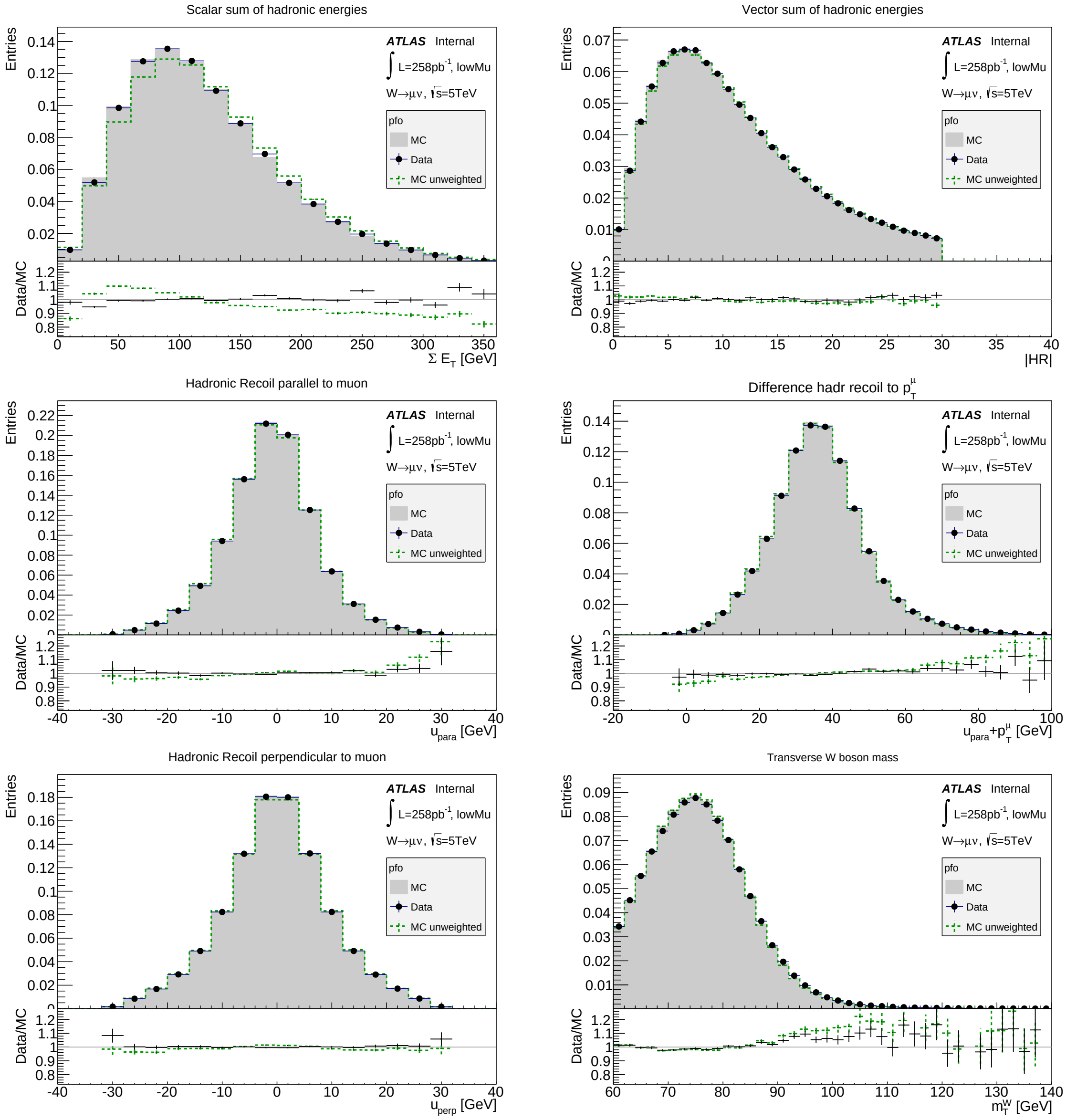

Figure H.4.: Fully reweighted hadronic recoil distributions for the pfo algorithm with the $W \to \mu\nu$ selection in the 5 TeV dataset.

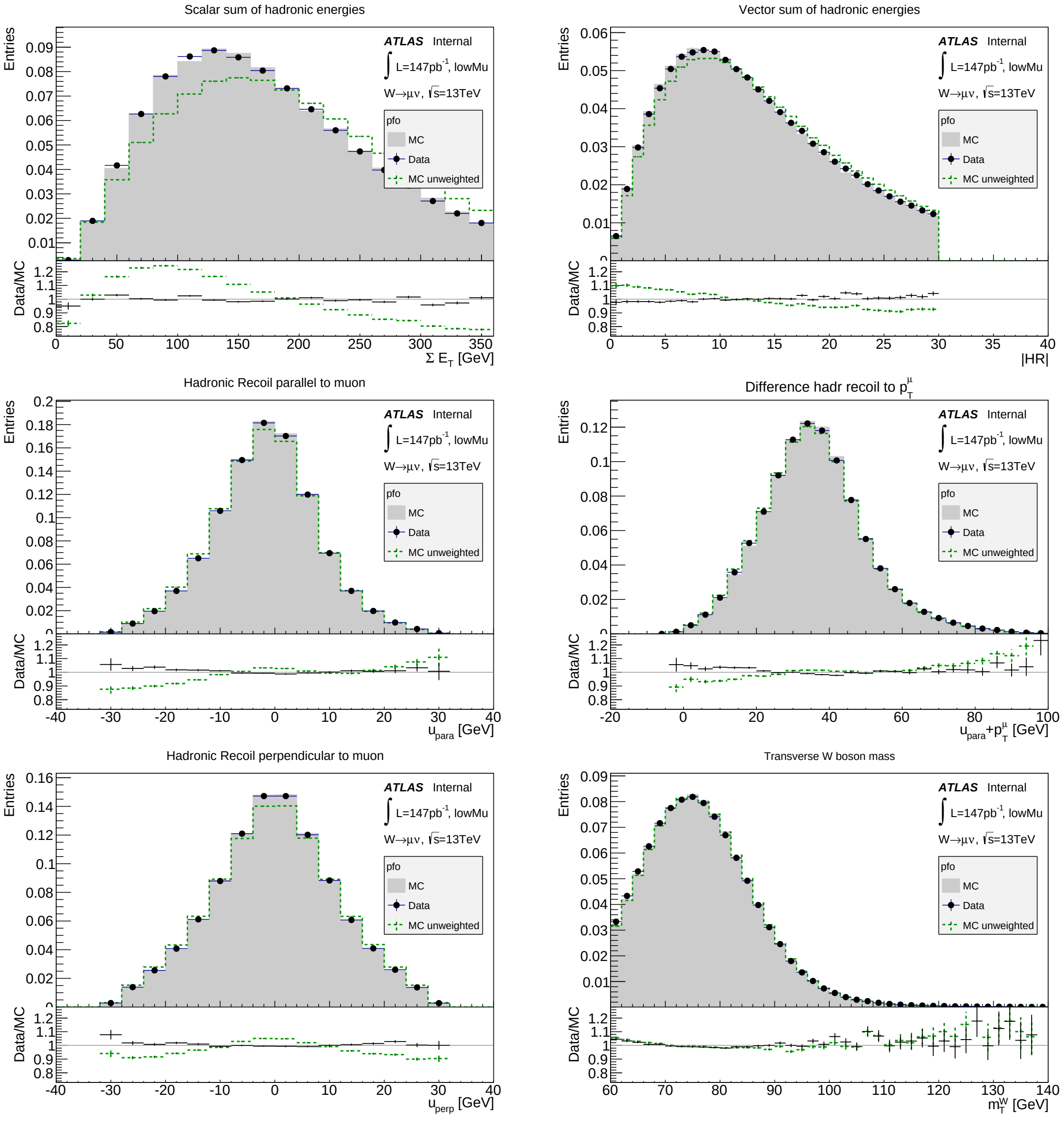

Figure H.5.: Fully reweighted hadronic recoil distributions for the pfo algorithm with the $W \to \mu\nu$ selection in the 13 TeV dataset.

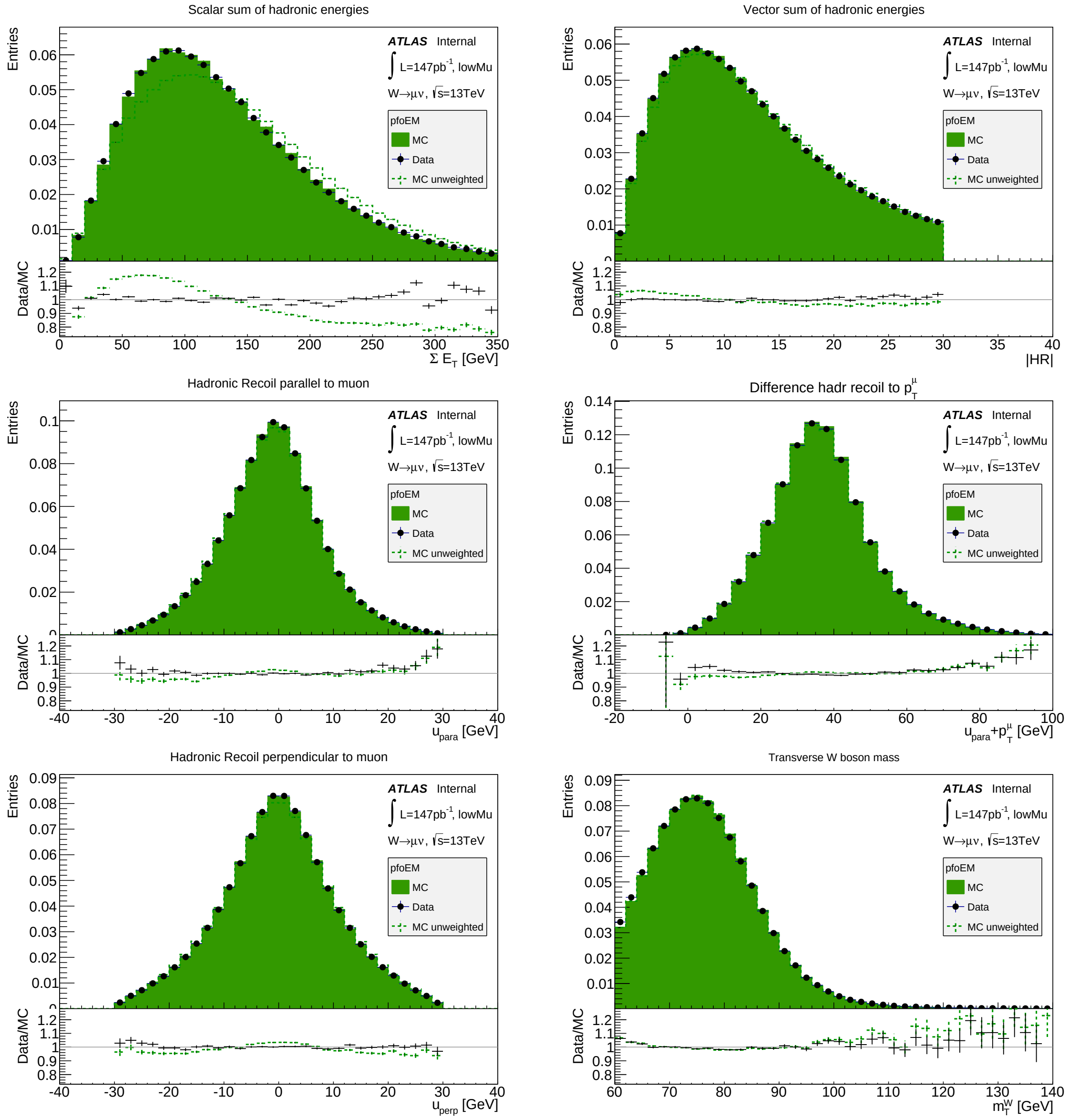

Figure H.6.: Fully reweighted hadronic recoil distributions for the pfoEM algorithm with the $W \to \mu\nu$ selection in the 13 TeV dataset.

Bibliography

[1] D. HANNEKE, S. FOGWELL HOOGERHEIDE and G. GABRIELSE. *Cavity control of a single-electron quantum cyclotron: Measuring the electron magnetic moment*. Phys. Rev. A, **83**:052122 (2011).

[2] T. AOYAMA, M. HAYAKAWA, T. KINOSHITA and M. NIO. *Tenth-order electron anomalous magnetic moment: Contribution of diagrams without closed lepton loops*. Phys. Rev. D, **91**:033006 (2015).

[3] CDF COLLABORATION. *Observation of Top Quark Production in $\overline{p}p$ Collisions with the Collider Detector at Fermilab*. Phys. Rev. Lett., **74**:2626–2631 (1995).

[4] D0 COLLABORATION. *Search for High Mass Top Quark Production in $p\overline{p}$ Collisions at $\sqrt{s} =$ 1.8 TeV*. Phys. Rev. Lett., **74**:2422–2426 (1995).

[5] ATLAS COLLABORATION. *Observation of a new particle in the search for the Standard Model Higgs boson with the ATLAS detector at the LHC*. Phys.Lett., **B716**:1–29 (2012).

[6] CMS COLLABORATION. *Observation of a new boson at a mass of* 125 *GeV with the CMS experiment at the LHC*. Phys.Lett., **B716**:30–61 (2012).

[7] DONUT COLLABORATION. *Observation of tau neutrino interactions*. Physics Letters B, **504**(3):218 – 224 (2001).

[8] GFITTER COLLABORATION. *Update of the global electroweak fit and constraints on two-Higgs-doublet models*. Eur. Phys. J. C (submitted) (2018).

[9] ATLAS COLLABORATION. *Measurement of the W-boson mass in pp collisions at $\sqrt{s} = 7$ TeV with the ATLAS detector*. The European Physical Journal C, **78**(2):110 (2018).

[10] P. W. HIGGS. *Broken symmetries, massless particles and gauge fields*. Phys.Lett., **12**:132–133 (1964).

[11] F. ENGLERT and R. BROUT. *Broken symmetry and the mass of gauge vector mesons.* Phys.Rev.Lett., **13**:321–323 (1964).

[12] M. TANABASHI ET AL. (PARTICLE DATA GROUP). *The Review of Particle Physics.* Phys. Rev. D, **98**:030001 (2018).

[13] B. POVH, K. RITH, C. SCHOLZ and F. ZETSCHE. *Teilchen und Kerne.: Eine Einführung in die physikalischen Konzepte.* Physics and astronomy online library. Springer (2004). ISBN 9783540210658.

[14] F. HALZEN and A. MARTIN. *QUARKS & LEPTONS: AN INTRODUCTORY COURSE IN MODERN PARTICLE PHYSICS.* Wiley India Pvt. Limited (2008). ISBN 9788126516568.

[15] C. H. LAI (EDITOR). *Selected papers on Gauge Theory of Weak and Electromagnetic Interactions.* World Scientific, Singapore (1981). ISBN 9971-83-023-x.

[16] M. KOBAYASHI and T. MASKAWA. *CP-Violation in the Renormalizable Theory of Weak Interaction.* Progress of Theoretical Physics, **49**(2):652–657 (1973).

[17] FT2 (WIKIMEDIA COMMONS). *Spontaneous symmetry breaking - published under the CC BY-SA 3.0 licence.* `https://en.wikipedia.org/wiki/File:Spontaneous_symmetry_breaking_(explanatory_diagram).png` (2012).

[18] R. FEYNMAN. *Space - time approach to quantum electrodynamics.* Phys.Rev., **76**:769–789 (1949).

[19] D. GRIFFITHS. *Introduction to Elementary Particles.* Physics textbook. Wiley (2008). ISBN 9783527406012.

[20] J. SCHWINGER. *Selected Papers on Quantum Electrodynamics.* Dover books on engineering and engineering physics. Dover Publications (1958). ISBN 9780486604442.

[21] R. K. ELLIS, W. J. STIRLING and B. R. WEBBER. *QCD and collider physics.* Camb. Monogr. Part. Phys. Nucl. Phys. Cosmol., **8**:1–435 (1996).

[22] S. D. DRELL and T.-M. YAN. *Massive Lepton-Pair Production in Hadron-Hadron Collisions at High Energies.* Phys. Rev. Lett., **25**:316–320 (1970).

[23] ATLAS COLLABORATION. *Summary plots from the ATLAS Standard Model physics group.* `https://atlas.web.cern.ch/Atlas/GROUPS/PHYSICS/CombinedSummaryPlots/SM/`.

[24] ATLAS COLLABORATION. *Precision measurement and interpretation of inclusive W^+,W^- and Z/γ* production cross sections with the ATLAS detector.* The European Physical Journal C, **77**(6):367 (2017).

[25] ATLAS COLLABORATION. *Measurement of $W\pm$ and Z-boson production cross sections in pp collisions at with the ATLAS detector.* Physics Letters B, **759**:601 – 621 (2016).

[26] ATLAS COLLABORATION. *Measurements of the top-quark pair to Z-boson cross section ratios at* $\sqrt{s} = 13, 8, 7 TeV$ *with the ATLAS detector*. Journal of High Energy Physics, **2017**(2):117 (2017).

[27] S. WEINBERG. *A model of leptons*. Phys.Rev.Lett., **19**:1264–1266 (1967).

[28] C. H. ALBRIGHT. *y and* ν *distributions for neutral current reactions of the Weinberg-type*. Nuclear Physics B, **70**(3):486 – 500 (1974).

[29] J. F. WHEATER and C. H. LLEWELLYN SMITH. *Electroweak Radiative Corrections to Neutrino and Electron Scattering and the Value of* $\sin^2\theta_W$. Nucl. Phys., **B208**:27 (1982). [Erratum: Nucl. Phys.B226,547(1983)].

[30] UA1 COLLABORATION (G. ARNISON ET AL.). *Experimental observation of isolated large transverse energy electrons with associated missing energy at* $\sqrt{s} = 540 GeV$. Physics Letters B, **122**(1):103 – 116 (1983).

[31] UA1 COLLABORATION (G. ARNISON ET AL.). *Experimental Observation of Lepton Pairs of Invariant Mass Around* $95 GeV/c^2$ *at the CERN SPS Collider*. Phys. Lett. B, **126**(5):398–410 (1983).

[32] UA1 COLLABORATION. *Further evidence for charged intermediate vector bosons at the SPS collider*. Physics Letters B, **129**(3-4):273–282 (1983).

[33] CERN. *The Large Electron-Positron Collider*. `http://cds.cern.ch/record/1997351` (2012).

[34] THE LEP ELECTROWEAK WORKING GROUP. *Precision electroweak measurements on the Z resonance*. Physics Reports, **427**(5):257 – 454 (2006).

[35] THE LEP ELECTROWEAK WORKING GROUP. *Electroweak measurements in electron–positron collisions at W-boson-pair energies at LEP*. Physics Reports, **532**(4):119 – 244 (2013).

[36] CDF COLLABORATION, D0 COLLABORATION. *Combination of CDF and D0 W-Boson Mass Measurements*. Phys. Rev., **D88**(5):052018 (2013).

[37] BELGIUM, DENMARK, FRANCE, GREECE, ITALY, NETHERLANDS, NORWAY, SWEDEN, SWITZERLAND, UNITED-KINGDOM, WESTERN GERMANY, YUGOSLAVIA. *Convention for the establishment of a european organization for nuclear research*. `http://council.web.cern.ch/council/en/governance/Convention.html`.

[38] T. MASSAM, T. MULLER, B. RIGHINI, M. SCHNEEGANS and A. ZICHICHI. *Experimental observation of antideuteron production*. Il Nuovo Cimento A, **63**(1):10–14 (1965).

[39] GARGAMELLE NEUTRINO COLLABORATION (F.J. HASERT ET AL.). *Observation of Neutrino Like Interactions Without Muon Or Electron in the Gargamelle Neutrino Experiment*. Phys. Lett., **B46**:138–140 (1973).

[40] UA2 Collaboration (P. Bagnaia et al.). *Evidence for Z0 —> e+ e- at the CERN anti-p p Collider*. Phys. Lett., **B129**:130–140 (1983).

[41] UA2 Collaboration. *Observation of single isolated electrons of high transverse momentum in events with missing transverse energy at the CERN pp collider*. Physics Letters B, **122**(5):476 – 485 (1983).

[42] CERN. *About CERN, Online Documentation*. `http://home.cern/about` (2018).

[43] Christiane Lefevre (ATLAS Experiment). *The CERN accelerator complex*. `http://cds.cern.ch/record/1260465` (2008). CERN-DI-0812015.

[44] L. Evans and P. Bryant. *LHC Machine*. JINST, **3**:S08001 (2008).

[45] ATLAS Collaboration. *ATLAS detector and physics performance: Technical Design Report, 1*. Technical Design Report ATLAS (1999). CERN-LHCC-99-014.

[46] ATLAS Collaboration. *ATLAS luminosity public results for Run2*. `http://twiki.cern.ch/twiki/bin/view/AtlasPublic/LuminosityPublicResultsRun2` (2017).

[47] ATLAS Collaboration. *ATLAS luminosity public results*. `http://twiki.cern.ch/twiki/bin/view/AtlasPublic/LuminosityPublicResults` (2012).

[48] R. Alemany-Fernandez, E. Bravin, L. Drosdal, A. Gorzawski, V. Kain, M. Lamont, A. Macpherson, G. Papotti, M. Pojer, L. Ponce, S. Redaelli, G. Roy, M. Solfaroli Camillocci, W. Venturini and J. Wenninger. *Operation and Configuration of the LHC in Run 1* (2013).

[49] R. Bruce et al. *LHC Run 2: Results and challenges*. In *Proceedings, 57th ICFA Advanced Beam Dynamics Workshop on High-Intensity and High-Brightness Hadron Beams (HB2016): Malmö, Sweden, July 3-8, 2016*, MOAM5P50 (2016).

[50] J. Boyd, C. Schwick. *Feedback from the experiments on the 2017 run*. In *Proceedings of the 8th LHC Operations Evian Workshop* (2017).

[51] CERN. *The High-Luminosity LHC*. `https://cds.cern.ch/record/2114693` (2015).

[52] I. Bejar Alonso and L. Rossi. *HiLumi LHC Technical Design Report: Deliverable: D1.10*. Technical Report CERN-ACC-2015-0140 (2015).

[53] CMS Collaboration. *The CMS experiment at the CERN LHC*. JINST, **3**:S08004 (2008).

[54] ATLAS Collaboration. *The ATLAS Experiment at the CERN Large Hadron Collider*. Journal of Instrumentation, **3**(08):S08003 (2008).

[55] LHCb Collaboration. *The LHCb Detector at the LHC*. JINST, **3**:S08005 (2008).

[56] ALICE COLLABORATION. *The ALICE experiment at the CERN LHC.* JINST, **3**:S08002 (2008).

[57] TOTEM COLLABORATION. *The TOTEM Experiment at the CERN Large Hadron Collider.* JINST, **3**:S08007 (2008).

[58] LHCF COLLABORATION. *The LHCf detector at the CERN Large Hadron Collider.* JINST, **3**:S08006 (2008).

[59] J. L. PINFOLD. *The MoEDAL Experiment at the LHC – a New Light on the Terascale Frontier.* J. Phys. Conf. Ser., **631**(1):012014 (2015).

[60] ATLAS COLLABORATION. *ATLAS Higgs Physics public results.* `http://twiki.cern.ch/twiki/bin/view/AtlasPublic/HiggsPublicResults` (2018).

[61] ATLAS COLLABORATION. *ATLAS experiment - public results.* `https://twiki.cern.ch/twiki/bin/view/AtlasPublic`.

[62] M. CAPEANS, G. DARBO, K. EINSWEILLER, M. ELSING, T. FLICK, M. GARCIA-SCIVERES, C. GEMME, H. PERNEGGER, O. ROHNE and R. VUILLERMET. *ATLAS Insertable B-Layer Technical Design Report.* Technical Report CERN-LHCC-2010-013. ATLAS-TDR-19 (2010).

[63] K. POTAMIANOS. *The upgraded Pixel detector and the commissioning of the Inner Detector tracking of the ATLAS experiment for Run-2 at the Large Hadron Collider.* PoS, **EPS-HEP2015**:261 (2015).

[64] ATLAS COLLABORATION. *Performance of the ATLAS muon trigger in pp collisions at $\sqrt{s} = 8$ TeV.* Eur. Phys. J., **C75**:120 (2015).

[65] ATLAS COLLABORATION. *Performance of the ATLAS trigger system in 2015.* The European Physical Journal C, **77**(5):317 (2017).

[66] ATLAS COLLABORATION. *Topological cell clustering in the ATLAS calorimeters and its performance in LHC Run 1.* The European Physical Journal C, **77**(7):490 (2017).

[67] ATLAS COLLABORATION. *Measurement of the muon reconstruction performance of the ATLAS detector using 2011 and 2012 LHC proton-proton collision data.* The European Physical Journal C, **74**(11):3130 (2014).

[68] SLAC NATIONAL ACCELERATOR LABORATORY. *Monte Carlo Simulations.* `https://theory.slac.stanford.edu/our-research/simulations`.

[69] H.-L. LAI, M. GUZZI, J. HUSTON, Z. LI, P. M. NADOLSKY ET AL. *New parton distributions for collider physics.* Phys.Rev., **D82**:074024 (2010).

[70] A. MARTIN, W. STIRLING, R. THORNE and G. WATT. *Parton distributions for the LHC.* Eur.Phys.J., **C63**:189–285 (2009).

[71] J. ALWALL, M. HERQUET, F. MALTONI, O. MATTELAER and T. STELZER. *MadGraph 5: going beyond.* Journal of High Energy Physics, **2011**(6):128 (2011).

[72] S. FRIXIONE and B. R. WEBBER. *Matching NLO QCD computations and parton shower simulations.* JHEP, **0206**:029 (2002).

[73] M. L. MANGANO, M. MORETTI, F. PICCININI, R. PITTAU and A. D. POLOSA. *ALPGEN, a generator for hard multiparton processes in hadronic collisions.* JHEP, **0307**:001 (2003).

[74] T. GLEISBERG, S. HOECHE, F. KRAUSS, M. SCHONHERR, S. SCHUMANN ET AL. *Event generation with SHERPA 1.1.* JHEP, **0902**:007 (2009).

[75] T. SJOSTRAND, S. MRENNA and P. Z. SKANDS. *PYTHIA 6.4 Physics and Manual.* JHEP, **05**:026 (2006).

[76] S. FRIXIONE, P. NASON and C. OLEARI. *Matching NLO QCD computations with parton shower simulations: the POWHEG method.* JHEP, **0711**:070 (2007).

[77] M. BÄHR, S. GIESEKE, M. A. GIGG, D. GRELLSCHEID, K. HAMILTON, O. LATUNDE-DADA, S. PLÄTZER, P. RICHARDSON, M. H. SEYMOUR, A. SHERSTNEV and B. R. WEBBER. *Herwig++ physics and manual.* The European Physical Journal C, **58**(4):639–707 (2008).

[78] T. SJÖSTRAND, S. MRENNA and P. SKANDS. *A brief introduction to PYTHIA 8.1.* Computer Physics Communications, **178**(11):852 – 867 (2008).

[79] ATLAS COLLABORATION. *The ATLAS Simulation Infrastructure.* The European Physical Journal C, **70**(3):823–874 (2010).

[80] GEANT4 COLLABORATION. *Geant4—a simulation toolkit.* Nuclear Instruments and Methods in Physics Research Section A: Accelerators, Spectrometers, Detectors and Associated Equipment, **506**(3):250 – 303 (2003).

[81] M. SCHOTT, G. SIRAGUSA, J. CUTH and T.-H. LIN. *Measurement of m_W at 7 TeV: Reconstruction of the hadronic recoil.* Technical Report ATL-COM-PHYS-2014-1435, CERN, Geneva (2014).

[82] M. HODGKINSON, D. TOVEY AND R. DUXFIELD FOR THE ATLAS COLLABORATION. *Energy Flow Reconstruction with the eflowRec Combined Reconstruction Software in Athena 15.6.9.8.* Technical Report ATL-PHYS-INT-2011-031, CERN, Geneva (2011).

[83] CHRIS YOUNG. *Particle Flow in ATLAS.* Overview talk in the Physics and Performance Week Meeting, `https://indico.cern.ch/event/270837/contributions/1610774/attachments/486436/672566/Presentation.pdf` (2013).

[84] J. SMITH, W. L. VAN NEERVEN and J. A. M. VERMASEREN. *Transverse Mass and Width of the W Boson.* Phys. Rev. Lett., **50**:1738–1740 (1983).

[85] ATLAS COLLABORATION. *Expected performance of the ATLAS experiment: detector, trigger and physics v.1-3* (2009). ArXiv:0901.0512.

[86] M. KRASNY, F. FAYETTE, W. PŁACZEK and A. SIÓDMOK. *Z boson as the "standard candle" for high-precision W boson physics at LHC*. The European Physical Journal C, **51**(3):607–617 (2007).

[87] F. FAYETTE, M. W. KRASNY, W. PŁACZEK and A. SIÓDMOK. *Measurement of $M_{W^+} - M_{W^-}$ at LHC*. The European Physical Journal C, **63**(1):33–56 (2009).

[88] G. BREIT and E. WIGNER. *Capture of Slow Neutrons*. Phys. Rev., **49**:519–531 (1936).

[89] C. BERGER. *Elementarteilchenphysik: Von den Grundlagen zu den modernen Experimenten*. Springer-Lehrbuch. Springer Berlin Heidelberg (2014). ISBN 9783642417528.

[90] D. BARDIN, A. LEIKE, T. RIEMANN and M. SACHWITZ. *Energy-dependent width effects in $e+e-$-annihilation near the Z-boson pole*. Physics Letters B, **206**(3):539 – 542 (1988).

[91] N. ANDARI, M. BOONEKAMP, R. HANNA and S. CAMARDA. *Measurement of m_W at 7 TeV: Physics modeling*. Technical Report ATL-COM-PHYS-2014-1436, CERN, Geneva (2014).

[92] G. BOZZI, L. CITELLI and A. VICINI. *Parton density function uncertainties on the W boson mass measurement from the lepton transverse momentum distribution*. Phys. Rev. D, **91**:113005 (2015).

[93] T. MELIA, P. NASON, R. RONTSCH and G. ZANDERIGHI. *W^+W^-, WZ and ZZ production in the POWHEG BOX*. JHEP, **1111**:078 (2011).

[94] S. DULAT, T.-J. HOU, J. GAO, M. GUZZI, J. HUSTON, P. NADOLSKY, J. PUMPLIN, C. SCHMIDT, D. STUMP and C.-P. YUAN. *New parton distribution functions from a global analysis of quantum chromodynamics*. Phys. Rev. D, **93**:033006 (2016).

[95] ATLAS COLLABORATION. *Measurement of the Z/γ^* boson transverse momentum distribution in pp collisions at $\sqrt{s} = 7$ TeV with the ATLAS detector*. Journal of High Energy Physics, **2014**(9):145 (2014).

[96] J. PUMPLIN, D. R. STUMP, J. HUSTON, H. L. LAI, P. M. NADOLSKY and W. K. TUNG. *New generation of parton distributions with uncertainties from global QCD analysis*. JHEP, **07**:012 (2002).

[97] P. GOLONKA and Z. WAS. *PHOTOS Monte Carlo: a precision tool for QED corrections in Z and W decays*. The European Physical Journal C - Particles and Fields, **45**(1):97–107 (2006).

[98] D. J. LANGE. *The EvtGen particle decay simulation package*. Nucl. Instrum. Meth., **A462**:152–155 (2001).

[99] ATLAS COLLABORATION. *Summary of ATLAS Pythia 8 tunes*. Technical Report ATL-PHYS-PUB-2012-003, CERN, Geneva (2012).

[100] ATLAS COLLABORATION. *A study of the Pythia 8 description of ATLAS minimum bias measurements with the Donnachie-Landshoff diffractive model*. Technical Report ATL-PHYS-PUB-2016-017, CERN, Geneva (2016).

[101] ATLAS COLLABORATION. *Muon reconstruction performance of the ATLAS detector in proton–proton collision data at* $\sqrt{s} = 13\,TeV$. The European Physical Journal C, **76**(5):292 (2016).

[102] ATLAS COLLABORATION. *Expected electron performance in the ATLAS experiment*. Technical Report ATL-PHYS-PUB-2011-006, CERN, Geneva (2011).

[103] ATLAS COLLABORATION. *Performance of the ATLAS muon trigger in pp collisions at* $\sqrt{s} = 8\,TeV$. The European Physical Journal C, **75**(3):120 (2015).

[104] ATLAS COLLABORATION. *Performance of the ATLAS trigger system in 2015*. The European Physical Journal C, **77**(5):317 (2017).

[105] T. HRYN'OVA and K. NAGANO. *Trigger Menu Strategy for Run 2*. Technical Report ATL-COM-DAQ-2014-054, CERN, Geneva (2014).

[106] ATLAS COLLABORATION. *Electron efficiency measurements with the ATLAS detector using the 2015 LHC proton-proton collision data*. Technical Report ATLAS-CONF-2016-024, CERN, Geneva (2016).

[107] ATLAS COLLABORATION. *Luminosity determination in pp collisions at* $\sqrt{s} = 8\,TeV$ *using the ATLAS detector at the LHC*. The European Physical Journal C, **76**(12):653 (2016).

[108] C. WU and C. WEIREN. *Reviews Of Accelerator Science And Technology - Volume 7: Colliders* (2015).

[109] O. BEHNKE, K. KRONINGER, G. SCHOTT and T. SCHORNER-SADENIUS. *Data Analysis in High Energy Physics: A Practical Guide to Statistical Methods*. Wiley-VCH, 1st edition (2013). ISBN 3527410589, 9783527410583.

[110] *ATLAS Computing Acknowledgements*. Technical Report ATL-GEN-PUB-2016-002, CERN, Geneva (2016).

Acknowledgements

On these final pages I would like to express my gratitude to all those who supported me, in one way or the other, during my past years at the university.

Firstly, I would like to thank Prof. Dr. Thomas Trefzger, who provided me an opportunity to join the chair of Physics and its Didactics throughout the years, as a Bachelor student, as a Master student and finally as a PhD student and who gave me access to the ATLAS research facilities. Without this support it would not have been possible to conduct my research.

Secondly, I would like to express my sincere gratitude to my PhD advisor Prof. Dr. Raimund Ströhmer for the continuous support of my study and related research, for his excellent supervision and guidance, his immense knowledge and his patience. The innumerable discussions on the W mass measurement, but also on physics in general, enlarged my knowledge immensely!

Doing research in modern particle physics usually means to work in a collaboration with scientists from all over the world. I can only mention a little aspect of the combined efforts. Of course ATLAS - as the biggest machine on earth - can only be run with the help of many, many people and very, very large computing resources [110].

I did my thesis project as part of the ATLAS W-mass working group. I would like to thank its current but also its former members, who always had an open mind for questions and new suggestions. My work was only possible with the infrastructure provided by the people of this group.

Next to my main thesis project I contributed to the muon software validation. Also here I would like to thank the people of this group for the assignments and the advice. I'd like to give special thanks to Jochen Meyer, who did not only start as my Bachelor thesis advisor, but continued to be really helpful over the past years and whom I could address with any question, especially when it comes to our beloved muons.

I would like to say my very special thanks to Daniel Adlkofer, Martin Baußenwein and Deb Sankar Bhattacharya, who have read carefully and critically through different parts of the thesis and provided very useful comments.

My time at the Würzburg Physics Department was made even more enjoyable because of my fellow students and colleagues, who became dear friends over time. A special remark goes to my offices mates, my lunch time buddies and the coffee break group - I will miss

all of you very much! It was such a lovely time and I really enjoyed your company during the many hours at work but also in our free time. The constant supply of distractions you provided were so much fun! I hope, the red sofa coffee breaks continues even without me being around. Keep up the wonderful team spirit, which developed over the past years and which I enjoyed so much!

During my time as a PhD student I was not only able to perform my personal research but to also bring a little piece of it to the public. Our outreach project, which is part of the Netzwerk Teilchenwelt, became an enjoyable part of my daily tasks. It was a funny coincidence, that one of the main topics we introduced to school students, were the W bosons. We looked for its decay into electrons and muons and tediously counted W^+ and W^- bosons in a graphical display. It could have not been closer to my personal research, although I admit that programming made my part much easier than the student's work ;) This was a wonderful opportunity to share my knowledge and improve my skills to explain and present complex matter to a group of curious students.

I would like to thank the people of the Netzwerk, especially our coordination in Dresden, for their continuous support, the warm social interactions and the help with any issues we faced. My sincere thanks also go to my local team - we organized so many events, I cannot count how often we ran to the printer, we carried out many masterclasses together and fetched a lot of dry ice on the way. What was always important to me, we also discussed a lot how to make things better, how to explain the complex physics in a more understandable way and planned for new events to come up. Without your support, it would have not been possible to manage this task! My thanks also go to the people who were not directly involved, but helped us out, whenever time was short. Thank you all!

Finally I would like to thank my family for their very warm and never ending support. During the last ten years, which I spent at the university for my study and my PhD thesis, I could always rely on you! Martin, you did not only suffer through any exam with me, but you always gave me a bit of extra motivation and moral support. Thank you for always being there!